Oscillatory Flows Round Combinations of Cylinders

Jianhong Wang

Doctor of Philosophy

The University of Edinburgh

1998

Abstract

Comprehensive experimental and computer simulational studies have been carried out to measure the velocity fields in oscillatory flows around combinations of cylinders and also the forces acting on the cylinders in oscillatory flow. Particle Image Velocimetry (PIV) has been used to measure the instantaneous velocity flow fields. The strengths of the vortices in the immediate vicinity of the cylinders were calculated. Simultaneous measurements have also been made of both the inline force and lift force using a transducer installed at the end of one of the cylinders. The numerical simulation study used a random vortex method with three overlapping meshes. Forces on the cylinders , together with the corresponding velocity vector fields, were simulated and comparisons made with the experimental results.

The combinations of cylinders were : (a) a square array of four cylinders with the dimensions chosen so that the array was an approximate scale model of the Heidrun Tension Leg Platform, (b) two cylinders in tandem with different distances between them, (c) a single cylinder. The Keulegan-Carpenter numbers (KC) were 5, 8, 10 ,13, 20, the Reynolds numbers (Re) were 2500, 4000, 5000, 6500 and 10000 and the viscous parameter ($\beta = R_e / KC$) was set at 500.

A comparison of the experimental results with the numerical simulations showed good agreement. For the single cylinder the main frequency component of the lift force shifted from the first harmonic, to the second, and then the third harmonic of the oscillatory flow when the KC number and oscillatory velocity increases . For the four cylinder array, in which the distance between the cylinders was greater than 2.5 times the cylinder diameter , the main frequency component of the lift force shifted from the first harmonic to the second as the KC number and oscillatory velocity increased; the third harmonic was relatively small. The strength and fundamental frequency of the force both increased faster than for the single cylinder case. For the two tandem cylinders, the fundamental frequency of the lift force was twice the frequency of the oscillatory flow when the distance between the two cylinders was smaller than 2.5

times their diameter. When the oscillatory velocity increased, the fundamental frequency of the force had a tendency to change to the oscillatory flow frequency, especially when the distance between the cylinders is 1.5 times their diameter. The strength of the lift force on the two cylinders was bigger than that on single cylinder. The quantitative analysis of vortex strength has shown, in general, the vortex strength increases with KC numbers for single cylinder and two tandem cylinders. For two cylinder cases a wider gap between the cylinders will make a larger and stronger vortex at same KC number condition. Some of the differences between the experimental and numerical results have been discussed.

Declaration

This thesis has been composed by myself and, except where stated, the work contained is my own.

Jianhong Wang

May, 1998

Acknowledgments

I wish to give my heartfelt thanks to my supervisors, Professor Clive Greated and Dr. Francis Barnes. Not only have they provided excellent support, guidance and advice throughout, but they have also given me, an overseas student, a lot of care and help and have shown me great kindness and friendliness. I am very happy to have had their supervision and I have learnt a lot from them, it is my luck in life.

My sincere appreciation goes to Professor Peter Stansby and Professor Haigui Kang for allowing their Vortex Method model and forces transducer, respectively, to be used in my research and for their good advice. I wish to thank them very much indeed.

I would like to thank my colleagues in the Fluids Group, they have made my time as a postgraduate researcher most enjoyable. They have provided continuing advice, help, suggestions, friendship to me. I have benefited from this and they will be kept in my heart forever. Special thanks to Callum Gray, David Hann, Alistair Young, Jim Buick , David Sharp, Alistair Arnott, John Cosgrove and David Forehand for reading and correcting many parts of this thesis. I would like to thank Frank Morris for his invaluable technical help and enlightenment and Mr. Jim King and the rest of the technicians for their excellent help.

My greatest gratitude is for my family. It is the love from my family that has supported me to finish my thesis. I am luck to have my family and all their understanding, patience, care, encouragement, help, happiness and humour. Many, many thanks for everything !

Table of Contents

Chapter 1

Introduction

1.1 General Background

The offshore industry has a history dating for over 50 years. Its birth was in the Gulf of Mexico where in 1947 the first platform was installed in 1947 in 6 metres of water . At present the industry is capable of drilling to a water depth of around 2300m (Mississippi Canyon), while for a producing well, the water depth record is around 1600m [1]. In the near future a water depth of 2500m or beyond will be achievable; the deep, deeper and beyond will become the direction of oil industry in the sea.

It has been estimated that the reserves in the major oily basins of whole globe, excluding gas, exceed 40 bbo (billion barrels of oil) , or 6.7 billion m^3, in water depths greater than 200 meters. The estimated reserves offshore of West Africa are 18bbo or 2.9 billion m^3, although these don't include recent deepwater discoveries in SE Asia and other emerging opportunities . The oil industry is already expected to invest between US$ 43 and 60 billion in the region in the next ten to twenty years. The two major oil corporations---EXXON and SHELL --- have been obtaining licences on a global basis, as is shown in Fig.1.1

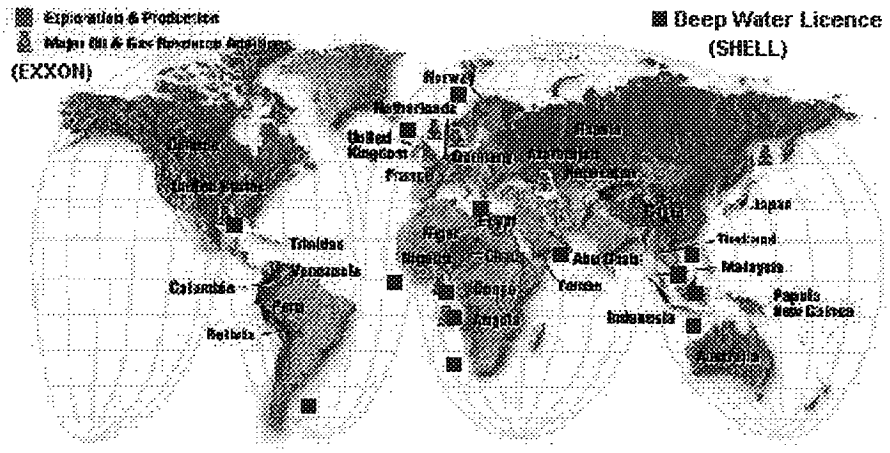

Fig. 1.1 The fields of EXXON and SHELL operation .

With oil drilling moving to deeper water, more exacting requirements for oil platforms have been put forward. The cost of the rigs has to be reduced for the oil market whilst the bearing of platform must be increased for harsh sea conditions and deep water. Due to these requirements, various oil platform systems have been developed or improved. Fig.1.2 shows production systems of the 1990s. These often combine subsea wellheads and manifold centres with several types of floating platforms. The role of fixed platforms , however, is not over.

Fig 1.2 illustrates several kinds of main oil platforms used in the sea : the template structure, the concrete gravity platform, the steel gravity platform , the Popeye subsea system, FPSO (Floating Production, Storage and Offloading unit) and TLP (Tension Leg Platform) . The template structure is especially suited to soft-soil regions. In regions where hard soil conditions exist and pile driving is more difficult, the concrete gravity platform is applied . This relies on its own weight to hold it in place against the large lateral loads from wind, waves, and current. The advantage of a semi-submersible over an FPSO is perceived to be its quiet motions in seaway; favourable for both the production risers and the separators. On the negative side, a semi-submersible has no storage capacity for produced crude, and thus requires a permanently moored storage tanker near it, a dual shuttle tanker scheme, or a pipeline to shore.

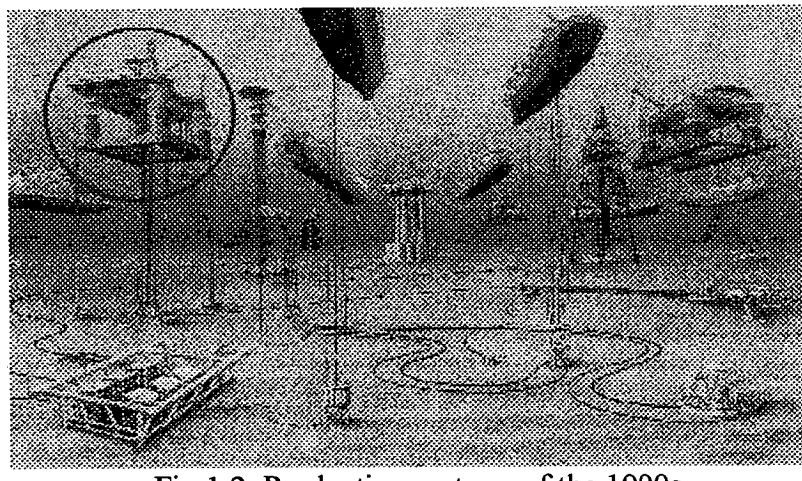

Fig.1.2 Production systems of the 1990s

In Fig.1.2 , the system marked by a circle is a TLP(Tension Leg Platform). The TLP concept [1] [4] was used for the first time in 1984 by Conoco in the British Hutton field in the North Sea. Its structure is semi-submersible. Under the platform deck its

four massive circular legs are connected from their ends by pontoons. The platform is moored by the tension mooring cables fixed to the sea bed.The advantages of TLP are not only that is able to carry out combined production and drilling operations but also it can be installed on many different areas. Its cost of a unit is not as strongly influenced by the water depth as is the case with fixed platforms, Just like all other floating systems, TLP's can in principle be reused at another location. Fig.1.3 is The Snorre TLP.

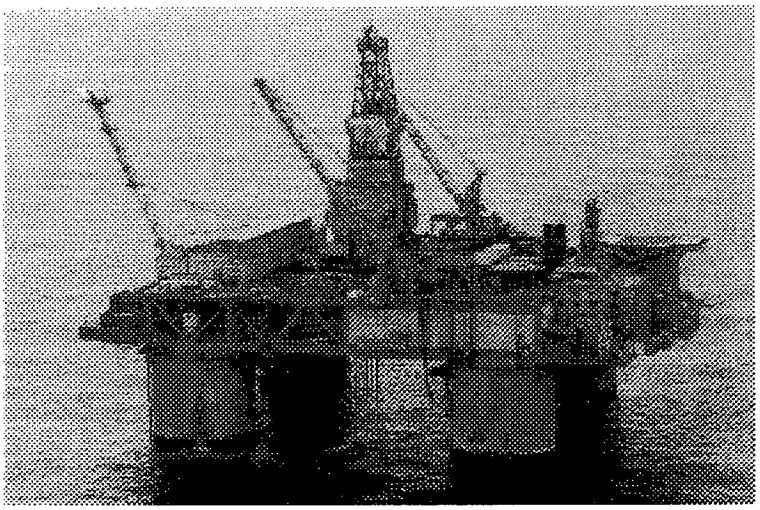

Fig.1.3 The Snorre TLP

This shows all features of a tension leg platform, except the most important one , the tethered mooring system, which remains completely under water. The water depth at this site is 309m. Snorre was installed in 1992.

In the tension-leg design, vertical members are used to anchor the platform to the seafloor. This upper part of the structure is designed with a large amount of excessive buoyancy so as to keep the vertical members in tension. Due to this tension, the platform remains virtually horizontal under wave action. Lateral excursions are also limited by the vertical members, since such movements necessarily cause them to develop a restoring force. A major advantage of the tension-leg concept is its relative cost insensitivity to increased water depths. At the present time, it appears that the main limitation on the tension-leg platform arises from dynamic inertia forces associated with the lateral oscillations of the platform in waves. These become significant at water depths of about 3000.[24]

As the oil industry moves into deeper waters the main challenges are related to improving the technology, as well as reducing costs and lead times for the field development components. Considering TLP are being installed in different far sea areas, it will be still a key reseach aspect to investigate and study wave forces acting on the four circular legs of TLP.

1.2 Force Measurement

In the design of offshore structure, the environmental loading exerted on the structure must be calculated or estimated prior to the structure being built and installed. The details of the environmental forces dominate the structure design, as can be seen from the sequence of events in the design of an offshore structure.

1 Identify need.

2 Evaluate environmental and local site conditions

3 Make preliminary design proposals with major emphasis given to the method of installation to be employed.

4 Evaluate these in terms of economics, construction and installation difficulties, foundation requirements, and so on, and select final design form.

5 Size and detail the chosen form to carry required loads and environmental forces.

6 Finally, evaluate the design to ensure that it can withstand the loadings associated with transportation to and installation at the offshore site.

In the above events, the sizing of the structure to carry the operational loads is a relatively simple matter, but the inclusion of environmental loadings generally requires several trial-and-error iterations since a change in size of a structural member changes the magnitude of the environmental loading exerted on it, and on the structure as a whole. In general , force measurement is an important element in offshore structure design.

In seeking the main features of the forces exerted on the structure by the flows , many simplified experiments have been carried out , one aspect of these experiments being oscillatory flow round cylinders.The cylinder is a basic structure in offshore engineering and provides a simple model of the legs of the oil platform; the oscillatory

flow is a standardized wave and can be represented by a sinusoid or cosine function. This kind of simplification can give the key features of research problem and is easy to set up as a model both in the laboratory and for numerical simulation.

The research has been mainly undertaken in two ways : laboratory experiments such as described in references [5,6,7] and computer simulation such as [8,9,10]. The research interests were generally focused on two problems : the force investigation [11,12,13] and the identification of flow features [14,15,16]. According to force properties, the forces acting on the cylinder were the inline force or drag force, lift force and pressure. The flow patterns were very helpful in understanding the force evolution on the cylinders due to the flows.

1.3 Patterns and Velocity of Flow

1.3.1 Velocity visualization

Before PIV (Particle Image Velocimetry) was developed, measurement of the velocity field of a flow was difficult. In laboratory experiments the flow patterns study and force measurement were normally carried out separately . The methods used to obtain the flow patterns could only give a qualitative analysis of flow fields, such as Dye, Smoke, Vapor and Tufts and the hydrogen bubble technique , etc.[25] The Laser Doppler Anemometry (LDA) technique, since its inception in 1966, has undergone continuous development, utilising the laser as a non-intrusive flow measuring system[17]. It is, however, only capable of measuring the flow velocity at a single point along with the velocity profile in some area. For providing a quantitative map of instantaneous flow velocities the PIV technique is much better than LDA. Using PIV , it becomes possible to investigate the relationship between the flow velocity (or vorticity) field and the forces and hence it is of great help in improving our understanding of flow behaviours and their forces. As the PIV technique and its analysis system are still currently in a developing stage , to apply PIV to obtain more detail of the flow round cylinders will give benefits in both theoretical research and in technique development.

PIV is a simultaneous, non-intrusive, full field flow measuring technique. It combines

flow visualisation with quantitative measurements and thus provides experimental fluid mechanics

with its most powerful tool so far. The brief outline of the PIV application is :

(1) Illuminate the flow using a pulsed laser for high-speed flow ,or CW (constant wave) laser for slower flows. In our experimental research a CW laser was used.

(2) If the fluid is seeded with suitable particles either method will then produce a series of images of the seeding either on film using a standard camera or else on computer screen by using a CCD camera. If the shutter is left open for a sufficient period then each seeding particle will produce a series of images whose spacing is directly proportional to the local velocity field.

(3) Divided the whole field into many interrogation areas with the same size; each small interrogation on the film, or on the screen of the computer , will contain the images of several seeding particles. By using an analysis system with auto- or cross-correlation, the PIV measurements can then be used to obtains a set of velocity vectors each of which is an average velocity on every interrogation area.

Regarding the laboratory flow simulation , there are a few alternative methods. For example, an oscillatory flow may be generated in the laboratory using a sinusoidal motion of water. In general, there are three kinds ways we can do this: by placing fixed cylinders beneath a standing wave [18], by using the resonance of a large U-tube[6] and by oscillating cylinders in still water[5]. The detail of the differences and identities of the methods can be found in Chapter 2. For obtaining the flow velocity field and simultaneous force record ,in our experiments we chose the third way; that is to oscillate the cylinder in the still water of a towing tank. The method is good at both giving an adjustable view area for taking a photograph and for installing a transducer for force measurement.

1.3.2 Vortex Patterns[20]

The analysis of vortex patterns is necessary for tracing the vortex shedding and understanding the flow features . The theories of the flow boundary layer and vortex shedding were built on the study of vortex patterns . The vortex patterns also show us the detail of flow action around the cylinders.

When a cylinder is subjected to a harmonic flow normal to its axis, the flow does not only accelerate from and deccelerate to zero but also changes its direction during each cycle. This produces a reversal of the wake from the downstream to the upstream side whenever the velocity changes sign. The separation points undergo large excursions. The boundary layer on the cylinder's surface may also change from fully laminar to partially or fully turbulent states and the Reynolds number may range from subcritical to post-supercritical over a given cycle. The vortices which have been or are being formed or shed during the first half of the flow period are also reversed around the cylinder when the wake is reversed and this process will give rise to a transverse force (as a consequence of their convection) with or without additional vortex shedding [21] . This effect is particuarly pronounced for amplitudes of flow oscillation for which the number of newly formed vortices during the period of flow reversal is not much greater than that of the vortices which have survived dissipation (laminar and or turbulent) and convected around the cylinder during the wake reversal. Particularly significant are the changes in the lift, drag, and inertial forces when the reversely-convected vortices are not symmetric.

The formation of vortices starts from vorticity generation in the boundary layer of the body surface. Fluid particles come to rest at the surface of a stationary structure in a flow. This is the well-known no slip boundary condition.Vorticity is generated in the boundary layers of structures in fluid flows. The boundary layer vorticity convects aft and coalesces into discrete swirling vortices in the near wake. These vortices generate oscillations of the near wake. Feedback from the near wake oscillations to the separation points leads to the periodic shedding of vortices with alternate-sign circulation giving the famous Von Karman vortex-street. Structural vibration can synchronize with the periodic vortex shedding, so that vortex shedding can induce damaging large-amplitude vibrations of flexible structures in fluid flows .Since the vortex pattern is a good tool to explain the activity of flow and interaction between flow and structure it is analysed many times in the thesis.

1.4 Numerical Simulation

In the research here a vortex method has been chosen as a numerical simulation tool, the particular method used being that developed by Prof. Stansby of Manchester University.

The development of vortex motions in fluid flow is responsible for some of the most fascinating aspects of fluid mechnics, such as mixing, shearing, transport and instability. In recent years vortex methods have emerged as a new class of powerful numerical techniques to analyze and compute vortex motions. It has been applied to a variety of fluid flow problems, its essential aspect being the focus on the vorticity of a flow.

1.4.1 Velocity And Vorticity

Traditionally, a flow is described by the Navier-Stokes equations, which are written in terms of the fluid velocity at any point and express Newton's law that force equals mass times acceleration. Since the vorticity ω is defined to be the curl of the velocity ($\omega = \nabla \times \mathbf{u}$), the vorticity may be derived from knowledge of the fluid velocity field. Meantime the reverse observation will be equally important: the velocity may be determined from the vorticity by means of an integral.

Equations of motion in terms of velocity are especially convenient when boundary conditions are introduced. For instance with a flow around an object then if we divide the velocity **u** into components normal and tangental to the solid surface, u_n and u_τ respectively, then we have the boundary conditions, $u_n = 0$, which means that fluid cannot pass through the obstacle, and $u_\tau = 0$ which enforces the fact that fluid in direct contact with the surface must itself not slip. However, the boundary conditions for the vorticity are not as straightforward.

The vorticity of a fluid emphasizes the positions and rotation strengths of the fluid mass at any time, some flow configurations are most readily understood through a consideration of the vorticity and a vorticity formulation could reduce the mathematical description to its essential components. The physical meaning of the tangential boundary conditions becomes apparent; by requiring that solid surfaces 'grab' on to the flow, a large shearing vorticity must be imparted to the flow. Thus the boundary conditions serve to confine the flow ($u_n = 0$) and add vorticity ($u_\tau = 0$).

The vorticity is the gradient of velocity, the enforced $u_\tau = 0$ giving a shear tangential velocity boundary layer in which velocity increases from zero to main flow velocity, so creating new vorticity . See Fig.1.4.

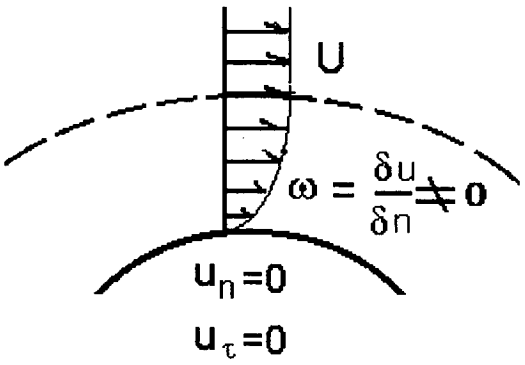

Fig 1.4 Boundary condition

In two special cases, a vorticity formulation becomes particularly simple. If the flow is inviscid, that is without viscosity or 'friction' in the flow, vorticity moves without diffusing. Alternatively, in the absence of any vorticity $\omega = 0$, the problem reduces to one of potential flow requiring the solution of Laplace's equation in the given domain.

1.4.2 Numerical Approximation

An approximation based on a vorticity formulation can focus computational resources by following the limited amount of vorticity in the system rather than computing the velocity **u** which exists everywhere.

The first numerical calculation of a flow using an approximation to the vorticity equation is due to Rosenhead[22] , who studied the evolution of a vortex sheet. Since the velocity may be recovered from the vorticity , and the flow is assumed inviscid , all of the dynamics are contained in the evolution of this infinitely thin sheet of vorticity, in a real physical flow, the sheet has a finite thickness. Rosenhead approximated the motion of the vortex sheet by discretizing the infinite line of vorticity into a finite number of discrete point vortices. Each point vortex induces a velocity field of the form $1/r$, where r is distance to the vortex. By superposition, the evolution of a finite collection of point vortices, initially placed along the line where $\omega \neq 0$, could be calculated.

1.4.3 Vortex Method

The vortex method as a practical technique began with the calculations of flow past a cylinder by Chorin[23] . Several factors contributed to the success of these calculations. First, discrete vortex elements were used , which induced a bounded velocity field with finite kinetic energy. Second, the diffusion of vorticity was simulated by means of a random walk imposed on the vortex trajectories. Third, the no-slip $(u_\tau = 0)$ tangential velocity boundary condition was enforced by the creation of new vorticity. Finally, the method was applied to viscous flow past cylinders, where integrated quantities such as the drag could be calculated and compared to the results of physical experiments.

1.4.4 Application Of The Method

Now vortex methods are a practical tool for computing a wide variety of engineering flows , these approaches linking together a variety of other techniques for approximating vorticity, such as point vortex methods, vortex-in-cell algorithms, and discrete Kutta-condition models[22].

The model I used in my PhD research was given by Professor Stansby and has been found to provide a satisfactory model. It includes random walks, vortex-in-cell algorithms and used an overlapping mesh system with different cell sizes for these meshes and can be applied to flows past multiple cylinders. The simulation outputs are the stream function, which can show the features of the flow field and force coefficients, and pressure distribution, to give the evolution of the force acting on the cylinder with time.

1.5 Aim of Present Study

The general aim for this research is to investigate and measure the instantaneous velocity field of the oscillatory flow round the cylinders and to find the features of the vorticity of the velocity fields, especially the vortex strength, whilst also measuring the evolution of the force acting on the cylinders . The key point is to obtain the simultaneous character and data regarding the flow fields and forces acting on the cylinders. On the other hand, the numerical simulation is performed to give some predictions of the velocity field and force for cases which are difficult to investigate in

laboratory experiments, and to find further applications of the model. These are very helpful to understand better the mechanisms and processes of the oscillatory flow past the combination of the cylinders. They are also important references for offshore engineering .

In particular, the experimental parameters and combined configurations of the cylinders in the research described here are different from the majority of work done by other people ; and it is a new experimental method that the velocity field and force evolution are recorded at the same time in the research on the oscillatory flow around the cylinders. To combine the PIV and force measurment in one experiment has been done by almost no one before --- these that have shown the significance of our research here.

1.5.1 Parameters

One of the important parameters of the flow is the amplitude of fluid motion relative to cylinder size, which is usually expressed as the Keulegan-Carpenter number. For a oscillating cylinder in still water tank, KC=2πA/D, where A is the amplitude of the cylinder motion and D is the cylinder diameter. In my research, the Keulegan-Carpenter(KC) numbers chosen for single cylinder and the four cylinder array were 5, 8, 10, 13, 20. These KC numbers were in a zone in which lift force coefficients varied significantly.The gap between two neighbour cylinders in the four cylinders array is 79mm. For the two tandem cylinders, the KC numbers were 5, 8, 10, but the distance between the two cylinders was changeable between 50mm and 25mm. For the small amplitude oscillatory flow study, KC number could be viewed as a ratio of the amplitude of oscillatory flow to the diameter of the cylinder, so a smaller KC number means a smaller amplitude oscillatory flow. Because of the limitations of mechanical properties of PIV and the experimental model, KC numbers were greater than 5 in our experimental situation. For these KC numbers a better PIV record of the velocity field can be obtained. These KC number were also comparable the numerical simulation by the vortex method model. The Reynolds number were 2500, 4000,5000, 6500 and 10000 .The viscous parameter $\beta = R_e / KC$ was set at 500.

1.5.2 Laboratory Experiments

(1) Single cylinder cases, the measurement of instantaneous velocity fields, the calculation of the vorticity field and vortex strengths, the test of in-line and lift forces. The experiments were for all five different KC numbers

(2) Two tandem cylinders, there were the two distance arrangements, which were represented by a ratio of distance between two centres of two cylinders and their diameter (*Distance/diameter*), 2.0 and 1.5. Measurements were made for three values KC number, 5, 8, 10 . The instantaneous velocity fields, vorticity fields, vortex strengths, in-line force and lift force were measured .

(3) Four cylinders array , same as the single cylinder cases. No distance change.

1.5.3 Numerical Simulation

Most of the experimental cases have been simulated. Values were found for the force coefficients of the inline force, lift force and the pressure distribution on the surfaces of the cylinders. The flow fields were vector fields, the stream function fields and the streamline field. The vorticity fields were also calculated . For single cylinder, KC numbers are 5, 8, 10, 13 and 20 . In the case of two cylinders only the values 5,8,10 were used . For the four cylinder array, the KC number are 5, 8, 10 in computer simulation and the values are 5,8,10,13 and 20 in lab experiment.

1.6 Reference

[1] T.N.Warren , Offshore The Future Deepens, BOSS'97 , July,1997.The Nethelands

[2] An Open University oceanography course team, The Ocean Basins: Their Structure And Evolution. 1991, Pergamon Press Ltd, Headington Hill Hall, Oxford, England.

[3] An annual report of EXXON , Netscape : http://www.exxon.com/

[4] H. Veldman, G. Largers, Offshore 50 Years, Chapter 6, 1997, Delft, The Netherlands

[5] C.H.K. Williamson, Sinusoidal flow relative to circular cylinders, (1985), J. Fluid Mech. Vol. 155, pp141-174.

[6] D.J. Maull and M.G.Milliner , Sinusoidal flow past a circular cylinder, (1978) Coastal engineering, vol. 2 pp149-168.

[7] C.Barbi, D.P.Favier, C.A.Maresca, Vortex shedding and lock-on of a circular cylinder in oscillatory flow, (1986) J. Fluid Mech. Vol.170, pp527-544.

[8] P.A.Smith and P.K.Stansby, Viscous oscillatory flows around cylindrical bodies at low keulegan-carpenter numbers using the vortex method, (1991) J. of Fluids and Structures , vol 5, pp339-361.

[9] D.M.Greaves and A.G.L.Borthwick, Adaptive quadtree grids applied to the computation of flow past circular cylinders , (1997) Proceedings of BOSS'97, Vol . 2 pp 11-24.

[10] A. Slaouti and X.L.Bao, On the use of the morison equation in the vortex shedding range of keulegan-carpenter numbers from 6 to 22, (1997) Proceedings of BOSS'97, Vol.2, pp47-63.

[11] P.B.Bearman, M.J.Downie, J.M.R.Graham and E.D.Obasaju, Force on cylinders in viscous oscillatory flow at low keulegan-carpenter numbers, (1985), J.Fluid Mech. Vol 154, pp337-356.

[12] P.W.Beaman, J.M..R.Graham, E.D.Obasaju and G.M.Drossopoulos ,The influence of corner radius on the forces experienced by cylindrical bluff bodies in oscillatory flow, (1984), Applied ocean research, vol. 6, no. 2,pp83-89.

[13] P.K.Stansby, Forces on a circular cylinder in elliptical orbital flows at low keulegan-carpenter numbers, (1993) Applied ocean Research. Vol.15, pp281-292.

[14] K.Lam and W.C.Cheung, Phenomena of vortex shedding and flow interference of three cylinders in different equilateral arrangements, (1988), J.Fluid Mech. Vol 196, pp1-26.

[15] T.Sarpkaya and W.Butterworth , Separation points on a cylinder in oscillating flow, (1992) , J. Offshore mechanics and Arctic Engineering, vol114, pp28-35.

[16] P.K.Stansby and A.Slaouti, Simulation of vortex shdding including blockage by the random-vortex and other methods, (1993), J.numerical methods in fluids, vol.17, pp 1003-1013.

[17] T.S.Durrani and C.A.Greated , Laser systems in flow measurement (1977) Plenum Press, New York

[18] G.H. Keulegan, L.H. Carpenter, Forces on cylinders and plates in an oscillating fluid, (1958) J.Res. Nat.Bur. Stand., 60(5)

[20] Sheldon I. Green (Editor) Fluid Vortices, (1995) Kluwer Academic Publishers,

The Netherlands.

[21] Sarpkaya & Isaacson, Mechanics Of Wave Forces On Offshore Structures, 1981, Van nostrand Reinhold Company Inc. New York

[22] Karl E. Gustafson, James A. Sethian (Editors) , Vortex Methods and Vortex Motion, 1991, Society for Industrial and Applied Mathematics, U.S.A

[23] A.J.Chorin, Numerical study of slightly viscous flow, J.Fluid Mech. 57(1973) pp.785-796.

[24] T.H. Dawson, Offshore Structural Engineering, (1983) Prentice-hall Inc. New Jersey ,U.S.A.

[25] W.Merzkirch, Flow Visualization , 1974, Academic Press , New York and London.

Chapter 2

Experimental Methods And Technique

2.1 Introduction

In order that we can investigate the behaviour of oscillatory flow around combinations of cylinders in the laboratory, some modifications had to be done to the facilities. Since the PIV technique presently used at Edinburgh can only measure two dimensions of velocity, the experimental oscillatory flow is limited to a two-dimensional flow normal to the cross-section of the model of the legs of a TLP. The oscillatory flow is simulated using a towing tank . The towing tank had a bigger visible experimental area and a simpler structure than the U-tube apparatus could have. The oscillatory flow is generated by moving the model sinusoidally in still water. Since it is known[1] that the resulting velocity fields are kinematically identical to these encountered by stationary cylinders in oscillatory flow. The proof of this is as follows: In the case of a stationary cylinder and an oscillatory flow passing it, we have an inertial frame. In the situation of a cylinder doing oscillatory motion in a still water, we have a non-inertial frame. Considering general 3 dimensional conditions, we can describe the two frames as (X,Y,Z, T) --- inertial frame and (X', Y', Z', T') --- non-inertial frame (Fig.2.1).

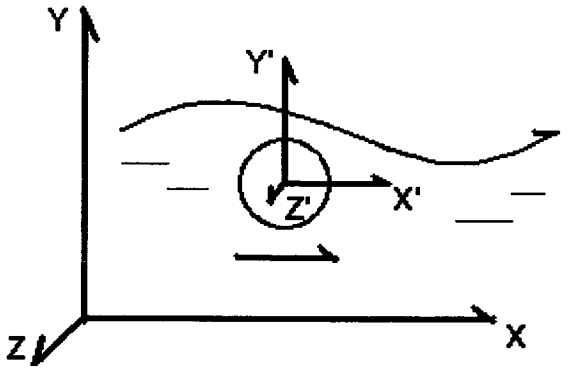

Fig. 2.1 Inertial frame and non-inertial frame

The non-inertial frame oscillates in relation to the inertial frame. The varibles relationship between the two frames in their origins are :

$$X = A\sin\omega t \ , \ Y, \ Z, \ T \qquad (2.1)$$

$$X' = X - A\sin\omega t,\quad Y' = Y,\quad Z' = Z,\quad T' = T \tag{2.2}$$

For convenience, we will write (X, Y, Z) $\equiv (x_1, x_2, x_3)$.

For incompressible flow, the Navier-Stokes equation and continuity equation in the inertial frame are:

$$\frac{\partial u_i}{\partial t} + u_j \frac{\partial u_i}{\partial x_j} = -\frac{1}{\rho}\frac{\partial p}{\partial x} + \nu \frac{\partial^2 u_i}{\partial x_j^2} \tag{2.3}$$

$$\frac{\partial u_j}{\partial x'_j} = 0 \tag{2.4}$$

where i = 1, 2, 3. j =1, 2, 3

Consider the relationship of the derivative between the two frames

$$\frac{\partial f}{\partial x} = \frac{\partial f}{\partial x'}\frac{\partial x'}{\partial x} + \frac{\partial f}{\partial t'}\frac{\partial t'}{\partial x} = \frac{\partial f}{\partial x'} \tag{2.5}$$

$$\frac{\partial f}{\partial t} = \frac{\partial f}{\partial x'}\frac{\partial x'}{\partial t} + \frac{\partial f}{\partial t'}\frac{\partial t'}{\partial t} = -\frac{\partial f}{\partial x'}a\omega\cos\omega t + \frac{\partial f}{\partial t'} \tag{2.6}$$

Here f is any variable. From (2.2), $\frac{\partial x'}{\partial x} = 1$, $\frac{\partial t'}{\partial x} = 0$, $\frac{\partial t'}{\partial t} = 1$

Hence :

$$\frac{\partial u_i}{\partial t'} - a\omega\cos\omega t\frac{\partial u_i}{\partial x'} + u_j\frac{\partial u_i}{\partial x_j'} = -\frac{1}{\rho}\frac{\partial p}{\partial x_i'} + \nu\frac{\partial^2 u_i}{\partial x_j'^2} \tag{2.7}$$

$$\frac{\partial u_j}{\partial x_j'} = 0 \tag{2.8}$$

The origin of the non-inertial frame moves with velocity :

$$(u' = \frac{\partial x'}{\partial t'} \ , \ v' = \frac{\partial y'}{\partial t'} \ , \ w' = \frac{\partial z'}{\partial t'}) = (\ a\omega \cos\omega t \ , 0 , 0) \quad (2.9)$$

Hence :

$$u' = u - a\omega \cos\omega t \ , \quad v' = v \ , \quad w' = w \qquad (2.10)$$

or $$u = u' + a\omega \cos\omega t \ , \quad v = v' \ , \quad w = w' \qquad (2.11)$$

Now equation (2.7) , using (2.11) , becomes :

$$\frac{\partial u'}{\partial t'} - a\omega^2 \sin\omega t' \delta_i - a\omega \cos\omega t' \frac{\partial u'_i}{\partial x'} + u'_j \frac{\partial u'_i}{\partial x'_j} + a\omega \cos\omega t' \frac{\partial u'_i}{\partial x'_j} \delta_i$$

$$= -\frac{1}{\rho} \frac{\partial p}{\partial x'_i} + \nu \frac{\partial^2 u'}{\partial x'^2_j} \qquad (2.12)$$

Here $\delta_i = 1$ if $i = 1$ (u) ; $\delta_i = 0$ if $i \neq 1$ (v,w).

The equation (2.12) can be simplifed :

$$\frac{\partial u_i'}{\partial t'} - a\omega^2 \sin\omega t' \delta_i + u_j' \frac{\partial u_i'}{\partial x_j'} = -\frac{1}{\rho} \frac{\partial p}{\partial x_i'} + \nu \frac{\partial^2 u_i'}{\partial x_j'^2} \qquad (2.13)$$

and

$$\frac{\partial u_i'}{\partial t'} + u_j' \frac{\partial u_i'}{\partial x_j'} = -\frac{1}{\rho} \frac{\partial p}{\partial x_i'} + a\omega^2 \sin\omega t' \delta_i + \nu \frac{\partial^2 u_i'}{\partial x_j'^2} \qquad (2.14)$$

Let $p' = p - \rho a\omega^2 x \sin\omega t'$, or $p = p' + \rho a\omega^2 x \sin\omega t'$

Then $$-\frac{1}{\rho} \frac{\partial p}{\partial x'} = -\frac{1}{\rho} \frac{\partial p'}{\partial x'} - a\omega^2 \sin\omega t' ,$$

So equation (2.14) becames :

$$\frac{\partial u_i'}{\partial t'} + u_j' \frac{\partial u_i'}{\partial x_j'} = -\frac{1}{\rho}\frac{\partial p'}{\partial x_i'} + \nu \frac{\partial^2 u_i'}{\partial x_j'^2} \tag{2.15}$$

Using (2.11) the equation (2.8) can be rewritten into :

$$\frac{\partial u_j'}{\partial x_j'} = 0 \tag{2.16}$$

Now equations (2.15) and (2.16) are identical to equations (2.3) and (2.4).

The motion in the non-inertial frame is governed by the same equations as those in the inertial, but with a modified pressure field. Thus, solutions will be the same in boundary value problems ,

$\vec{u} = -\vec{i}\,U$ at ∞

$\vec{u} = 0$ at r=a (a = radius of cylinder)

$\vec{u}' = -\vec{i}\,U$ at ∞

$\vec{u}' = 0$ at r=a (a = radius of cylinder)

The only difference is that in the case of oscillatory flow past a fixed cylinder the pressure includes the additional term $\rho a\omega^2 x \sin\omega t'$. Its gradient is just that required to accelerate the flow with magnitude $\frac{\partial u}{\partial t}$. When integrated around the cylinder, the additional term gives rise to an inertia force per unit length :

$$\rho \pi r^2 \frac{\partial u}{\partial t} = \rho(\pi d^2/4)\frac{\partial u}{\partial t} \tag{2.17}$$

For this reason, the inertia coefficient in Morison's force equation is written as $C_M = 1 + C_m$, this is for the case of an oscillatory flow past a fixed cylinder . C_m only for the case of oscillation of a cylinder in still fluid [27]. The lift force, caused by vortices shedding, is normal to the inertial force direction. So there is no difference between the inertial and noninertial frames. Thus data obtained through oscillation of a cylinder in still water is applicable to the wave force problem, or more precisely, the oscillation of a cylinder in still water is kinematically identical to the oscillation of the water past a fixed cylinder.

2.2 Design Of The Experimental Model

A model of the legs of a TLP was made using transparent plastic tubes. Four tube cylinders are arranged into a square array. A ratio of diameter of cylinder and distance between centres of any two cylinders are derived from a real TLP. Their sizes are shown in Fig.2.2 .

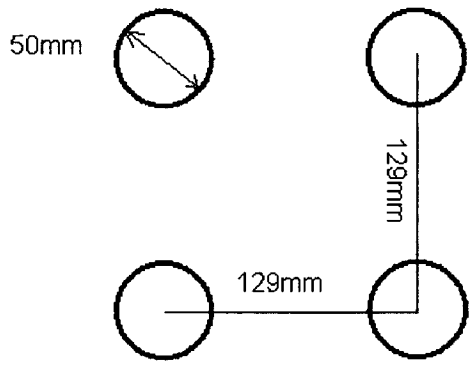

Fig 2.2 Four cylinders square array

Because the flow has been assumed as two dimensional, along the direction of cylinder length flow motion was consided as the same on any cross-section. Thus in experiments, the position of the chosen two dimension cross section was adjustable.The ends of the cylinders were fixed onto two transparent plastic discs which were then attached to the trolley through two perspex plates. The experiment was carried on in a glass towing tank. The cylinder model was moved sinusoidally in the tank by the use of a computer controlled trolley. A photograph of the apparatus is shown in Fig2.3

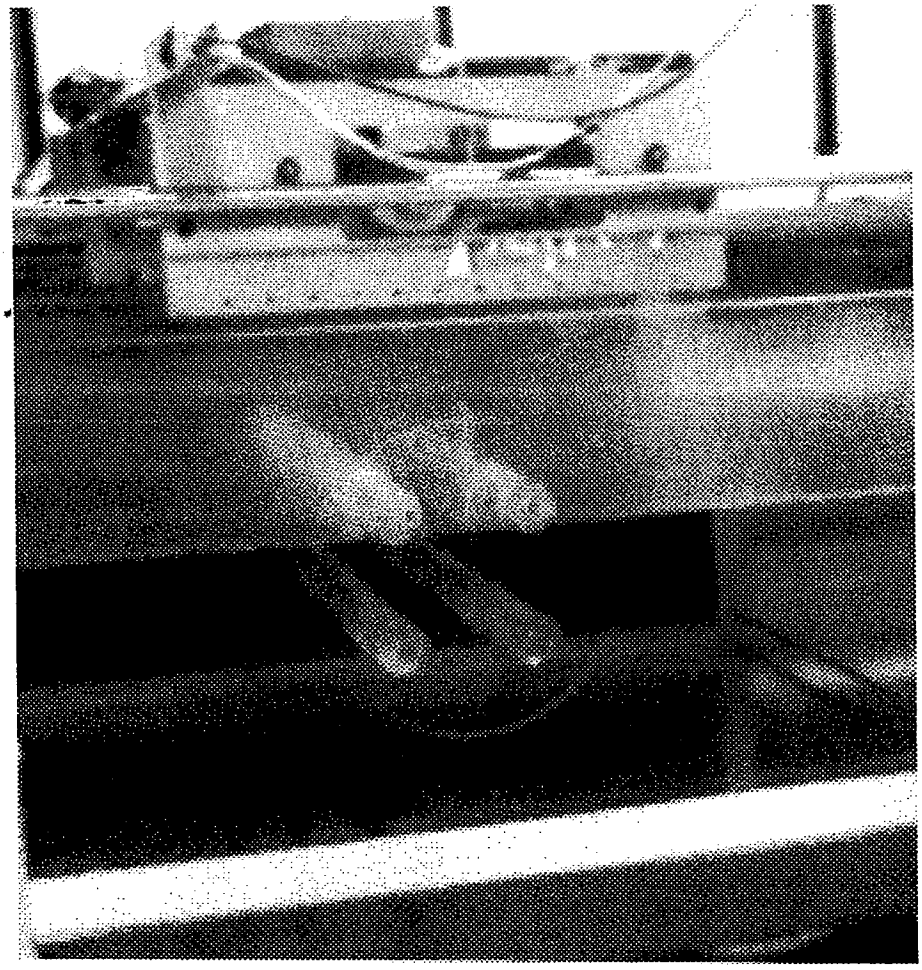

Fig 2.3 Four cylinder model and experimental facilities

In order to investigate the basic situation of oscillatory flow round single cylinder, a single circular cylinder model (Fig 2.4) was also made. It was easy to change the four cylinders model into one cylinder or two cylinders.

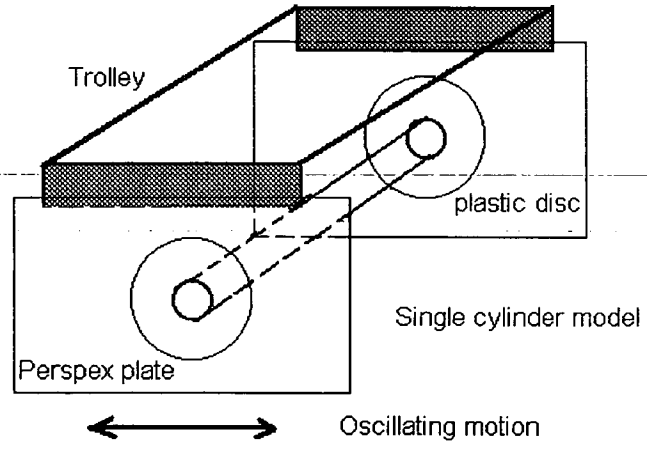

Fig 2.4 Single cylinder model

To investigate the influence of different separation distances between two cylinders, two tandem cylinder models were designed. Because the ratio of distance between two neighbour cylinders and the diameter of cylinder was 2.5 :1 for the four cylinders array case (129mm : 50mm $\approx$2.5 : 1), the ratios for the two cylinder case was chosen as 2 : 1 and 1.5 : 1 . The distances between two centres of cylinders were 100 mm and 75mm as shown in Fig 2.5

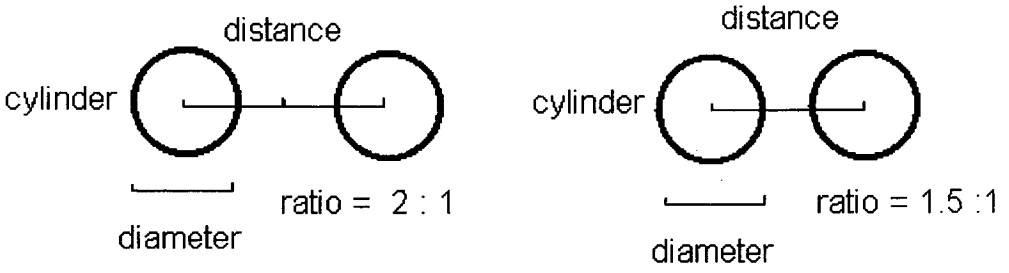

Fig 2.5 Two tandem cylinders models

A transparent plastic material was used to make the cylinders in order that the laser ray could pass through it easily and illuminate the areas round cylinders. Several holes were made at the ends of the cylinders in order that water could fill the model when it was submerged (fig 2.6). This prevented light reflection and refraction effects caused by air in the tubes

Fig 2.6 A transparent plastic cylinder

The dimensions of the glass tank are 6 meters long and 1 meter wide with a water depth of 0.5 meter. The distances from the model to the bottom of the tank and from the model to water surface are bigger than three times of the diameter of cylinder so that we could avoid the influence of boundary conditions of the glass tank[2].

A camera (Nikon 801) with a 50mm lens was used in the experiment. It was fixed on a tripod which was put at a side of the tank and faced one end of the model. An underwater

CCD camera for PIV flow mapping[3] has been developed, but one underwater CCD could only measure the velocities in a fan segement area that is in one side of a cylinder (Fig. 2.7)

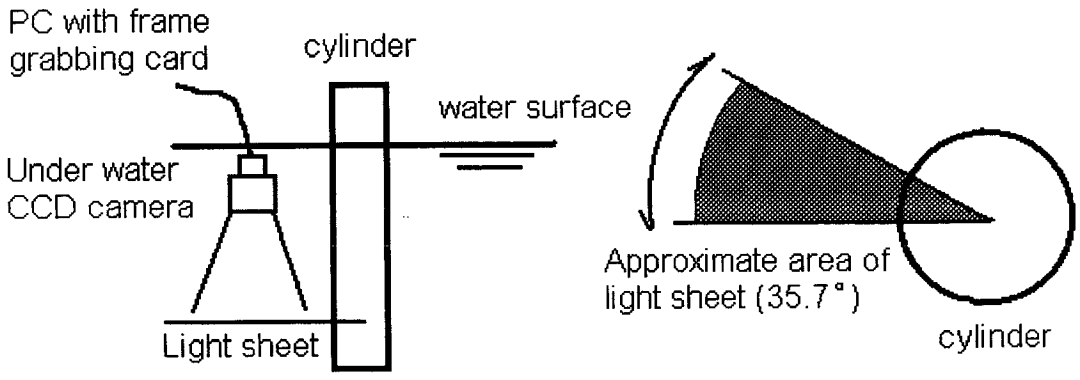

Fig 2.7 A cross section faces underwater CCD.

The velocity measurement can be only done in the area illuminated by laser light sheet, therefore for investigating a larger area including cylinders and their surroundings, an externally mounted camera was more suitable. The camera could not be placed on top of the tank, for two reasons : the first was that the ripple on the water surface caused by the model motion in still water would scatter the laser light and make picture blurred, the second was that the trolley's frame would cover many parts of the cylinder model suspended beneath it.

2.3 PIV Technique

PIV (Particle image velocimetry) is a highly accurate three stage method of producing detailed two-dimensional vector representations of flows in both liquids and gases[4,5] Its use is increasing in laboratories worldwide but laser doppler anemometry(LDA) is still widely used since it can make a high speed data logging .

The first stage in the PIV method is to illuminate the measurement flow area which has been seeded by neutrally buoyant seeding particles. The illuminating light is strobed, pulsed or scanned in order to achieve a number of images of the particles.

The second stage is to record the image of the buoyant seeding particles in the flow.

This is done by either photographing the flow with a still camera to produce a negative or using a CCD(Charged-Coupled Device) camera to store a bitmap file in a computer. The developed negative shows the images of the seeding particles as dark dots against a pale background. The bitmap file in computer from CCD camera grabbing or a scanning machine of negative shows the seeding particles as white dots against a dark background (Fig. 2.8)

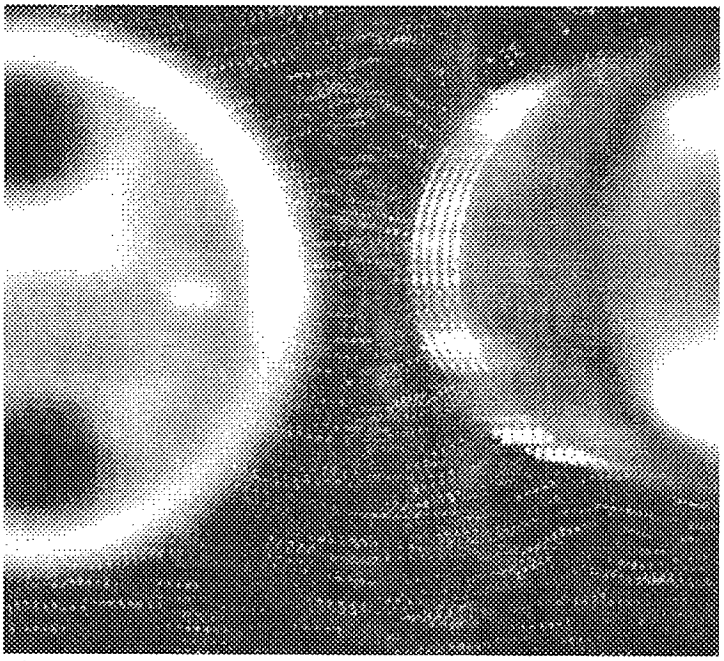

Fig 2.8 Scanned bitmap file from a developed PIV negative showing multiple particle images

The stroboscopic laser illumination ensures that several exposures of each seeding particle are recorded on each frame of film and this clearly shows the movement of each particle while the camera shutter is open.

The third stage of the method is the automated analysis of the negative, or its bitmap file to yield the flow velocity information. The proceeding is done by a software called VIDPIV.

2.3.1 Illumination System

Illumination for the PIV system is provided by a continuous wavelength Argon-ion laser with a peak output of 15W and a wavelength of about 490nm. Helium-Neon and Argon-ion are two types continous wave lasers which are commonly utilised as light

source in PIV. Helium-Neon lasers emit red light with a wavelength of 638nm. The output power ranges up to around 100mW, the beam is narrow (around 1 mm) and remains highly collimated due to the small divergence of the beam path. Helium-Neon lasers are typically utilised as a light source in low velocity flows where the flow region is small. Argon-ion lasers are used in faster moving flows and where a larger region of the flow field is of interest. Argon-ion lasers emit both green and blue radiation in 400-530nm range and have a power output ranging up to 30 W.

For safety reasons the laser is situated away from the flume in a room by itself . The arrangement is good since all of the noisy, heat-producing accessories which go along with such a high powered laser can be conveniently hidden behind the door.The laser beam travels to the flume along a totally enclosed path at floor level, its precise direction controlled by four independently adjustable mirrors. The laser beam can also be diverted to other experimental areas within the laboratory.

There are two means of providing the stroboscopic laser illumination required by PIV. One is to expand the laser beam into a sheet by shining it through a cylindrical lens .The pulsing of the light can then be controlled by shining the laser beam through a beam chopper, for example, a spinning disc with a gap cut in it [6]. Its diagram is shown in Fig.2.9.

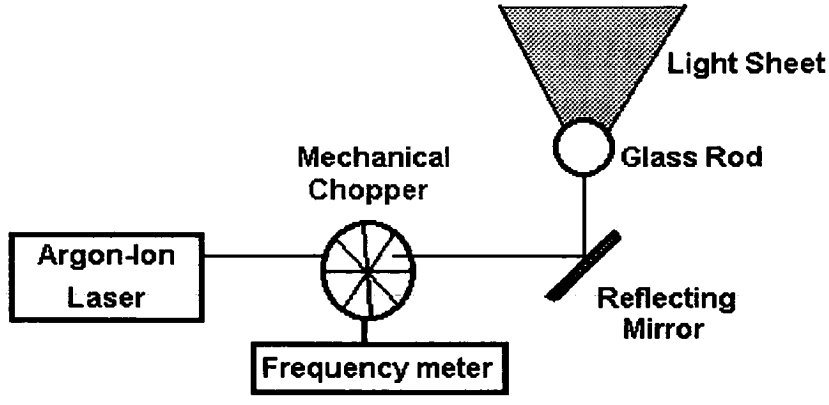

Fig 2.9 An expanding beam system

From Fig 2.9 it can be seen that a continuous wave laser can be chopped into pulses, then expanded into a fan shape light sheet. This leads to problems of over-exposure in

the middle of the flow field and loss of images due to under exposure at the edges. The other method which is employed at the University of Edinburgh, is the scanning beam method. A diagram of the method used for this study is shown in Fig2.10.

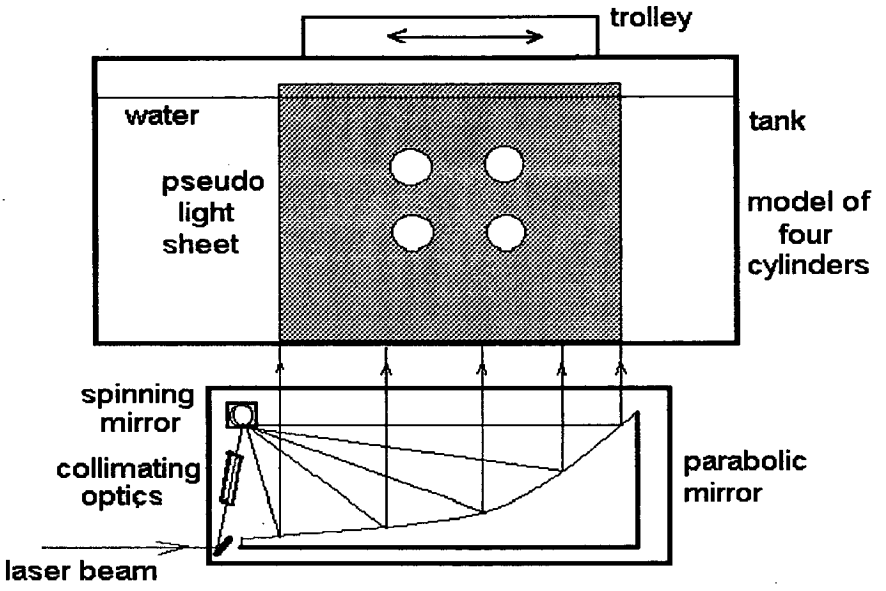

Fig. 2.10 The scanning beam system

For this method the laser beam is directed, via focusing and collimating lenses, on to an eight sided spinning mirror under the flume which reflects the light onto a parabolic mirror. The spinning mirror is situated at the focus of the paraboala ensuring that the beam is always reflected vertically upward from the parabolic mirror. The light sheet can illuminate a 1m long section of the flow, and is only 2-3mm thick. As the octagonal mirror spins the laser beam is scanned up the parabola and the effect in the flume is to produce a vertical laser beam which scans through the water from left to right eight times during each rotation of the mirror.(See fig.2.11)

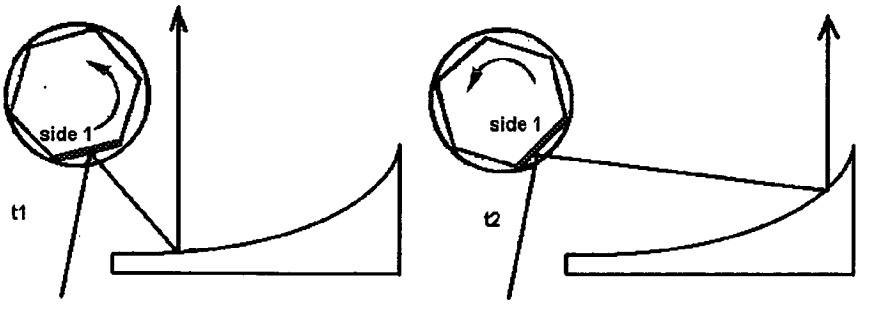

Fig 2.11 The procedure for scanning the beam

The parabolic mirror is constructed from a machined plate of aluminium, 20mm thick. The reflecting surface is made by optically coating a thin strip of perspex and carefully sticking this to the parabolic face of the aluminium plate. In geometric optics, a parabolic mirror of radius L will collimate a diverging light source that is place at L/2. In the PIV a parabolic mirror can maintain a large wide vertical light sheet , minimise light losses and ensure that seeding particles getting the same light intensity.

The focusing and collimating lenses is an achromatic telescope arrangement. The beam from the Argon-ion laser has nine wavelengths, consequently achromatic lenses can focus the beam much better than conventional lenses. The multiple wavelengths are formed by transitions from several excited states of the singly ionised Argon atom. The most predominant one has a wavelength of 488nm. Although it is possible to select a particular wavelength output, this is not desirable for this application because of the corresponding power reduction. Fig 2.12 gives a diagram of the collimating optics .

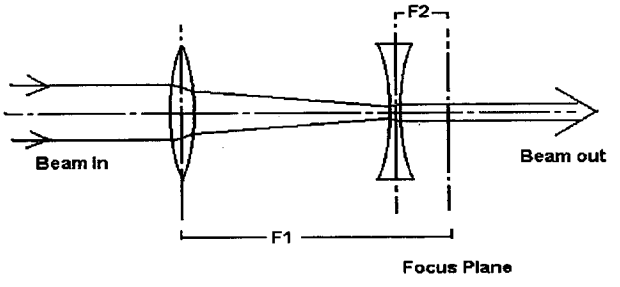

Fig 2.12 An achromatic collimating arrangement

The second cocave lens prevents the beam from converging to the focus of the first convex lens and ionising air at the point where the light power is at its most intense.[7] The rotation rate of the spinning mirror can be varied from about 15rps to 250rps enabling PIV measurements to be carried out on flows of up to $10 ms^{-1}$ At higher rotation rates the scanning laser beam through the glass bottom of the flume appears as a sheet of light within the flume. The box containing the scanning beam system sits on rails under the flume so it can be easily moved along, allowing PIV to be used in a large part of the flume.

The main advantage of the scanning beam systerm is that it provides much higher levels of illumination than the cylindrical lens system since each seeding particle in the

water is illuminated by the full intensity of the laser beam during each scan rather than by a lower intensity expanded beam.So the rotating mirror is a good device.

The rotating speed can be determined through a calculation as follow :

1) seeding diameter $\approx 70\,\mu m$.(it is a mean particle diameter) The distance between two seeding particles (no overlap) should be 140 μm or $140*10^{-6}$ m .

2) $Time = \frac{Distance}{Velocity}$. If Vmax of the seeding particle is 130 mms^{-1} or $130*10^{-3} ms^{-1}$, the time of particle moving will be $T = \frac{140*10^{-6}}{130*10^{-3}} = 0.00108s$. If we want to get 5 images on a negative, the times will be $T*5 = 0.0054s$

3) Rotating mirror speed: the mirror has 8 faces, every face gives out a flash. So a frequency of flash will be $f = \frac{1}{8T} = \frac{1}{8*0.0054} = 23.1Hz$ (23rps).

2.3.2 Shifting System

PIV in its basic form derives velocity information from the separation of multiple particle images on a photograph. In general there is no way to tell which image is the first, and thus there exists an inherent ambiguity in the sense of the velocity measurement obtained at any given point. In many cases, there are both forward and reverse flows present. Also PIV in its basic form cannot positively measure a region of zero flow velocity--- it relies on measuring the separation of correlated particle images, and if the first and second images overlap, then no correlated separation will be visible and thus no velocity measurable.

To resolve the problems there are three methods present. One is the 'tracking method'. In the expanding beam system, some different size cuts were made on the chopper. So the particles are illuminated by a different light intensity in sucessive image records. According to the brightness of the particle images the direction of particle motion can be determined. But for zero velocity , it is still a problem because of the particles overlapping. On the other hand, the distribution of velocity that were measured from the tracking method is irregular, so vorticity calculation will be not easy. In the case the vorticity calculation can only be done after interpolating the irregular velocity data into a regular mesh. But any data interpolation will reduce the accuracy of the original

data.

Another method is to use crosscorrelation analysis. It acquires the first and second exposures on separate frames and then crosscorrelating produces a function with a single correlation peak. Because the positions of particles for successive light pulses are recorded separately, the direction of the flow is resolved unambiguously. Because the frames are separate, particles can be recognized and need not be displaced by more than one image diameter. So it can give a much extended dynamic range and can be used in the areas where the particle images number is less than three pairs within an interrogation area. This method is most convenient when using the CCD or video recorder. But it requires the CCD to have a high resolution and high data transfer rate (frame rate).

The other method is the shifting systerm. The normal optical camera has a high resolution, but a low frame rate, because of its mechanical properties. So the key problem is to find the displacement of particle images on a negative. The shifting system imposes a known shift on the flow vectors, and forces the sense of direction to be the same for each one. If the shift velocity is sufficiently large the second image will always be displaced in the direction of the shift relative to the first image and particle images which would have been coincident in areas of very low or zero flow velocity are now separated. There is no longer any ambiguity.The shift can be subsequently subtracted from the measured velocities to give the true flow field. The shift velocity is generated by rotating a plane mirror directly in front of the camera used for taking pictures of the seeded flow. The image shift system is shown in fig 2.13 .

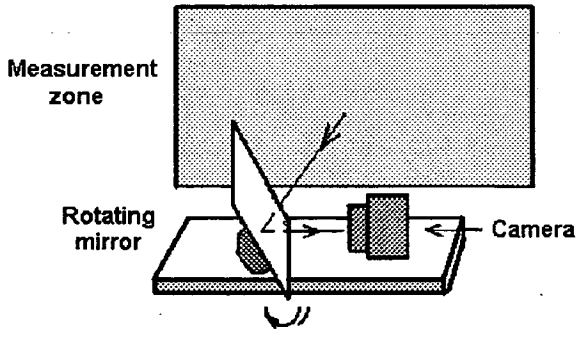

Fig.2.13 A rotating mirror image shifting system

The mirror rotates at a chosen, constant speed over a limited angle, the camera is fixed in position with respect to the rotating mirror assembly .

Determination of shift speed can be done as follows : The shifting speed as above mentioned is to add a speed with the same direction to every particle and separate the particles' images. So shifting velocity must be big enough and bigger than the maximum negative velocity (Fig 2.14)

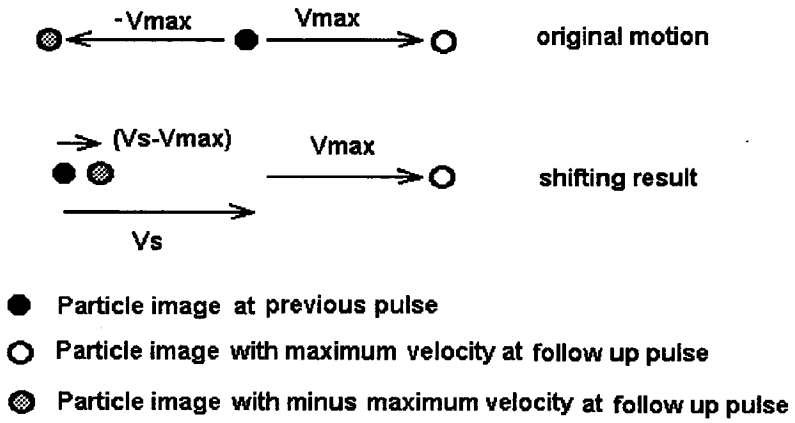

Fig 2.14 Illustration of shifting result

The shifting speed V_s at the centre of the frame is given by $2\omega L$. Where ω is the rotation rate and L is the optical distance from the mirror centre to the measurement zone. When maximum velocity of oscillation is $130 mms^{-1}$, L is 320mm, to choose a V_s= 180 mms^{-1} (> 130 mms^{-1}). Then 180=2 x 320 x ω, ω=0.28125 rad s^{-1}, or $\omega = 16.11^{o}s^{-1}$. In control system of image shifting, the choice of V_s is $5^{o}s^{-1}$, $10^{o}s^{-1}$, $15^{o}s^{-1}$, ... and so on , so a $V_s = 15^{o}s^{-1}$ is choosen.

2.3.3 Taking Photographs

To take a PIV picture is to record an image of the seeding in the flow.

2.3.3.1 Camera

The camera used in this study is a Nikon F-80 l fitted with an 50mm lens. The camera shutter speed is totally governed by the rotation rate of the spinning octagonal mirror and set to ensure that at least two, and preferably five or six images of each seeding particle are recorded on the film. For example, a mirror rotation rate of 23 Hz (rps), it

means that the mirror rotates 23 times per second, and in a rotation there are 8 flashes (8 mirror faces) . So it would require a camera shutter speed 1/30 second to produce five or six images on the film. Because $5 \div (23*8) = 0.0\dot{2}7\dot{s}$. The camera has shutter speed 125, 60, 30,15 and so on, so we choose 1/30=0.033 second. The aperture of camera is set to 2.8 to obtain an adequate amount of light reaching the film. The computer controls the camera trigger at any desired phase of an oscillatory flow, when the image shifting system and the trolley were at the suitable position for a frame to be taken. The average mirror angle is 45^{o} during each exposure. It takes about 30ms for the shutter of the camera to be fully open after the trigger pulse is sent. This information is entered into the PC controlling the mirror and the system automatically calculates the necessary accelerations (mirror from the still to the speed of shifting rotation) and the time to trigger the camera.

2.3.3.2 Film

The film used throughout is 135 format Kodak TMAX 100 ASA and TMAX 400 ASA. They provides a good compromise between light sensitivity and resolution, with about 100 lines per millimetre and 400 lines per millimetre. Because the cylinders model is fixed on the perspex discs then mounted in the towing tank, the edges of the discs have the same brightness as that of particle images on the film. The mark of the disc edges gives some blind areas where no velocity can be obtained. TMAX 400 can give a better contrast or clearer particle images and brighter edge marks. TMAX100 has a lower sensitivity and gives a low intensity particle images and blurred edge marks. See the U shape white shadow in Fig 2.15.

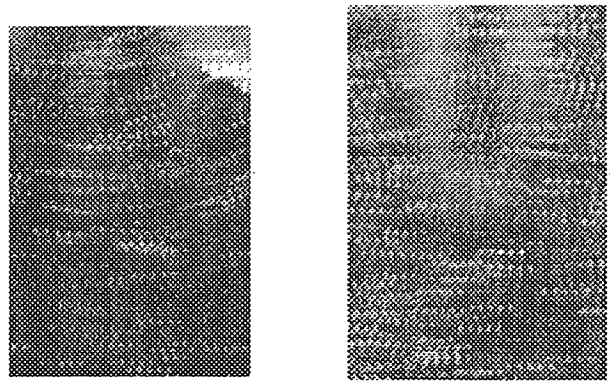

Fig 2.15 A comparison between TMAX 100 and TMAX400 films

All the PIV film were developed in a darkroom. The film is wound on to a reel and placed in the development tank with Kodak T-Max developer typically for about 7 minutes and the temperature of the developer is about $23^{o}C$. During the development period the tank is agitated every 30 seconds to replenish the surface of the negatives with fresh developer. After development the film is fixed in a bath of Amfixer for about 7 minutes, again agitating every 30 seconds. The final stage of development is to wash the film in running water for about 20 minutes to remove all trace of chemicals before hanging the film up to dry. Somtimes the processing of film needs to be a bit longer if seeding particle illumination is poor. This is usually due to the laser whose output drops below 13W when the mirrors at either end of the tube require cleaning. Under these situation the development time may be increased 1 or 2 minutes.

2.3.3.3 Magnification

Magnification is the ratio of a distance on a negative and the distance in the experimental tank. When the camera is moved in different experiments, the new magnification must be determined before PIV pictures can be taken. This is done by photographing a regular grid placed in the light sheet in the flume. Three marks are made on the grid and their position are measured by a ruler. Then the magnification is determined by studying the marks on the developed negative with a travelling microscope. In fact, in the software of PIV analysis there is a function named as '*scaling*' which can calculate out the magnification using the real position data of the three marks. A grid negative with three marks can be seen in Fig 2.16.

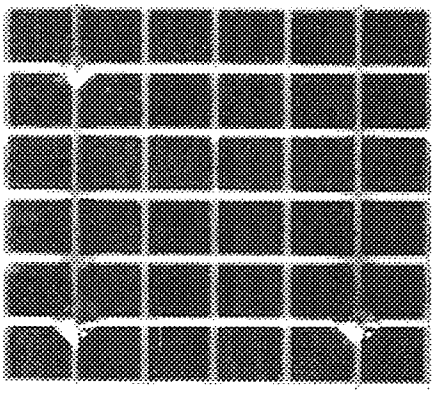

Fig 2.16 A negative of the grid with three marks

2.3.3.4 Seeding

The seeding particle used in the experiments is conifer pollen. The average diameter of the seed is $70\,\mu m$. Its colour is light yellow which is good for reflecting laser light and shows bright dots in the water after illuminated by a laser beam. The seeding particles do not always remain suspended in the water due to their tendency to float and to adhere to structures within the flume. So an uneven distribution of the seeding density can often be seen in the water, especially near the bottom of the tank, where it is easy to find there are some parts of the water with no seeding or not enough seeding. The conifer pollen seeding particles have a slight positive buoyancy, if left in still water, they rise with a speed of about 0.25mm/s. After soaked the pollen particles are easy to stick each other and become into some bigger particles. They can make bad smell when the particles have been in water of flume for a long time. So water have to be changed often.

Another kind of seeding particles are silver coated hollow glass spheres which are made from tiny hollow glass balls. Their mean size is a bit smaller than that of the pollen, about $44\,\mu m$ and the colour is light grey. Because they have smaller sizes and grey colour, they are slight darker than pollen seeding after illuminated in the water. The specific gravity is near to that of water, so their speed of rise are smaller than pollen's and can be distributed evenly in water. And the seeding particles have no bad smell at all and do not stick each other. They can be recycling and the original price is cheaper than that of pollen.

2.3.3.5 Phase determination

The phases of oscillatory flow that will be measured can be determined in two ways . One is to choose the phases in the program which controls the trolley moving. The second is to choose the phases in the operation of shifting system. The program controlling the trolley commands the trolley doing a sinusoidal motion . The period, time and smoothness of the oscillation motion can be adjusted in the program. The phases and periods when a photograph is taken is set in the program which then sends the trigger signal to the camera. The camera gets the signal and then takes the pictures

at the given phases. Because of the time of the mechanical action of camera and signal transmitting , only one picture can be taken in a oscillatory period.

Before the image shifting system can work, some controlling parameters need to be given to the system . The total time of the operation should be considered. It is shown in Fig 2.17.

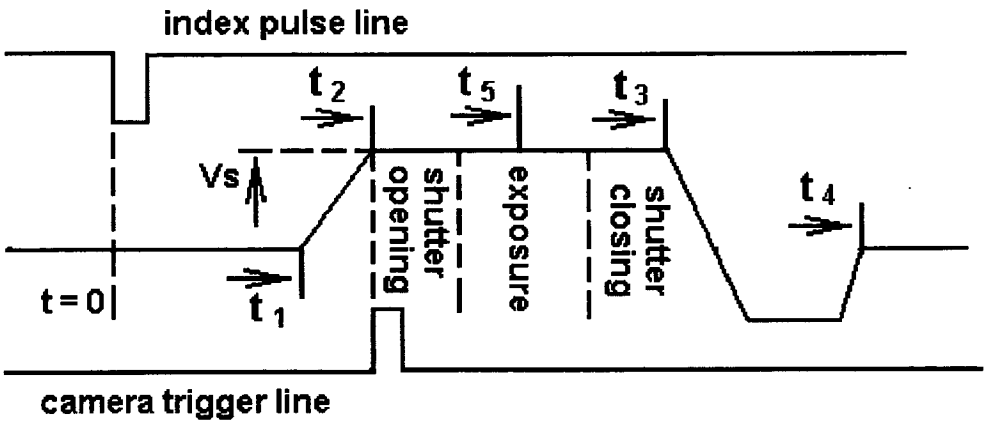

Fig 2.17 A velocity profile of the shifting mirror motion

In Fig 2.17 t_1 is the delay from reception of index pulse to start of motion; t_2 is the acceleration time of mirror from still to rotation speed ; t_3 is the constant shift velocity time ; t_4 is the 'return to home' time ; t_5 is the time to reach 45 degrees position ; Vs is shift velocity. For a chosen phase, the trigger signal should be sent a bit earlier. Normally the time to the Nikon F-80 1 is about 30ms.

2.4 Inherent Errors And Limitations In PIV

2.4.1 Inherent errors

Despite the high accuracy of the PIV method the errors involved in the technique must be considered. The work about this topic has been carried out by a number of people[9] [10] [11] [4] [7]. The errors come from two sources : random errors and system errors. Most of these errors are small due to the use of precision equipment or by exercising great care when carrying out the experiments.

Random errors

There are some main sources of random errors inherent in the PIV method :

a) focus of the camera

b) measurement of the laser beam scan rate

c) thickness of the illumination plane

d) camera misalignment

Systematic errors

The main systematic errors arising in the PIV method are:

a) refraction by the glass walls of the flume and the water

b) edge effects due to lens aberration

c) analysis rig calibration

d) illumination plane distortion

e) scanning beam return time

f) discrepancy between water flow and seeding movements

Morrison[4] has given a table for both errors*:

Source of error	Systematic Error	Random Error
photographic magnification		0.2%
Photographic distortion	0.0%~0.3%	
Illumination plane flatness	0.0%~0.3%	
Illumination plane thickness		0.1%
Illumination scan time	0.0%~0.2%	
Illumination interval		0.2%
Positive seeding buoyancy	0.2%	
Totals	0.2%~0.8%	0.3%

Table 2.1 Summary of the errors inherent in the PIV method

*The illumination system , shifting system , seedings and films used in my experiments were almost the same as Morrison's

2.4.2 Limitations

For the research of cylinders model immersed in water, the application of PIV technique has some more limitations and they will result in some errors.

a) Light reduction

The light sheet of the Laser goes through the one or two plastic tubes and its intensity is reduced by the tubes scattering and absorbing. So near the water surface the light is weaker than it is on the bottom (Fig.2.18)

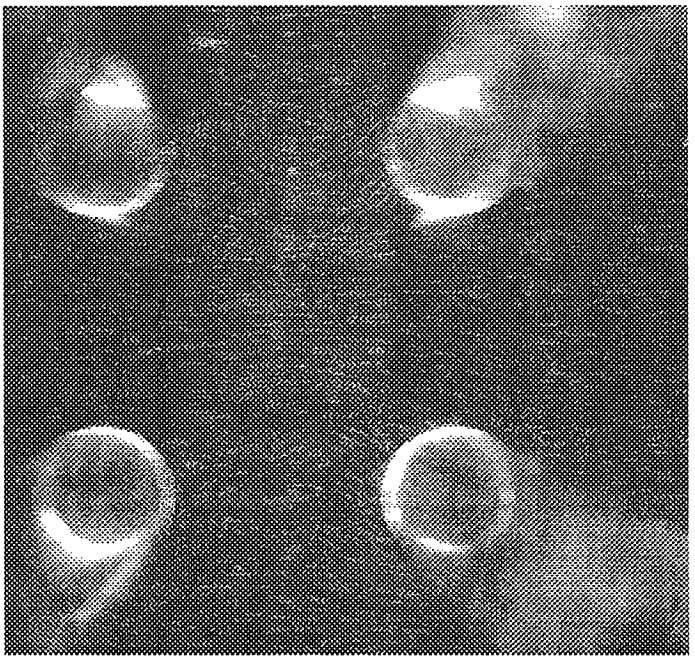

It can be seen from the picture in the left side that there are two vertical dark stripes caused by the cylinders. The laser rays are emitted from the bottom. Below the pair of lower cylinders, there is no dark strip; between the two pairs of cylinders rows the two dark stripes are clear;

Fig 2.18 The difference of light intensity in a illumination area.

above the upper cylinders the two stripes are darker. The seeding particle images are difficult to recognize at the top of the picture. This problem may be not an serious influence because vortices are normally generated at both the right and left sides of the cylinders and along the direction of the flow. These areas are bright light fields .

b) Model covering

When a camera takes a picture, the objects which are nearer the camera will give a bigger image. The laser sheet is located inside of the flume, so some portions of the cylinders project in front of the sheet. They left some big images and covered many

parts of measurement area, such as Fig 2.18. Fig 2.19 shows the positions which are in front of laser sheet in the tank.

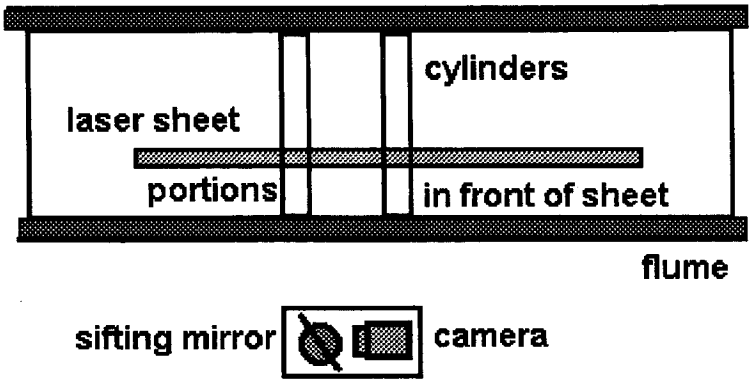

Fig 2.19 A plan view of PIV experiments

When the flow speed is low, the sizes of the vortices are small and the main active area of the vortices is round the surface of the cylinders. The covering effect is serious. The edges of model disc supporting the cylinders in the water will reflect the laser light and give noise images and result in wrong velocities such as Fig 2.20.

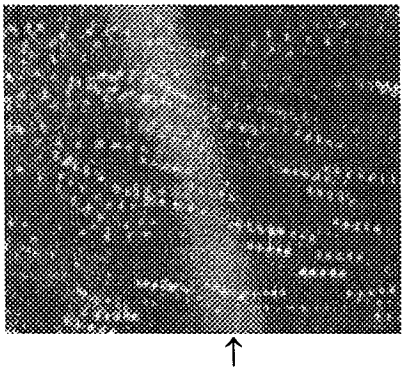

Fig 2.20 A noise image in a negative

c) Analysis resolution

Flow velocities are analysed by calculating the average velocities on many small interrogation squares on the negative. The size of the interrogation areas is constant for a chosen negative. But in the case when the flow velocity is large , the flow generates a number of vortices and their sizes and velocities are very different. If we use a large interrogation area, the small vortices would not appear; if we use a small interrogation area, it would get some wrong velocities at big velocity point. In some areas particles change their motion directions and move slowly, this will make particle

images into streaks which will also give wrong velocities. These cases are shown in Fig 2.21. In Fig 2.21, 1 and 2 indicate two small vortices and they couldn't be analysed out in the vector map. 4 indicates a few streaks which can only be noise. 5 was a cylinder's image.

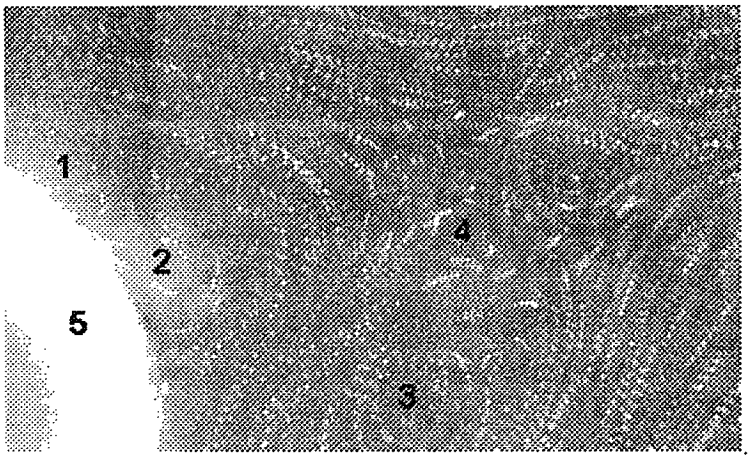

Fig 2.21 Some errors sources in a negative

d) Conclusions

These errors have different magnitudes with respect to velocities. Not all of them are proportional to velocity. For example, the error of seeding buoyancy will be smaller when the velocity is increased. For the variation of shift velocity across frame, according to Morrison's statistics and comparison[4] the error increases with rotation speed. The rotation speed of shifting system is proportional to velocity, so the error of shifting will be bigger when the velocity is increased. In general, the combined error is not over 2%~3% . So the inherent accuracy of the PIV has shown it to be an excellent technique

2.5 VIDPIV Analysis

The data processing of a PIV negative is done using software called VIDPIV. It is a PIV analysis, processing and presentation program for use with the Microsoft Windows operating system. This requires that analysable images must be in a digitised form as Windows bitmap files with 256 grey levels and may be acquired directly from the flow of interest by CCD camera or digitised from a photographic film or negative scanner. In this research the developed negatives are digitised by a Nikon negative scanner.

2.5.1 Basic principle

2.5.1.1 Correlation processing for PIV

The task of PIV interrogation processing is to extract flow displacement from the random carrier background. This PIV analysis employs the correlation algorithms. First the PIV bitmap is divided into many interrogation areas which have the same size. Then the average velocity is calculated on every small interrogation area. Thus a whole velocity field can be obtained. Fig 2.22 has shown a patch of a negative(left picture) and an interrogation area (right picture) from the patch. The interrogation area consists of 32 x 32 pixels.

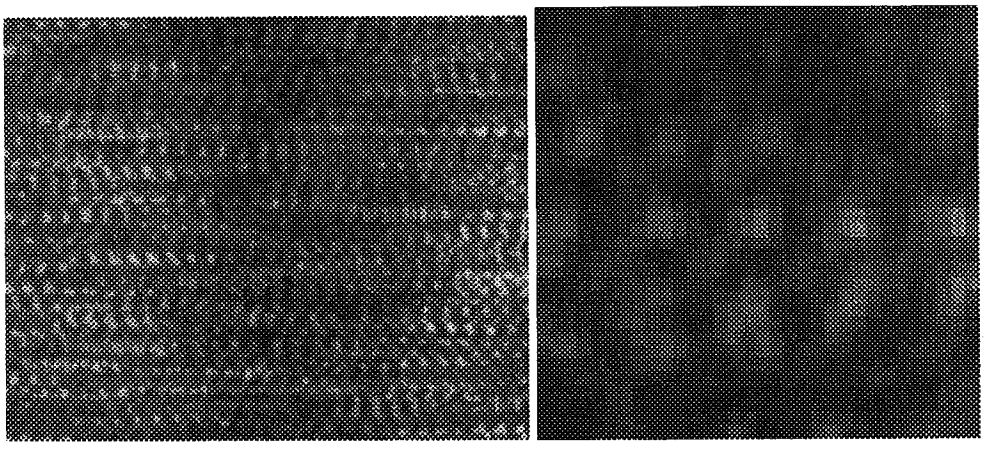

Fig 2.22 A PIV negative and an interrogation area

In ideal circumstances a local interrogation area will consist of a number of particle image pairs of identical separation. In such a case, if the positions of the particles can be identified it would be easy to produce an algorithm that would seek the most common particle separation from all possible separations. The most common form of PIV point processing is based on correlation processing. The general correlation function[12] is :

$$R_A(S_X, S_y) = \sum\sum A(x,y)B(x - s_X, y - s_y)dS_X dS_Y \qquad (2.18)$$

here A(x,y) and $B(x - s_X, y - s_Y)$ are the brightness of the pixel series in the interrogation. They correspond to the intensity distribution of a local interrogation area. The output of the function $R_A(S_X, S_Y)$ is the correlation function from which the

local displacement is measured. $R_A(S_X, S_Y)$ can be analysed by looking for the largest value of correlation which corresponds to the most common displacement in the local interrogation area.

2.5.1.2 Autocorrelation

When A(x,y) and $B(x - s_X, y - s_Y)$ are two identical series (in the same interrogation area), the output function $R_A(S_X, S_Y)$ is called the Autocorrelation function. An example of autocorrelation is shown in Fig. 2.23.

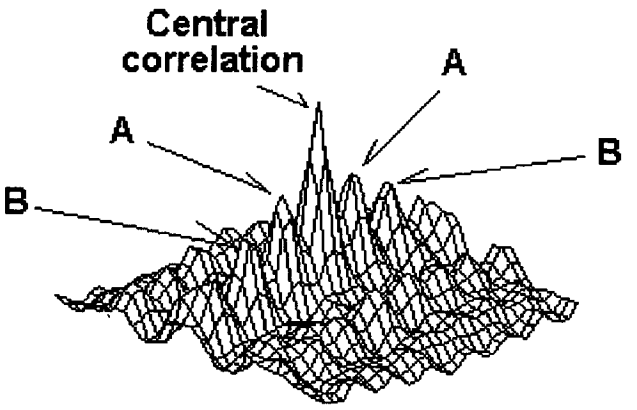

Fig 2.23 Autocorrelation function

Here the central correlation is the self correlation of pixels series, which is the highest peak in the 3d correlation space and is discarded . 'A' is the most common displacement correlation. 'B' is the second common displacement correlation. The distance from the central correlation peak to either of the displacement correlation peaks is proportional to the average particle displacement within the interrogation area. The autocorrelation function has 180 degree rotational symmetry. Since Autocorrelation show two possible the velocity directions using the correlation peaks, there is no way to determine exact direction of the velocity from Autocorrelation. It is necessary that for a PIV image to tell which exposure came first. In our study the autocorrelation has been used, but a shifting system was used to help to tell direction (See Section 2.3.2)

2.5.1.3 Crosscorrelation

When A(x,y) and $B(x - s_X, y - s_Y)$ are not identical the function $R_A(S_X, S_Y)$ is called

the cross-correlation function. The input intensity distributions A(x,y) and $B(x-s_x, y-s_y)$ may be from the same image frame (different interrogation areas) or separate image frames (two interrogation areas have the same position in the separate image frames.) The latter input approach is the most effective for PIV because the order in which particles are recorded is known and so the direction of the flow is unambiguous. The crosscorrelation function resulting from correlation of a displaced particle distribution between two separately recorded images is shown in Fig. 2.24[13]

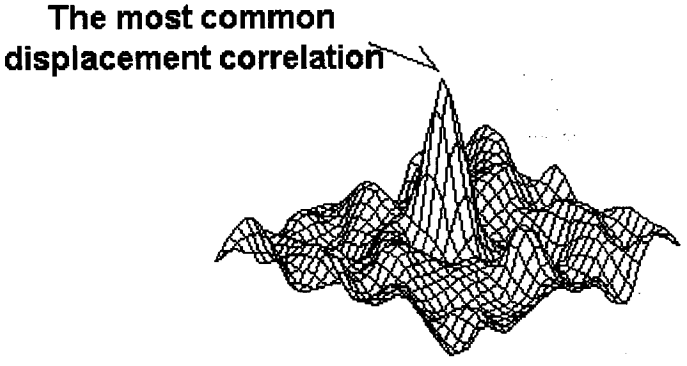

Fig 2.24 Cosscorrelation function for separate images

There is no self correlation peak in this case as there are no identical parts in both interrogation areas. Also there is no symmetry in the cross-correlation function either as the directional ambiguity that arises from recording both exposures onto the same image is removed. Additional benefits from recording successive exposures onto separate frames is that zero velocities can be resolved and shorter pulse separations used which improves the spatial resolution and the velocity dynamic range. The fundamental difficulty in separately recording successive exposures is that a very high frame rate is needed for small pulse separations. Developments in this area are to use mulitple CCD camera [14] and high frame rate CCD camera. At present the high frame rate has arrived up to 25 frames per second. If using double CCD cameras the frame rate can get up to 50 frames per second.

2.5.2 Generic processing

Once a PIV image has been acquired it remains to extract as much meaningful data from it as possible. The generic processing for PIV images is as follows:

A) Outline areas of PIV record that should be marked out. Add annotation features such as the shapes of the model which are in the measurement area, or text to highlight significant features.

B) Generate image/object scaling function or calibration function from actual PIV image with datum marks by datum dialogue function of Vidpiv.

C) Divide image into local interrogation grid. Attempt analysis with parameters set to values inferred from known information. Evaluate results and repeat with adjusted values if necessary.

D) Save vector data, scaling information and annotation information

E) Filter vector data according to velocity magnitude, direction and signal-noise ratio. This stage allows patently invalid data to be excluded at an early stage.

F) Perform vector validation to remove erroneous outliers from vector data.

G) Interpolate new velocity values into holes left from validation.

H) Smooth data by median, spectral or other techniques to reduce the influence of random errors.

I) Visualise data to gain insight into significant fluid dynamic features.
(In practise visualisation is not one later part of the process but present from start to finish. The raw image file is represented and viewable to evaluate its quality, correlation functions are visualised to estimate the suitability of analysis parameters and output vector values are visualised to confirm successful analysis and post processing).

J) Extract quantitative information and transform to derivative fields such as vorticity, shear or other.

2.5.3 A improved interpolating algorithm

In previours version of Vidpiv software, the vacant measurement sites reinterpolated using a linear interpolation algorithm[12]. This kind of interpolations applies only if sufficient neighbouring data exist. But in many situations vacant data could be a area not only a point. These vacant data may result in interpolation failure and difficulties in the vorticity calculation. So a comparison of different interpolations was performed and the weight function interpolation was determined as the most suiltable algrithm at present. So the new version of VIDPIV has adopted the weight function interpolation. This interpolation is better and faster than other algorithms[15].

2.5.3.1 Interpolation environment in Vidpiv

Before considering algorithms for interpolation it is necessary to consider the nature of the velocity vector data produced from PIV measurements. They are :

1) The points to be predicted, and nearby valid data points, are in the same co-ordinate system and all of them are at regular grid points.
2) Velocity values typically vary progressively across the measurement grid.
3) The use of image shifting or cross-correlation mean that reversing and zero velocities are present in the data sets.
4) Individual data points have a random uncertainty component arising from fundamental sources such as random correlation noise and velocity gradient bias.
5) vector data from non-stereo PIV measurement has two in-plane components and covers a two-dimensional area.

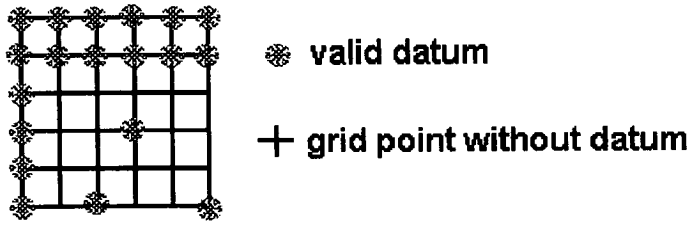

Fig 2.25 A simulated data grid waiting to be interpolated

2.5.3.2 Limitations of other interpolations

There are many of interpolation algorithms documented on the literature which are applicable to different types of data [16][17] . Not all schemes are suitable for PIV interpolation.

1) Two Point Linear Interpolation

This approach is simple to implement and offers the possibility of rapid computation. However two point linear interpolation requires that the prediction point must be bewteen two valid points. The linear approach is also only suitable for interpolation, not extrapolation.

2) Higher Order(Polynomial) Interpolation

This scheme does not require that the interval between data points be equally spaced. However, the data must be monotonic and this is too strict for our data environment.

In addition the scheme has a special limitation for regular grid of PIV data. This Lagrange bivariate higher order interpolation polynomial can be written as

$$P_{m,n}(x,y) = \sum_{i=0}^{m}\sum_{j=0}^{n} X_{m,i}(x)Y_{n,j}(y)f_{i,j} \qquad (2.18)$$

here $$X_{m,j}(x) = \frac{(x-x_0)(x-x_1).....(x-x_n)}{(x_i-x_0)(x_i-x_1).....(x_i-x_n)} \qquad (2.19)$$

$$Y_{n,j}(y) = \frac{(y-y_0)(y-y_1).....(y-y_n)}{(y_j-y_0)(y_j-y_1).....(y_j-y_n)} \qquad (2.20)$$

In all of three formulas x and y are coordinate values of data. When the positions of the data points are on the same grid row or column in the x or y direction, the $X_{m,i}(x)$ and $Y_{n,j}(y)$ will have a 0 denominator and tend to ∞. For this reason the scheme is unsuitable for PIV interpolation.

3) Bivariate (Polynomial) Spline

A spline function interpolation is well known as a good interpolation method which has some virtues. The degree of the interpolating polynomial is small, this can save computation time while in most cases achieving satisfactory accuracy by using different polynomials locally across the whole vector map. There is no special requirement that the data must be on a regular grid.

A spline function of degree n with data points at x_i i=0.1,...n is a function F(x) with the properties (i) On each subinterval $[x_{i-1}, x_i]$, $1 \le i \le n$, F(x) is a polynomial of degree n. (ii) F(x) and its first (n-1) derivatives are continuous on interval [a,b]. If n is taken as three the spline function is called a cubic spline which can be denoted as $P_3(x)$. The interpolation procedure in the one dimensional case is to subdivide the given interval [a, b] into a number of subintervals $[x_{i-1}, x_i]$, $1 \le i \le n$. A cubic polynomial $P_{i,3}(x_i)$ on the subinterval $[x_{i-1}, x_i]$ can be obtained by using the conditions:

$$P_{i,3}(x_{i-1}) = f_{i-1}, \quad P_{i,3}(x_i) = f_i, \quad P'_{i,3}(x_{i-1}) = f'_{i-1}, \quad P'_{i,3}(x_i) = f'_i \qquad (2.21)$$

where $f(x)$ is a function of unknown form for which we know only its values x_i i=0,1,...n. $f(x_i)$. Then to approach the $f(x_i)$ by an equation of $P_{i,3}(x_i)$:

$$P_3(x) = \sum_{i=0}^{n} N_i(x) f(x_i) + \sum_{i=0}^{n} H_i(x) f'(x_i) \qquad (2.22)$$

where $N_i(x)$ and $H_i(x)$ are two functions of coordinate values of data points and prediction points.

Once $P_3(x)$ is obtained, put the position x of prediction points into it, a prediction value can be got. An interpolation is finished.

From equation (2.22), the key problem is to get $f'(x)$. Because the second derivative of $P_{i,3}(x_i)$ is continuous we can differentiate it twice at $x_i \pm \varepsilon$, $\varepsilon > 0$, $1 \le i \le n$, and get $P''(x_i + \varepsilon)$ and $P''(x_i - \varepsilon)$. Equating $P''(x_i + \varepsilon) = P''(x_i - \varepsilon)$, n-1 equations in n+1 unknowns $f'_0, f'_1, \ldots, f'_n$ can be built. If f'' at the two end points i=0 and i=n are prescribed, we can get an equation set. To solve the equation set, f' at every nodal point can be found. So the spline interpolation will work when putting a x_i ($x_{\min} \le x_i \le x_{\max}$) into $P_3(x)$. For bivariate interpolation, the prediction point (x_i, y_j) must be in an area of ($x_{\min} \le x_i \le x_{\max}$) and ($y_{\min} \le y_j \le y_{\max}$). This requirement means the spline scheme is doing an exact interpolation, it is not suitable for extrapolation as it needs a prediction point between any two valid data points. In PIV interpolation environment, it will often appear that all of the valid data points are on one side of prediction point such as is illustrated in Fig 2.26. For this reason the spline method cannot be used in velocity approximation for PIV.

4) Newton's Bivariate Interpolation

This scheme is specially suitable for equally spaced data on a grid. Although our data is also on a regular grid, the Newton's bivariate interpolation needs complete data about the prediction point so that it can do the forward, reverse and central difference

operations. PIV data is randomly distributed on the regular grid, a number of the grid data points are empty (see Fig. 2.26) The requirement for complete data round the prediction point for finite differecing is not satisfied and so Newton's bivariate interpolation is not suitable for PIV interpolation.

5) Least Square Interpolation

Least square approximations are commonly used approximations. It uses the Euclidean square norm $\|x\| = (\sum_{i=1}^{n} |x_i|^2)^{1/2}$ or $\|f\| = (\sum_{i=1}^{n} w(x_i) f^2(x_i))^{1/2}$, where $w(x) > 0$ is a weight function. The best approximation in the least square sense is defined as that for which the constants c_i , i=0,1,..., n are determined so that the aggregate of $w(x)f^2(x)$ over a given summed domain D is as small as possible. For functions whose values are given at $N+1$ points $x_0, x_1, \ldots, x_n$, the equation will be :

$$I(c_0, c_1, \ldots, c_n) = \sum_{k=0}^{n} w(x_k)[f(x_k) - \sum_{i=0}^{n} c_i \phi_i(x_k)]^2 = \min \qquad (2.23)$$

Here the coordinate functions $\phi_i(x)$ are usually chosen as $\phi_i(x) = x^i$, i=0,1,...,n , and $w(x) = 1$. The necessary conditions for equation (2.23) to have a minimum value is that $\frac{\partial I}{\partial c_i} = 0$, i=0, 1, ..., n . This gives n+1 linear equations for n+1 unknown constants $c_0, c_1, \ldots, c_n$.

Thus equation (2.23) becomes :

$$\sum_{k=0}^{n} w(x_k)[f(x_k) - \sum_{i=0}^{n} c_i \phi_i(x_k)]\phi_j(x_k) = 0 \quad , \text{j=0,1,...n} \qquad (2.24)$$

When the values of c_i are found, through solving the equation set (2.24), the approximating function is built. Then substitute x, the prediction point for x_k, the value of prediction is $= \sum_{i=0}^{n} c_i \phi_i(x_k)$.

At first this scheme seems well suited as it has no special requirements for the data. However, for the PIV application here there are at least two problems. The first is the time of computation which becomes longer because of the iterative calculations required for solving the equations. The second is the singular matrix which will appear when solving equations(2.24) by Gaussian elimination. In the triangular coefficient matrix of the (2.24), the elements on the diagonal position of the matrix must not be zero because they will be used as denominators. The elements are a sum of the distances from the data points to the prediction point. Normally, a zero value will not happen when the data and prediction coordinate systems are different. However, in the PIV results the data points and prediction points are all on the same grid and the summed distances are calculated in two dimensions x and y, respectively. The data points may be positioned directly about the prediction points, and so distances to the prediction point will be positive or negative. The unit of distance is the normalised grid separation and on summation it is possible to get a zero as shown in Fig.2.26.

If there is one zero value on the diagonal positions of the matrix, the matrix will be singular and the computation will fail. So Least square interpolation is not suitable for using here.

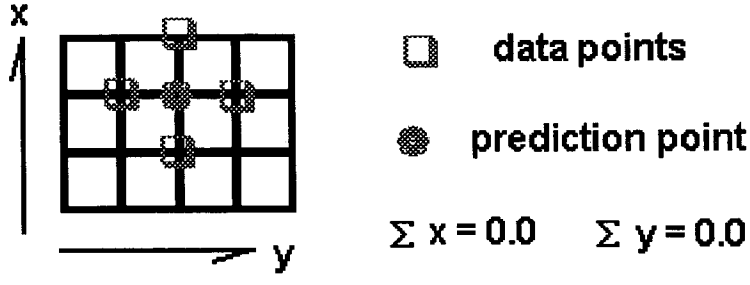

Fig 2.26 Summation of gridpoint position

2.5.3.3 Weight function interpolation

The common form of weight function interpolation is :

$$F(x,y) = \frac{\sum_{h=1}^{m} W_h(x,y) f_h}{\sum_{h=1}^{m} W_h(x,y)} \qquad (2.25)$$

where $W_h(x,y)$ is a weight function. When the function value f_h is taken to give an approximate value at the prediction point; the nearer the data point is to the prediction point, the greater its influence is on the ultimate value at the prediction point. Only the absolute distance is considered in the calculation. If D is the distance of the prediction point from the data point then $D=\sqrt{(x-x_h)^2+(y-y_h)^2}$, and D always has a value greater than 0 and so the possibility of a singularity is avoided. This scheme is not sensitive to the position of the data points as the weighting function is dependant on absolute distance only. For the cases of data points and prediction points in the same mesh coordinate system the method is simple and convenient . So the weight function scheme seems suitable for PIV data interpolation. For generating a weight function there are some different methods, in which two common forms are easy to be used.

One has an exponential form $W_h(x,y)=\exp(-\frac{D^2}{4E})$, where E is an experimental constant. It may be taken as 1. The other has an inverse square form $W_h(x,y)=D_h^{-2}$. The two weight functions are shown in Fig. 2.27.

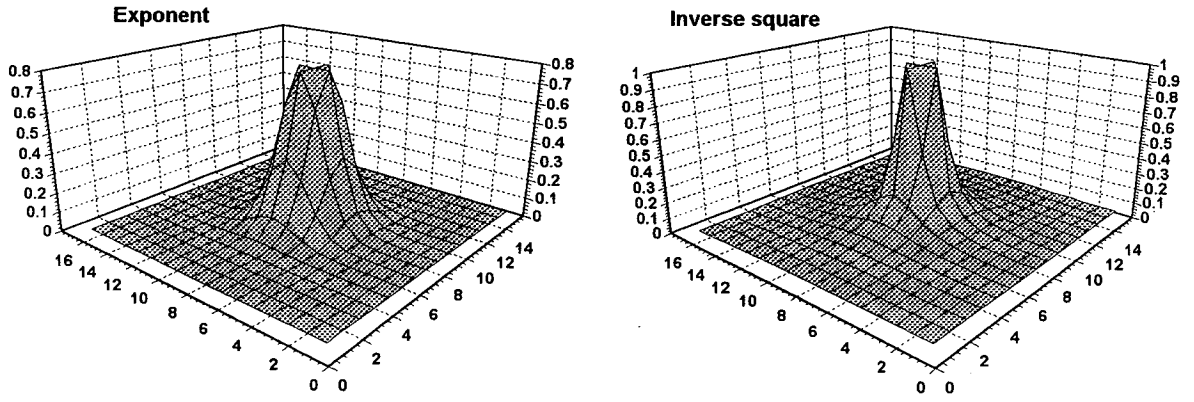

Fig 2.27 Two weight function forms

In Fig. 2.27, two 3-D surface shows have no top points on them. Because the top point is distance to the prediction point from itself . The Fig. 2.27 shows the exponential function has a more smooth weight gradient than that of inverse square function. In the experimental comparison between the two weight functions, no obvious differences have been found. In the improved Vidpiv version the exponential weight function is used.

In the selection of neighbouring points, the nearest values are the most reliable for interpolation and are used first moving progressively to more distant points if insufficient nearest points are available. See Fig.2.28

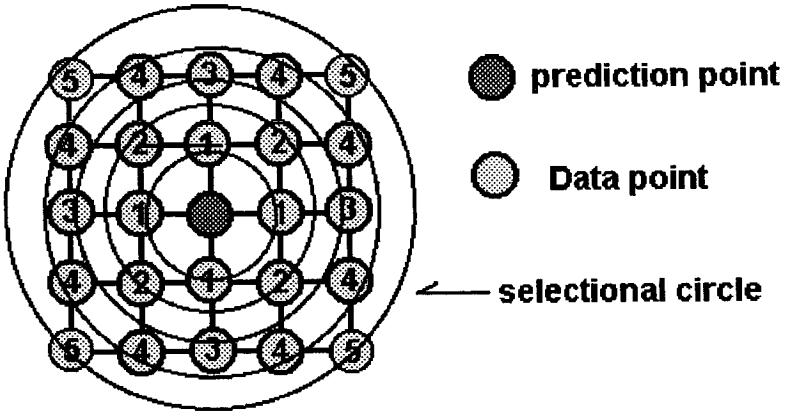

Fig 2.28 The order of the data selection

Data points beyond the region indicated in Fig. 2.29 will tend to be less and less useful for prediction. When in selected circles there are four data available, stop selecting and do the interpolation calculation. For a large interpolation area, the order of operation is to interpolate points with most supporting data first, then moving progressively to more isolated points. The result of previous interpolations may be used to support interpolation in a subsequent pass. So the isolated points can be changed into non-isolated. The results of the exponent weight interpolation are satisfactory. See Fig 2.29

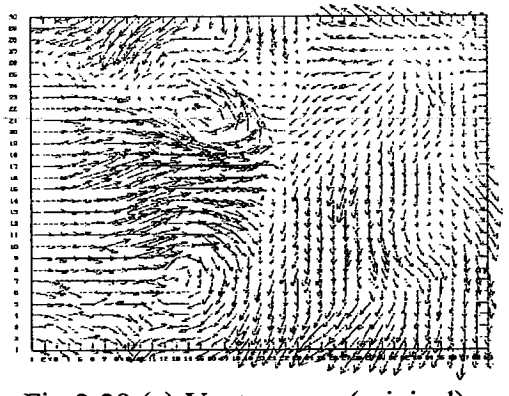

Fig 2.29 (a) Vector map (original)

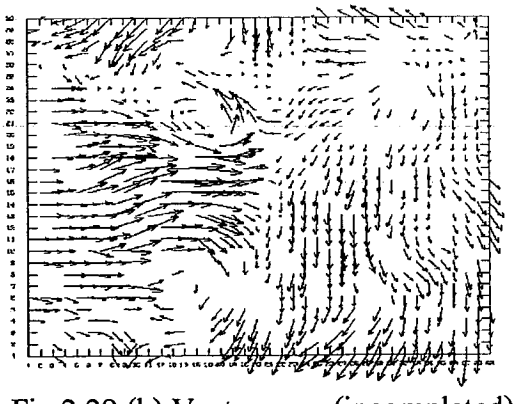

Fig 2.29 (b) Vector map (incompleted)

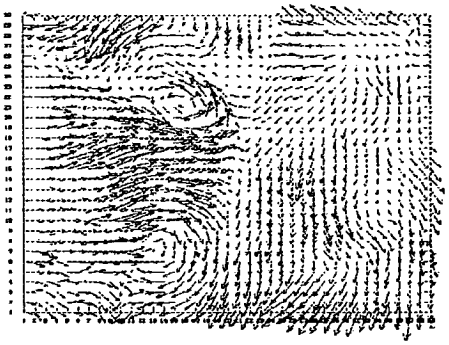

Fig 2.29 (c) Vector map (interpolated)

2.6 Vorticity and Vortex Strength Calculations

2.6.1 Definition of Vorticity

The vorticity is an important parameter used to describe flow field features. It shows the flow velocity gradient and flow rotation direction and intensity. The definition of vorticity in Cartesian coordinates for two dimensions :

$$Vorticity = \frac{\partial \mathrm{v}}{\partial x} - \frac{\partial u}{\partial y} \qquad (2.26)$$

In equation (2.26) the first item in the right describes the gradient of the y component of the velocity in the x direction; the second item in the right is the gradient of the x component of the velocity in the y direction. Because the motion of the flow is continuity, when $\frac{\partial \mathrm{v}}{\partial x} > 0$ it means that y component of velocity increases along x direction and has a positive rotation . When $\frac{\partial \mathrm{v}}{\partial x} < 0$ it means that y component of velocity decreases along x direction and has a negative rotation. When $-\frac{\partial u}{\partial y} > 0$ it means that x component of velocity decreases along y direction and has a positive rotation. When $-\frac{\partial u}{\partial y} < 0$ it means that x component of velocity increases alongy direction and has a negative rotation. These can be seen in Fig. 2.30

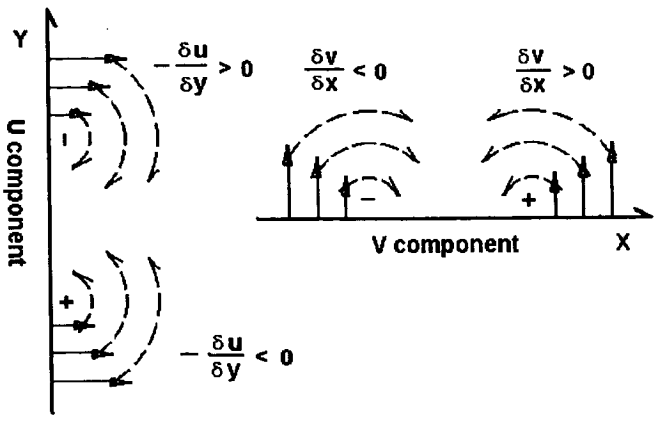

Fig 2.30 Vorticity visulization

2.6.2 Vorticity calculation

In the present version of Vidpiv, only vorticity on a rectanguar area can be calculated. This is not suitable for the cases of flow passing objects. In the cases, objects immersed in water and their interfaces with water are irregular. So vorticity can not be calculated by Vidpiv .There are a few methods to calculate the vorticity. In the analysis here the vorticity calculation is done as follows:

1) to choose the interesting areas of velocity field , cut the part of objects which are in the flow field.

2) considering definition of the vorticity and using the differential method, the value of the vorticity at every point of grid could only relation with the values at four points round itself . These values could be used to calculate $\frac{\partial v}{\partial x}$ and $\frac{\partial u}{\partial y}$.

3) to find if the calculated point has got sufficient neighbour values of four velocity data which are at the positions as Fig 2.31

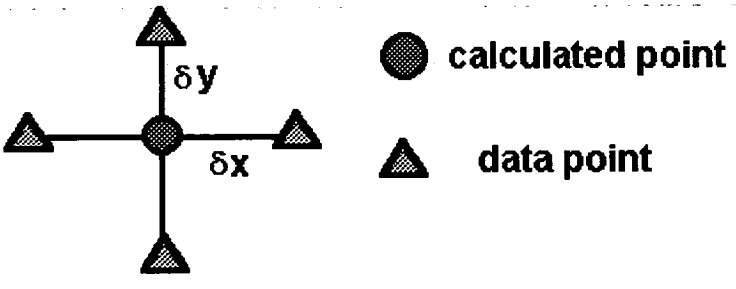

Fig 2.31 the position of data points

If it has not got four data points, to give up calculation at the point. So before calculating a vorticity , the data number is counted first. This is repeated for every calculated point. It is a quick and easy procedure.

4) to calculate the vorticity on whole flow area which could have a irregular border and occasionally a few empty points. A result of the vorticity calculation as Fig 2.32

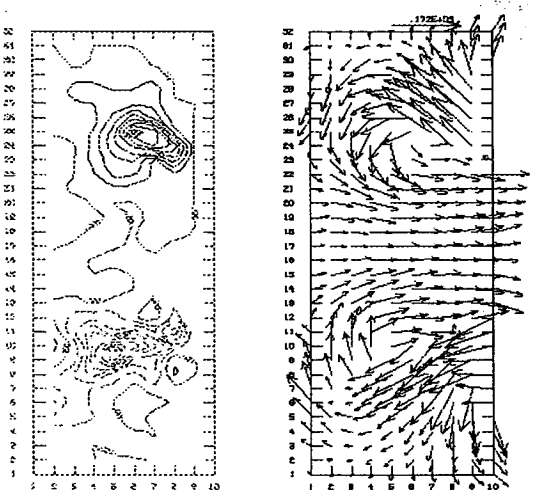

Fig 2.32 Vorticity field (dash lines mean negative area) and velocity field of PIV

2.6.3 Vortex strength calculation

The vortex strength is calculated by integrating the vorticity values of the vortex over a given area, such as equation 2.27 :

$$K = \int \vec{\omega} \bullet d\vec{a} \qquad (2.27)$$

where K is vortex strength, ω is vorticity value, $d\vec{a}$ is the element of area over which the vorticity is being integrated. In practice the integration is replaced by summation, $d\vec{a}$ was the grid separations ($\Delta x \Delta y$) which was used in the PIV analysis.

The summation method has to be simplified because the shape of the vortex and its boundary changing with different vortices. A good method, according to Corlett[28]'s research, should be : it allowed for variable vortex shapes and only summed those points which had a vorticity above a certain boundary value. So the boundary selection was very important for the summation, strictly the sum area is defined by the zero

vorticity contour, however in calculation this was not a feasible choice due to presence of background vorticity. It therefore was necessary to define another, seemingly more arbitrary, boundary. Corlett [28] had found that using the 10% ω_{max} of a vortex as its boundary was reasonable and practicable. In this study the ω_{max} was easy to be found and the boundary had to combine the contour of 10% ω_{max} and vortex shape shown by vector map. This is caused by the existence of background vorticity, in the section 2.6.1 it has been shown that a positive or negative vorticity value was decided by gradient of velocity in direction and amount, it can have nonzero vorticity on the area with no vortex, or have positive values in a negative vortex beause of some vectors moving slightly anticlockwise. The basic procedure of vortex strength in the study is:

a) to choose a vortex by vector map.
b) to calculate the vorticity on the vortex area.
c) to find the maximum value of the vorticity in the vortex.
d) to draw the 10% ω_{max} contour
e) to sum the vorticity values which have vorticities above the boundary value. Then a total vortex strength is obtained
f) to divide the total vortex strength by the number of points which joined the summation of vortex strength. Then an average vortex strength is obtained.

2.7 Force Measurement

There are different methods to test the forces on the cylinders acting by the oscillatory flows. The most basic test instrument is a strain gauge in these measurement methods. The force measurement is carried out by sensitive reaction of strain gauge to force action.

2.7.1 Principle of measruring

The most popular electrical elements used in force measurements[18] [19] include the resistance stain gauge, the semiconductor strain gauge, and piezoelectric transducers. In general, the strain gauge measures force indirectly by measuring the deflection it produces in a calibrated carrier; the piezoelectric transducer responds directly to the force applied. In experiments of this research , the resistance stain gauge were used. The resistance strain gauge is a resistive element which changes in length, hence

resistance, as the force applied to the base on which it is mounted causes stretching or compression. The process is that strain induced in a wire will increase the resistance since the crytal lattice is bound to distort as the wire becomes longer and thinner, but it is likely that the characteristic three-dimensional atomic pattern of a particular metal will also be affected, and thus its resistivity. It is perhaps the most well-known transducer for converting force into an electrical variable.

There are several typical patterns of the resistance strain gauges in use. The bonded devices are considerably more practical and are in much wider use than other devices. The bonded strain gauges consist of a thin wire of conducting film arranged in a coplanar pattern and cemented to a base or carrier. It is shown in Fig. 2.33

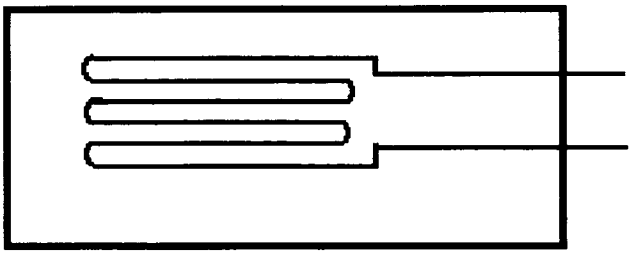

Fig. 2.33 A bonded wire strain gauge

Force acting on the base will cause the wire to elongate or shorten, which will cause the resistance to increase or decrease.

$$R = \rho L / A \quad , \quad \Delta R / R = K \Delta L / L \qquad (2.27)$$

here R is resistance of the strain gauge, L is length of wire, A is cross section of the wire, ρ is resistivity of the wire, K is the gauge factor which is a function of the conductor material.

For investigating dynamic strain phenomena, in principle a simple circuit used is the common Wheatstone bridge.[20] It is shown in Fig.2.34

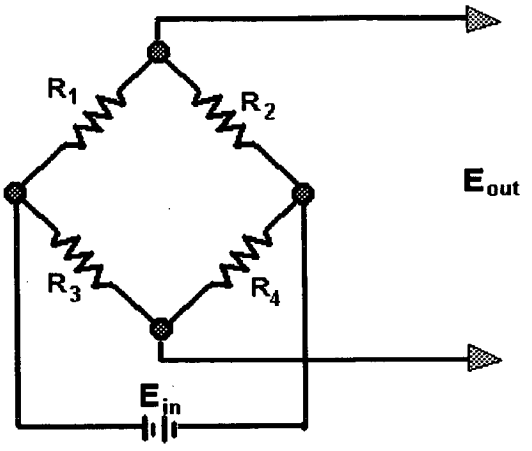

Fig. 2.34 A full bridge circuit

In the simplest form, a bridge consists of four two-terminal elements connected to form a quadrilateral, a source of excitation(voltage or current)--connected along one of the diagonals, and a detector of voltage or current—comprising the other diagonal. The detector, in effect, measures the difference between the outputs of two potentiometric dividers connected across the excitation supply. For this bridge, E(out) is :

$$E_{out} = \frac{R_1}{R_1 + R_2} E_{in} - \frac{R_3}{R_3 + R_4} E_{in} = \frac{R_1 R_4 - R_2 R_3}{(R_1 + R_2)(R_3 + R_4)} E_{in} \qquad (2.28)$$

When $R_1 = R_2 = R_3 = R_4$, the bridge is at balance, $E_{out} = 0$. When testing force, a strain gauge instead of a R, for example, R_1 is installed in the bridge. The original resistance of the strain gauge meets the requirement of $R_1 R_4 = R_2 R_3$ Then the resistance of the strain gauge will undergo a change when force loaded . The bridge balance is broken and there is an electricity signal at E_{out} . It is called readout. Normally the readout is quite small $\Delta R_1 << R_1$, so the readout will be

$$\Delta E_{out} = \frac{E_{in}}{4} \frac{\Delta R_1}{R_1} \qquad (2.29)$$

The strain gauge is sensitive to temperature. The reaction of strain gauge to temperature can cause a resistance change, and it must be avoided. A method to avoid

this is called temperature compensation[21] [19]. It uses a full bridge with two strain gauges arranged orthogonal each other and had the same resistance ($R_1 = R_2 = R$). It is shown in Fig. 2.35.

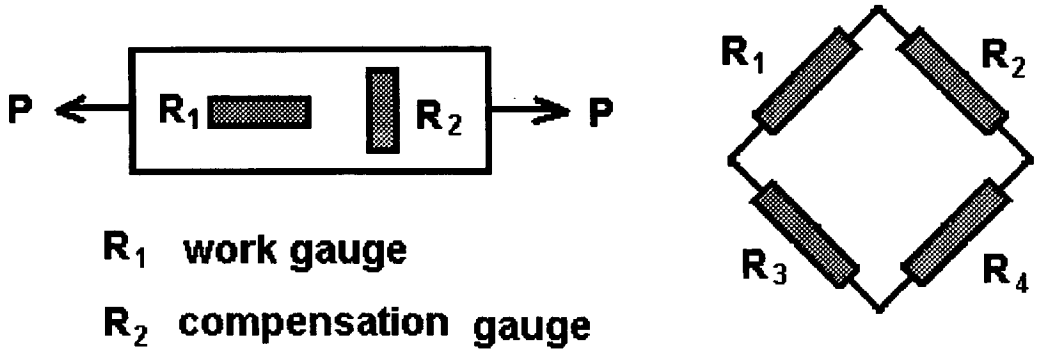

Fig.3.35 An arrangement of temperature compensation gauge

R_1 is working gauge, which is mounted in a direction of maximum strain. R_2 is a dummy gauge, or called compensation gauge, which is installed in a direction of minimum strain, so that it only reacts temperature variation. For R_1, its resistance change has two parts: one is caused by the stretch force; other is caused by temperature, $\frac{\Delta R_1}{R_1} = \frac{\Delta R_1}{R_1}|_F + \frac{\Delta R_1}{R_1}|_T$, let $\frac{\Delta R_1}{R_1}|_F = K\varepsilon_F$. ε_F is output of electric signal which is caused by force loaded. For R_2, it has an influence of stretch force in cross direction of the gauge and resistance change with temperature, $\frac{\Delta R_2}{R_2} = \frac{\Delta R_2}{R_2}|_F + \frac{\Delta R_2}{R_2}|_T$, $\frac{\Delta R_2}{R_2}|_F = K(-\mu\varepsilon_F)$. $-\mu$ means that the output at the cross direction is different from at length direction. To use equation (2.28), the output will be $\Delta E_{out} = \frac{E_{in}}{4} K(1+\mu)\varepsilon_F$ .This scheme is not only to delete the influence of temperature but increasing output power, it is now $(1+\mu)$ time of orignal signal.

2.7.2 Some measurement methods

For measurement of force acting cylinder by oscillatory flow, there are several different test methods.

1) Two Ends Test

This method has been used by T.Sarpkaya[22] and S.Kuhtz, P.W.Bearman[23]. The experiments were carried out in the U tube. The working section is in the horizontal limb. The water in the U tube is maintained constant amplitude oscillations by an air blower attached to the top of one of the vertical limbs. The force measurement happened at two ends of the cylinder. The force measuring system was composed of two stainless steel load cells, one at either end of the cylinder, so that the force could be measured independently of the point of application, by simply summing the outputs of the two cells. The gauges were connected to form a full brige. The whole equipment arrangement can be seen in Fig. 2.36

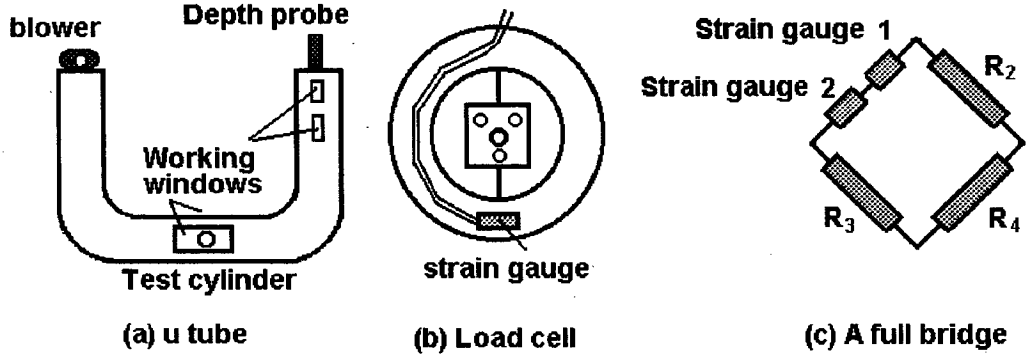

Fig 2.36 Method 1 of force measurement

When two strain gauges are put in the same arm of a full bridge, there will be a stronger output signal and according to equation (2.28) , the outputs of two cells need only simply summing. But this method can only test the total force experienced by the cylinder. Because the cylinder has been fixed on two ends and two strain gauges in one arm of the circuit could tell force with no direction difference.

2) Points Test

This method has been used by E.D.Obasaju and P.W.Bearman [24]. The experiments were carried out in an open water channel. Above the working section there is a carriage which can be driven in sinusoidal motions. Models are mounted vertically in the channel. The top end of each cylinder was clamped to the carriage and bottom end was about 1 cm above the floor of the channel.

The cylinder had pairs of pressure tappings with the tappings placed diametrically opposite each other. When investigating the forces acting at a cross-section of the

cylinder , the tappings were located at mid-span between the end plates. The pairs of tappings were led to two pairs of pressure the transducers which were mounted on the carriage. The outputs of the transducers forming a pair were subtracted from each other ($\Delta P = P_1 - P_2$) and the resulting pressure-difference signals from two pairs were recorded simultaneously with the displacement signal. In the case of the sectional - force measurements, the pressure difference across the oscillating cylinder at ±90° to the line of motion was always monitored.

For this experimental equipment arrangement, it is inconvenient to take a simultaneous picture of flow round the cylinder during test force. Because oscillatory water surface exists, it will cause light scattering. And camera or CCD camera arrangement is also a problem because of the carriage above the channel. A brief equipments arrangement can be seen in Fig. 2.37

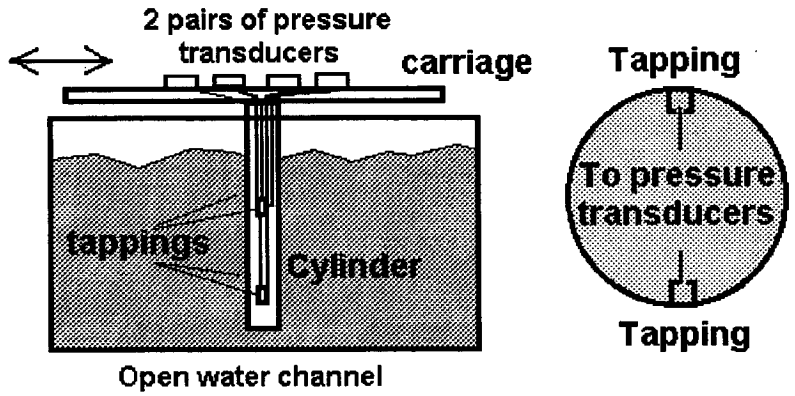

Fig 2.37 Method 2 of force measurement

3) Dry Test

This method has been used by C.H.K. Williamson [25]. Its force sensors are out of water. The experimental rig is similar to the points test. The oscillating cylinder rig in which vertical cylinders are horizontally oscillated is shown in Fig. 2.38. The strain gauges are attached to the surface of the cylinder between the perspex plate and the water surface for force measurements. So the strain gauges keep dry during experiments.

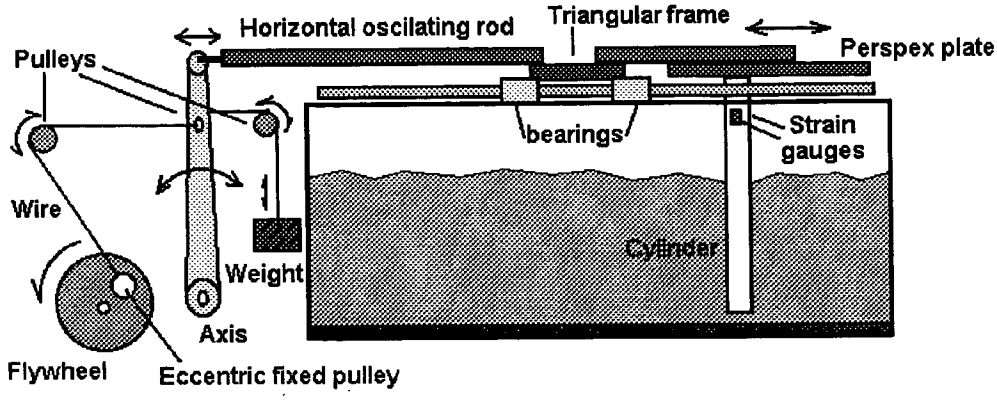

Fig 2.38 Method 3 of force measurement

In this experiment, flow visualization was done by phtographing with a Nikon motordrive camera vertically downwards from above the horizontal perspex plate. An unobstructed view around the cylinders was obtained. The surface of the water is sprinkled with aluminium powder and light sources comprise two slide projectors of 250W each and 1000 W Halogen bulb placed around the tank edges. The camera may be fixed with respect to the cylinder or fixed with respect to the undisturbed fluid. Williamson thought that the framework fixed to fluid is in general more effective than one fixed with respect to the cylinder, since it allows vortices to be observed without the masking effect of a superposed stream velocity. The method Williamson used is an improvement of point test , but it still suffer the problem of water surface scattering .It couldn't test the flow velocity and only showed some flow patterns.

For above three methods, method one can test total force acting on the cylinder and flow visualization in the same time. Method two and method three can do force components (drag force, lift force) test but their flow pattern visualization have some difficulties and sometimes have to be done in separated tanks such as the U tube. [23][24] .For getting flow velocity field round the cylinder and force components measurement in a simultaneous moment, the equipment arrangement invloved in my experiments is shown in the follow section 2.7.3 .

2.7.3 The method used here

In order to carry out the experiments mentioned above, there are two basic conditions we need to meet. One is to avoid the camera facing the water surface when flow measurement is being done. The other is to fix only one end of cylinder, this will allow

the cylinder to bend when flow forces act on it, so that force components can be measured.

For condition one, we used a towing tank and the cylinder was horizontally arranged in the tank. When the cylinder was immersed in the tank, its cross section was normal to water surface. Then the glass wall of the towing tank was chosen as PIV view area which was parallel to the cross section of the cylinder. Thus the water surface didn't face the camera. For condition two, we used a transducer which was fixed between one end of the cylinder and the model frame. The model frame was parallel to the glass wall of the tank as shown in Fig. 2.3 and Fig. 2.4. The transducer was water proof and can be immersed in water with the cylinder. The cables of the transducer had no influence on the background of the flow field because the tranducer was behind of the Laser sheet. The basic arrangement of the transducer is shown in Fig. 2.39.

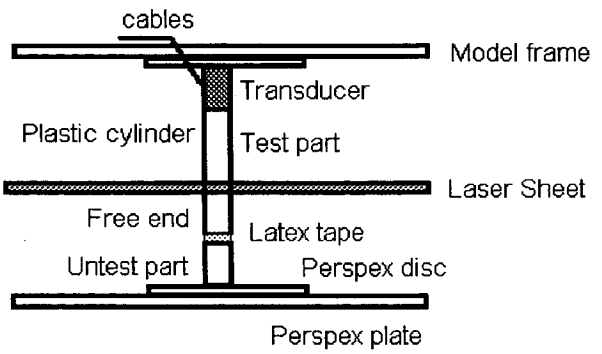

Fig 2.39 A plan view of transducer arrangement

For making a free end of the cylinder, the cylinder was cut into two portions. The nontest portion had a the same length as the transducer. Because there must be no gap between the transducer and the test part of cylinder, the two free ends of cylinder are wound by Latex tape. This kind of material was soft and elastic so it allowed the test part of the cylinder to bend freely and stops the flow going through the gap and making a small jet.

The transducer can measure two components of the force. It had two full bridge circuits , each had got its own temperature compensation element. Every circuit tested one force component in one direction. The oscillatory flow force acting on the cylinder

was divided into two components : the X direction force which was parallel to the direction of the trolley motion called the in-line force and the Y direction force normal to the directions of trolley motion called the lift force.

The force signal record system was composed of a power supply , two level amplifiers and a data logging system which digitised the force voltage signal into digitization . The force measurement system is shown in Fig. 2.40.

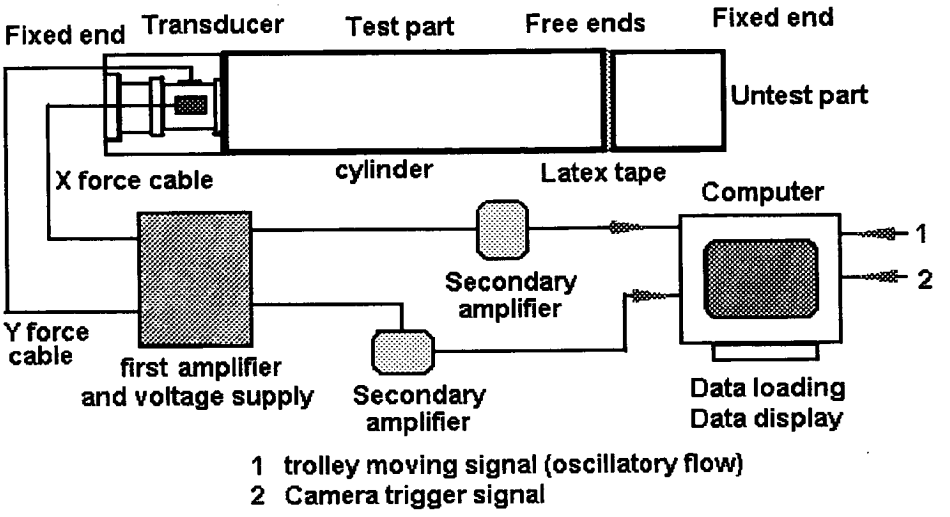

Fig 2.40 Force measurement system

First level amplifier and power supply ('E_{in}' as fig 2.34) connected the strain gauges and built two complete full bridges. The computer digitised the voltage signals from the transducer with a sampling frequency of 16Hz. The flow field photographing was begun at the seventh period of the oscillation in order to avoid instabilities associated with the initial motion. Using this system the simultaneous force records and flow velocity field can be obtained. Following the camera trigger signal, the position of the velocity field which matched the force evoluting line can be found. A record display can be seen in Fig 2.41.

In Fig 2.41, the trigger number shows the time when the flow pictures were taken. As an example, the number 4 picture just matches a peak in the lift force. Although we cannot know when the peak of the lift force will appear , we can only choose to trigger

at pre-fixed phases. Sometimes we can catch a few pictures coincident with the peak of a force, such as number 4.

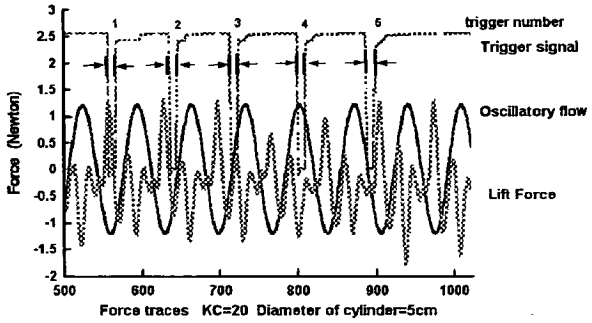

Fig 2.41 Signals record display (Force signals have been converted)

As an example, the number 4 picture just matches a peak in the lift force. Although we cannot know when the peak of the lift force will appear , we can only choose to trigger at different phases. Sometimes we can catch a few pictures coincident with the peak of a force.

2.7.4 The calibration of force measurement

The calibration for the transducer is to obtain a force signal rule in the experimental environment. Then a conversion ratio from signal voltage to force unit can be calculated. The force calibration must be done before every force measurement experiment starts. Of course it can also be done after the experiment, but the experimental apparatus and environment should keep the same situation as in experiments.

A weight of 500 gram is used in the calibration and the calibration is assumed as linear in the experiment. First in the waterless environment, the signal of the strain gauges was recorded with no force acting on . Then the weight of 500 gram was loaded on the cylinder which needed to be done for both the x and y dirctions respectively. Between zero weight and 500 gram , force signal variation of transducer was assumed as a linear increase. Considering gravity, the 500 gram loading unit conversion was 0.5 kg*9.8 m/(s*s)=4.9 Newton; no force loading the output was 5 volts, so signal variation was represented by | signal -5.0 volts | (absolute values).

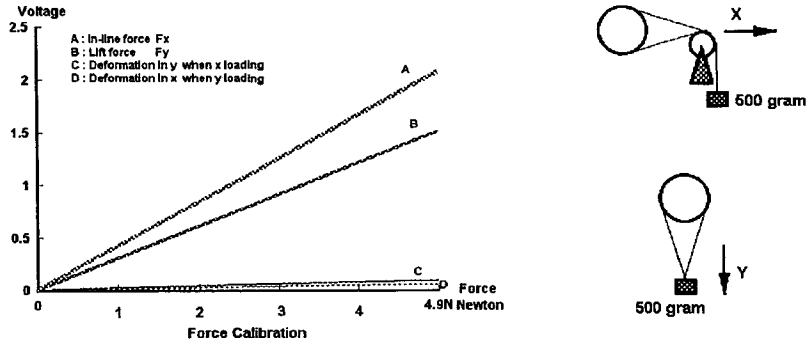

Fig 2.42 Force calibration : Record (left) , Test (right)

According to Fig 2.42 (left) a vary ratio (cotangent of the lines) can be calculated out. ΔForce/ΔVoltage / length of the cylinder = Force variation about per voltage on unit cross section of the cylinder. Once the conversion ratio was obtained , it will be applied on the data from the same experiment.

2.8 Force Analysis

2.8.1 The strength of the forces

In the raw data there is some noise , so a smoothing process over sequences of five samples is done first. Its formula is :

$$X_i = (X_{i-2} + X_{i-1} + X_i + X_{i+1} + X_{i+2}) / 5 \qquad (2.30)$$

here X is sample in data series, the first two data and the last two data cannot be smoothed, so they are kept as raw data. The smooth number 5 was decided after a few tests of different smooth numbers. It can reduce the noise and keep the most of original nature of the data series, see Fig 2.43

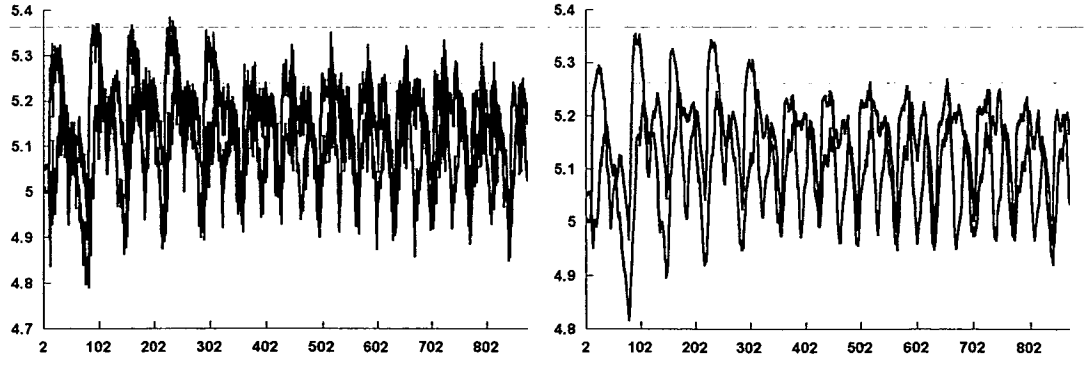

Fig 2.43 A comparision between raw data (left) and five samples smooth result (right)

For oscillatory flows, the force signal varies between the two directions of oscillation. So the analysis of the force strength should avoid a subtracting forces with opposite directions. The average strength of the force is calculated from:

$$F = \sqrt{\sum_{t}^{N} (X_t - \bar{X})^2 / N} \qquad (t = 1, 2, \ldots N) \qquad (2.31)$$

where X_t is a force sample and N is the total number of data samples in a series, $\bar{X}$ is mean value of the series. F is a statistic average for experimental data series. After these calculations, the forces in different situations can be compared each other.

2.8.2 The frequency of the forces

For obtaining force evolution information, the frequency of the force variation was calculated. We considered a data series composed of many different periods waves and were interested in finding its main wave component which was represented by frequency of the wave. The frequency component presented in a data series were defined by the power spectrum:[26]

$$S_k^2 = (A_k^2 + B_k^2) \qquad (2.32)$$

where k. was wave number and

$$A_k = \frac{2}{n} \sum_{t=1}^{n} X_t \cos\left[\frac{2k\pi}{n}(t-1)\right] \qquad (2.33)$$

$$B_k = \frac{2}{n} \sum_{t=1}^{n} X_t \sin\left[\frac{2k\pi}{n}(t-1)\right] \qquad (2.34)$$

where t =1, 2 ... n was the sample number of a data series; n was the total number of a data series; X_t was the sample of a data series.

For displaying the force power spectrum in the frequency area , a formular between wave number and frequency has to be used, it is (2.35):

$$f = \frac{k}{n} \tag{2.35}$$

Before the power spectrum is calculated, all data series have undergone a 5 points smoothing.

2.9 Some Problems In PIV Application

2.9.1 PIV Technique

PIV technique is an effective method to measure the velocities of flow motion at present. It will obtain a wider application in the future. The main problem in measurement of the flow past the cylinders is that we couldn't obtain good velocity in the flow boundary areas of the cylinder surface. In fact the problem will happen on any interface between the flow and the offshore structure model. Because the cylinder is immersed in the water, some parts of the flow around the cylinder are obscured by the cylinder body itself when the PIV picture is taken. Vortex shedding occurs close to the surface of the model, so the area is a key investigated area. But it is difficult to obtain the detail of the vortex shedding, specially when vortex is small and the oscillatory flows are at a low KC numbers.

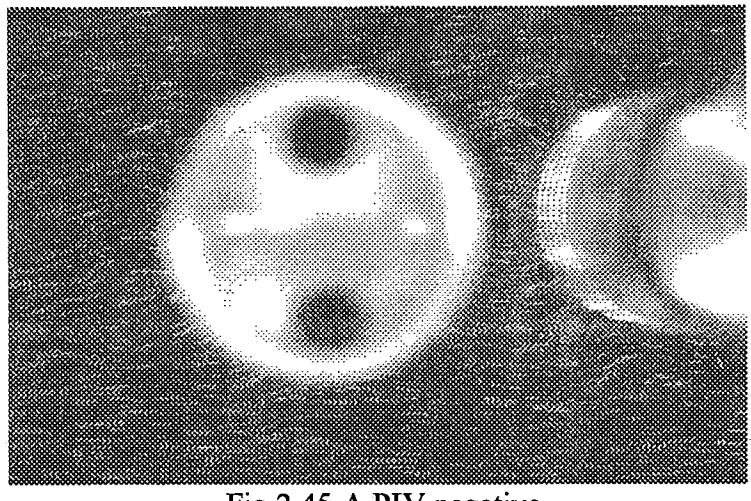

Fig 2.45 A PIV negative

In the Fig 2.45 we can see nothing on the right side of the right cylinder, meantime the surface of the left cylinder in laser sheet has been covered by the end of the cylinder which is nearer to the camera. In the middle area between two cylinders we can only see a thin flow area. For a so thin gap, several images of one particle will occupy fully

it . Then only a few velocities can be obtained from the particle images in the gap, they couldn't give a good description of the vortices which are around the cylinder surface. Although this is a clear picture, we cannot still find vortex information from it. The possible ways of resolving this problem may be 1) to move the camera nearer to the laser sheet, this will cause a smaller view area and obtain a high resolution picture which could describe more details of the flow in the small area; 2) to change more the angles between camera and the model area, to obtain the more pictures at different parts of the flow surrounding the cylinder, then draw the flow whole behavior from all of the pictures. 3) to use more cameras at different positions at the same moment, which purpose is similar to that in the second method. 4) to choose a two CCD camera and use crosscorrelation, which will give more spaces on the negative for more particles in the gap because the crosscorrelation requires only one image for one particle.

2.9.2 Velocity Analysis

The velocity given by the PIV is the average velocity on a square interrogation area on the negative. Beause the edges of the cylinder and the most offshore structures models are non-straight lines, the velocity information in the interrogation areas round the surface of the cylinder will be not enough. So the wrong velocity easily appears on the interface areas between flow and structures, see Fig 2.46 So many people are looking for the better ways to work out the flow velocity at these special areas. Some people combine the tracking method with area average method together, to find more reasonable direction and size of the velocity on the interrogation areas. Some people use spectrum coefficient polynomial to simulate the path of the particles, then to obtain a better velocity.

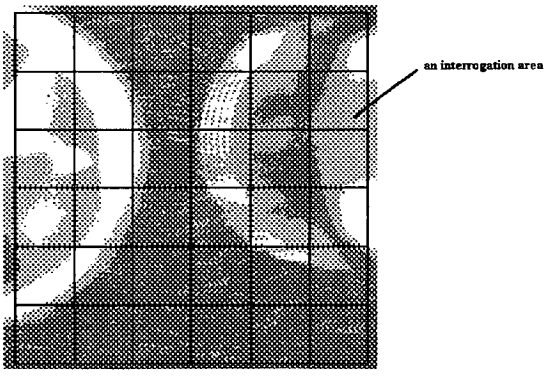

Fig 2.46 The interrogation mesh

For interpolation of velocity data, using the exponent scheme[see chapter 2] a quick complete and improved data field can be obtained. But any interpolation method must depend on the neighbour data. The scheme is usually carried out according to an order from the left to the right and from the top to the bottom of the interpolation area. It can't guarantee the data which are used first (at the left and the top) are better than others, so some error component may introduce in when the interpolation is done for an relative big area. For separated points or small patch, the exponent scheme is quite satisfactory.

References

[1] C.J.Garrison, A review of drag and inertia force on circular cylinders, (1980) The 12th annual offshore technology conference, Houston Texas, U.S.A May, 1980.

[2] Manual of model experiments of offshore engineering , May, 1989 , pp60, The Dept. Of Civil Engineering, Dalian University of Technology, P.R. of China

[3] A. Arnott and T. P. Dewhirst and J. Pullen and C. A. Greated, Underwater CCD Cameras for PIV Flow Mapping, Journal of Laser Technology, Vol.29, No.1, pp45-50, 1997

[4] I.G.Morrison, The Hydrodynamic Performance of an Oscillating Water Column Wave Energy Converter, Charpter 2, PhD thesis , 1995, The Edinburgh University

[5] T.Bruce, W.J.Easson, C.Gray, C.A.Greated, D.R.McCluskey, D.J.Skyner, Guide for PIV Mesurement, 1994, The University of Edinburgh

[6] A.Aroussi, Y.-Y. Yun, I. Grant, Experimental verification of numerical simulation of turbulent flow past enclosures in offshore structures, (1992), Optics and Lasers in Engineering, Vol 16, pp391-409.

[7] P.A.Quinn, Breaking Waves on Beaches, Charpter 2, Ph.D Thesis, 1995, The University of Edinburgh

[8] J.A.Cosgrove, Measurement of Two-Phase Flow Using Particle ImageVelocimetry, Charpter 4, Ph.D Thesis, 1997, The University of Edinburgh

[9] C.Gray , The Development of Particle Image Velocimetry for Water Wave Studies. PhD Thesis, The University of Edinburgh.1989

[10] P.A.Quinn, D.J.Skyner, C.Gray, C.A.Greated, W.J.Easson, A Critical Analysis of the Particle Image Velocimetry Techniques as Applied to Water Waves, (1993) Flow visualization and Image Analysis , Kluwer Academic Publishers, The Netherlands

[11] R.D.Keane, & R.J.Adrian, Optimization of Particle Image Velocimeters PartI: Double Pulsed Systems. Meas.Sci.&

[12] Optical Flow System Ltd. Vidpiv Manual ,1994, Edinburgh

[13] D.B.Hann, simultaneous Measurement of Acoustic Fields and Flow fields using Optical Methods, . PhD Thesis, The University of Edinburgh. 1996

[14] T.P.Dewhirst, M.L.Jakobsen & C.A.Greated, Multiple CCD camera DPIV for Force and Acceleration Measurements in High Speed Flows, 1995

[15] J.Wang, C. Gray and F. Barnes, A comparison between interpolation algrithms for post processing of particle image velocimetry data, Proceedings of International Seminar on optical Methods and Data Processing in Heat and Fluid Flow, April,1996 pp291-300.

[16] John Todd, Basic Numerical Mathematics , Vol. Numerical Analysis, Charpter 8, 1980, Academic Press, Inc. New York

[17] J.L.Mohamed and J.E.Walsh, Numerical Algorithms, Charpter 10, Charpter 16, 1986, Clarendon Press, Oxford

[18] Daniel H. Sheingold, Transducer Interfacing Handbook --- A Guide to Analog Signal Conditioning , Analog Devices, Inc. U.S.A 1980

[19] H.K.P.Neubert, Strain Gauges :Kinds and Uses , Macmillan & Co Ltd 1967

[20] Ir.J.J. Koch, Ir. R.G. Boiten, Ir. A.L.Biermasz, G.P.Roszbach and G.W.Van Santen, Strain Gauges : Theory and Application, Netherlands, 1952

[21] H.Chang, Apparatus of Mechanical Process Test , April, 1984, Northeast University of Technology, P.R. of China

[22] T.Sarpakaya, Force on a circular cylinder in viscous oscillatory flow at low Keulegan-Carpenter numbers, J.Fluid Mech. (1986), vol 165, pp.61-71.

[23] S.Kuhtz, P.W.Bearman and J.M.R.Graham, Experiments on fixed and compliant cylinders in oscillatory flow at low β numbers , (1997) The proceedings of BOSS'97 vol 2, pp 79-93.

[24] E.D.Obasaju, P.W.Bearman and J.M.R. Graham , A study of forces, circulation and vortex patterns around acircular cylinder in oscillating flow, (1988) J.Fluid Mech. Vol 196, pp467-494

[25] C.H.K.Williamson, Sinusoidal Flow Relative To Circular Cylinders, (1985), J.Fluid Mech. Vol 155, pp 144-174 .

[26] M.K.Jain, S.R.K.Lyengar and R.K.Jain, Numerical Methods for Scientific and Engineering Computation, 1985, wiley Eastern Limited, New Delhi India

[27] T.Sarpkaya & M.Isaacson, Mechanics of Wave Forces on Offshore Structures,

Chapter 3 (1981), Van Nostrand Reinhold Company Inc. New York, U.S.A

[28] A.E.Corlett , A near wake study of vortex shedding from bluff bodies at low Reynolds numbers, PhD thesis , The University of Edinburgh, 1997.

Chapter 3

Numerical Simulation

3.1 The Principles of the vortex Method

The vortex method focuses on the vorticity of a flow, which is the local 'rotation' of the fluid.[1] In an incompressible fluid, the time evolution of vorticity dictates the essential physics of the unfolding flow.

3.1.1. Basic principle

The basic concept of the approach of the vortex method is to represent the flow by discrete vortices that move with the flow[2]. These vortices are generated at the interfaces between the fluid and its boundaries, then move in space and change their strength with time through diffusive and convective processes.

For the vortices in a flow using trajectory equation we can track them. The trajectories of these elements are given by the definitions of fluid velocity :

$$\frac{dx}{dt} = u \quad , \quad \frac{dy}{dt} = v \qquad (3.1)$$

If we know the velocities, these equations can be integrated and will yield the position of each vortex, then the velocity field at each point and time can be obtained, see Fig 3.1.

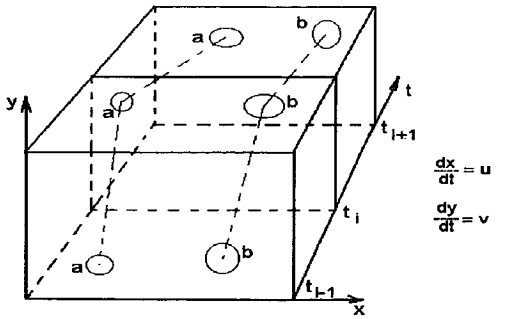

Fig 3.1 The basic concept of the vortex method

3.1.2.Governing equations

The Navier-Stokes equations are the basic governing quations for a moving fluid. When the flow is an incompressible viscous flow, the Navier-Stokes equations are :

$$\rho\frac{D\boldsymbol{u}}{Dt} = -\nabla P + \mu \ \nabla^2\boldsymbol{u} \qquad \text{in D} \qquad (3.2) \qquad \text{equation of motion}$$

$$\nabla \bullet \boldsymbol{u} = 0 \qquad \text{in D} \qquad (3.3) \qquad \text{continuity equation}$$

$$\boldsymbol{u} = 0 \qquad \text{on } \partial D \qquad (3.4) \qquad \text{boundary condition}$$

where ρ is the density of the fluid and μ is the dynamic viscosity.

Equation (3.2) is an expression of Newton's law $\mathbf{F} = m\mathbf{a}$ and $\mu\nabla^2\mathbf{u}$ gives the viscous property of the flow, while (3.3) states that the flow is incompressible . In three dimensional space, when the flow is compressed in the vertical direction and the flow has convergence, in the horizontal plane it must have divergence. For the two dimentional case, if the flow is compressed in x direction, it will stretch in the y direction. The boundary conditions (3.4) require that both the normal and tangential components of **u** vanish on walls.

The vorticity equation will give a quantitative description of the transport and evolution of vortices as mentioned in chapter 2.6. Vorticity ($\vec{\omega} = curl\mathbf{u}$) is a vector field which gives a microscopic measure of the rotation at any point in the fluid. The significance and importance of vorticity[3] for the description and understanding of fluid flow stems from two facts, Firstly, $\vec{\omega}$ may be inverted to give the velocity field as an integral over the vorticity field. and, secondly when the viscous diffusion of vorticity is negligible, the fluid is barotropic (i.e., the density ρ is a single-valued function of the pressure P) and external forces are conservative, then the vorticity satisfies conservation principles (the Helmholtz laws) which allows the vorticity to be 'followed'. In particular, vorticity is not created and a compact distribution of vorticity remains compact, so that the structure and evolution of the fluid flow is more economically described in terms of the vorticity field than in terms of the velocity field.

In two special cases, a vorticity formula becomes particularly simple. If the flow is

inviscid; that is, one in which vorticity does not diffuse due to viscosity or 'friction' in the flow, patches of vorticity are self-advected and move without diffusing. In addition, in the absence of any vorticity ($\omega = 0$), the problem reduces to one of potential flow requiring the solution of Laplace's equation in the given domain.

The vorticity equation is deduced by applying the curl operation throughout the motion and contiuity equations. The vorticity equation is :

$$\frac{D\omega}{D\ t} = \nu\ \nabla^2\omega \qquad (3.5)$$

or $$\frac{\partial\ \omega}{\partial\ t} = -(u \bullet \nabla)\omega + \nu\ \nabla^2\omega \qquad (3.6)$$

where ν is the kinematic viscosity, equal to μ/ρ.

In equation (3.6), the term on the left hand side is a local one. It shows that vorticity varies with time in a manner governed by the terms on the right hand side of (3.6). The first term on the right-hand side is vorticity convection, which means vorticity motion in space (a transport of the vorticity gradient by the motion of the fluid). The second term on the right-hand side is vorticity diffusion, which causes the vorticity strength to grow smaller and smaller with time and space.

In the limit of infinite Reynolds number, the diffusion term disappears, and only the normal boundary condition can be imposed. In the special case of two-dimensional flow, the vorticity vector ω is normal to the velocity **u.**

The conditions for which the vorticity inversion is possible and **u** can be determined uniquely are as follows, (they are sufficient but not necessary):

(1) The velocity field is solenoidal, that is div **u** = 0.

(This condition is satisfied if the fluid is incompressible)

(2) The region occupied by the fluid is singly connected.

(3) The normal component of fluid velocity, $\mathbf{u}_n$ is given on all bounding surfaces S.

(4) The velocity vanishes at infinity when the fluid is unbounded.

(5) The normal component of vorticity vanishes on S.

(6) The vorticity field is compact.

The velocity is then given uniquely by the sum of a solenoidal vector potential component and an irrotational scalar component

$$\mathbf{u}(\mathbf{x},t) = \vec{k}\nabla\ \Psi + \nabla\Phi \tag{3.7}$$

In (3.7) $\vec{k}\nabla\Psi$ is a solenoidal field satisfying

$$curl\vec{k}\nabla\Psi = \vec{k}\nabla^2\Psi = \vec{\omega} \tag{3.8}$$

where Ψ is termed the stream function and $\nabla\Phi$ is determined uniquely by the classical potential problem

$$\nabla^2\Phi = 0, \qquad \frac{\partial\Phi}{\partial n} = U_n - \vec{k}\nabla\Psi \bullet \vec{n} \qquad \text{on S, } \Phi \to 0 \qquad as \quad x \to \infty \tag{3.9}$$

in which Φ is termed the velocity potential. $\nabla\Phi$ is the irrotational , solenoidal field which can be added to satisfy a single boundary condition on the velocity field on S. If there is no bounding surface, $\Phi = 0$.

Considering the viscosity exists only in a thin boundary layer around the surface of the objects immersed in the flow, outside of this the flow can be seen as an inviscid irrotational potential flow. The stream function equation is :

$$\nabla^2\Psi = -\omega \tag{3.10}$$

This is a Poisson equation. For two dimensional flow, the stream function $\Psi(x,y) = C$ represents a stream line. Solving (3.10) vorticity ω can be converted into the stream function Ψ, then the velocity can be found from :

$$u = \frac{\partial\Psi}{\partial y} \qquad ; \qquad v = -\frac{\partial\Psi}{\partial x} \tag{3.11}$$

If we want to get the displacement of every vortex at every time step , the formulae are:

$$dX = Udt \qquad dY = Vdt \tag{3.12}$$

A regular mesh is used to resolve the Poisson's equation, so the data required is obtained by interpolating the vorticity of the vortices onto the mesh points first. Using the stream function, Ψ, of the results of the Poisson's equation, the velocity at each mesh point can be obtained. Then a second interpolation is made in order to get the new velocity of each vortex back. Now the displacement of each vortex can be caculated from (3.12) and thus the new positions of the vortices in a successive time step can be obtained and a new flow field is determined. Whilst solving the Poisson equations , the convection and diffusion of the vorticity (or vortices) are simulated.

3.2 Vorticity Transport In Vortex Method

We now wish to solve the vorticity equation (3.6):

$$\frac{\partial \omega}{\partial t} = -(u \bullet \nabla)\omega + \nu \nabla^2 \omega \tag{3.6}$$

In (3.6) the first term on the right is the nonlinear convection term and the second term is the linear diffusion term. u is the local instantaneous velocity. In order to solve the equation, (3.6) is split into two parts by the fractional step method: it discretizes the problem in time but not in space, i.e. it considers the evolution of a system of particles with a discrete timestep, Δt. We will denote the approximate vorticity distribution at time $n\Delta t$ by ω^n.

Suppose we decompose the vorticity update $\frac{\partial \omega}{\partial t}$ into two terms as follows[4].

$$\left[\frac{\partial \omega}{\partial t}\right]_1 = \nu \nabla^2 \omega \tag{3.13}$$

$$\left[\frac{\partial \omega}{\partial t}\right]_2 = -(u \bullet \nabla)\omega \qquad (3.14)$$

Let $\left[\frac{\partial \omega}{\partial t}\right]_1^{n+1}$ be the solution at timestep $(n+1)\Delta t$ of the pure convection equation (3.13) with $\omega_1^n = \omega^n$. The solution to this equation is approximated by the integration along particle(vortex) trajectories using the discrete vortex cell-cloud method. Similarly, let $\left[\frac{\partial \omega}{\partial t}\right]_2^{n+1}$ be the approximate solution to the diffusion equation (3.14) with $\omega_2^n = \omega^n$. Molecular diffusion is simulated through the use of random walks. Then letting $\omega^{n+1} = \omega_1^{n+1} + \omega_2^{n+1}$ at the end of the timestep, we should get a solution to (3.6) as $\Delta t \to 0$. This technique is known as 'operator splitting'.

A variety of numerical experiments have been performed to examine the error associated with a random walk solution to the diffusion equation in the vortex method. They verified convergence of the random walk algorithm applied to a model problem.

3.2.1 Convection of Vortices

The convection of vortices is simulated by letting them move about in flow field. Helmholtz's vortex law points out that vorticity in a fluid is convected with the local fluid velocity. An alternative statement of Kelvin's Theorem is that vortex lines are material lines, convected with the local fluid velocity. So to move a vortex, we need to know its velocity. Throughout this process the strength of vortex will change as well.

3.2.1.1 Cell-Could Method[5][2]

Assuming some vortices in a flow field, a uniform rectangular grid is set up with square cells for the field. The discrete vorticity field is interpolated onto neighboring gridpoints, and a fast Poisson solver is used to find the stream function at these gridpoints. Finite-difference approximations then yield the velocity field at the gridpoints, which is then interpolated back to the vortex locations. This is called the 'vortex-in-cell' technique.

In detail, we consider a discrete vortex at P, which has a circulation Γ and contributes to the vorticity at the four mesh points of the cell in which it is situated. It is shown in Fig.3.2.

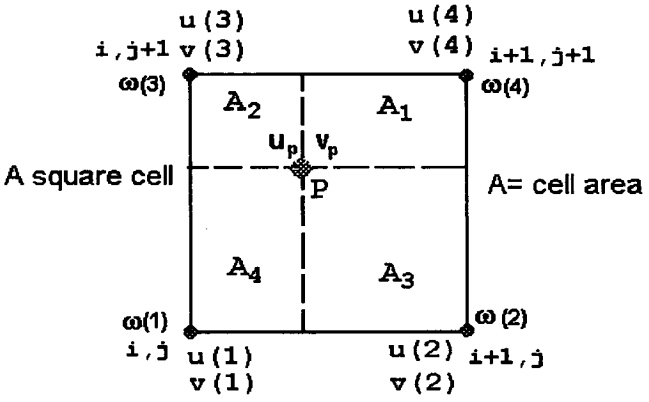

Fig. 3.2 A vortex at point P in a mesh cell

In Fig.3.2 a vortex of circulation Γ at ***P*** generates vorticity at the ***k***th mesh point:

$$\omega(k) = A_k \Gamma / A^2, \qquad k = 1,2,3,4 \qquad (3.15)$$

where A is the cell area. Equation (3.15) is applied to each vortex to give the complete vorticity field specified at the mesh points. This treatment is termed a weighting scheme where the area of A_i is the weight coefficient. The vorticity ω (k) can be used in the Poisson's equation (3.10) to calculate the stream function Ψ and the orthogonal components of velocity are obtained by equation (3.11). Values of Ψ may be calculated at the mesh points by solving Poisson's equation in finite difference form. If ***i,j*** is a mesh point, the equation (3.10) is approximated by :

$$(\psi_{i+1,j} - 2\psi_{i,j} + \psi_{i-1,j}) / H^2 + (\psi_{i,j+1} - 2\psi_{i,j} + \psi_{i,j-1}) / H^2 = -\omega_{i,j} \qquad (3.16)$$

where H is the cell dimension.

Equation (3.16) may be solved very efficiently through the use of Fast Fourier Transforms and so the stream function distribution is thus obtained. The velocity at any vortex point is found by first calculating the velocity at the mesh points of the cell from:

$$u_{i,j} = (\psi_{i,j+1} - \psi_{i,j-1}) / 2H \qquad (3.17a)$$

$$v_{i,j} = (\psi_{i+1,j} - \psi_{i-1,j}) / 2H \qquad (3.17b)$$

and then interpolating them back to the positions of the vortices. (see Fig.3.2):

$$u_p = \sum_{k=1}^{4} u(k) A_k / A \qquad (3.18a)$$

$$v_p = \sum_{k=1}^{4} v(k) A_k / A \qquad (3.18b)$$

Now the velocities of the vortices have been obtained. This process in which the cell area weight has been applied twice is called the weight method or vortex-in-cell method. The first use is to distribute the circulation of the vortex to the mesh points surrounding it, the second use is to interpolate the velocity components of the vortex at P .

3.2.1.2 Boundary values of Ψ

The boundary values of Ψ must be specified for the solution of equation (3.16). They may include the influence of an incident flow and in the calculation here, the incident flow is an oscillatory flow which has a form : $U = A\sin(\omega t)$. The boundary values have to be continuous on boundary lines. They have a simple form as shown in Fig 3.3.

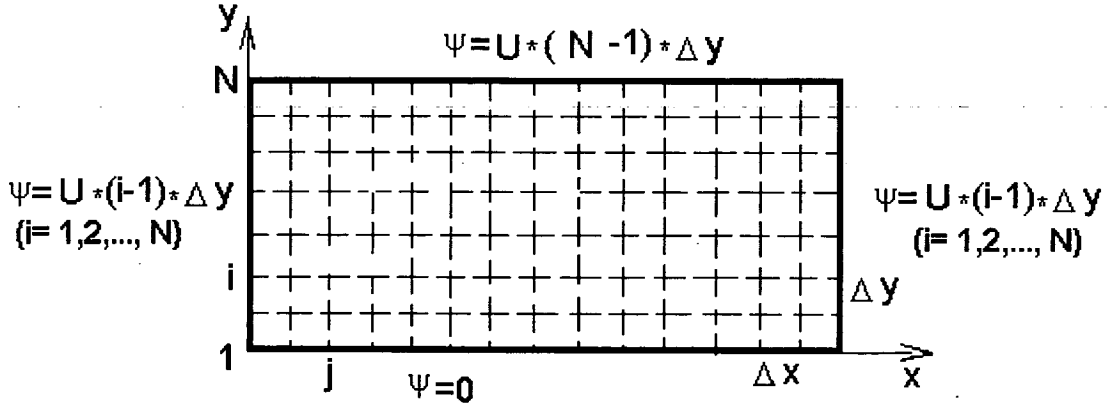

Fig 3.3 Integral mesh and boundary values

The boundary values are obviously continuous in space at every integral step. At the bottom boundary the values of the stream function Ψ are zero. Along both sides the values of Ψ are given as the gradient of Ψ, from zero to a maximum of $\Psi = U*(N-1)*\Delta Y$, the maximum value equals to the values at the top boundary. The strength of the boundary values varies with time , due to the oscillatory nature of the flow $U = A\sin(\omega t)$ and so the boundary values are themselves oscillatory . In the first half period of oscillation, the boundary values are greater than or equal to zero and in the second half period of oscillation, the boundary values are less than or equal to zero. For overlapping meshes, the boundary values of the interior meshes are obtained by linear interpolation of the Ψ field on the exterior mesh.

3.2.1.3 Vortices moving

After the Poisson's equation solution and weight scheme applications, the velocities of the vortices can be found. The vortices may be moved in successive time steps Δt by a first-order scheme:

$$x_p(t+\Delta t) = x_p(t) + (U + u_p(t))\Delta t \qquad (3.19a)$$

$$y_p(t+\Delta t) = y_p(t) + (V + v_p(t))\Delta t \qquad (3.19b)$$

where x and y are the orthogonal coordinates of a vortex, and where u and v are velocities in the x and y directions due to the interaction between the vortex and the flow. U and V are the corresponding components of the incident velocity of the onset flow.

3.2.2 Diffusion of vortices

For equation (3.13) of vortex diffusion, ω comes from the solution of the Poisson's equation. The effect of viscosity is simulated by a random walks method.

3.2.2.1 Random walks method[2]

The motion of a diffusing vortex of initial strength Γ centred on the origin of the

(r,θ) plane is described by the diffusion equation (3.12), expressed in polar coordinates,

$$\frac{\partial \omega}{\partial t} = \nu\left\{\frac{\partial^2 \omega}{\partial r^2} + \frac{1}{r}\frac{\partial \omega}{\partial r}\right\} \qquad (3.20)$$

from which we may obtain the well known solution for the subsequent vorticity distribution in space and time,

$$\omega(r,t) = \frac{\Gamma}{4\pi\nu t} e^{(-r^2/4\nu t)} \qquad (3.21)$$

This exact solution is shown in Fig 3.4

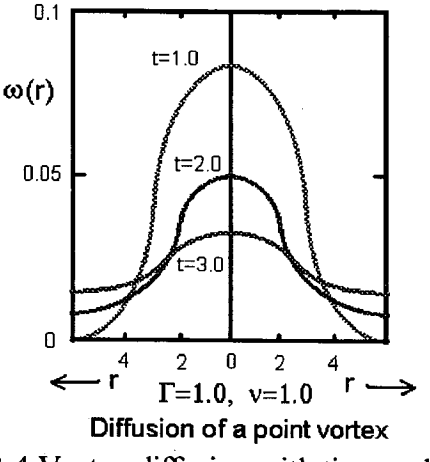

Fig. 3.4 Vortex diffusion with time and radius

Vorticity strength inversely proportional to time and radius, as can be seen in Fig 3.4 where the strength of vorticity is growing weaker with time and radius (or distance). This numerical diffusion process is simulated by the random walks method. The random walk method is based upon a numerical simulation of this diffused vorticity by an equivalent cloud of discretised vortex elements. As illustrated in Fig 3.5, we replace the vortex Γ by N elements each of strength Γ/N located at the origin at time t=0 but free to move independently. Some time later the diffused vorticity may be represented by scattering the elements over the (r,θ) plane. The angles and distances of the moving elements are determined by random numbers , see Fig.3.5.

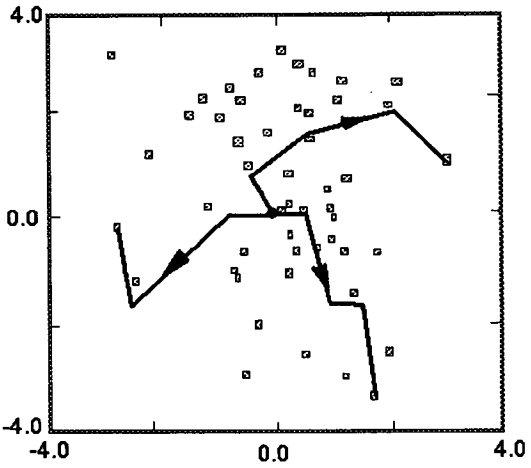

Fig 3.5 Random diffusion walks

This random walk method requires a very large number of vortices for accurate simulations of flows which need a long time evolution to establish their unsteady characteristics. This number may be around 10^5.

The velocities are obtained by directly summing the contributions from each vortex, so we will encounter some technical limitations in that we must choose a suitable value for N and that we must delete some vortices downstream of the flow. Random walks are added to the orthogonal components of a vortex displacement during each time step so that:

$$x(t+\Delta t) = x(t) + \eta_1 \qquad (3.22a)$$

$$y(t+\Delta t) = y(t) + \eta_2 \qquad (3.22b)$$

where η_1 and η_2 are Gaussianly distributed random variables with zero mean and standard deviation $(2\nu\Delta t)^{1/2}$.

3.2.2.2 Vortex Movement

1) Movement in a flow field

The new position of a vortex due to convection and diffusion may be given by:

$$x(t+\Delta t) = x(t) + (U + u(t))\Delta t + \eta_1 \qquad (3.23a)$$

$$y(t+\Delta t) = y(t) + (V + v(t))\Delta t + \eta_2 \qquad (3.23b)$$

At very high Reynolds numbers, vortex movement due to diffusion is often small compared to movement due to convection. To improve the accuracy of the convection method, vortices are moved according to a second-order scheme for which:

$$x(t+\Delta t) = x(t) + 0.5\left[(U + u(t)) + (U + u'(t))\right] \qquad (3.24a)$$

$$y(t+\Delta t) = y(t) + 0.5\left[(V + v(t)) + (V + v'(t))\right] \qquad (3.24b)$$

where $u'(t)$ and $v'(t)$ are the velocities at position:

$$x' = x(t) + (U + u(t))\Delta t \qquad (3.25a)$$

$$y' = y(t) + (V + v(t))\Delta t \qquad (3.25b)$$

In this method the vortices are initially advanced using the first-order scheme (equation(3.19a,b)). The stream function distribution is then recalculated and corrections are added to $x(t+\Delta t)$ and $y(t+\Delta t)$ following equation (3.24a,b).

2) Movement close to the body

There are two kinds of simulations : the mirror image and absorption

A)The method of image [6][7]

The concept of the image method is : to suppose that a system S of sources and sinks exists in a fluid possessing one or more boundaries C. If by placing a system S'of sources and sinks in the region outside C and then allowing the fluid to have access to the whole region, we get C as a streamline, then the system S' is said to be the image in C of the system S. Fig 3.6(a)

For the case of a vortex , suppose there is a line vortex of strength Γ at a distance d from a rigid plane wall x=0, as in Fig 3.6 (b). Imagine that the region $x \leq 0$ is also

filled with fluid and that there is an equal and opposite vortex, i.e. of strength $-\Gamma$, at the mirror-image point, as in Fig. 3.6(c).

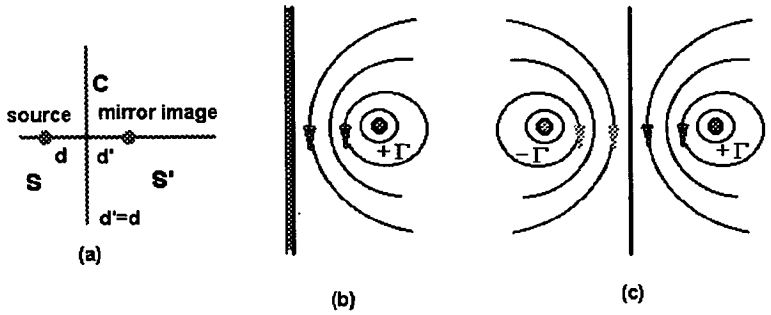

Fig 3.6 Flow and its mirror image system

The reason for doing this is that the x-components of velocity of the two vortices obviously cancel on x=0, so there is no normal velocity component there. Thus the complex potential

$$\Psi = -\frac{i\Gamma}{2\pi}\log(z-d)+\frac{i\Gamma}{2\pi}\log(z+d) \qquad (3.26)$$

serves not only for the flow problem in fig. 3.6(c) but also for the flow in the presence of a wall in Fig 3.6(b). The image method can thus be applied in order to obtain flows that satisfy the boundary conditions. In numerical calulations, the method of mirror image can be used to solve the problems that arise when vortices move across the rigid boundaries of the cylinders.

To maintain the condition of constant surface circulation flux (equivalently vorticity gradient) during a time step, vortices which cross inside a surface may be reflected back to their exterior mirror-image positions[2], as Fig 3.7. The mirror -image position of a vortex is decided uniquely by its angule θ and the distance ε between the vortex and cylinder surface.

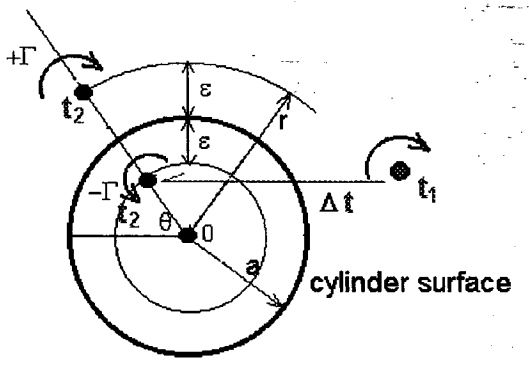

Fig 3.7. Mirror image system for modelling a point vortex close to a cylinder

B) Absorption Method[8]

In the code we used here , an absorption method is applied. When a vortex is found to cross inside the surface of the cylinder, the vortex will be deleted or absorbed with its strength being used to generate new vortices. This new vorticity sheet is generated on the surface of the cylinder.

Using absorption, there are fewer vortices in the flow than by the method of image, and hence it will be easier to obtain convergent results. In order to maintain the constant circulation flux condition, a modification is required to the random walk distribution for a proportion of the vortices created.

3.3 Overlapping Meshes

3.3.1 Advantage

A strong advantage of overlapping meshes is that it can minimize the computing time[9][10]. The vortex method requires a lot of time in order to simulate the flow field which involve a range of vortex sizes from the length scale of the problem, such as the maximum oscillatory velocity, to the mesh cell size, Δx. This is simply in order to reach a statistically distinct realisation of the flow. The cell size obviously determines the smallest scale of inviscid motion which may be represented. A very small scale is required on the cylinder boundary, for the boundary layer, while a large scale will be adequate to transport large vortex structures which have been convected large distances from the body. For this situation, the length of integral step Δt will be limited by the mesh cell size, Δx, according to the requirement for integral convergence,

$$\frac{u\Delta t}{\Delta x} \leq 1 \qquad (3.27)$$

where u is the velocity of the flow. So, a large amount of the work carried out by the simulation arises from the small size of the time step compared to the correlation period of the large structures. Overlapping meshes increase the efficiency of the simulation by using meshes of different resolution for differenct parts of the flow.

3.3.2 Basic Process

Here, we consider three overlapping meshes. An inner polar mesh, just large enough to cover the body(a circular cylinder), is used to provide sufficient definition for the boundary. The intermediate mesh with rectangular frame covers the 'formation region', where vorticity shed from the surface forms large-scale structures which are eventually convected downstream on the outer mesh. See Fig 3.8

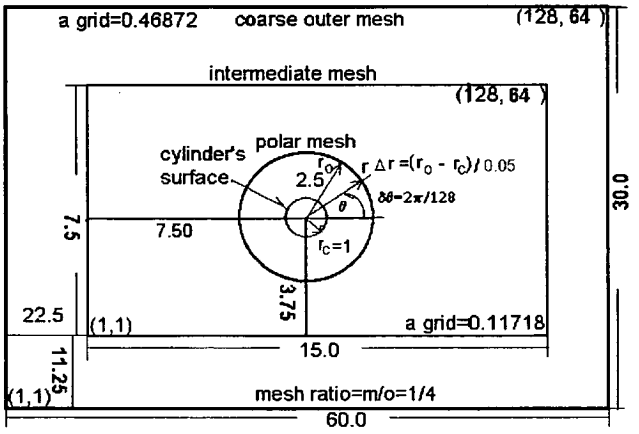

Fig 3.8 Overlapping meshes

The calculation is as follows: The discrete vortices determine the vorticity distribution on the outer mesh. The boundary condition for Poisson's equation is fixed and the stream function distribution is calculated and stored. The discrete vortices inside the intermediate mesh determine its vorticity distribution and the stream function on the outer mesh determines the boundary values through linear interpolation. The stream function on this mesh is calculated and stored. The process is repeated for the inner mesh with boundary conditions obtained from the intermediate mesh. There are two closed circular boundaries in the polar mesh. For convenience the mesh points on a larger mesh coincide with those on the smaller mesh where these overlap. Poisson's

equation is thus solved three times and the velocity of a vortex is calculated from the stream function distribution of the mesh with the smallest possible cell size.

3.3.3 Model Arrangements

A) The Polar Mesh[11]

A polar mesh has a uniform mesh size in the coordinate system (r, θ), as shown in Fig 3.9, defined over an annular region outside the cylinder surface $(1 < r < r_o)$. At the node(i,j), r =j and θ=i Δ θ. Here $\Delta\theta = 2\pi / 128; i = 0,\ldots,128; j = 0,\ldots 30$. Fine resolution is required near to the surface of the cylinder, whereas progressively coarser resolution is acceptable with increasing radial distance. The mesh is coincident with the surface of the cylinder along its inner boundary, enabling the surface boundary conditions to be satisfied simply and precisely. A fine radial spacing given by $\sqrt{4\Delta t / \mathrm{Re}}$ is used at the surface of cylinder to give good definition in the boundary layers. Its value will decrease with increasing Reynolds number (Re) which means that the boundary layer is getting thinner as the Reynolds number increases.

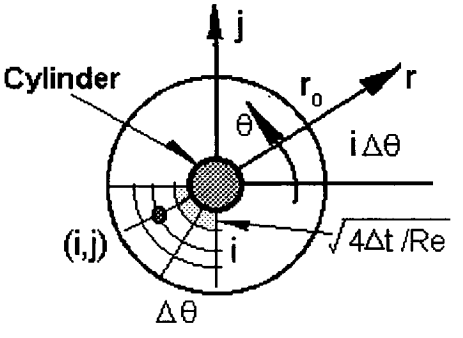

Fig 3.9 A polar mesh

It is also used in solving the Poisson's equation on the polar mesh. The Poisson's equation (3.10) may be written in the polar coordinate system(r', θ):

$$\frac{\partial^2 \Psi}{\partial \theta^2} + a(r')\frac{\partial^2 \Psi}{\partial r'} + b(r')\frac{\partial \Psi}{\partial r'} = -\omega r^2 \qquad (3.28)$$

where $$a(r') = \left(r\frac{dr'}{dr}\right)^2, \qquad (3.29)$$

$$b(r') = r\frac{dr'}{dr} + r^2\frac{d^2r'}{dr^2}, \tag{3.30}$$

$$r = B(e^{Ar'} - 1) + 1 \tag{3.31}$$

The constants A and B in equation (3.31) are fixed by the radial mesh spacing at the cylinder surface and by the value of the outer radius (r_o) which has been shown in Fig.3.9.

B) Multi-cylinder meshes

For the two cylinder case, the mesh arrangement is as Fig.3.10

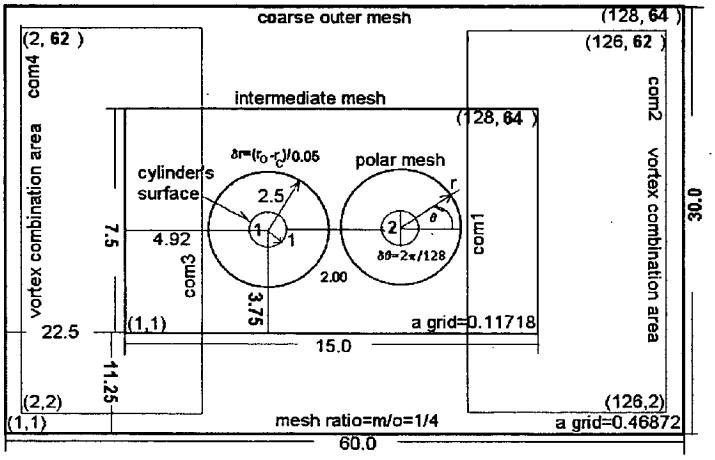

Fig 3.10 Two cylinders model mesh

When the distance between the two cylinders needs to be changed, the two cylinders will be placed in the positions which are symmetrical about the center of the rectangular meshes. All cylinders have their own polar mesh, which can not overlap each other. This means if two cylinders are quite near each other , the outer radius of their polar meshes must be shrunk. The cell size of the coarse outer mesh is four times larger than that of the intermediate mesh. The results will be given on the coarse outer mesh.

For the four cylinder case , the overlapping mesh, with a square outline, is shown in Fig 3.11.

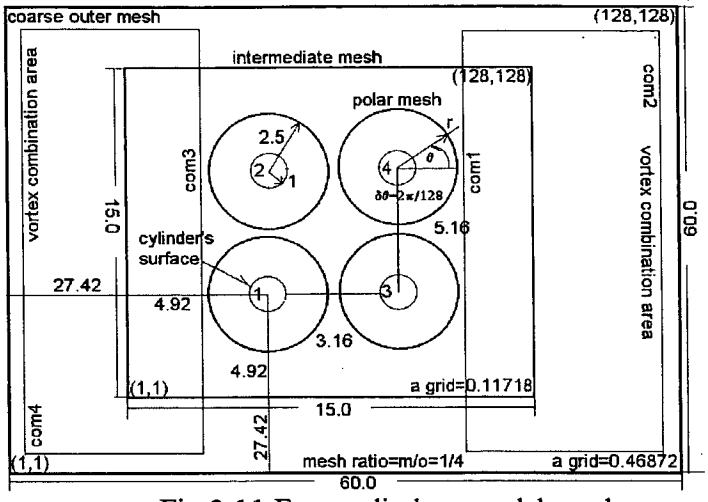

Fig 3.11 Four cylinders model meshes

3.4 Reducing The Number of Vortices

During the evolution of the flow, new vortices appear at the cylinder's surface and old vortices move away from the cylinder, so that the number of vortices will increase quickly with time. This rapid increase in number of vortices will be especially obvious at big Keulegan-Carpenter numbers, and they will occupy a huge amount of memory in the computer. The operation count for each timestep is of order NlogN, where N is the number of grid points on the mesh, whereas direct summation for L vortices would produce an operation count of order L^2. Obviously, when the number of cylinders increases, N and L will grow as the double of this number. It is therefore necessary to regularly reduce the number of vortices present in the simulation. There are several ways in which this reduction may be acheived.

3.4.1 Control of Number of New Vortices

New vortices are generated on the surfaces of the cylinders and, the number of new vortices is determined by the segments on the surfaces. The number of the segments is chosen before integration starts and so it is necessary to make a suitable choice. In the code here the segment number is :

$$N_v = 120 / (\textit{cylinder number})\text{; if there is only a single cylinder } N_v = 60 .$$

So for the single cylinder and two cylinder cases, the number of new vortices for each cylinder is 60. For the two cylinders model, the total number of new vortices will be

120. For four cylinders, there are 30 new vortices at each cylinder, but the total number will still be 120. N_v must not be too small, according to [11], or the integration may fail to converge. When a long time step is used, a large value of N_v is required for convergence.

3.4.2 Absorption at Surface

In section 3.2.2.2 we have mentioned the application of the absorption method when vortices cross the cylinder boundaries. In this way, those vortices will be deleted from the flow field and the number of vortices is then reduced. At each step, the position of every vortex is examined. If a vortex falls inside of a cylinder, the vortex is sent to a deletion queue, then those vortices still in existence are sorted out. The circulation carried by the deleted vortices is automatically included in that of the newly created vortices, maintaining the correct flux of circulation. The circulation is equal to the new circulation created at the ith node and the circulation carried by deleted vortices crossing the ith surface segment.

3.4.3 Limitation of Minimum Vorticity

In the code a minimum vorticity strength is specified before integration begins. The vorticity of every vortex is compared to the minimum value regularly during integration. If the strength of the vorticity is smaller than the specified minimum , the vortex will be removed from the flow field.

After testing different Vmin values , from 0.001 to 0.01, we found that the influence of the Vmin in the model is mainly the output of the force coefficients and computer space saving, and the two problems influences each other. If a larger Vmin is choosen , more vortices will be deleted from the vortex collectional queue and more space can be saved , this will allow the integration to carry on smoothly. But the force coefficients are calculated from the surface circulation which is decided by surface vortices, too many vortices are deleted , the force coefficient simulation may be unsatisfactory.

For example, in a single cylinder case the conditions are KC =10 and space size (vortices dimension) = 500000 , to use a Vmin of 0.001 will result in the integration

stops on half way or a shorter time since the space has been full. A Vmin of 0.01 under the same conditions could keep the integration several times longer than using a smaller Vmin. But different Vmin values will cause the change of the force coefficients , it is impossible that a larger Vmin will give definitely a better simulation of the force coefficient. The formulae of the force coefficients in the model are :

$$C_l = \frac{\Delta\theta}{\Delta t}\sum_{j=0}^{128}\left[\cos(j\Delta\theta)\sum_{i=1}^{j}\Gamma(i,0)\right] \quad (*) \qquad C_l = -\frac{\Delta\theta}{\Delta t}\sum_{j=0}^{128}\left[\sin(j\Delta\theta)\sum_{i}^{j}\Gamma(i,0)\right] \quad (**)$$

where $\Gamma(i,0)$ is the circulation of the vortices on the surfaces of the cylinders, it is a function of the vorticity. When the Vmin is changed the vorticity around the cylinders will be tidied up according to the Vmin value. Then the circulation $\Gamma(i,0)$ will have some changes and further cause force coefficient values change. The assessment of a suitable Vmin is carried out by comparing the frequency of the force coefficients with that of the Lab experimental results.

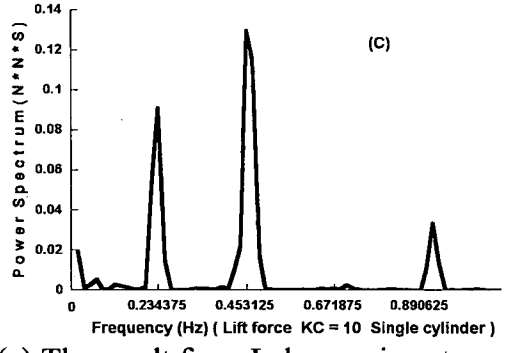

(a) The result from Lab experiment

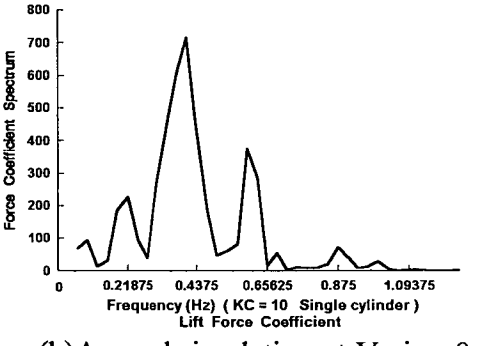

(b)A good simulation at Vmin =0.006

The component of the first harmonic is similar to the second harmonic and a bit smaller

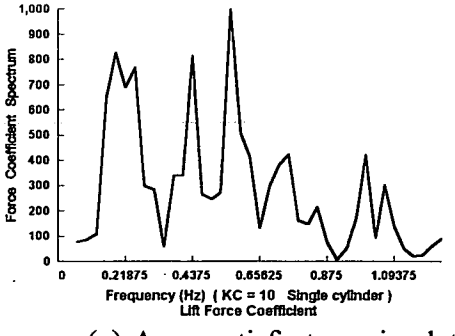

(c) An unsatisfactory simulation at Vmin=0.003

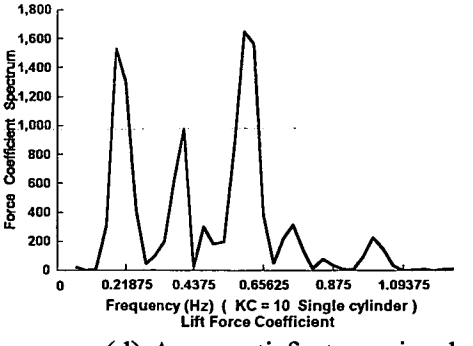

(d) An unsatisfactory simulation at Vmin=0.01

The component of the first harmonic is too small or has none.

Fig 3.12 An influence on the force coefficient by Vmin

After a lot of tests, it is found that a Vmin with value around 0.005 is suitable.

3.4.4 Diffusion Reduction

From section 3.2.2.1, we know that the diffusion is simulated by dividing an original vortex into many vortices and then letting them move about. The number of these vortices is determined by a formula :

$$n = 1 + |\Gamma| / \Gamma_o \qquad (3.32)$$

where Γ is the original circulation at a segment, Γ_o is the maximum magnitude of circulation for a vortex , which has been specified. In the code it equals Vmin. A smaller Γ_o will give a greater number of vortices, so a suitable Γ_o will control the number of vortices appearing in the flow field.

3.4.5 Combination of Vortices

The vortices which have moved downstream can be reduced in number by replacing them with point vortices on the grid points of the outer mesh. This is an advantage of the vortex method.

The process is as follows (Fig 3.13). Those vortices which have been assigned to the grid points of the outer mesh never exist as vortices in the flow field, so the total number of vortices is thus reduced. The process of interpolating the vorticity on to a mesh can introduce significant inaccuracy into the computation of vortex intercation. In the close interaction between neighboring vortices , the smearing of vorticity onto an intermediate mesh can introduce artificial viscosity which dominates the physical viscosity of the system, so we divide the computation into near and far-field effects. The combination technique is for the contribution of the far-field effects and is carried out on the coarse outer mesh.

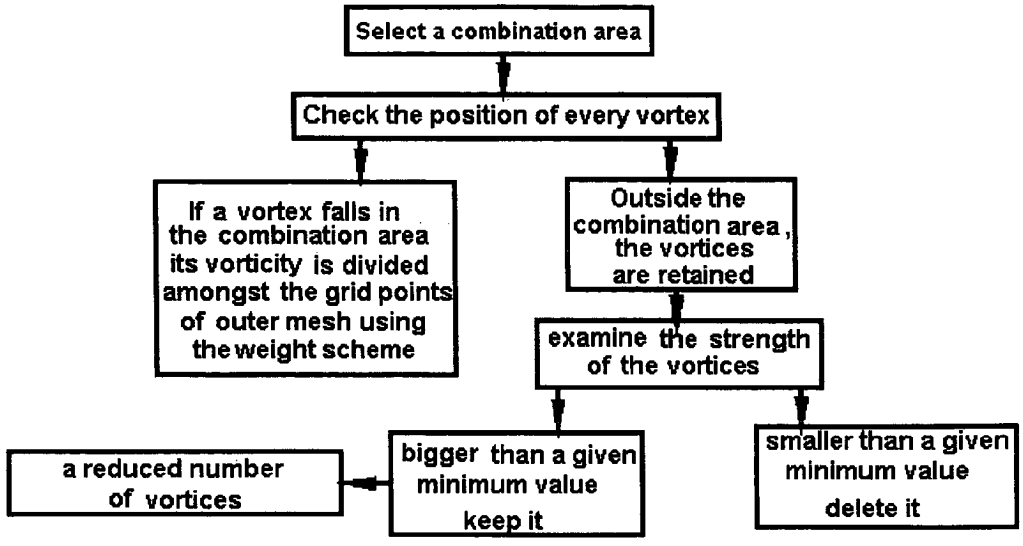

Fig 3.13 The process of combining vortices

The suitable combination areas, the size of the area , the start time and frequency of combination have to be dermined by test. The combination area is at down stream of the cylinder; for an oscillatory flow, the position of the combination area changes with each half period. This is shown in Fig 3.10 and Fig3.11. The frequency of the combination for per period and the combination area size depends on the KC number and cylinder number. Because the number of vortices is proportional to the KC number and the number of cylinders, the frequency and area of the combination is proportional to both parameters, too.

3.5.Generation of new vortices

3.5.1 New Vortices Source Area

In all real flows a boundary shear layer develops adjacent to the surface of a body. Across the boundary layer, the velocity of the potential flow just outside the layer undergoes a smooth but rapid change to precisely zero—corresponding to no slip or viscous adherence—on the surface of the body.See Fig. 3.14.

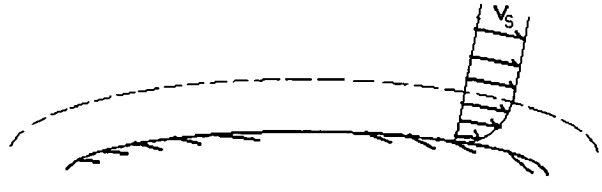

Fig 3.14 A boundary layer

In this boundary layer, inviscid theory fails and viscous effects are important, even though they are negligible in the main part of the flow. The action of viscosity is to cause the vorticity in this shear layer to diffuse normal to the surface, resulting in the familiar viscous boundary layer.

In the case of simple shear flow, **u**=[u(y),0,0] ,the fluid immediately above some level y=constant exerts a stress, i.e. a force per unit area of contact, on the fluid immediately below, and vice versa. For an inviscid fluid this stress has no tangential component τ, but for a viscous fluid τ is typically non-zero and proportional to the velocity gradient, i.e.

$$\tau = \mu \frac{du}{dy} \qquad (3.33)$$

The velocity gradients in a boundary layer are much larger than they are in the main part of the flow, because a substantial change in velocity is taking place across a very thin layer. In this way the viscous stress (3.33) becomes significant in a boundary layer, even though μ (dynamic viscosity) is small enough for viscous effects to be negligible elsewhere in the flow. The observed flow of a low-viscosity fluid past a circular cylinder is quite different from that predicted by inviscid theory. There is a massive separation of the boundary layer giving rise to a large vorticity-filled wake. From a mathematical point of view, what happens in the limit $\mu \to 0$ may be quite different to what happens when $\mu = 0$.

The thickness of the boundary layer is related to the Reynolds number, [12]. As the Reynolds number increases, the boundary layer becomes thinner. This can be seen in Fig 3.15

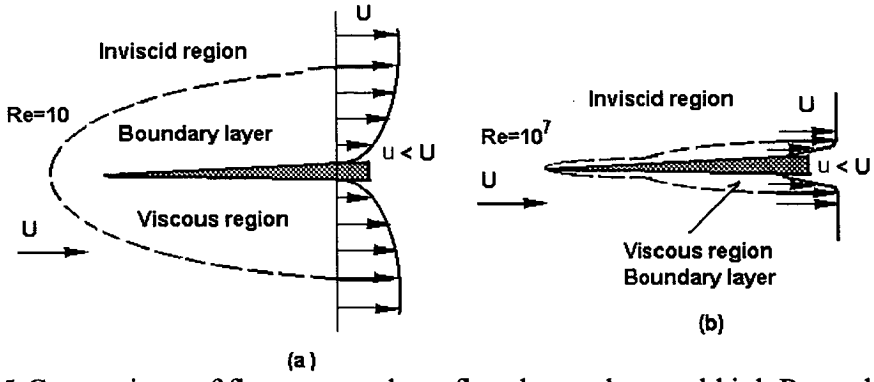

Fig. 3.15 Comparison of flow past a sharp flat plate at low and high Reynolds numbers (a) laminar, low Reynolds number; (b) high Renolds number flow

Suppose that we were able gradually to reduce the fluid viscosity to zero in a real fluid flow. In the limit, due to progressive reduction of viscous diffusion, the boundary layer would approach infinitesimal thickness. As the viscosity approached zero and the Reynolds number approached infinity, the body surface would be covered with an infinitely thin vorticity sheet $\gamma(p)$. Fig .3.16

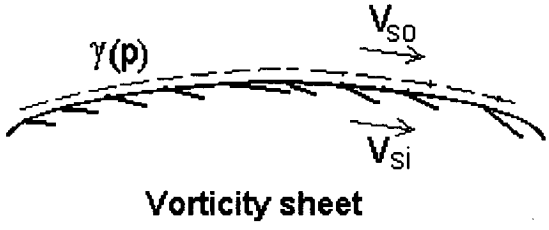

Fig 3.16 Vorticity Sheet

In Fig.3.16, V_{so} and V_{si} are velocities just outside and inside the vorticity sheet. The fluid velocity would change discontinuously across the sheet from zero beneath the sheet to V_{so} parallel to the surface just above the sheet. In the case of a real flow with extremely high Reynolds number, leaving aside the additional features connected with instabilities in the shear layer itself, the inviscid potential flow can be thought of as a special type of infinite Reynolds number flow. An irrotational potential flow thus comprises a surface vorticity sheet covering the body surface, separating the irrotational flow of the outer domain from the motionless inner domain. The initial strength of vortices will be generated from this layer. In this sense the surface vorticity is precisely that of the physical reality of a real infinte Reynolds number (but fully attached) flow and is therefore the most natural of all numerical methods for potential flow analysis.

3.5.2 The Surface Boundary Condition

A) Normal Boundary Condition

The normal boundary condition is **u•n=0** on the boundary ∂D, it means that fluid cannot pass through the obstacle. For both inviscid and viscous flow, the addition of the normal boundary condition on the solid surface is not difficult.

Given a region D, suppose that **u•n=0** on the boundary ∂D, where **n** is the inward normal vector. Let $\mathbf{u}_{Vor}(\mathbf{x},t)$ be the velocity field obtained from the distribution of vorticity and consider a potential flow, $\mathbf{u}_{pot} = \nabla\phi$, such that $(\mathbf{u}_{pot} + \mathbf{u}_{vor}) \bullet \mathbf{n} = \mathbf{0}$ on ∂D. A combination of the vorticity flow $\mathbf{u}_{vor}$ and the potential flow $\mathbf{u}_{pot}$ will yield a flow which satisfies the normal boundary condition by construction and has the same vorticity, since $\nabla \times \mathbf{u}_{pot} = \nabla \times \nabla\phi = 0$.

B) Tangential Boundary Condition

The tangential no-slip condition is **u•τ**=0 on the boundary ∂D(τ is the unit tangent to the solid surface of the body). It conveys the fact that fluid in direct contact with the surface of the body must be stationary.

This condition considerably complicates the case of viscous flow. In a thin boundary layer, let **u**=(u,v) and suppose that the x axis is tangential to the surface of the body. Then $\partial u/\partial y$, which is the derivative of the tangential velocity in the direction normal to the surface, must be large. On the other hand, $\partial v/\partial x$, which is the derivative of the normal velocity along the surface, is small, since, by the addition of the potential flow, v is zero along the x-axis. Since vorticity is defined by $\omega = \partial v/\partial x - \partial u/\partial y$, the tangential boundary condition is a major source of vorticity in the flow. At large Reynolds numbers, particularly in the case of bluff bodies, streamlines break away near the sides of the body and enclose the fluid behind the body in an unsteady manner. This boundary layer separation leads to the downstream shedding of large physical vortices.

At each time step the condition of zero velocity on the surface must be re-established. To achieve this, a new vortex sheet is created on the surface by way of a boundary integral calculation which gives the potential flow condition. The normal velocity and

the velocity on the inside of the sheet are set to zero.

3.5.3 The New Vortices and Their Strength

Vorticity creation occurs throughout the entire boundary layer. The length of the boundary is broken up into intervals, and within each interval a smoothed vortex element is created at each time step. See fig 3.17.

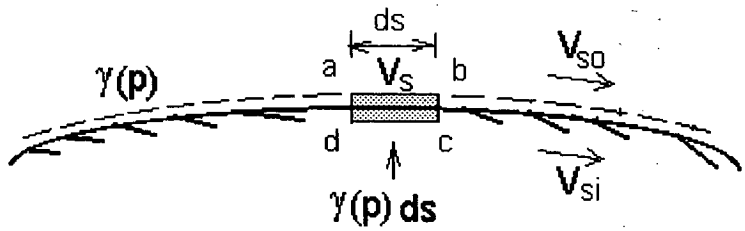

Fig 3.17 Vorticity element

The strength of each element is chosen to give a zero the tangential velocity, and so by construction, the no-slip condition is satisfied.

There are two advantages to this technique. First, no a prior assumption about the location of the separation point is made, since the entire body acts as a line source of vorticity. Second, since vortex elements with smoothed velocity fields are used, more vortices may be used to resolve the vortex sheet along the boundary while avoiding the instabilities that plague point vortex approximations.

3.5.3.1 Circulation, vorticity and tangential velocity

In the theory of invisicid fluids, vortices are often idealized by supposing that the vorticity is concentrated along a line, the total strength remaining finite. Then the circulation in any circuit which is threaded by one of those line vortices is equal to the strength of the vortex[18]. So the vortex strength, vorticity, is related to the fluid circulation Γ. Its definition for any closed contour, C, in a fluid is:

$$\Gamma = \oint_c \vec{u} \bullet d\vec{l} = \int_s \vec{\omega} \bullet \vec{n} ds \qquad (3.34)$$

where S is an arbitrary curved surface. The circulation is a scalar quantity , equal to the integrated component of vorticity normal to the surface around which Γ is taken. We shall suppose that the relation is that described by a right-hand-threaded screw. We first define abcd – as shown in Fig 3.16 --- to be the contour surrounding a small vorticity element γ(p)ds where ab and dc are parallel to the streamlines, while da and cb are normal to them. Now γ(p) is defined as the vorticity strength per unit length at point p. The circulation around abcd may be equated to the total amount of vorticity enclosed by the contour, that is:

$$(v_{ab} + v_{bc} + v_{cd} + v_{da})ds = \gamma(p)ds \qquad (3.35)$$

where v_{bc} and v_{da} are zero because da and cb are normal to the streamlines. $v_{ab} = v_{so}$ and $v_{cd} = v_{si}$ are the fluid velocities just outside and inside the sheet vortex which must be parallel to the surface.

So $$(v_{so} - v_{si})ds = \gamma(p)ds \qquad (3.36)$$

According to the boundary condition, let $v_{si} = 0$, then (3.36) becomes :

$$v_{so} = v_s = \gamma(p) \qquad (3.37)$$

This equation tells us that the potential flow velocity close to the body surface, v_s, is exactly equal to the surface vorticity $\gamma(p)$.

3.5.3.2 The boundary integral method[5]

In two dimensions the stream function, which is assumed to satisfy Laplace's equation, $\nabla^2\Psi = 0$, can be considered to be produced by a distribution of vorticity along a contour C and is given by :

$$\Psi(x,y) = \frac{1}{2\pi}\int_C \gamma(q)\ln[r(q)]ds \qquad (3.38)$$

where C is parameterised by the variable s, $r(q)$ is the distance between (x,y) and the point q on the contour in question and $\gamma(q)$ is the strength of the vorticity distribution at that point. Then the velocity at (x,y) is given by :

$$\mathbf{u} = \nabla \times (\Psi \mathbf{k}) \tag{3.39}$$

where **k** is the unit vector in the z direction, normal to the x, y plane. A limiting analysis shows that the singular contribution to $\mathbf{u}_p$ due to the infinitesimal section of C surrounding the point P=(x,y) is equal to $(-\gamma(p)/2)\mathbf{t}$ on the external side of C and $(\gamma(p)/2)\mathbf{t}$ on the internal side, where **t** is the tangential unit vector at P , in the clockwise direction. There is a jump in the tangential velocity component across C of magnitude $\gamma(p)$. For the points on the outside of the boundary, equation (3.39) can be writen :

$$\mathbf{u}_p = -\frac{\gamma(p)}{2}\mathbf{t}_p + P\int_C \frac{\gamma(q)}{2\pi}\nabla_p \times \ln(r(q))\mathbf{k}ds \tag{3.40}$$

and similarly on the inside of C , it will be :

$$\mathbf{u}_p = \frac{\gamma(p)}{2}\mathbf{t}_p + P\int_C \frac{\gamma(q)}{2\pi}\nabla_p \times \ln(r(q))\mathbf{k}ds \tag{3.41}$$

In (3.40) and (3.41) the P before the integral sign indicates that the principal value of the integral should be taken. If a surface vorticity distribution makes the contour a streamline then the velocity induced inside the contour is zero everywhere. (Ψ is a constant on C). So, setting the internal tangential velocity equal to zero, gives :

$$\mathbf{u}_p^{\infty} \bullet \mathbf{t}_p + \frac{\gamma(P)}{2} + P\int_C \frac{\gamma(q)}{2\pi}[\nabla_p \times \ln(r(q))\mathbf{k}] \bullet \mathbf{t}_p ds = 0 \tag{3.42}$$

where $\mathbf{u}_p^{\infty}$ is the unperturbed velocity at P (the onset flow).

The external tangential velocity is :

$$u_p^t = \mathbf{u}_p^\infty \bullet \mathbf{t}_p - \frac{\gamma(p)}{2} + P\int_C \frac{\gamma(q)}{2\pi}[\nabla_p \times \ln(r(q))\mathbf{k}] \bullet \mathbf{t}_p ds \qquad (3.43)$$

Substituting (3.42) into (3.43), we obtain :

$$u_p^t = -\gamma(p) \qquad (3.44)$$

So once the unknown vorticity distribution is determined, the external tangential velocity is known immediately.

In order to solve the boundary integral equation, the cylinder's body contour is first divided into M sections, each carrying a distribution γ. Each section is then approximated by a straight line segment along which the vorticity is constant. See Fig. 3.18 The discrete approximation to equation (3.42) is written for the midpoint of each segment as follows:

$$u_\infty^t(I) + \frac{\gamma(I)}{2} + \sum_{\substack{J=1 \\ J\neq I}}^{M} \int_{SA}^{SB} \frac{\gamma(J)}{2\pi}[\nabla_p \times \ln(r(J))\mathbf{k}] \bullet \mathbf{t}_p ds = 0 \qquad (3.45)$$

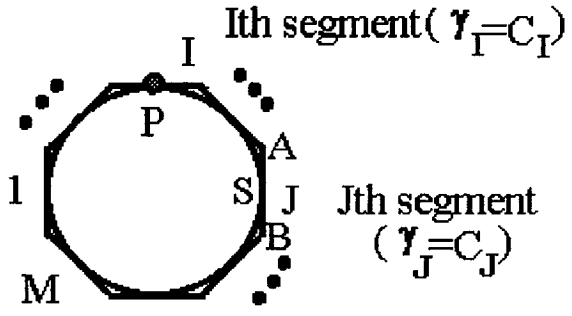

Fig 3.18 Surface segments

In equation (3.45) , $u_\infty^t(I)$ is the onset tangential velocity at the Ith midpoint, $\gamma(I)$ is the strength of the Ith segment and SA, SB are the ends of the Jth segment with vorticity $\gamma(J)$. The integral under summation is the tangential velocity component induced at the Ith midpoint by the Jth segment of vorticity.

Equation (3.45) can be written in matrix form as :

$$\mathbf{K\gamma=b} \qquad (3.46)$$

where $K(I,J) = \begin{cases} \dfrac{1}{2\pi}\int_{SA}^{SB}[\nabla_p \times \ln(r(J))\mathbf{k}] \bullet \mathbf{t}_p ds \ldots\ldots\ldots\ldots I \neq J \\ 0.5 \ldots\ldots\ldots\ldots\ldots\ldots\ldots\ldots\ldots\ldots\ldots\ldots I = J \end{cases}$

and

$$b(I) = -u'_\infty(I)$$

The matrix $\boldsymbol{K}$ is only dependent on the geometry of the body surface and $\boldsymbol{b}$ is a function of the onset tangential velocity at the midpoint of each segment. **K** is called an influence matrix, its properties determine whether or not there are unique solutions to the system of simultaneous equations for the M unknown strengths. (**K** cannot be zero, or (3.46) has no solution or no unique solution).

When **K** is non-singular, a solution for γ can be determined from :

$$\gamma = [\mathbf{K}]^{-1}\mathbf{b} \qquad (3.47)$$

Equation (3.47) is solved for γ before the integration begins.

3.5.3.3 New vortices at each integral step

New vortices are created along the surface of the cylinder (r =1) at each time step, it is to simulate the creation of vorticity due to the action of viscosity at a solid boundary. In a polar coordinate system (r', θ), Poisson's equation may be written :

$$\frac{\partial^2 \Psi}{\partial \theta^2} + a(r')\frac{\partial^2 \Psi}{\partial r'^2} + b(r')\frac{\partial \Psi}{\partial r'} = -\omega r^2 \qquad (3.48)$$

where $a(r') = (r\frac{dr'}{dr})^2$, $b(r') = r\frac{dr'}{dr} + r^2\frac{d^2r'}{dr^2}$,

$$r = B(e^{Ar'} - 1) + 1$$

u is related to Ψ through the equation :

$$\mathbf{u} = \frac{\mathbf{r}}{r}\frac{\partial\Psi}{\partial\theta} - \theta\frac{\partial\Psi}{\partial r} \qquad (3.49)$$

The boundary conditions are, for t>0

$\Psi = 0$ *when* $r \le 1$,

$\frac{\partial\Psi}{\partial r} \to -\sin\theta$ *as* $r \to \infty$.

$\mathbf{u}\bullet\theta=0$ when r $\le$ 1

$\omega \to 0$ *as* $r \to \infty$

The boundary conditions set the velocity within the cylinder surface to zero and state that the vorticity and the perturbations caused in the flow are small at large distances from the cylinder. From the boundary conditions, $\Psi = \Psi(r)$ along r =1, the finite difference analogue of (3.48) reduces to :

$$\omega(i,0) = -a(0)[\Psi(i,1) - 2\Psi(i,0) + \Psi(i,-1)] - \frac{1}{2}b(0)[\Psi(i,1) - \Psi(i,-1)] \qquad (3.50)$$

and in (3.48) , $\frac{\partial\Psi}{\partial\theta} = 0$, $\frac{\partial^2\Psi}{\partial r'^2} = (\Psi(i,j+1) - 2\Psi(i,j) + \Psi(i,j-1))/r^2$ and

$\frac{\partial\Psi}{\partial r'} = \frac{1}{2r}(\Psi(i,j+1) - \Psi(i,j-1))$. In order to satisfy the boundary conditions the

stream function must be a constant at all points inside the cylinder. Therefore we set $\Psi(i,-1) = \Psi(i,0) = 0$. See Fig. 3.19.

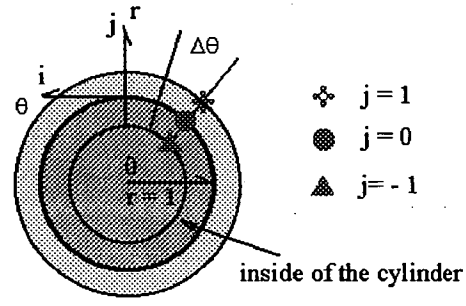

Fig 3.19 A polar coordinate system

Equation (3.50) becomes :

$$\omega(i,0) = -[a(0) + \frac{1}{2}b(0)]\Psi(i,1) \qquad (3.51)$$

where Ψ is obtained from previous solutions of Poisson's equation on the overlapping meshes. An additional circulation $\Gamma(i,0)$ must be introduced at the surface node (i,0), given by

$$\Gamma(i,0) = \Delta\theta\,\omega(i,0)\frac{dr}{dr'}\Big|_{r'=0} - \Gamma'(i,0) \qquad (3.52)$$

where $\Gamma'(i,0)$ is the circulation distributed onto the mesh from the old vortices. The additional circulation $\Gamma(i,0)$ is shared between the newly created vortices where the number of new vortices created at each surface node is determined by a given Nv, See section 3.4.1.

3.6 The force calculation

3.6.1 Forces Acting on The Cylinder[13]

The forces acting on the cylinder due to the flow are divided into two components : in-line force and lift force. The in-line force is described by Morison's equation; it is assumed to be given by the linear sum of the inertial and drag forces. The lift force, perpendicular to the fluid particle direction, is caused by the shedding of vortices from

the cylinder.

3.6.1.1 In-line Force

For the component of the forces acting on the cylinder due to the harmonically oscillating flow parallel to the relative motion of the flow, the experimental studies of Morison and his co-workers (1950) have provided a useful approximation. The force is divided into two parts, one due to the drag, as in the case of flow of constant velocity, and the other due to the acceleration or deceleration of the fluid. This concept necessitates the introduction of a drag coefficient Cd and an inertial coefficient Cm in the expression for the force. In particular, if **F** is the in-line force per unit length experienced by a cylinder, then

$$F = \frac{1}{2} C_d \rho D |U| U + C_m \rho \frac{\pi D^2}{4} \frac{dU}{dt} \qquad (3.53)$$

where U and dU/dt represent the undisturbed velocity and the acceleration of the fluid respectively while D is diameter of the cylinder and ρ is the density of the fluid. The drag force can be also divided into two parts[12][14] produced by viscous friction along the surface and by an asymmetric pressure distribution on the upstream and downstream side of the cylinder. The difference between the high pressure in the front stagnation region and the low pressure in the rear separated region causes a large drag contribution known as pressure drag. This is added to the integrated shear stress or friction drag of the body, which it often exceeds:

$$C_D = C_{D,pres} + C_{D,fric}$$

The relative contribution of friction and pressure drag depends upon the body shape, and in particular its thickness. At zero thickness the body is a flat plate and exhibits 100 percent friction drag. For a circular cylinder, the friction drag is only about 3 percent. The theoretical inviscid pressure distirbution on a circular cylinder is shown in Fig.3.20. [12][16]

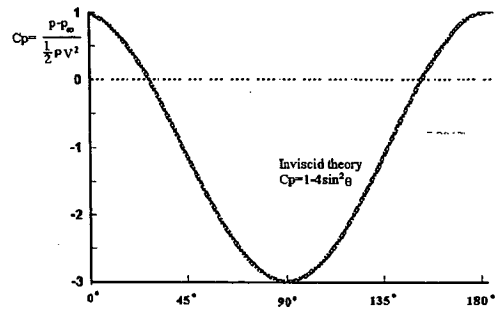

Fig 3.20 Theoretical surface pressure distribution of a flow past a circular cylinder

where P∞ and V are the pressure and velocity in the free stream. P is the normal pressure at an angular distance θ from the forward stagnation point.

The drag coefficient C_D and inertial coeffient C_M can be obtained by dividing the mean drag and inertia per unit length by $\frac{1}{2}\rho U_o^2 D$, where U_o is the undisturbed stream velocity. Keulegan and Carpenter expressed the force in terms of a Fourier series assuming the force to be an odd-harmonic function of $\theta = 2\pi t / T$, i.e., F(θ)=-F(θ+π),

and $2F/(\rho D U_m^2) = 2(A_1 \sin\theta + A_3 \sin 3\theta + A_5 \sin 5\theta + \ldots$

$$B_1 \cos\theta + B_3 \cos 3\theta + B_5 \cos 5\theta + \ldots] \qquad (3.54)$$

Keulegan and Carpenter were able to reconcile Eq.(3.54) with the equation proposed by Morison by rewriting it in the following form:

$$2F/(\rho D U_m^2) = \frac{\pi^2}{K} C_M \sin\theta + 2[A_3 \sin 3\theta + A_5 \sin 5\theta + \ldots]$$

$$-C_D |\cos\theta| \cos\theta + 2[B_3 \cos 3\theta + B_5 \cos 5\theta + \ldots] \qquad (3.55)$$

where K is the Keulegan-Carpenter number (=U_M T/D), and U is assumed to be given by U=-U_m cosθ. Evidently , equation (3.55) reduces to the equation proposed by Morrison, i.e.,

$$2F/(\rho D U_m^2) = \frac{\pi^2}{K} C_M \sin\theta - C_D |\cos\theta \,| \cos\theta \qquad (3.56)$$

provided that the coefficients C_D and C_M are independent of θ , i.e., each term has the same constant value (dependent on K and Re) and A_i and B_i are zero for i ≥ 3. The Fourier averages of C_D and C_M are obtained by multiplying both sides of equation (3.56) once by cosθ and once by sinθ and then integrating between the limits θ=0 and θ=2π. This procedure yields:

$$C_d = -\frac{3}{4}\int_0^{2\pi} \frac{F\cos\theta}{\rho D U_m^2} d\theta \qquad (3.57)$$

$$C_m = \frac{2U_m T}{\pi^3 D}\int_0^{2\pi} \frac{F\sin\theta}{\rho D U_m^2} d\theta \qquad (3.58)$$

3.6.1.2 Lift Force

Lift force is the component of the resultant force exerted by a fluid on a body perpendicular to the relative motion of the fluid[15]. Consider an inviscid flow in which there is a vortex sheet consisting of vortices of equal strength K and equal spacing **a** as in Fig 3.21

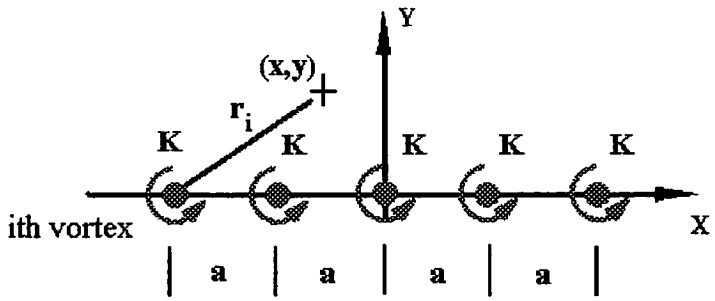

Fig 3.21 An vortex sheet with equal vortex strength

The ith vortex in Fig 3.21 has a stream function $\Psi_i = -K\ln r_i$ so the total sheet has a combined stream function :

$$\Psi = -K\sum_{i=1}^{n} \ln r_i \qquad (3.59)$$

The stream function for flow past a circular cylinder with circulation centered at the

origin, is a uniform stream plus a doublet and a vortex :

$$\Psi = U_\infty r\sin\theta - \frac{\lambda\sin\theta}{r} - K\ln r + constant \qquad (3.60)$$

The doublet strength λ has units of velocity times length squared. For convenience, let $\lambda = U_\infty a^2$, where a is a length, and let the arbitrary constant in equation (3.60) equal K$\ln a$. Then the stream function becomes :

$$\Psi = U_\infty \sin\theta(r - \frac{a^2}{r}) - K\ln\frac{r}{a} \qquad (3.61)$$

The streamlines are plotted in Fig 3.22:

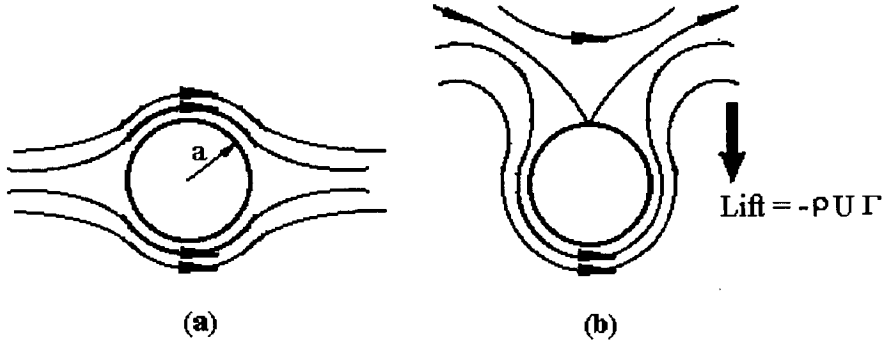

Fig 3.22 Flow past a circular cylinder with circulation
(a) K/U_∞ **a**=0 (b) K/U_∞ **a**=2.0

here K/U_∞**a** is the dimensionless vortex strength. For both cases the line Ψ=0 corresponds to the circle r =a, that is ,the shape of the cylinder surface. As circulation Γ=2πK (by defining a circular path of radius r around the vortex center) increases, the velocity becomes faster and faster below the cylinder and slower and slower above it. The streamline patterns in Fig 3.22 show that the velocity on the top of the cylinder is less and therefore, from Bernoulli's equation, the pressure is higher, (there is no viscous force here) so a force pointing towards the bottom is caused by the pressures difference. This is known as the lift force. According to inviscid theory, the lift force per unit length of cylinder immersed in a uniform stream is equal to $\rho U_\infty \Gamma$, where Γ is the total net circulation contained within the body shape. The direction of the lift is 90° to the stream direction, rotating in the opposite direction to the circulation.

The lift force is a consequence of the pressure gradient across the wake. In harmonic flow the alternating pressure gradient increases with increasing asymmetry in the strength and position of the vortices. This asymmetry is proportional to the KC numbers of the ocillatory flow. Part of this asymmetry is due to the shedding of one or two new vortices and part due to the movement of the vortices shed in the previous half cycle back towards the cylinder. Neither the convected vortices nor the ones newly shed are necessarily symmetrical and result in a maximum wake asymmetry. The interaction of the convected vortices with the flow about the cylinder enhances the asymmetry by forcing the shedding of a new vortex from the side of the cylinder nearest to the convected vortex.

When the vortex-shedding frequency happens to match the natural frequency of an elastic or elastically mounted rigid cylinder, the transverse force will make its greatest contribution to fatigue damage. The magnification of the lift force due to dynamic response is greatest when the vortex-shedding dominant frequency coincides with the structure's natural frequency and the degree of magnification depends on the damping of the system. The oscillation of the cylinder caused by the lift force is referred to as vortex-induced resonant oscillation. When the frequencies of vortex shedding and the body oscillation collapse into a single frequency close to the natural frequency of the body, the phenomenon is known by various names: lock-in, locking-on, self-excited oscillations, and so on.

So lift force are important not only because of their magnitude but also because of their alternating nature, which under certain circumstances may lead to lock-in or vortex synchronization. This phenomenon may cause failure due to fatigue and increased in-line force. [13]

The usual equation of lift force is :

$$Lift \quad Force = C_{L:}\rho D\frac{U^2}{2} \qquad (3.62)$$

where C_L is the lift coefficient. It is represented by:

$$C_L = \frac{2F_L}{\rho D U_\infty^2} \tag{3.63}$$

or

$$C_L = 2\int_0^{2\pi} \frac{F \sin\theta}{\rho D U_\infty^2} d\theta \tag{3.64}$$

C_L is a function of Keulegan-Carpenter number and Reynolds number.

3.6.2 Force and Circulation

The force acting on a cylinder in a steady uniform flow can be represented by circulation according to the momentum theorem[17]. A control surface, S is selected as in Fig 3.23 comprising the outer circle of radius r_1, the inner circle of radius a, and the cut connecting them. If we neglect body forces, the momentum theorem, expressing the fact that the momentum flux through the surface is equal to the force acting on the boundary, is

$$\iint_S \mathbf{V}(\rho \mathbf{V} \bullet \mathbf{n})\mathbf{d}s = -\iint_S \mathbf{pnd}s \tag{3.65}$$

The direction of the integrations , is indicated by the arrows in Fig 3.22.

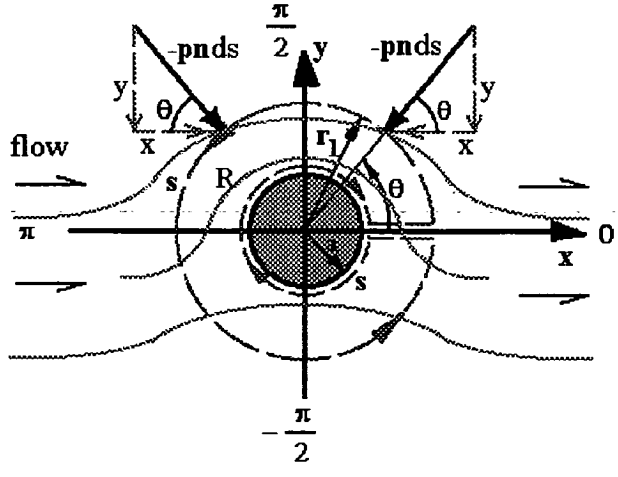

Fig 3.23 Control surface in the flow about a circular cylinder

It keeps the region R always to the left of the path (r_1 goes counterclockwisely and **a** moves clockwisely). When the width of the cut approaches zero, the two integrals along that part of the path vanish, and taking into account that at the streamline $r = a$, $\mathbf{v} \bullet \mathbf{n} = u_r = 0$, equation (3.65) may be expressed:

$$\int_0^{2\pi} \mathbf{v}\rho u_r r_1 d\theta = -\mathbf{F}_e - \int_0^{2\pi} p\mathbf{n} r_1 d\theta \tag{3.66}$$

where $-\mathbf{F}_e = -\int_0^{2\pi} p\mathbf{n} a d\theta = -\mathbf{i}F_x - \mathbf{j}F_y$ is the force exerted on the fluid per unit length of the inner cylinder. Considering any segment of width dy parallel to the x axis, it is clear from Fig3.22 that since the streamline configuration and therefore the pressures acting on the boundaries are symmetrical about the y- axis, $\mathbf{F}_x$ must vanish. Thus the x component of the momentum of an element of fluid entering the contour from the left must equal that when it leaves to the right, and the force acting on the inner cylinder becomes:

$$\mathbf{F}_e = \mathbf{j}F_y = \mathbf{j}\left(\underbrace{-2\int_{-\pi/2}^{\pi/2} r_1 p \sin\theta d\theta}_{(I)} - \underbrace{\int_0^{2\pi} \rho r_1 u_r v d\theta}_{(II)} \right) \tag{3.67}$$

where v is the y component of the velocity.

Substituting Bernoulli's equation $p = p_o - \frac{1}{2}\rho V^2$ into (3.67), the first pressure integral splits into (I) becomes two parts. Since the flow is irrotational, p_o is constant and the term $\int_{-\pi/2}^{\pi/2} p_o r_1 \sin\theta d\theta$ vanishes. Thus

$$(\mathbf{I}) = \rho r_1 \int_{-\pi/2}^{\pi/2} V^2 \sin\theta d\theta \tag{3.68}$$

V can be found from (3.61) which may be rewritten as :

$$\Psi = U_\infty r \sin\theta (1 - \frac{a^2}{r^2}) - K \ln \frac{r}{a} \tag{3.69}$$

Substituing $y = r\sin\theta$ and K=Γ/2π into (3.69),

$$\Psi = U_\infty y(1-\frac{a^2}{r^2}) + \frac{\Gamma}{2\pi}\ln(\frac{r}{a}) \tag{3.70}$$

$$u_r = \frac{1}{r}\frac{\partial\Psi}{\partial\theta} = \frac{1}{r}U_\infty r\cos\theta(1-\frac{a^2}{r^2}) = U_\infty(1-\frac{a^2}{r^2}) \tag{3.71}$$

$$u_\theta = -\frac{\partial\Psi}{\partial r} = -U_\infty\sin\theta(1+\frac{a^2}{r^2}) - \frac{\Gamma}{2\pi r} \tag{3.72}$$

$$V^2 = u_r^2 + u_\theta^2$$

Since $\int_{-\pi/2}^{\pi/2}\cos^2\theta\sin\theta d\theta = \int_{-\pi/2}^{\pi/2}\sin^3\theta d\theta = \int_{-\pi/2}^{\pi/2}\sin\theta d\theta = 0$

equation (3.68) can be written

$$(\mathbf{I}) = \rho r_1\int_{-\pi/2}^{\pi/2}\frac{U_\infty\Gamma}{\pi r_1}(1+\frac{a^2}{r_1^2})\sin^2\theta d\theta = \frac{1}{2}\rho U_\infty\Gamma(1+\frac{a^2}{r_1^2}) \tag{3.73}$$

If $r_1 = a$, this calculation gives the force components simply by an integration of the pressure force over the body surface. That is, since $u_r = 0$ *at* $r_1 = a$, the term (II) in equation (3.67) vanishes, and the force components are

$$F_x = 0 \qquad F_y = \rho U_\infty\Gamma \tag{3.74}$$

At r = r_1 $$F_y = \frac{1}{2}\rho U_\infty\Gamma(1+\frac{a^2}{r_1^2}) + \frac{1}{2}\rho U_\infty\Gamma(1-\frac{a^2}{r_1^2}) \tag{3.75}$$

or $$F_x = 0 \qquad F_y = \rho U_\infty\Gamma$$

In vector notation, $\mathbf{F}=\rho\mathbf{U}_\infty\times\Gamma$

where Γ is the circulation vector; its direction is determined by the right-hand-screw rule. The force acts normal to Γ and $\mathbf{U}_\infty$.

There are many possible discussions about zero drag , but one point in particular needs to be mentioned, a low-viscosity fluid giving a drag force quite different from that predicted by inviscid theory. As $\nu \to 0$, the mainstream flow speed would decrease very substantially along the boundary at the rear of the cylinder, and there would therefore be a strong adverse pressure gradient.

3.6.3 Force Coefficients

If F is the component in an arbitrarily chosen direction of the force on the obstacle due to the system of stresses over its surface and S is some representative area associated with the obstacle, then the non-dimensional quantity $F/(\frac{1}{2}\rho U^2 S)$ is called a force coefficient. It can depend only on a non-dimensional combination of U, S, ρ, and ν, and must therefore be a function of Reynolds number only. In the case of flow past an infinte cylinder, per unit length of the cylinder, the force coefficients are defined by :

In-line force coefficient : $$C_I = \frac{F_{in}}{\frac{1}{2}\rho U^2 d} = \frac{F_I}{\rho U^2 a} \qquad (3.76)$$

Lift force coefficient : $$C_L = \frac{F_L}{\frac{1}{2}\rho U^2 d} = \frac{F_L}{\rho U^2 a} \qquad (3.77)$$

where d is the diameter of the cylinder and a is radius of the cylinder. Both coefficients are still function of Re only. Using non-dimensional quantities, a force coefficient will have the same value whatever units are employed for measurement.

3.6.4 Calculation of Forces and Coefficients

The viscous flow of an incompressible fluid, with constant kinematic viscosity ν and density ρ, past a circular cylinder is governed by the Navier-Stokes and continuity equations. In non-dimensional form, these may be written :

$$\frac{\partial \mathbf{u}}{\partial t} = -\frac{1}{\rho}\nabla P - (\mathbf{u} \bullet \nabla)\mathbf{u} + \nu \nabla^2 \mathbf{u} \tag{3.78}$$

$$\nabla \bullet \mathbf{u} = 0 \tag{3.79}$$

The dependent variables are the velocity **u** and pressure P.

The velocity **u** and its time derivative ($\partial \mathbf{u} / \partial t$) are equal to zero along the surface of the cylinder so equation (3.78) therefore simplifies to

$$\frac{1}{\rho}\nabla P = \nu \nabla^2 \mathbf{u} = \nu \, [\nabla(\nabla \bullet \mathbf{u}) - \nabla \times \nabla \times \mathbf{u}] \tag{3.80}$$

Substituting (3.79) and $\omega = \nabla \times \mathbf{u}$ into (3.80), using polar coordinates (r, θ), gives :

$$\frac{1}{\rho}\frac{\partial P}{\partial \theta} = -\nu \frac{\partial \omega}{\partial r} \tag{3.81}$$

The right-hand side of (3.81) represents the flux of circulation per unit length across the cylinder surface ($\Gamma = \int \vec{\omega} \, ds$). The surface of the cylinder is divided into N small elements of arclength Δθ (Δθ=2π/N), the flux of circulation at a point on the cylinder surface situated within the ith surface element (aΔθ) will be $(1/a\Delta\theta)\partial(\Delta\Gamma_i)/\partial t$ [19]. Here a is the cylinder radius. The surface element can be seen in Fig.3.24.

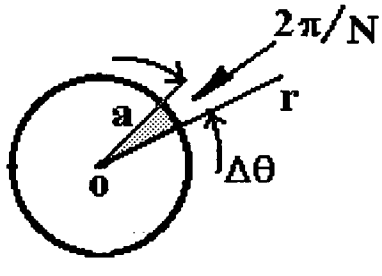

Fig 3.24 A surface element

Thus $\partial(\Delta\Gamma_i)/\partial t$ approximates the rate at which circulation crosses the surface element :

$$\frac{\partial}{\partial t}(\Delta\Gamma_i) = -\nu a \Delta\theta \frac{\partial \omega}{\partial r}\Big|_{\theta = i\Delta\theta} \tag{3.82}$$

for the transport of momentum, integrating the tangential component of (3.81) along the ith surface element on the surface gives :

$$\Delta p_i = -\nu \rho a \Delta\theta \frac{\partial \omega}{\partial r}\Big|_{\theta = i\Delta\theta} \tag{3.83}$$

where Δp_i is the pressure change along the element. From (3.82) and (3.83) , this is given by:

$$\Delta p_i = \rho \frac{\partial}{\partial t}(\Delta \Gamma_i) \qquad (3.84)$$

Then giving a definition of $\delta \Gamma_i$, letting it represent the circulation carried by vortices crossing the ith surface element in a time increment Δt, we have

$$\delta \Gamma_i = \frac{\partial}{\partial t}(\Delta \Gamma_i)\Delta t \qquad (3.85)$$

The pressure p_i at θ = i Δθ , relative to a reference pressure p_o at θ = 0, is given by

$$p_i = p_o + \frac{\rho}{\Delta t}\sum_{j=1}^{i} \delta \Gamma_j \qquad (3.86)$$

Since the surface pressure can contain no discontinuities, $p_N = p_o$ and $\sum_{j=1}^{N} \delta \Gamma_j = 0$.

Thus the sum of the circulation is carried by vortices crossing the cylinder surface, and the net circulation remains zero. It satisfies Kelvin's Theorem $\frac{D\Gamma}{Dt} = 0$ [20]. Flow which is initially irrotational cannot generate circulation. Furthermore, if viscosity is only significant in a finite region, the circulation at infinity is constant. For a two dimensional cylinder, its bound circulation must be equal in magnitude but opposite in sign to all the shed circulation in the wake.

From equations (3.82) and (3.83) the change in pressure around the cylinder and the circulation are dependent solely upon the normal gradient of vorticity at the surface ($\partial \omega / \partial r$) which is calculated in the following manner. The vortices are sorted into 'boxes' as in Fig.3.25. These boxes are defined by the segments in the s direction and by a distance σ in the normal direction where σ is the standard deviation of the random walk for the Reynolds number concerned. Using the relationship between circulation and vorticity (3.82), the total circulation in the boxes given by (3.47) and (3.52) is divided by the area to give the vorticity at the centre of each box, ω_1 and ω_2. The gradient of the vorticity at the surface is thus estimated as $(\omega_2 - \omega_1)/\sigma$.

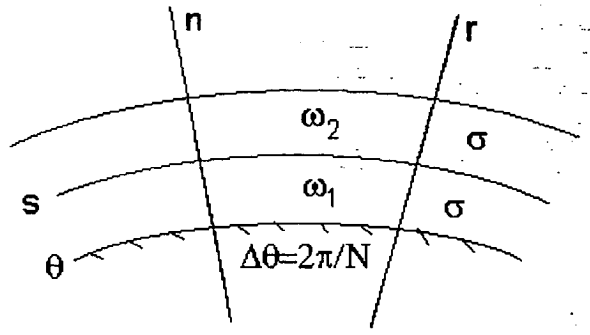

Fig3.25 Scheme used for calculating the surface vorticity gradient

The pressure distribution around the surface of the cylinder is obtained by a summation of the perssure increments given by (3.83). When integration around the surface has been completed the pressure does not, in ingeneral , return to its original value. This is inevitable since the pressure contains a random component, but it may also be due to the imperfect resolution of the flow. These factors cannot be separated, so the errors must be compensated for in some way. By averaging over several time steps, the errors can be close to zero in the computation. This is the long-term mean of the closing errors [5]. We now summarize the force calculation process.

(a) The relevant formulae are:

$$P_i = P_o + \frac{\rho}{\Delta t}\sum_{j=1}^{i}\delta\Gamma_i \qquad \text{from (3.86)}$$

$$= P_o + \frac{\rho}{\Delta t}\sum_{j=1}^{i}\frac{\partial}{\partial t}(\Delta\Gamma_i)\Delta t \qquad \text{from (3.85)}$$

$$= P_o + \frac{\rho}{\Delta t}\sum_{j=1}^{i}(-\nu a\Delta\theta\frac{\partial\omega}{\partial r}\Big|_{\theta=i\Delta\theta})\Delta t \qquad \text{from (3.82)}$$

$$= P_o + \nu\rho\Delta t\sum_{j=1}^{i}\frac{\partial\omega}{\partial r}\frac{a\Delta\theta}{\Delta t}$$

where ρ is water density and is equal to $1\text{x}10^3\ \ kg/m^3$ at room teperature; ν is kinematic viscosity and is equal to $1\text{x}10^6\ m^2/s$; Δt is the time step. So for any time step, the pressure at an element will be simply :

$$P_i = P_o + \sum_{j=1}^{i} \frac{\Delta\omega}{\Delta r} \frac{a\Delta\theta}{\Delta t} \tag{3.87}$$

(b) The computational algorithm is:

1) obtain ω_1 by (3.51) and ω_2 by weight interpolation of Ψ on the intermediate mesh
2) correct the values of $\frac{\partial\omega}{\partial r}$ by the long-term mean of the closing errors
3) correct the values of $\frac{\partial\omega}{\partial r}$ by introducing the influence of old vortex strength and maintaining the correct flux of circulation.
4) calculate $\sum_{j=1}^{i} \frac{\partial\omega}{\partial r} \frac{a\Delta\theta}{\Delta t}$, in order to get the P_i which includes the component P_o
5) substract P_o from P_i . P_o is the pressure at the initial front stagnation point.

The in-line and lift coefficients , corresponding to the force components directed respectively along $\theta = \pi$ and $\theta = \frac{1}{2}\pi$, can be calculated by integrating of the pressure distribution.

$$C_I = \frac{\Delta\theta}{\Delta t} \sum_{j=0}^{128} \left[\cos(j\Delta\theta) \sum_{i=1}^{j} \Gamma(i,0) \right] \tag{3.88}$$

$$C_I = -\frac{\Delta\theta}{\Delta t} \sum_{j=0}^{128} \left[\sin(j\Delta\theta) \sum_{i}^{j} \Gamma(i,0) \right] \tag{3.89}$$

where value of 128 refers to the number of segments on the cylinder surface. P.K.Stansby etc.[11][21] performed some comparisons between the different calculations of force coefficient and an expression for the force coefficients given by Quartepelle & Napolitano :

$$C_I = \sum_{i=1}^{L} \Gamma_i \left[\frac{u_i \sin(2\theta_i) - v_i \cos(2\theta_i)}{r_i^2} \right] \tag{3.90}$$

$$C_L = \sum_{i=1}^{L} \Gamma_i \left[\frac{v_i \sin(2\theta_i) + u_i \cos(2\theta_i)}{r_i^2} \right] \tag{3.91}$$

where the ith vortex is at position $\mathbf{r}_i = (r_i, \theta_i)$ and has velocity components u_i *and* v_i parallel to C_I *and* C_L respectively.

The results showed that there was good agreement between the time histories of inline force coefficients calculated by the two methods although the coefficients from the vortex method (3.88) contain a random component which is absent in the coefficient from (3.90).

3.7 Running Procedure of The Model

The sequence of steps involved in a vortex method simulation is as follows :

1). The body surface is replaced by a polygon of line segments and the influence matrix **K** is calculated. The matrix ***K*** is dependent only on the geometry of the body surface.

2) The inverse matrix $\mathbf{K}^{-1}$ is found and stored.

3) The stream function is set up on each cylinder surface, and the surface tangential velocities are computed in preparation for the boundary-integral calculation. The stream function is obtained by solving the Poisson's equation on the three over-lapping meshes. The surface tangential velocities are calculated from the stream function using equation (3.11) and then the constant vector term **b** in the the boundary-integral calculation is obtained, see equation (3.46).

4) The vortex-sheet strength distribution γ around each cylinder surface is obtained and converted into point vortices.

5) The overlapping mesh system is solved again, this time, including the new surface vorticity γ . Vortices move by first order time step by equation (3.19).

6) The new vortex sheet strength is computing using the zero-slip condition and equation (3.51).

7) The circulation on the cylinder surface is corrected. The influence of old vortices are included by the way of equation (3.52).

8) vortices are absorbed and diffused. Those that cross inside cylinders are absorbed (deleted) and their strength is used to correct the strengths of new vortices. The segments are replaced by one or more point vortices, according to the equation (3.32). Diffusion is simulated by equation (3.23).

9) Vortices convect according to a second order accurate scheme given by equation (3.24).

10) The forces are calculated. This is carried out according to the process described in (b) of section 3.6.4.

11) Combine downstream vortices.

12) The velocities can now be calculated through the overlapping mesh system.

The sequence is the repeated from stage 5. When the integral time step reaches a given termination time, the process ends, and the results of the simulation can be output.
The stream function calculation is the most time consuming part of the computation and this has to be carried out for the three meshes twice per time step for the second order as well as the first-order convection scheme.

3.8 The Modelling Results

Some example of simulation output are given below.

1) Stream Function Field

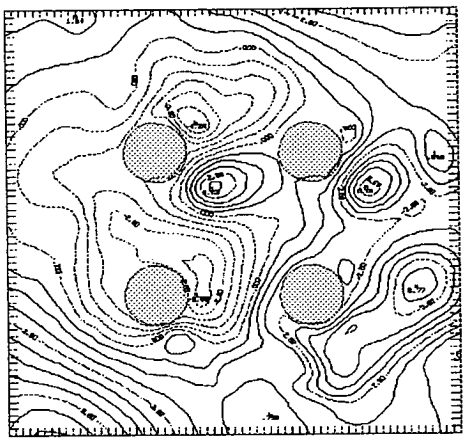

Fig 3.26 A Stream function field (Re=5000, Kc=10)

Fig 3.26 shows a 2-D stream function field . Here the solid lines represent positive values of the stream function. The closed solid line areas are positive vorticity areas. The dashed lines represent negative values of the stream function. The closed dashed line areas are negative vorticity areas.

Fig 3.27 is a three dimensional picture of the stream function. The data is the same as used in Fig 3.26.

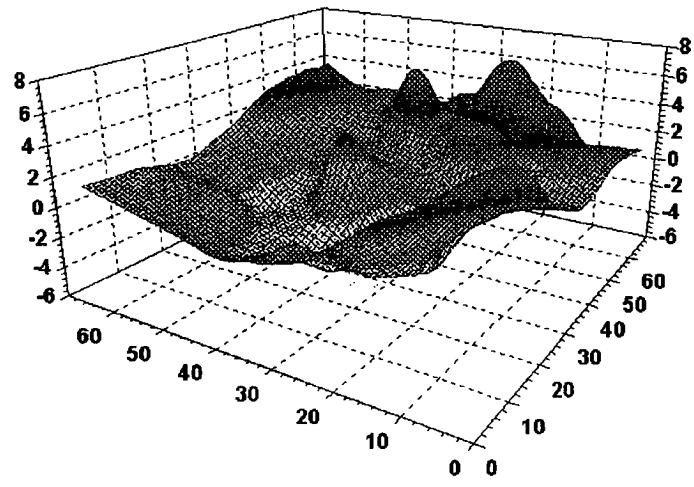

Fig. 3.27 A 3-D Stream function field (Re=5000, Kc=10)

It seems that the 2-D picture is much clearer than 3-D stream function picture.

2) Vector Field

This is a picture at phase π of oscillatory flow. The onset flow is from left to right. The main vortices are downstream of the cylinders and almost every cylinder has two opposite sign vortices behind it. The directions of flow rotation in the vortices are in good agrement with both experiment and theory. It can be found from Fig 3.28 that vortex shedding in the wake of the four cylinder structure (the right side) is one after another . The small one is shed after the big one , it is a basic phenomenon at KC=10. If KC number is smaller , for example it's 5, the vortex shedding will be two small vortices shedding at the same time.

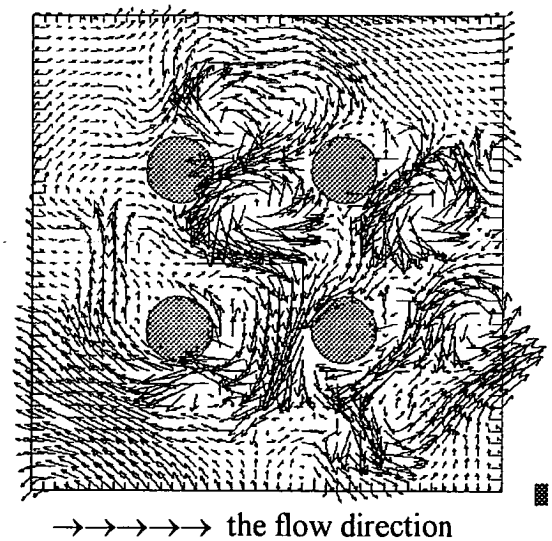

→→→→→ the flow direction

Fig 3.28 A vector field (Re=5000, Kc=10)

3. Stream Line Field

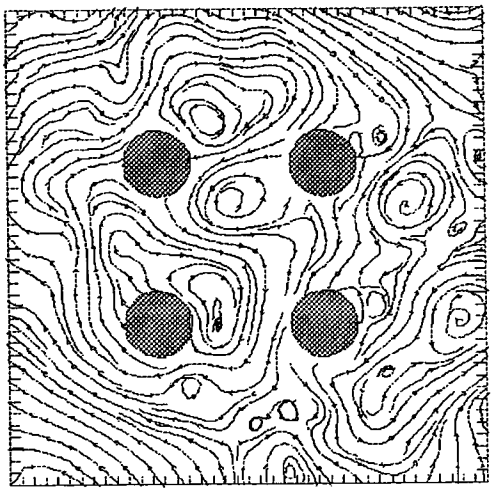

$\rightarrow\rightarrow\rightarrow\rightarrow\rightarrow$ the flow direction

Fig 3.29 A Stream line field (Re=5000, Kc=10)

The stream line field can show us the flow direction in the vortices, but cannot tell us the strength of velocity and vortices. For this information, an additional vorticity calculation has been carried out.

4) Vorticity Field

The solid lines in Fig 3.30 represent the positive vorticity areas. The dashed lines represent the negative vorticity areas. The strengths at the centres are indicated with + and – meaning positive and negative .

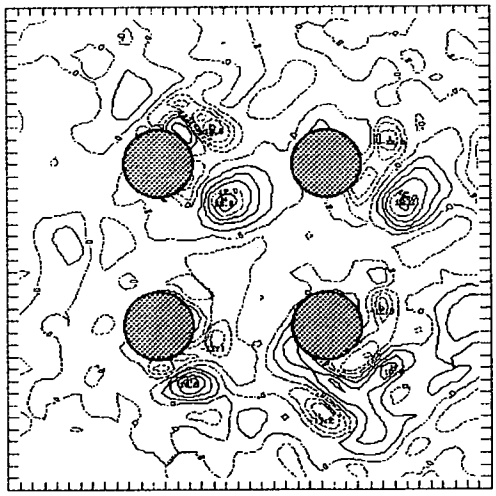

Fig 3.30 A vorticity field (Re=5000, Kc=10)

5) Time History of the Force Coefficients

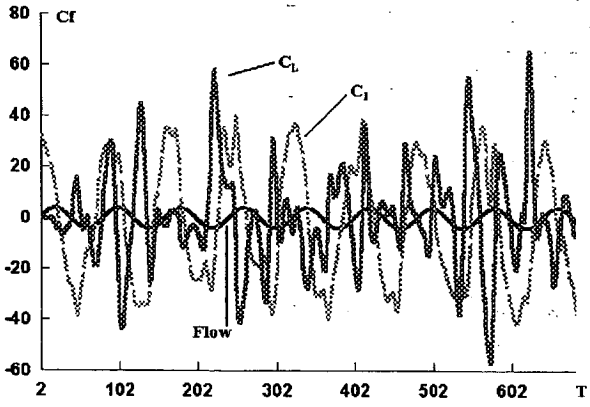

Fig 3.31 Time history of the force coefficients of one cylinder of a four cylinder array (Re=5000, Kc=10)

Here the evolution of the in-line force coefficient is similar to that of the oscillatory flow, and there is an initial phase difference between them. The evolution of the lift force coefficient in strength and frequency exhibits more random changes so further analysis of the force coefficients is required. In particular strength analysis and power spectrum analysis have been performed in order to compare with laboratory experimental results. (They are shown in following chapters)

6) Pressure Distribution Around The Cylinders

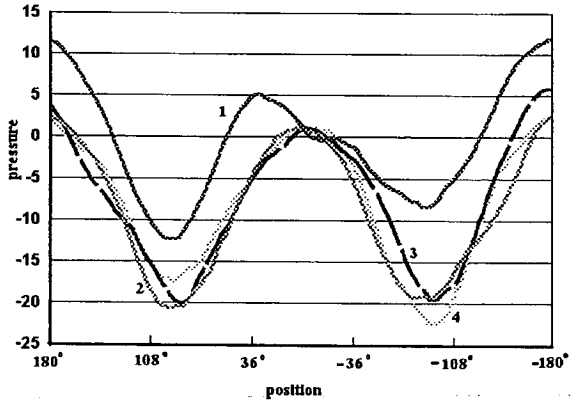

Fig 3.32 Surface pressure distribution about four cylinders Phase=π, Re=5000, Kc=10 , cyliners :1,2,3,4

Here the numbers 1, 2, 3, 4, pointed the pressure distribution lines of the four cylinders.

A 2-D plane plot gives another impression of pressure distribution, see Fig 3.31.

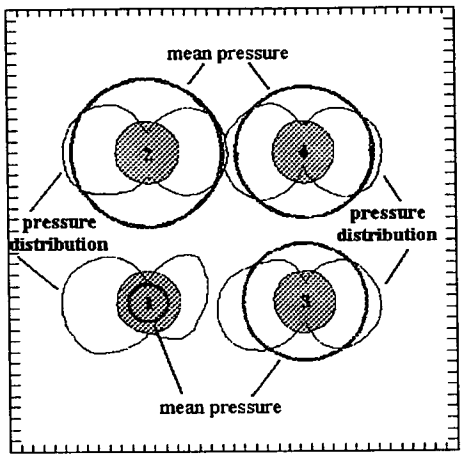

Fig 3.33 The pressure distribution around cylinders
Phase=π, Re=5000, Kc=10 , cyliners :1,2,3,4

All of the mean pressures are negative. In the direction of the in-line force, pressure is bigger than in the direction of the lift force .

3.9 Some problems

The numerical simulation can output many good simulational vector fields spectially at the phases π and 2π which are at minimum velocities phases. But at some other phases the numerical simulation can only give no vortex, which are different from the results of the lab PIV experiments. These usually happen at the phases which the oscillatory flow has maximum velocities or has changed their direction and increased their velocities from minimum values (See Fig 3.34 (a) with vortices and (b) without vortex).

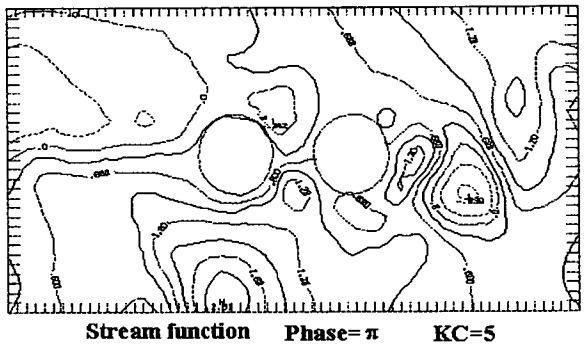

Fig 3.34 (a) Vortices in stream function field

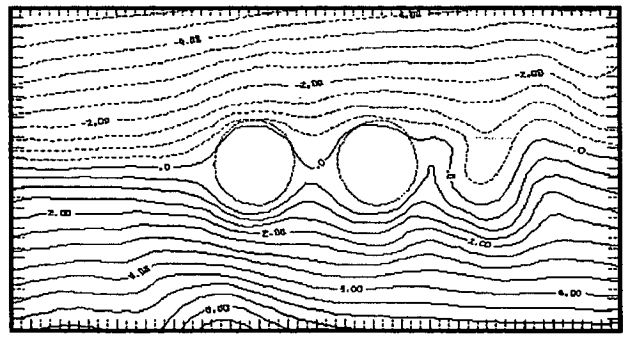

Fig 3.34 (b) Oscillatory flow in stream function field

This may be caused by the relative velocity. The strengths of velocities of the vortices are much smaller than maximum velocities of the oscillatory flow. They are some small disturbance in the oscillatory flow . When the oscillatory flow reaches its minimum velocity, the vortices can appear and be quite clear such as in Fig 3.34 (a). The strengths of the stream function of the vortices are respectively -0.24, 1.20, 2.31, 1.20, 0.6, -0.83 and 1.50 from left to right. In the some phases the main oscillatory flow could hide the vortices when the oscillatory flow increased its velocities, such as in the Fig 3.34 (b). The values of the stream function can be large up to 6.3 (on the bottom) and -5.1 (on the top), the gradient of stream function is also large. It will make big velocity, so the main big velocities will cover the small vortices and show only the feature of the main flow. This deviation from the experimental results should be improved.

3.10 References

[1] Karl E. Gustafson, James A. Sethian (Editors) , Vortex Methods and Vortex Motion, 1991, Society for Industrial and Applied Mathematics, U.S.A

[2] R.I.Lewis, Vortex element methods for fluid dynamic analysis of engineering systems, Cambridge University Press, 1991

[3]P.G.Saffman, Vortex Dynamics, 1992, Cambrige University Press

[4] A.Slaouti and P.K.Stansby, Flow around two circular cylinders by the random-vortex method , Journal of fluids and structures 1992 , vol 6, pp641-670

[5] P.K.Stansby and A.G.Dixon, Simulation of flows around cylinders by a Lagrangian vortex scheme, Applied Ocean Research, 1983, vol.5, No. 3, pp167-178

[6] L.M.Miline-Thomson, Theoretical Hydrodynamics, 1968, Magmillan & Co Ltd,

London

[7] D.J.Acheson, Elementary Fluid Dynamics, 1990, Clarendon Press, Oxford, U.S.A

[8] P.K.Stansby , Vortex Method Model Code, 1986, The University of Manchester, U.K.

[9] Charles Hirsch, Numerical Computation of Internal and External Flows Volume 2: Computational Methods for Inviscid and Viscous Flows, Charpter 15, 1991, John Wiley &Sons, Inc. New York, U.S.A

[10] P.R.Voke, Multiple mesh Simulation of Turbulence, Numerical Methods For Fluid Dynamics III, Edited by K.W.Morton and M.J.Baines, 1988, Clarendon Press, Oxford, U.S.A

[11] P.A.Smith and P.K.Stansby , Impulsively Started Flow Around A Circular Cylinder By The Vortex Method, Journal of Fluid Mech. 1988

[12] Frank M.White, Fluid Mechanics, 1979, McGraw-Hill Inc.

[13] Sarpkaya & Isaacson, Mechanics Of Wave Forces On Offshore Structures, 1981, Van nostrand Reinhold Company Inc. New York

[14] M.M.Zdravkovich , Flow Around Circular Cylinders :Vol 1 : Fundamentals (1997) Oxford University Press Inc. , New York

[15] Ranald V. Giles, Theory And Problems Of Fluid Mechanics And Hydraulics, (1962), McGraw-hill Book Company, U.S.A.

[16] S.Goldstein (Editor) , Modern Developments In Fluid Dynamics, Volume II, (1965), Dover Publications, Inc. U.S.A

[17] A.M.Kuethe and C.Chow, Foundations of Aerodynamics, Fourth Edition (1986) John Wiley and sons, Inc. Singapore

[18] S.Goldstein (Editor) , Modern Developments In Fluid Dynamics, Volume I, (1965), Dover Publications, Inc. U.S.A

[19] P.K.Stansby and P.A.Smith , Viscous forces on a circular cylinder in orbital flow at low Keulegan-Carpenter numbers, Journal of Fluid Mech. 1991,vol 229 pp. 159-171

[20] Edited by Sheldon I. Green Fluid Vortices 1995 Published by Kluwer Academic Publishers Printed in the Netherlands Charpter I , Charpter V

[21] P.K.Stansby and A.Slaouti , Simulation Of Vortex Shedding Including Blockage By The Random-Vortex And Other Methods, 1993, J. for numerical methods in fluids, vol. 17 pp1003-1013

Chapter 4

Oscillatory Flow Round Single Cylinder

4.1 Single cylinder in oscillatory flow

The subject of the oscillatory flow past the single circular cylinder has been studied for a long time. One of the main reasons is the direct engineering significance. The alternate shedding of vortices from the surface of the cylinder leads to large fluctuating pressure forces in a direction transverse to the flow (lift force), and may cause structural vibrations, acoustic noise, or resonance, which in some cases can trigger failure.

Because the action of the lift force is caused by vortex shedding , the research is usually carried out in two areas : the evolution of the force and the behaviour of the vortex. In the discussion of force evolution ,Sarpkaya[1] and Bearman[2] have provided much insight into the relationship between the force coefficient and the KC numbers, Reynolds numbers and β parameter. Sarpkaya's experiments were carried out with high β values(where β = Re/KC), ranging from 1000 to 15,000. In Bearman's experiments, β ranged from 200 – 2000. Neither Sarpkaya nor Bearman tested the case where β=500, a case which has been tested in this thesis. Their common conclusions were that for the inertia coefficient C_m versus KC number , the fit line of data had an opposite curvature to that of the drag coefficient C_D versus KC number . The peaks of the fit curves of the drag coefficient were at about KC =2 and between KC = 10 and KC = 15 ; the peak of the fit curves of inertia coefficient was between KC = 10 and KC = 15 , see Fig 4.1 (c) (d). The In-line force coefficient does not have this feature and decreases with KC number, see Fig 4.1 (a) (b).

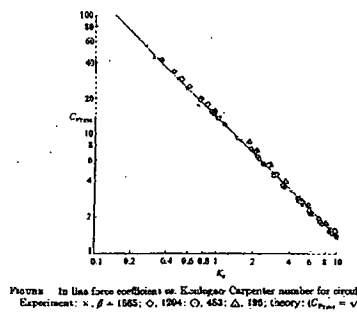

Fig 4.1 (a) In-line coefficient (Bearman)

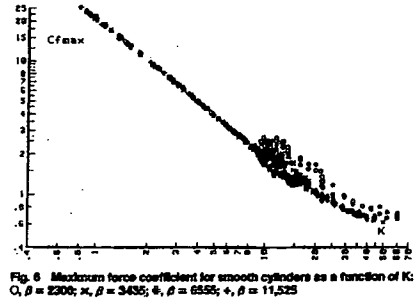

Fig 4.1 (b) Inline coefficient (Sarpkaya)

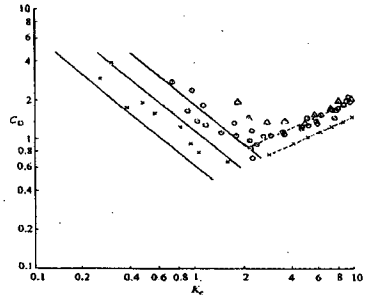

FIGURE 2. Drag coefficient vs. Keulegan–Carpenter number for circular cylinder. Experiment: ×, $\beta = 1665$; ○, 483; △, 196.

Fig 4.1 (c) Drag coefficient (Bearman)

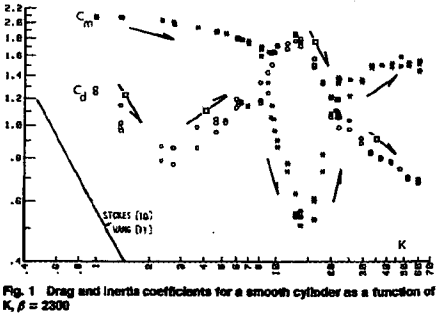

Fig. 1 Drag and inertia coefficients for a smooth cylinder as a function of K, $\beta = 2300$

Fig 4.1 (d)Drag (O) and inertia(*)coefficients (Sarpkaya)

Fig 4.1 Force coefficients vs KC number

The above experimental results were all measured using a U-tube. The U-tube gives a measure of the total force suffered by cylinder. The inertia and drag coefficients are then obtained using Morison's Equation[1] [2].

When an isolated cylinder is subjected to relative oscillatory flow , repeatable vortex-shedding patterns are found to occur with particular ranges of flow amplitude. Each of these patterns reflects the shedding of a particular number of vortices per half cycle.Williamson [3][4] and Bearman[5] have undertaken research to look at the vortex wake behind a bluff body . They divided the flow patterns according to the different KC number regimes and named them. Williamson's vortex flow regimes of a single cylinder is as Fig 4.2

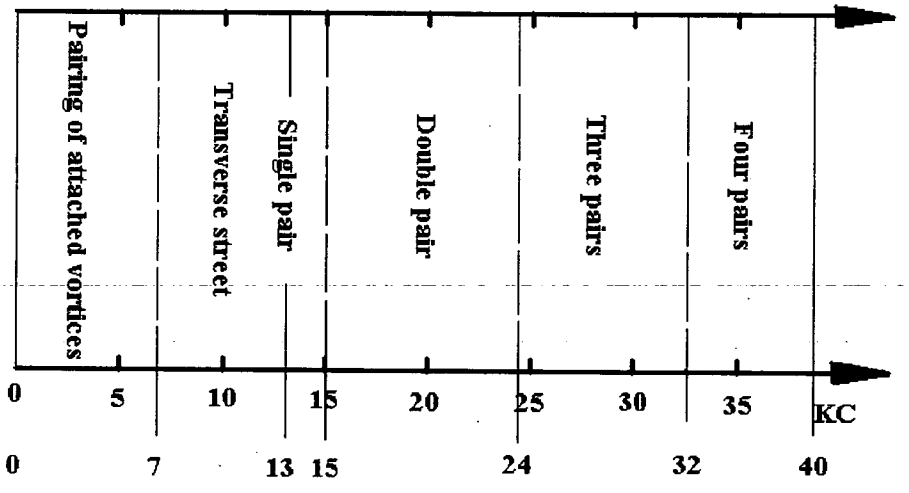

Fig 4.2 The ranges of KC number corresponding with each flow pattern

Each wake pattern may continue for a large number of cycles, but can intermittently

change from one mode to another. Williamson found that below KC=7 there are no major vortices shed during a half cycle although pairs of small vortices are formed each time the flow reverses. In the regime of KC from 7 to 15, there are the pairing of 'shed' vortices. The vortices move away from the local-flow region of the cylinder, roughly perpendicular to the oscillation direction. At the upper end of this range of amplitudes (between $13 < KC < 15$) the main vortex pattern comprises a series of pairs convecting away from the cylinder at roughly 45^0 to the cylinder-oscillation direction. In the double pair regime ($15 < KC < 24$) , as the flow amplitudes increase, so the single-pair pattern merges into a 'double-pair' wake. The latter wake comprises the shedding of two large vortices in each half cycle. And the formation of two pairs in each cycle. For KC in the three pair regime ($24 < KC < 32$) and the four pair regime ($32 < KC < 40$), the oscillation amplitudes are increased further , so the number of shed vortices in a half cycle increases too and, in the range $24 < KC < 32$, there are predominantly three vortices shed in each half cycle. In the range $32< KC < 40$, a further system of pairings occurs, in this case forming 4 pairs of vortices in a full cycle. Williamson has done flow pattern visualization with simultaneous force measurement, but it only is for β=255. (our experiments are for $\beta = 500$)

The divisions of flow pattern given by Bearman is as follows:
The range of KC from about 3 to 55, can be divided into the regimes 1) $KC \leq 4$, the symmetric regime, 2) $4 \leq KC \leq 8$, the asymmetric regime, 3) $8 \leq KC \leq 15$, the transverse regime, 4) $15 \leq KC \leq 22$, the diagonal regime, 5) $22 \leq KC \leq 30$, the third vortex regime , 6) $KC \geq 30$, the quasi-steady regime.

Bearman's visualization was performed in the U-tube at $\beta = 416$. The flow was visualized by using small polystyrene particles illuminated by narrow slits of light. Bearman observed that in the symmetric regime, there are two vortices having the same size and opposite signs formed in each half cycle. In the range $4< KC < 8$, the size of the two vortices change into one bigger and the other smaller, and when they go backwards with flow reversal, one increases its size and remains in next half cycle and the other dissipated. In the third regime, vortex activity is one-sided and two vortices with opposite signs are again shed in one complete cycle. The shed vortices

now form a pair and are able to convect to large distances from the model. In the diagonal regime a pair of vortices is shed in each half- cycle and the vortex pair in the one half-cycle is shed diametrically opposite to the pair in the previous half-cycle. In both the transverse and the diagonal regimes, vortex pairs convect at about 45° to the main flow, when view with the cylinder is fixed. The last two regimes are similar to Williamson's. Bearman found it was normal that there were several primary modes of flow pattern in one regime. It was observed that a vortex pattern can be stable over a large number of cycles and then change from one mode to another. Measurements have revealed that the change does not occur abruptly and that as a consequence, a large variety of secondary modes can be generated.

4.2 The parameters in the research here

4.2.1 Keulegan-Carpenter Number :

There are strong similarities between the wave flow past a section of a pile and a two dimensional sinusoidal flow past a circular section. The latter reference flow is conveniently obtained under laboratory conditions and may be used to generate a variety of pertinent experimental results. Keulegan and Carpenter (1958) investigated this flow and the characteristics of the drag and inertia coefficients corresponding to it. One of the important parameters of the flow is the amplitude of fluid motion relative to cylinder size, which is usually expressed as the Keulegan-Carpenter number. For a oscillating cylinder in still water tank, KC=2πA/D, where A is the amplitude of the cylinder motion and D is the cylinder diameter. For the oscillatory flow case,

$$A = \int_0^{\frac{T}{4}} U_{\max} \sin(\omega t) dt \quad \text{or} \quad A = \int_0^{\frac{\pi}{2}} \frac{U_{\max}}{\omega} \sin(\omega t) d(\omega t) \tag{4.1}$$

where $\omega = \frac{2\pi}{T}$ and T is the period of the cylinder motion.

$$KC = \frac{2\pi}{D} * \frac{T}{2\pi} U_{\max} \left[-\cos(\omega t) \right]_0^{\frac{\pi}{2}} = \frac{U_{\max} T}{D} \left[0 + 1 \right] = \frac{U_{\max} T}{D} \tag{4.2}$$

The magnitude of the KC number indicates the relative importance of the drag force and the inertia forces[6]. As $U_{Max}T$ is proportional to the distance travelled by the wave in one period and D is the cylinder diameter , the KC number can be thought of as a ratio of the sizes of wave and cylinder. If the diameter of cylinder is fixed, a big KC number will imply there is a big wave , a small value of KC number will imply a small wave .

According to Obasaju and Bearman [5] ,the transverse forces can be observed from about $KC \approx 4$. At lower KC numbers the force can be ignored . Recently the low KC numbers ($4 < KC \leq 10$) have received considerable attention because they are near to real ocean oscillatory flow conditions. The research will helpful for predictions of the wave forces on offshore structures.

So in the experiments here, D=50mm, T=5 seconds* are determined first, then

U_{max}=0.05 m/s	KC=5 ;	U_{max}= 0.08 m/s	KC=8 ,
U_{max}=0.1 m/s	KC=10,	U_{max}=0.13 m/s	KC=13,
U_{max}=0.2 m/s	KC=20		

4.2.2 Reynolds Number :

Reynolds number is defined as :

$$R_e = \frac{U_{max} D}{\nu} \qquad (4.3)$$

where D is the cylinder diameter , U_{max} is the maximum velocity of the cylinder and ν is the kinematic viscosity.

---

* The mechanical motion of the trolley in the towing tank requires sufficient time to change its motion direction and velocity periodically .

The Reynolds number gives a ratio of the inertia term and the viscous term in the Navier-Stokes equations and indicates the property of the fluid flow : whether the viscosity is important or not . For water (kinematic viscosity = $10^{-6}\ m^2 s^{-1}$ at room temperature) and a cylinder diameter D=0.05m. We have

$U_{max} = 0.05\, ms^{-1}$ $R_e = 2500$, $U_{max} = 0.08\, ms^{-1}$ $R_e = 4000$,

$U_{max} = 0.10\, ms^{-1}$ $R_e = 5000$, $U_{max} = 0.13\, ms^{-1}$ $R_e = 6500$,

$U_{max} = 0.20\, ms^{-1}$ $R_e = 10000$.

4.2.3 β Value

Following Sarpkaya[6] , β is called the 'frequency parameter' or the viscous-frequency parameter[2], or the viscous parameter [5]. β is the ratio of the Reynolds number to the Keulegan-Carpenter number :

$$\beta = \frac{\mathrm{Re}}{KC} = D^2 / \nu T$$

From the standpoint of dimensional analysis, either the Reynolds number or β could be used as an independent variable.

Sarpkaya[6] has pointed out that from the standpoint of laminar boundary layer theory, β represents the ratio of the rate of diffusion ν/δ^2 through a distance δ (where δ is the boundary layer thickness) to the rate of diffusion through a distance D (i.e., ν/D^2). This ratio is also equal to $(D/\delta)^2$ and, when it is large, gradients of velocity in the direction of flow are small compared with the gradients normal to the boundary, a situation to which the boundary-layer theory is applicable. In the experiments here, D and T are kept constant , so

$$\beta = \frac{(5*10^{-2})^2 m^2}{(10^{-6})(m^2/s)*5s} = 500.$$

β is a convenient parameter for periodic oscillatory flows, since for a given model size and fluid, the β parameter depends only on the flow frequency, whereas the Reynolds number depends on flow frequency and oscillation amplitude. In small-scale laboratory tank test the β parameter typically takes a value in the range 10^2 *to* 10^3.

4.3 The Results of Force Measurement

4.3.1 In-line force strength

The strength of the in-line force increases with KC number . See Fig 4.3. From Morison's equation [7]:

$$F = C_D \frac{1}{2} \rho D u|u| + C_M \frac{\rho \pi D^2}{4} \frac{du}{dt} \qquad (4.4)$$

The force is proportional to velocity u^2 and acceleration $\frac{du}{dt}$. The definition of KC equation (4.2) shows KC $\propto U_{max}$ of oscillatory flow . So a flow with a greater KC number will give a greater inline force on the cylinder. The inline force is mainly composed by three components (See Chapter 3, section 3.6.1.1) : inertia force, pressure drag force and friction drag force. The inertia force is due to the second term in equation (4.4) which is the acceleration or the deceleration of the flow . The pressure drag is caused by the first item in equation (4.4) , and associated with the distribution of the velocity of the flow around the cylinder and is proportional to u^2 . It is largely the difference between the high pressure in the front stagnation region and the low pressure in the rear separated region. The friction drag is the integrated shear stress. A flow with faster velocity will cause a larger acceleration on the front of the cylinder and a higher pressure on the front surface of the cylinder. Thus there will be a greater pressure difference along the flow direction . So the velocity variation dominates the inline force and results in the inline force increases with KC

number.

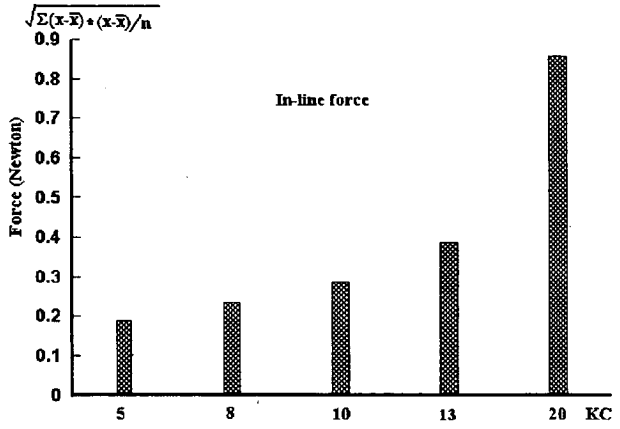

Fig 4.3 (a) In-line force strength of single cylinder

The strength of force is presented by mean root of square amplitude of its data series. The result is a statistical average for different experimental data series at the same KC number.

4.3.2 Lift force strength

When the KC number increases, the amplitude of the time-varying lift force increases too. The average strengths of the lift force for different KC numbers are shown in Fig.4.3(b).

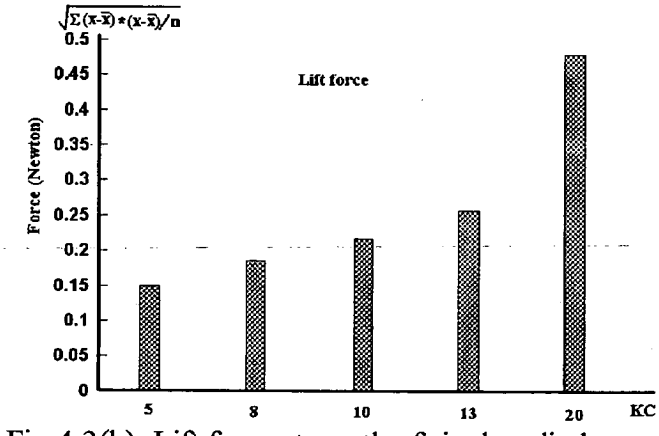

Fig 4.3(b) Lift force strength of single cylinder

The cause of the lift force is the difference in pressure between top and bottom of cylinder. The lift forces increase with KC number, as a result of greater strength vortex

shedding at higher KC values. The shedding occurs alternately from top or bottom in the experimental video recordings, the difference of vortices size at different KC numbers can be seen clearly . This kind of asymmetry vortex shedding is the cause of the random fluctuation of lift force with time. The greater vortex shedding causes the bigger difference of velocity and pressure distributions of the flow at top and bottom of the cylinder which in turn generates larger lift force. Normally the lift force is smaller than that of the in-line force in strength. Williamson [4] pointed out that it is evident that the lift-force amplitude can exceed the in-line force amplitude. In the results of experiments here this phenomenon was found too, although the statistical mean strength of lift forces was smaller. See Fig 4.5

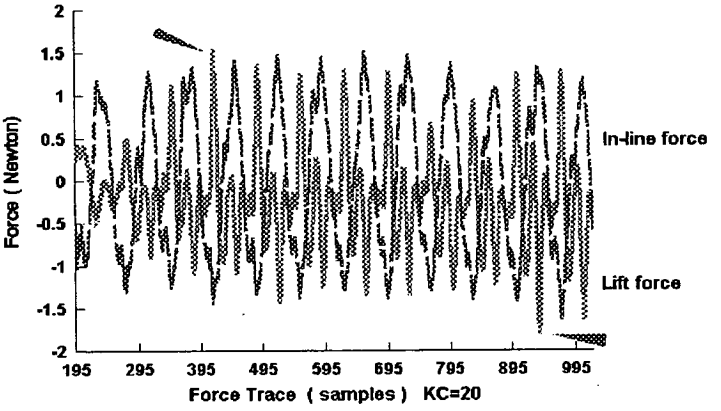

Fig 4.4 In-line force and lift force traces

In Fig 4.4, the two arrows indicate two cases where the lift force amplitude is greater than the inline force.

4.3.3 Force coefficients

The inertia coefficient C_m and the drag coefficient C_D in Morison's equation (4.4) are obtained by multiplying each side of (4.4) by cosωt to each side of (4.4) and integrating over the period of one cycle. This method for obtaining the force coefficient was used originally by Keulegan & Carpenter [8][6]

$$C_D = -\frac{3}{4}\int_0^{2\pi} \frac{F\cos\theta}{\rho D U_M^{\,2}} d\theta \qquad (4.5)$$

$$C_M = \frac{2U_M T}{\pi^3 D}\int_0^{2\pi} \frac{F\sin\theta}{\rho D U_M^2} d\theta \qquad (4.6)$$

So the theory formulae[9][2] are :

Inertia coefficient $C_M = 1 + 4(\pi\beta)^{-\frac{1}{2}} + O(\beta^{-1})$ (4.5)

Drag coefficient $C_D = \frac{3}{2}\pi^3 KC^{-1}(\pi\beta)^{-\frac{1}{2}} + O(\beta^{-1})$ (4.6)

In-line coefficient $C_{Frms} = \sqrt{2}\pi^2 / KC$ (4.7)

The equation (4.5) is for the case of oscillating cylinder in still water. In the case of a fixed circular cylinder in an oscillatory flow , the resulting force coefficients will be :

$$C_M = 2 + 4(\pi\beta)^{-\frac{1}{2}} + O(\beta^{-1}) \qquad (4.8)$$

The difference between (4.5) and (4.8) has been discussed in chapter 2 , section 2.1. The equation of C_D is the same in both cases. Here β is the viscous-frequency parameter which has been mentioned in section 4.2.3 . It can be found experimentally that the higher-order terms $O(\beta^{-1})$ in (4.5), (4.6) and (4.8) are likely to be unimportant but that the $\beta^{-\frac{1}{2}}$ terms can make a significant contribution to the force.

In the experiments here , the β is a constant 500, so C_M is a constant :

$$C_M = 1+4(\pi 500)^{-\frac{1}{2}} = 1.1$$

Bearman used a U-tube, and the cylinder was fixed. So his C_M came from equation (4.8).

C_D and C_{Frms} decrease with increasing KC numbers :

KC = 20	Cd = 0.058	$C_{Frms} = 0.698$
KC = 13	Cd = 0.089	$C_{Frms} = 1.074$
KC = 10	Cd = 0.116	$C_{Frms} = 1.396$
KC = 8	Cd = 0.145	$C_{Frms} = 1.745$
KC = 5	Cd = 0.233	$C_{Frms} = 2.792$

Fig 4.5 ,4.6 and 4.7 shows experimental and theoretical curves of C_{Frms} C_M and C_D versus KC. There β is a constant and equals 500.

These results are in good agreement with those of Sarpkaya and Bearman's . To compare the Fig 4.5 with Fig 4.1(a) and (b), the C_{Frms} decrease with KC number in both Figs. The values of the drag coefficient and inertia coefficient have their peaks at around KC = 10--13, see Fig 4.6 and Fig 4.7. When the KC number is smaller than 10, the inertia coefficent gradually decreases and drag coefficient increases. After 10 or 13, the coefficients display the opposite behaviour. Those are similar to Fig 4.1(c) and (d) which have been obtained by Sarpkaya and Bearman.

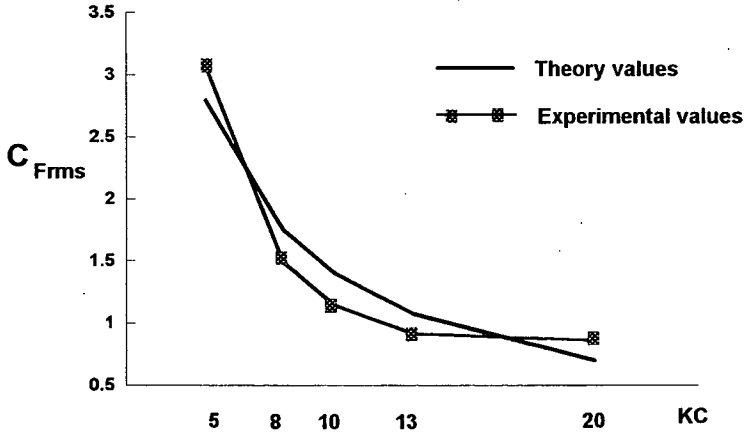

Fig 4.5 In-line force coefficient versus KC number

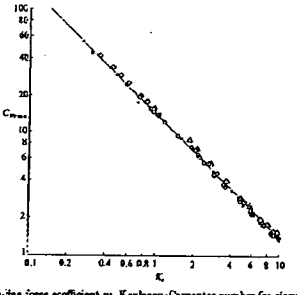

Fig 4.1(a)

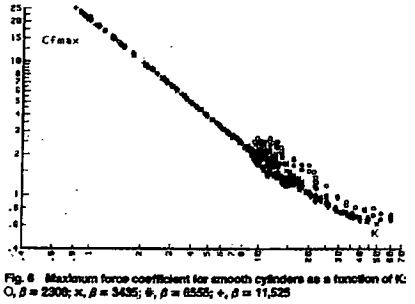

Fig 4.2 (b)

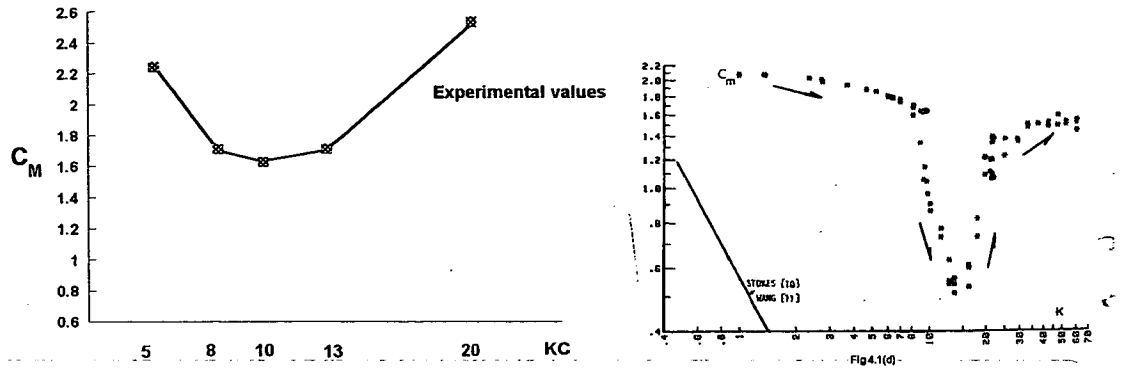

Fig 4.6 Inertia coefficient versus KC number

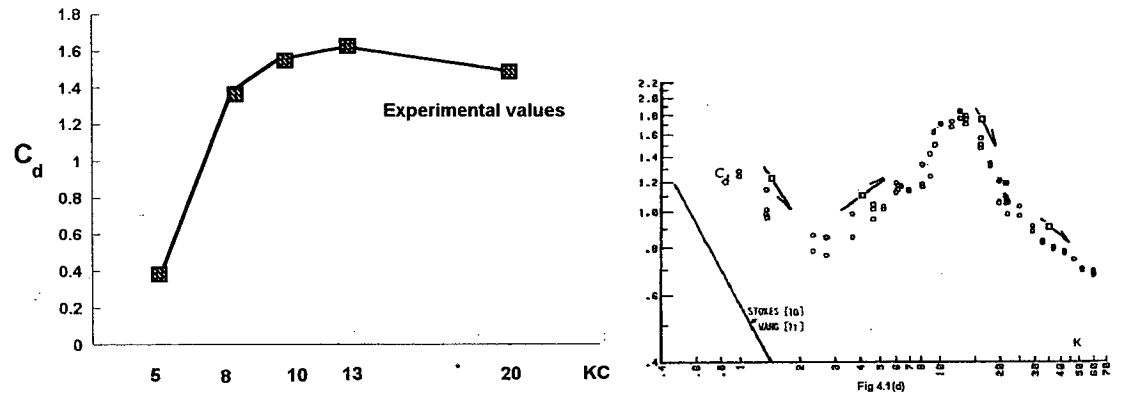

Fig 4.7 Drag coefficient versus KC number.

4.3.4 Frequency of The Force

The main component of the frequency power spectrum has been analysed for in-line force and lift force. The main frequency component of in-line force is normally the same as the frequency of oscillatory flow, see fig 4.8.(a) (b) (c) (d) (e)

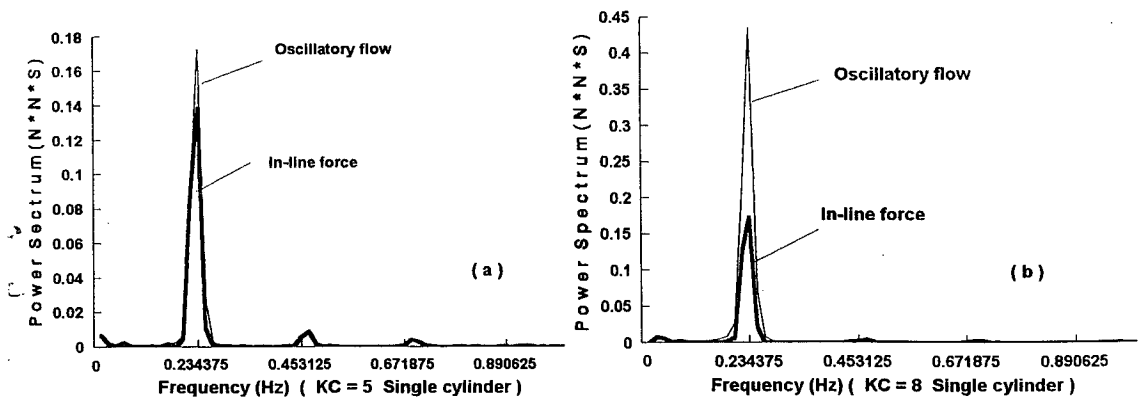

Fig 4.8(a)(b) Frequency of In-line force at different KC numbers

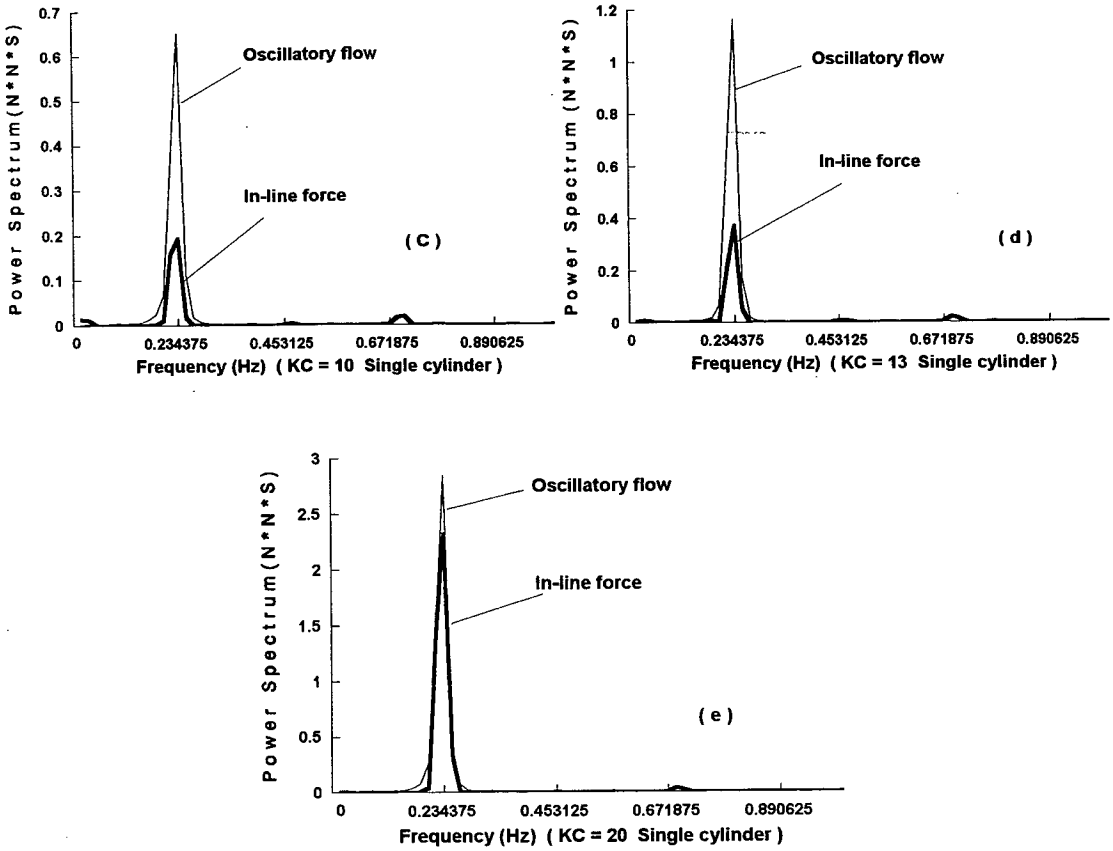

Fig 4.8(c) (d) (e) Frequency of In-line force at different KC numbers

The main frequency component of the lift force increases with KC number. From Fig 4.9 (a) (b) (c) (d) (e) , it can be found as the KC number increased, the main component of the frequency power spectrum for the lift force shifted progressively from the first to the third harmonic of that of oscillatory flow. It should be related to the vortex shedding frequency. The arrows in Fig 4.9 point at the frequency positions of the oscillatory flow.

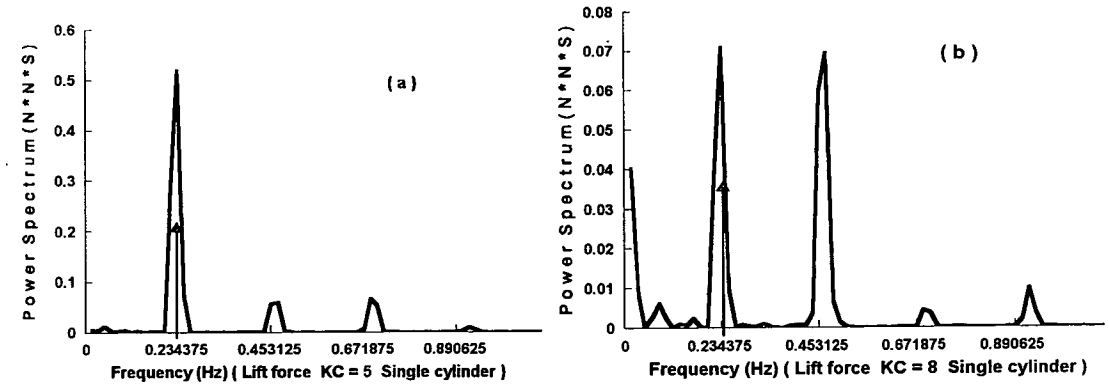

Fig 4.9(a) (b) Frequency of lift force at different KC numbers

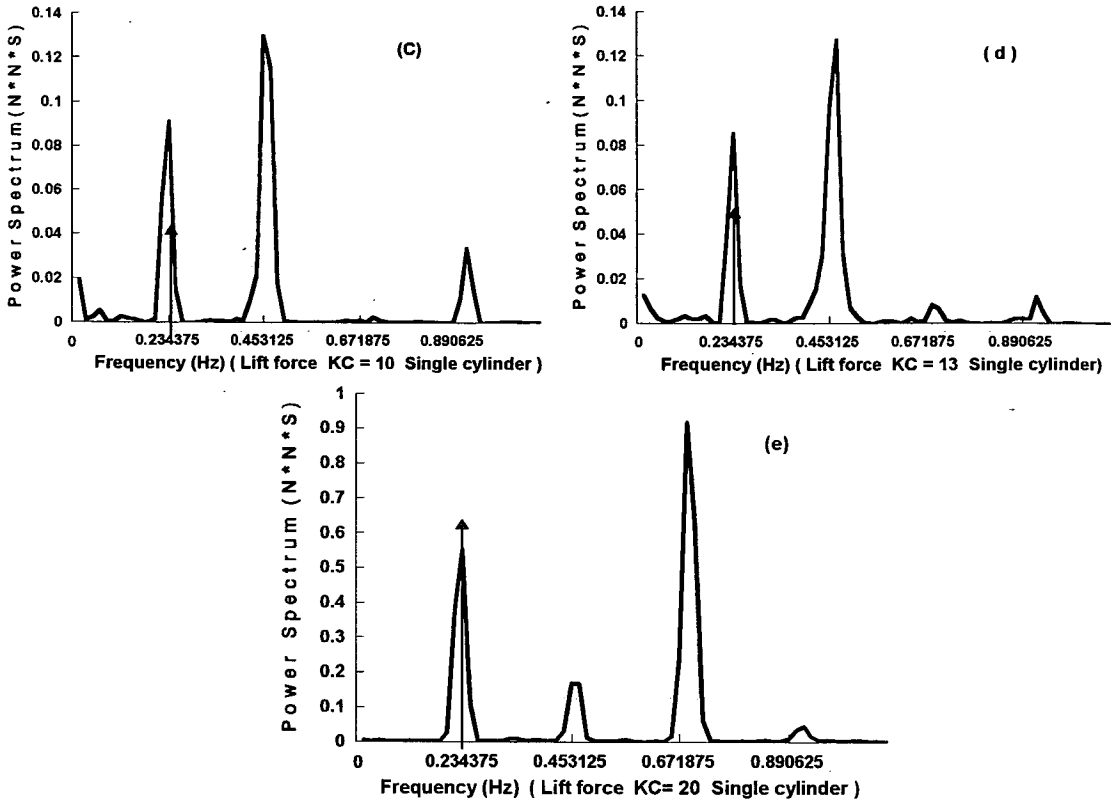

Fig 4.9 (c) (d) (e) Frequency of lift force at different KC numbers

4.4 The Flow Patterns and Their Velocity Fields

4.4.1 Vortex shedding patterns

The flow pattern visualization is done using video recordings in the PIV environment, such as Fig 4.10

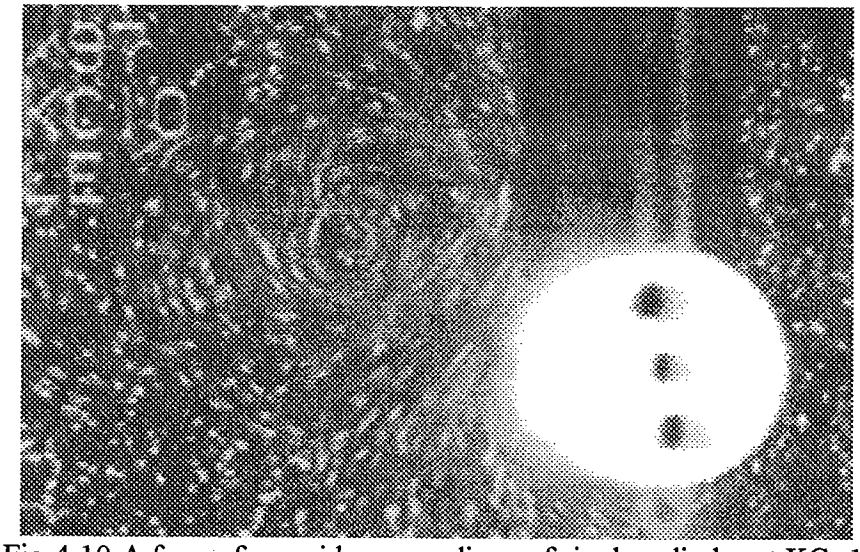

Fig 4.10 A frame from video recordings of single cylinder at KC=10

The white dots in Fig 4.10 are pollen seeds. The frame in the Fig 4.10 shows a vortex behind the cylinder. Its position is higher than the centre of the cylinder. Video recordings are a useful tool for helping us to trace the vortices movement and their positions. The experimental KC numbers are 5, 8, 10, 13 and 20 , fall within the Bearman's regimes : 2) $4 \leq KC \leq 8$, the asymmetric regime, 3) $8 \leq KC \leq 15$, the transverse regime and 4) $15 \leq KC \leq 22$, the diagonal regime . They are also within Williamson's regimes : 1) Pairing of attached vortices ; 2) Transverse street and single pair ; 3) Double pair . The video recording showed that the vortices shedding and moving show essentially similar characteristics to those described by Bearman and Williamson. When KC number is small such as KC =5 , the flow pattern is as Fig 4.11.

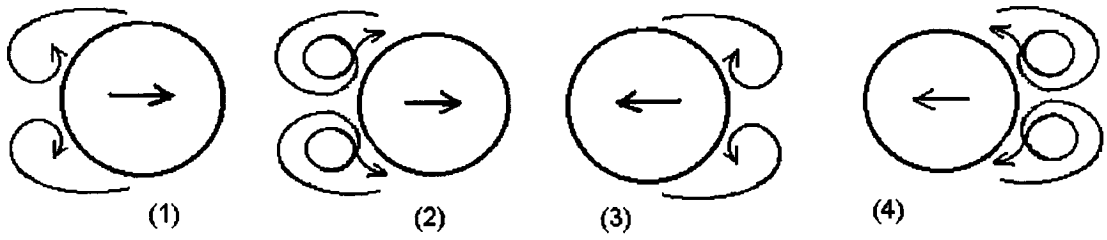

KC=5

Fig 4.11 Vortices pattern (1)

The pair of the vortices look symmetric and before completely shedding , they are pushed back to the other side of the cylinder and dissipated when the flow direction changes and another half oscillatory cycle starts. In their life cycle, they keep attaching to the cylinder surface. Williamson placed this KC number within the attached vortices regime and Bearman place it in the asymmetric regime. The main factors which cause the lift force are the different strengths of the pair of the vortices and different positions of their generations. Because of the resolution of video recording we couldn't give a good visualisation for these, but it is clear that the differences exist and results in a weak lift force.

At KC numbers 8, 10, and 13, the main features are similar to each other. First of all, the shed vortices behind the cylinder are asymmetrical, it will result in a larger difference in pressure than that at KC=5. This is one of reasons of the lift force larger than that at KC number =5. The size of vortices increases with KC number and the

angle between the moving direction of shed vortices and the direction of oscillatory flow increases with KC number. The two kinds of vortices shedding modes can be found. They are shown in Fig 4.12 and Fig 4.13. Either mode can appear randomly.

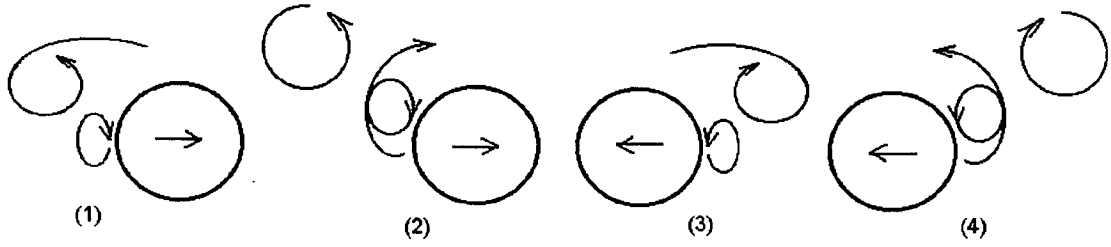

KC=10(1)

Fig 4.12 Vortices pattern (2) [mode one]

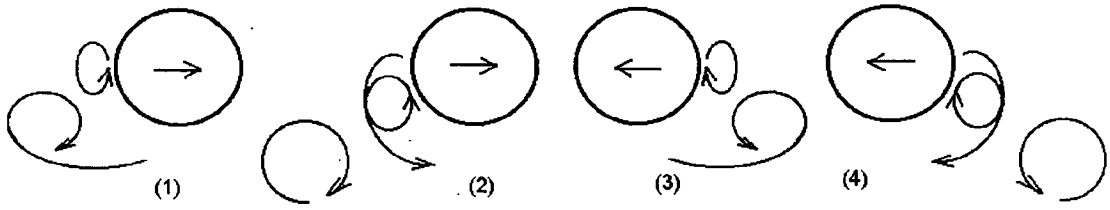

KC=10(2)

Fig 4.13 Vortices pattern (3) [mode two]

When KC number increases, the vortex strength is getting stronger (results of quantitative calculation have been shown in section 4.4.3 and section 4.4.4) From the vortices patterns , it can be found that one mode can keep many successive oscillatory cycles before changing into the other randomly. In mode one the vortices move along the top of the cylinder from one side to the other side of the cylinder ; their active area is the upper part of the cylinder. For mode two the vortices pass the cylinder along the bottom of the cylinder and go backwards or forwards with flow direction changing. Once the pattern mode changes from one to another , it will remain in the mode for many cycles.

Normally two vortices are at the same side of the cylinder before the flow changes direction. The two vortices are shed from the surface of the cylinder in different two half periods, the one shed first has a bigger size than that of the later shedding one. The larger, older vortex goes away from the cylinder in the wake, the smaller and younger vortex runs over the cylinder with its size increasing when the flow changes direction

and goes into the other half period. There another new vortex generates again on the surface of the cylinder , then shed and getting larger following the previous vortex. The process is repeated and in one cycle there are the two vortices shedding from and two vortices moving over the cylinder. These cause the pressure differences between the top and the bottom of the cylinder four times in one cycle, then they form the main frequency of the lift force of the second harmonic.

When KC numbers are in Bearman's transverse regime (8, 10, 13), we also found that the vortices do drift off the direction of the flow and go nearer and nearer the transverse direction with KC number increases. Williamson named the KC numbers range as Transverse Street and gave a photogragh of transverse street wake. In the wake there was a four vortex queue. So long transverse street hasn't been observed in the experiments here and Bearman did not mention it. It might be caused by a relative low Reynolds number of the flow. Because the β value is 255 for Williamson , 416 for Bearman and 500 for mine, if KC numbers are the same for the three of us, such as 12(Williamson's experiment), the Reynolds number will be 3060, 5000 and 6000 respectively. On the other hand, it may also be the ratios of the flow width and diameter of the cylinder which were used by Bearman and here are smaller than that of Williamson, the vortices have not had enough space to keep travelling for so long. The ratio in the Williamson's photogragh is radius of the cylinder : half width of the tank = 5 : 85 =0.005 ; and the ratio in my experiment is 25 : 250 = 0.1 , Williamson used a relative wider tank than mine. Bearman used a U-tube to give the flow visualization, and Williamson's flow patterns were obtained from a open towing tank.

KC = 20 has been put into 'the diagonal regime' by Bearman and for Williamson's regimes the KC number belongs to 'Double pairs'. Williamson said that this wake is the results of two vortices being shed in each half cycle. Fig 4.14 shows a flow pattern drawn according to the video recordings. If we divided the round cylinder section into eight equal segments, the vortex shedding paths do coincide approximately with the diagonal line of cylinder cross section.

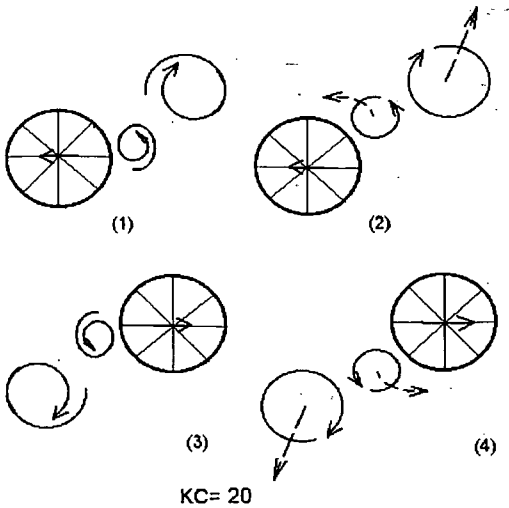

Fig 4.14 Vortex pattern (4)

From the video show we didn't find the double pairs at KC=20, but using PIV photograph, the more vortices can be found, see Fig 4.16 (b). So the lift force frequency has a main frequency peak which is the third harmonic of that of the oscillatory flow , see Fig 4.8. That means that in an oscillatory period, there are more than two vortices shedding. But the procedure has not been found properly by our observation , it is because the vortices are too small when they are on the surface of the cylinder. May be in the procedure the vortex has had some fast replacement or destruction. The numerical simulation has obtained a vortex pattern with three vortices at KC =20, see Fig 4.28.

4.4.2 The velocity field at the peak of lift force

In Fig 4.5 of the force trace chart , there were some interesting phenomena, and questions raised include: at the moment lift force amplitude exceeds the amplitude of in-line force, what did the flow pattern and its velocity field look like? When peak of the lift force line runs across the peak of the in-line force ,what did the flow pattern and its velocity field look like ? It was hard to get the record of pattern and velocity field at the moment which we want, although we can do simultaneous force measurement and velocity field record. Because above phenomena occurred randomly and unpredictable, we couldn't grab the frame which we hoped to get. Under the condition, we had to choose some special moments or phases in oscillatory cycles. We decided to let the camera automaticly take the phases : $0\ (2\pi)$, $\frac{1}{4}\pi$, $\frac{1}{2}\pi$, π and

$\frac{3}{2}\pi$. So we can get result shown as Fig 4.15.

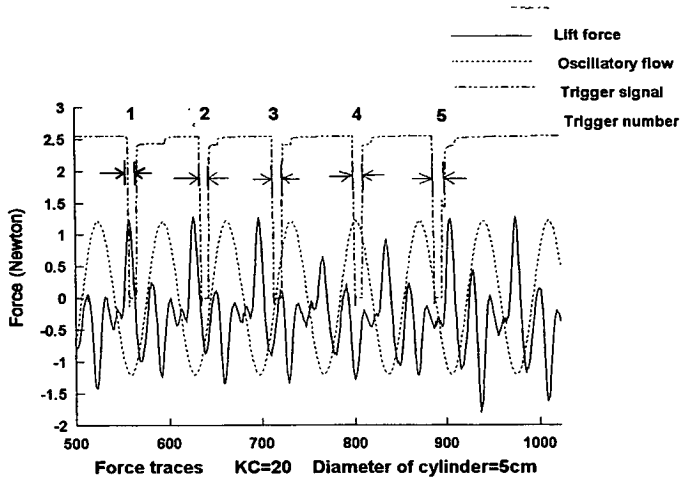

Fig 4.15 Lift force -time varying line at KC = 20

Because the lift force is more complex and very important, we concentrate on lift force variations and the velocity fields at special lift peaks. In Fig 4.15 the trigger number showed the position of taken photographs. No 1 : 0 or 2π; No 2 : $\frac{1}{4}\pi$, No 3 : $\frac{1}{2}\pi$; No 4 : π ; No 5 : $\frac{3}{2}\pi$. From the chart, we can found that sometimes the trigger coincided with the negative peak of the lift force such as No.2 and No 4 , and sometimes not. A largest negative peak of lift force happened beyond the given time period of the trigger (between 900-1000 along the x axis), so no velocity field can be obtained. Fig 4.16 is the PIV phtograph matching the trigger number 4 with a negative peak of lift force. Its corresponding PIV mapping is shown in Fig 4.17.

Fig 4.17 showed there were two vortices at the wake of the cylinder. The cylinder moved from right to left until a phase of smallest velocity(zero velocity). Large negative clockwise vortex is at upper right position of the cylinder wake . A positive anticlockwise vortex has just been shed. Against the surface of the cylinder there were a few small vortices. Fig 4.16(b) shows a close up of the area and about three new small vortices can be found. These small vortices had been mentioned by Stansby [10] , Bouard & Coutanceau [11] . Because of the limitation of PIV analysis, they are not visible in Fig 4.17.

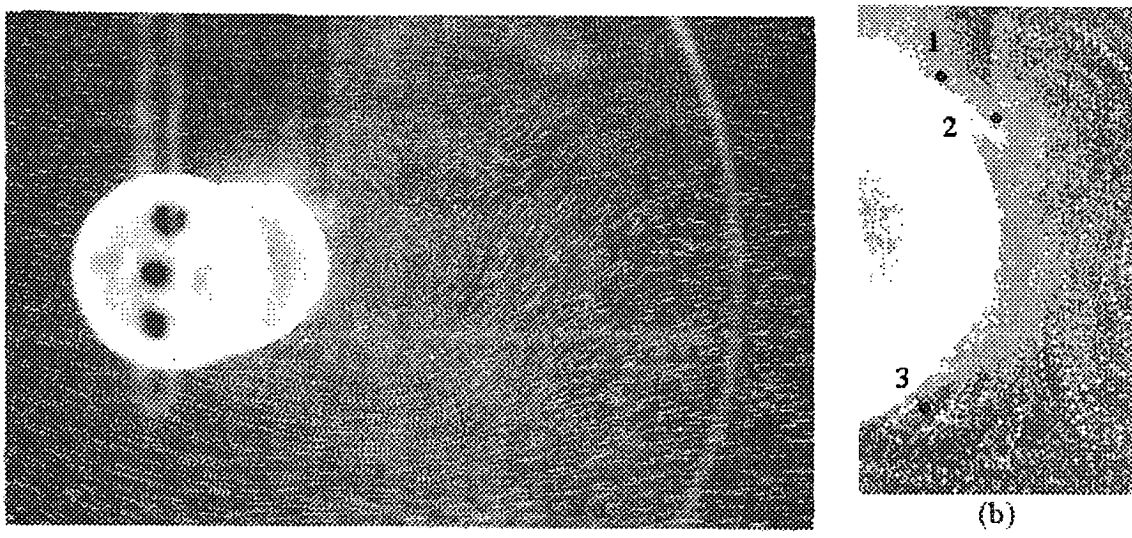

Fig 4.16 A PIV negative picture

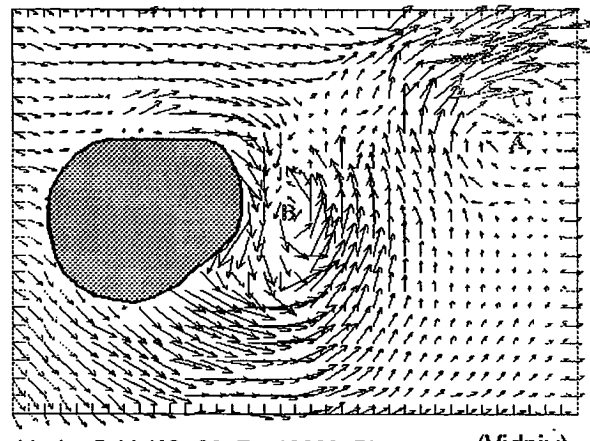

Fig 4.17 . The PIV velocity map at KC=20

For KC number = 13, a force varying line is shown in Fig 4.18.

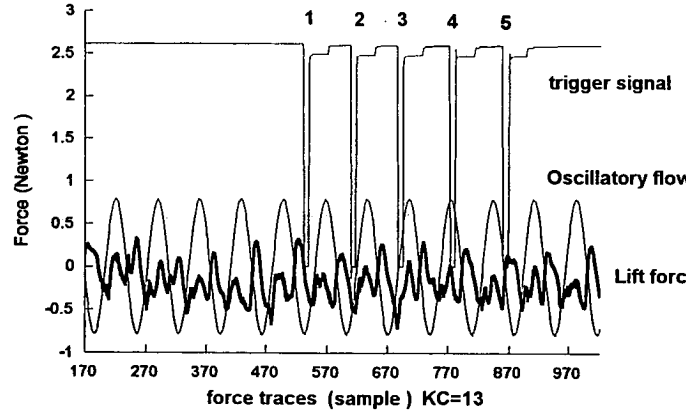

Fig 4.18 Lift force -time varying line at KC =13

The trigger No 2 at ¼ π just grab a negative peak of the lift force. The corresponding PIV mapping is shown in Fig 4.19

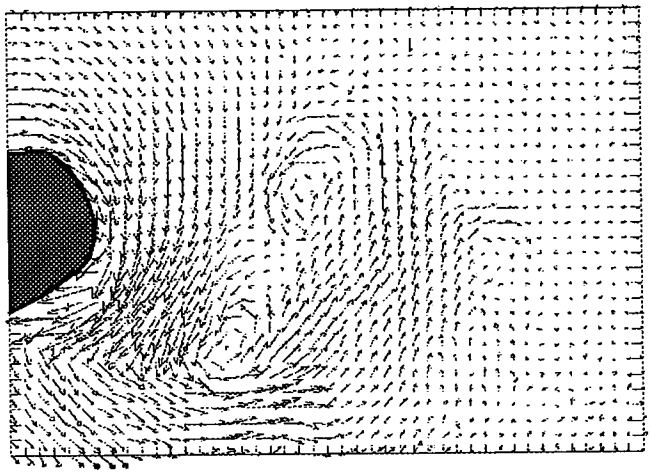

Fig 4.19 The PIV velocity map at KC= 13

In the phase, the cylinder moves from right to left and the vortices in wake show anticlockwise rotation. There should be new vortices which generate from the surface of the cylinder, but they can't be found from the PIV map. It may be caused by the relative position between cylinder and camera and the resolution of PIV map.

For KC=10, a vector map is shown in Fig 4.20. The map comes from PIV analysis at a positive peak of the lift force at phase π . For KC=8, a vector map is shown in Fig 4.21. The map comes from PIV analysis at a minus peak of the lift force . The phase is ½ π.

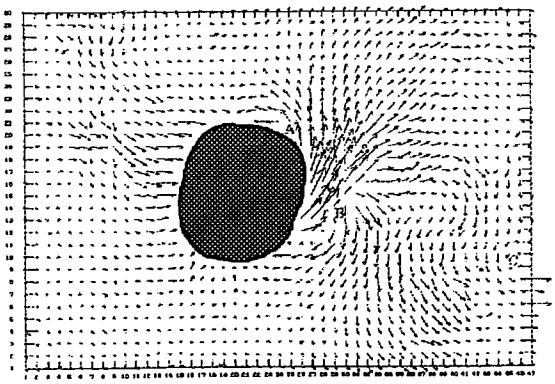

Fig 4.20 A PIV vector map at KC10

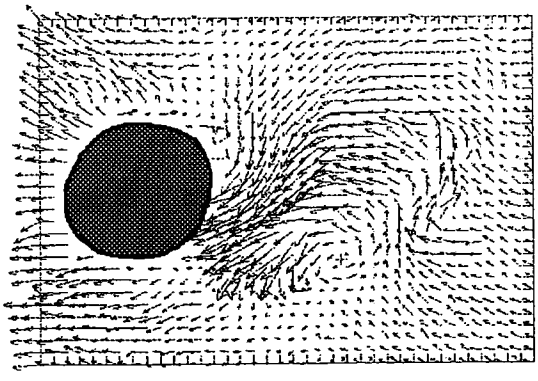

Fig 4.21 A PIV vector map at KC=8

Because of parallax in a photograph, the near end of the cylinder appears bigger than a far end, the part of the cylinder which is in front of the illumination sheet will cover some part of the flow field around the cylinder. In addition the angle at which the cylinder faced to the camera will also influence the interrogation area . This problem is most acute at KC=5. In this case the size of the vortices is very small and they lie just on the surface of the cylinder, so they are easily covered by the image of the cylinder body. Thus the small near-surface vortex structure is difficult to be shown and even the whole vortex cannot be seen. In PIV velocity analysis, each interrogation area is a small square but the profile of the cylinder is a curve line. When interrogation square moves along the surface of the cylinder, if there are not enough seeding images in the square, there will be no velocity analysed in the interrogation area. This problem will cause small vortices to be lost at the surface of the cylinder.

4.4.3 Some vorticity feature

The vorticity contour around the cylinder at phases corresponding to the peak of the lift force line, were also calculated. These are shown in Fig 4.22-4.23.

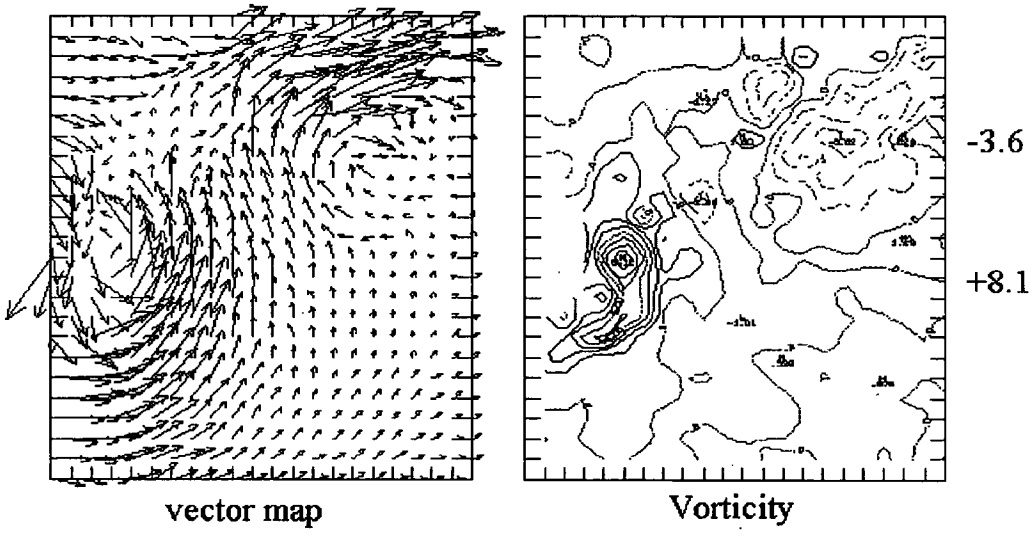

Fig 4.22 Velocity and vorticity maps at KC=20 Contour increment=1.0,
Numbers on outside the map are vorticity central values
Dash line is negative vorticity

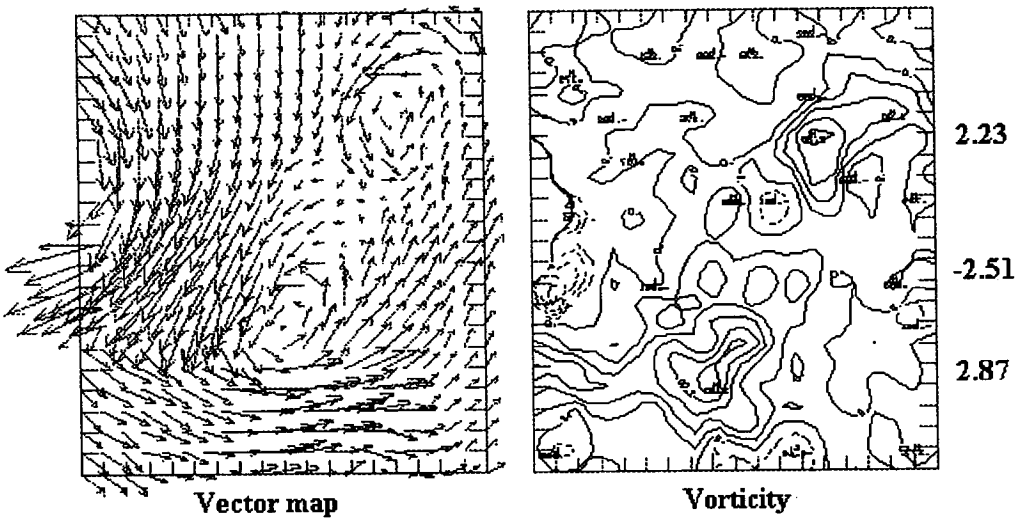

Fig 4.23 Velocity and vorticity maps at KC=13 Contour increment=0.5,
Numbers on outside of map are vorticity central values
Dash line is negative vorticity

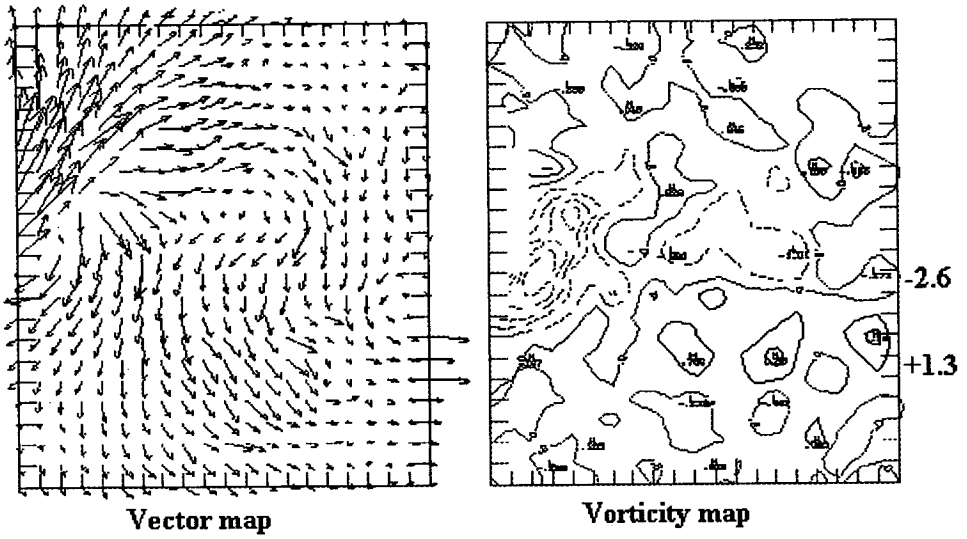

Fig 4.24 Velocity and vorticity maps at KC=10 Contour increment=0.5,
Numbers on outside the map are vorticity central values
Dash line is negative vorticity

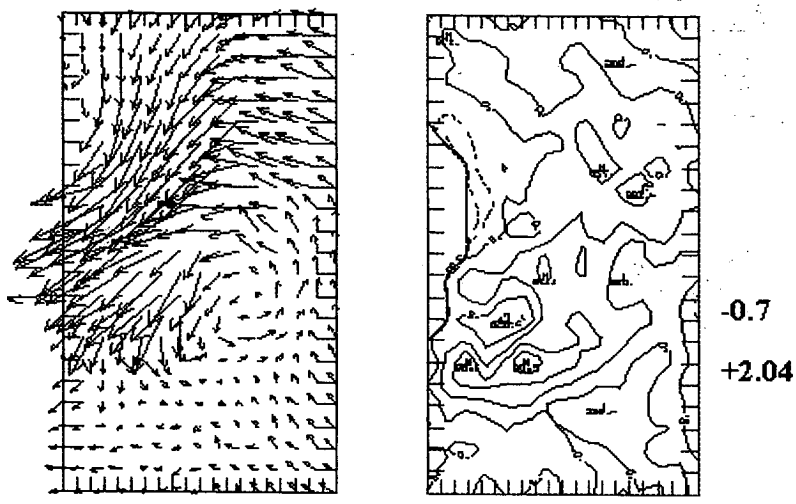

Fig 4.25 Velocity and vorticity maps at KC=8 Contour increment=0.5,
Numbers on outside the map are vorticity central values
Dash line is negative vorticity

In the vorticity maps, the strength variance of some vortices which were in the immediate vicinity of the cylinders did not vary with KC . The vorticity central values were similar at different KC numbers, but the differences in vorticity between positive and negative centres decrease when the KC number was smaller. They were as below:

At KC=20 : $\Delta\omega$ = 8.1-(-3.6) =11.7 (1/s) ; at KC=13, $\Delta\omega$ = 2.87-(-2.51)= 5.4 (1/s);

at KC=10 , $\Delta\omega$ = 1.3 - (-2.6) = 3.9 (1/s) , at KC=8 , $\Delta\omega$ = 2.04 -(-0.7)= 2.7 (1/s).

These difference between two vortices central values should influence the lift force strength. If two vortices shed with different vorticity central values , the lift force will has different reactions . Now the large difference occurred at a large KC number and the lift force strength is also large. That means that the difference of vorticity of the vortices is one of the reasons of lift force variance.

4.4.4 Vortex strength

According to the calculating method of vortex strength in Chapter 2 and [16], the maximum vorticity of a vortex was found first for the four vorticity fields in section 4.4.3.See Fig 4.26 (a) (b) (c) (d)

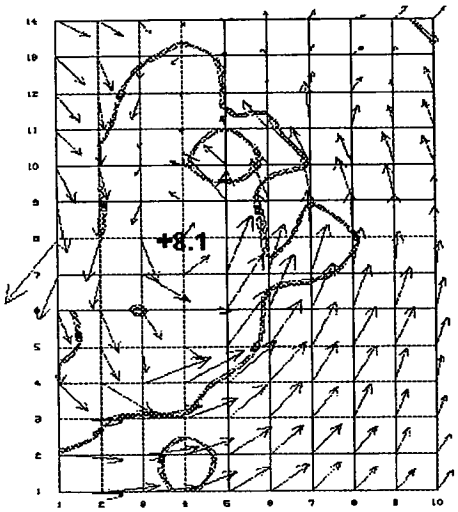

Fig 4.26 (a) KC=20 phase= π

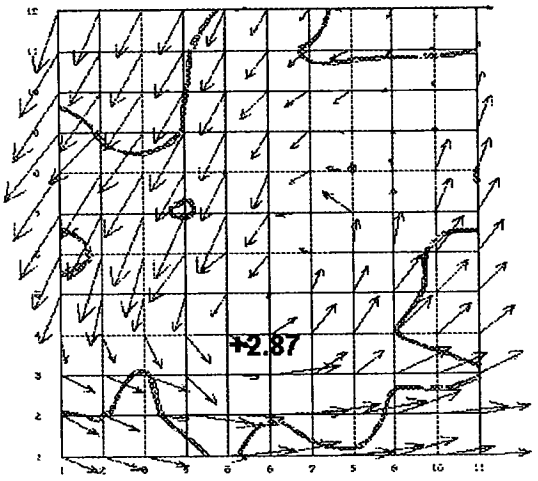

Fig 4.26 (b) KC=13 phase= 1/4 π

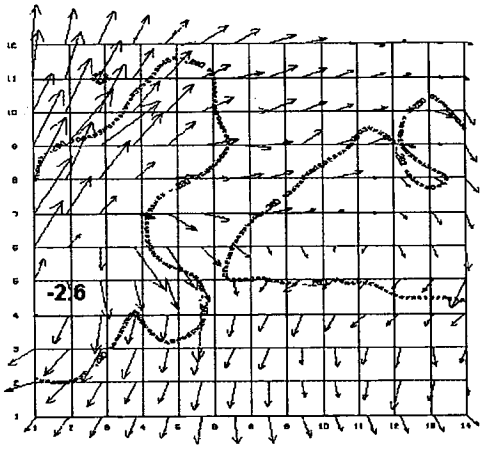

Fig 4.26 (c) KC=10 phase=π

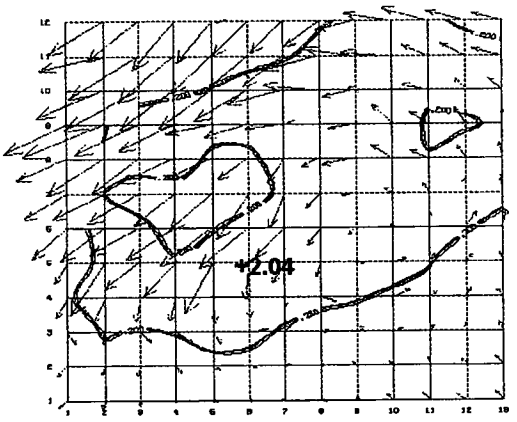

Fig 4.26 (d) KC=8 phase=1/2 π

Then the contuor with value of 1/10 maximum vorticity was used to represent the minimum vorticity perimeter for each vortex, such as the thick solid lines in the Fig 4.26. The contours were thought as the boundaries of the vortices and those points which had a vorticity above the boundary value were summed, the number of mesh points on which the vorticity values were calculated were also counted. The vortex strength was obtained and shown in table 4.1

KC number \ Vortex strength (k)		Total strength (Absolute value)	Average strength (Absolute value)
20	(+vortex)	107.16(38 points)	2.82
13	(+vortex)	81.20 (78 points)	1.04
10	(- vortex)	58.62 (65 points)	0.90
8	(+vortex)	51.11 (76 points)	0.67

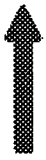

Table 4.1 Vortex strengths at different KC numbers

From Table 4.1 it can be found that the vortex strength was stronger at a larger KC number . When a stronger vortex shed, it will cause a large variance in the lift force.

4.5 The Results of Numerical Modelling

4.5.1 Frequency of force coefficient

The power spectrum analysis has shown that the numerical simulation is satisfactory for the results comparison with experiments. The main frequency component of the in-line force coefficient is the same as that of the oscillatory flow . The features of the lift force coefficients's frequency can be seen in Fig 4.27(a) (b) (c) (d) (e). On the frequency axis 0.0733 is the position of the frequency of the oscillatory flow and the in-line force coefficient, they are pointed by the arrows in the Figures

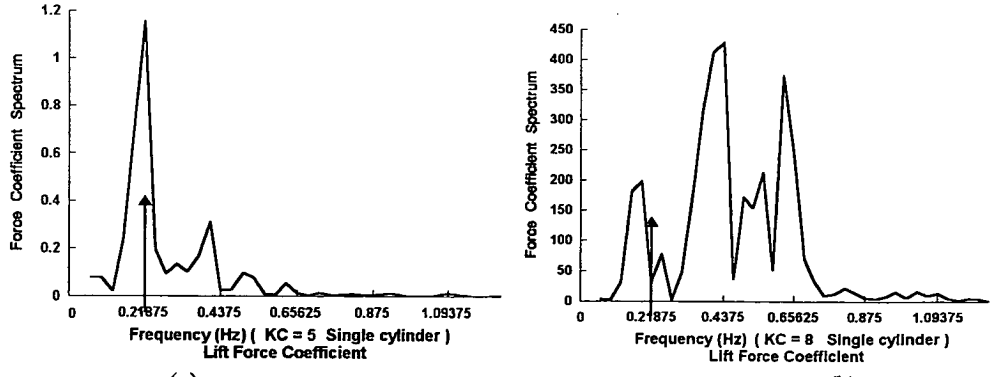

Fig 4.27 (a) (b) Numerical result of frequency of lift force coefficient

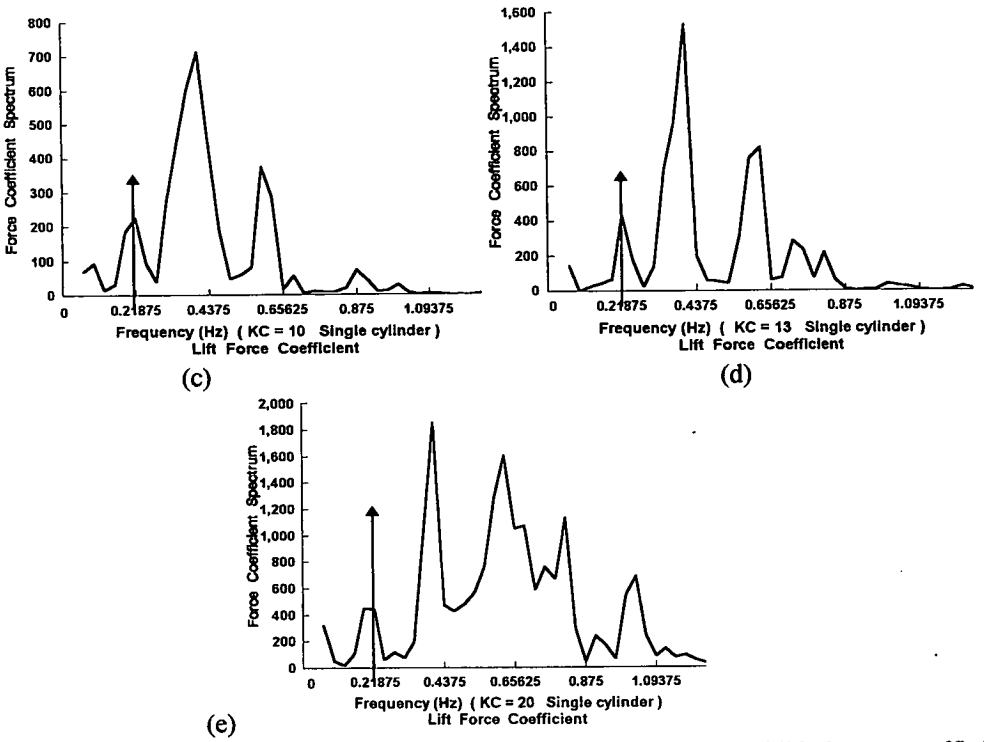

Fig 4.27 (c) (d) (e) Numerical result of frequency of lift force coefficient

At KC =5, the highest peak in the lift force coefficient frequency spectrum occurs at the second harmonic of the oscillatory flow. However, the first harmonic has a larger area which means that the frequency is also strong. In laboratory experimental results, the first harmonic was main component. At the KC number = 8 and KC =10, the lift force coefficients have their main frequency component at the second harmonic of the oscillatory flow. These were the same as the experimental results. At KC = 13 and 20 the main frequency components are the third and fourth harmonic of the oscillatory flow. It seems that the main frequency increases faster with KC number than that the experimental results.

The tendency of the lift force frequency to, on average, increase with KC number has been simulated well. When KC number increases, the frequency of vortices generate and shed increases, too . This is the basic reason for the main frequency of lift force or lift force coefficient sweeping to a higher harmonic component. So the numerical model can simulate well the frequency and strength increasing of the lift force with KC number , and at some KC numbers its results compared very well with experimental data.

4.5.2 Vector fields and their vorticity

The velocity simulation has provided many satisfactory results. Fig 4.28 showed a vector field at phase π when KC = 20.

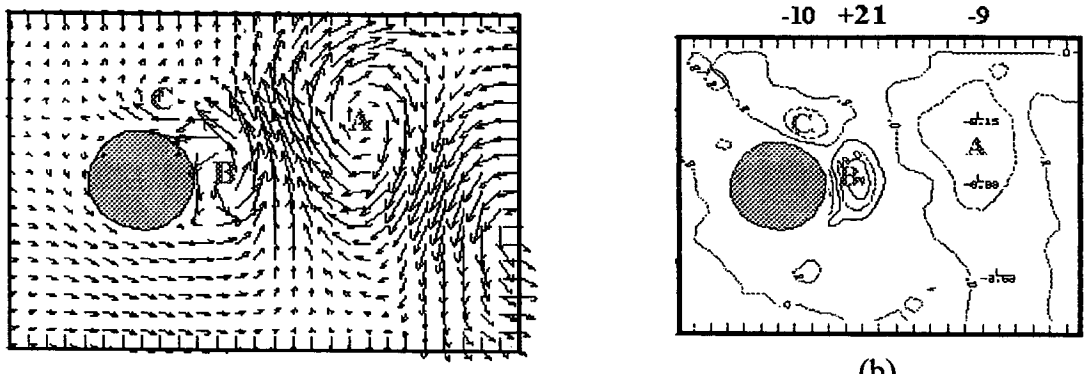

Fig 4.28 Vector and vorticity of computer simulation KC =20 Re=10000, Phase= π
Numbers on outside of the map(b) are vorticity central values.

To compare with Fig 4.16 and Fig 4.17, the numerical modelling simulated 3 vortices A, B, C . The vortex C can be seen in the PIV negative Fig 4.16 . Because the PIV analysis has its own inherent limitation, it cannot show the vortex C in Fig 4.17. At this point the numerical modelling gave a better show.

To compare with Fig 4.22 , a basic qualitative strength of vorticity distribution has been simulated out. The central absolute value of B is larger than that of the A. This was the same as the experimental results.

Fig 4.29 and 4.30 showed the vector fields at phase π when KC = 10 and KC=8

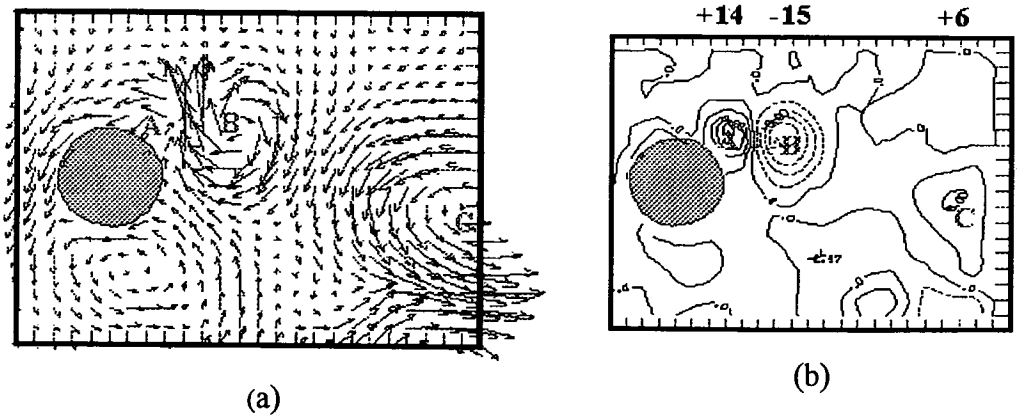

Fig 4.29 KC=10 , Phase = π
Numbers on outside of the map(b) are vorticity central values.

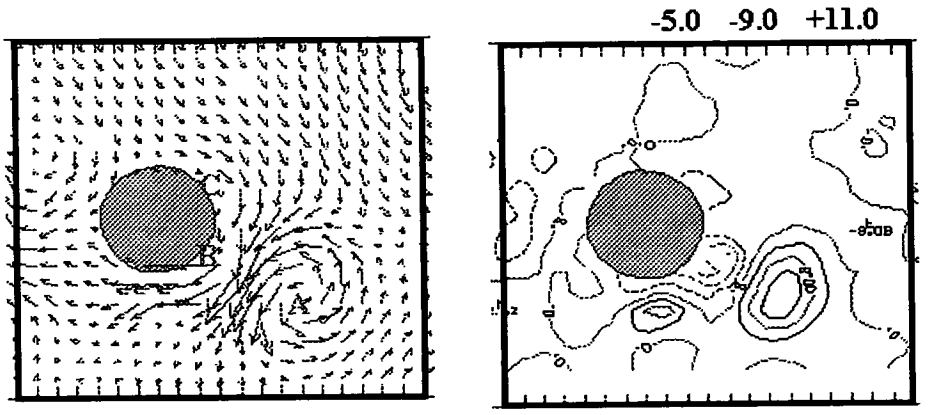

Fig 4.30 KC=8 , Phase = π
Numbers on outside of the map(b) are vorticity central values.

To compare with Fig 4.20 and Fig 4.24 of laboratory experimental result, the main three vortices have been simulated well. The vorticity difference between two vortices centres has a variance tendency the same as the analysis of experimental results.

Such as in Fig 4.28, $\Delta\omega = \omega(B) - \omega(A) = 21-(-9) = 30$;

in Fig 4.29, $\Delta\omega = \omega(C) - \omega(B) = 6-(-15) = 21$.

in Fig 4.30, $\Delta\omega = \omega(A) - \omega(B) = 11-(-9) = 20$

The differences in vorticity between positive and negative centres were less when the KC number was smaller. The feature is the same as the lift force strength .
For numerical modelling at the phases of $1/2\pi$, $3/2\pi$, which are maximum velocity phases , the main flow is much stronger, and vortices are small in their size and strength. In the numerical model, the vortices are a small perturbation on the big main flow. When the main flow has its greatest velocity, at the phases $1/2\pi$, $3/2\pi$, they will cover up the weak vortices. At π and 2π the main flow has its smallest velocity so vortices are clear to be shown

The Fig 4.31 showed a stream function map. It was at KC=8 and Phase = ½ π. It has presented the basic feature of the experimental results in Fig 4.21 , so the simulation was successful.

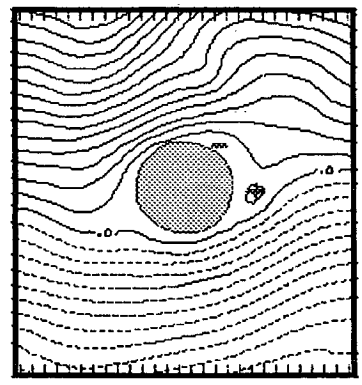

Fig 4.31 KC=10 , Phase =1/2 π

Using the numerical simulation we can investigate the process of the vortex evolution in its strength and its moving path for a short time . For example, we can output the result of every time step, which can be at every 1/40 π. Alternatively we can output succesive phases which has a time step of 0.0625s in the modelling. The experiment in laboratory couldn't obtain this kind of results because taking a photograph requires time for mechanical motion of the equipement.

Fig 4.32 showed a streamfunction field with the succesive phases from 15/20 π to 21/20 π. They are at KC =20 . In Fig 4.32 there is low centre of streamfunction at the downstrem side of the cylinder. Its strength increases with time (phases) and its moving path is crossing the main flow direction and goes up to 45 ° direction.

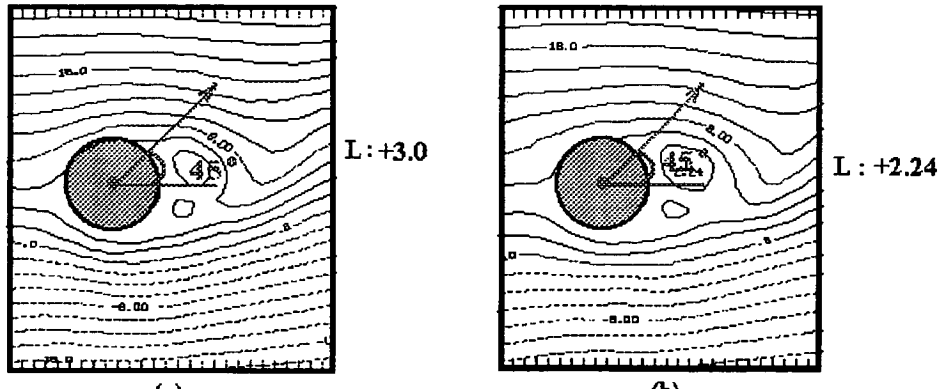

(a) 15/20 π (b) 16/20 π

Fig 4.32 (a) and (b) Streamfunction fields at different phases

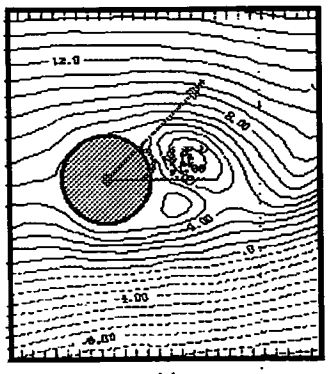

(c)

17/20 π

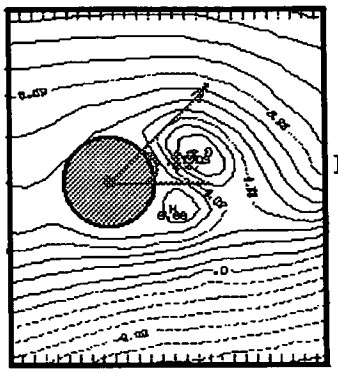

(d)

18/20 π

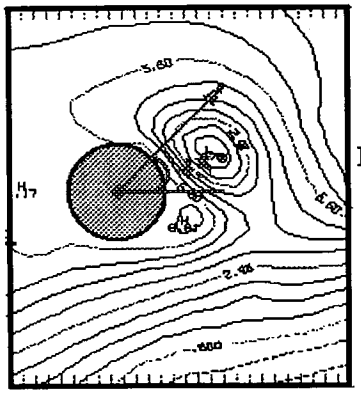

(e)

9/20 π

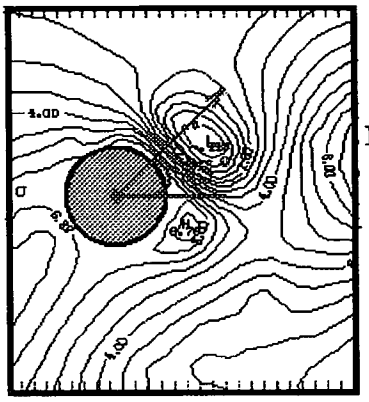

(f)

(20/20) π

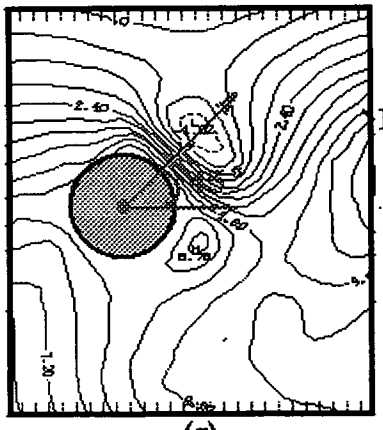

(g)

21/20 π

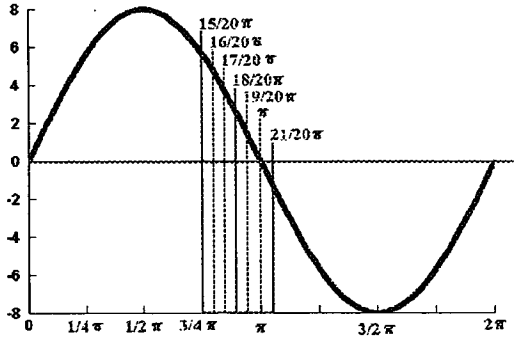

The phases at which streamfunction fields were shown.

Fig 4.32 Streamfunction fields at different phases

4.6 Conclusions

According to the above analysis , the following conclusions can be drawn from the results of this study.

1) Under oscillatory flow condition, the average strength of in-line force and lift force increase with KC number. The average strength of lift force is weaker than that of the in-line force, but in some special moments the amplitude of lift force evolution can be larger than that of the inline force.

2) When the KC number increases in the range 5 to 20, the main frequency components of the in-line force are the same as the oscillatory flow. And the main frequency of the lift force varies from the first up to the third harmonic of the oscillatory flow. The main frequency of the lift force is influenced by vortex shedding and vortex running over cylinder. According to video recording , PIV negative and numerical simulation, the number of vortex shedding in an oscillatory period increases with KC number.

3) The in-line force coefficient decreases with KC number from KC =5 to KC =20. The inertia force coefficient has a trough at round KC =10, before this number the coefficient decreases with KC and after it the coefficient increases with KC. The drag force coefficient has an evolutional tendency the inverse of the inertia coefficient. The drag coefficient has a positive peak around KC=13.

4) The vortex patterns show that size of the vortices expand with KC number increasing. At KC =5 the vortices are generated from the surface of the cylinder. They are in down stream side of the cylinder when flow past the cylinder. There are two symmetry and attached vortices, but their strengths should have slight difference. After KC =5 , the size of the vortices increases fast with flow velocity, the vortex shedding is one after another or called asymmetrical shedding. There are one vortex shedding and one vortex moving over cylinder in each half period of oscillatory flow and they should be one of reasons that the second harmonic is main frequency for KC = 8, 10 and 13. At KC=20, the shed vortices are more than one in each half period, so the main frequency moves to the third harmonic of the oscillatory flow. The moving paths of the shed vortices have larger angles with the direction of the oscillatory flow at bigger KC number . At KC = 20 the angle can be 45 ° or even over.

5) The vortex strength K showed that vortex strength increases with KC number when lift force is at its peak value. The vortex shedding causes a peak in the lift force variance with time and strong vortex shedding will make a large lift force amplitude. The vorticity central values have not too much variance at different KC number, but the difference in vorticity between the positive and the negative centres of vorticity decreases when KC number is smaller. It means that the two shed vortices with a large different strengths will cause a large lift force peak.

6) Computer simulation is basically successful. It can simulate the small vortices which are against the surface of the cylinder. In experiment some part which are in the vicinity of the cylinder cannot be seen because of the cylinder body covering. The numerical simulation can show us more detail in this areas.

7) Computer simulation is a helpful tool which can investigate the vortices evolution in a succesive phases and show the strength and moving path of vortices. It showed that vorticity at vortex centre increases when it move to 45 ° direction at the KC number = 20.

4.7 References

[1] T.Sarpkaya, Oscillating Flow About Smooth and rough cylinders, (1987), J.Offshore Mechanics and Arctic Engineering, Vol 109, pp307-313.

[2] P.W.Bearman, M.J.Downie, J.M.R.Graham and E.D.Obasaju, Force On Cylinders In Viscous Osillatory Flow At Low Keulegan-Carpenter Numbers, (1985) J.Fluid Mech.Vol 154, pp.337-356

[3] Sheldon I. Green (Editor) , Fluid Vortices, Charpt V Vortex Dynamics In The Wake Of A Cylinder, 1995, Kluwer Academic Publishers , Netherlands .

[4] C.H.K.Williamson, Sinusoidal Flow Relative To Circular Cylinders, (1985), J.Fluid Mech. Vol 155, pp 144-174 .

[5] E.D.Obasaju, P.W.Bearman and J.M.R. Graham , A study of forces, circulation and vortex patterns around acircular cylinder in oscillating flow, (1988) J.Fluid Mech. Vol 196, pp467-494

[6] T.Sarpkaya & M.Isaacson, Mechanics of Wave Forces on Offshore Structures, Chapter 1, Charpter 3 (1981), Van Nostrand Reinhold Company Inc. New York, U.S.A

[7] D.J.Maull and M.G.Milliner, Sinusoidal Flow Past A Circular Cylinder, (1978) Coastal Engineering , Vol 2 pp 149-168

[8] G.H.Keulegan & L.H.Carpenter, Forces on cylinders and plates in an oscillating fluid, 1958, J.Res.Nat.Bur.Standards, Vol 60, pp423-440

[9] T.Sarpkaya, Force On A Circular Cylinder In Viscous Oscillatory Flow At Low Keulegan-Carpenter Numbers, (1986) ,J.Fluid Mech., Vol 165, pp 61-71

[10] P.A.Smith and P.K.Stansby , Impulsively started flow around a circular cylinder by the vortex method, Journal of Fluid Mech. 1988

[11] R.Bouard & M.Coutanceau, The early stage of development of the wake behind an impulsively started cylinder for $40 < Re < 10^4$. (1980) J.Fluid Mech. Vol 101

[12] A.Slaouti and P.K.Stansby, Flow around two circular cylinders by the random-vortex method , Journal of fluids and structures 1992 , vol 6, pp641-670

[13] T.Sarpkaya, Vortex shedding and resistance in harmonic flow about smooth and rough circular cylinders at high Reynolds numbers, (1976) Tech Rep. NPS-59SL76021. Naval Postgraduate school, Monterey, CA.

[14] J.A.Roberson and C.T.Crowe , Engineering Fluid Mechanics,Chapter eleven 1997, John Wiley & Sons, Inc. Canada

[15] P.Justesen, A Numerical Study of Oscillating Flow Around A Circular Cylinder J. Fluid Mech. (1991) vol 222, pp. 157-196

[16] A.E.Corlett , A near wake study of vortex shedding from bluff bodies at low Reynolds numbers, PhD thesis , The University of Edinburgh, 1997.

Chapter 5

Oscillatory Flow Round Two Cylinders

5.1 The Flow Past Two Cylinders

5.1.1 Constant Flow Past Two Cylinders

There is an infinite number of possible arrangements of two parallel cylinders positioned at right angles to the approaching flow direction. Of the infinite arrangements, two distinct groups can be identified[1] : in one group, the cylinders are in a tandem arrangement, one behind the other at any longitudinal spacing; and in the second group, the cylinders face the flow side by side at any transverse spacing. All other combinations of longituditional and transverse spacings represent staggered arrangements.

According to a common description, the space between two cylinders is represented by the ratio T/D, where T is the distance between the centres of the two cylinders and D is the diameter of the cylinders. See Fig 5.1

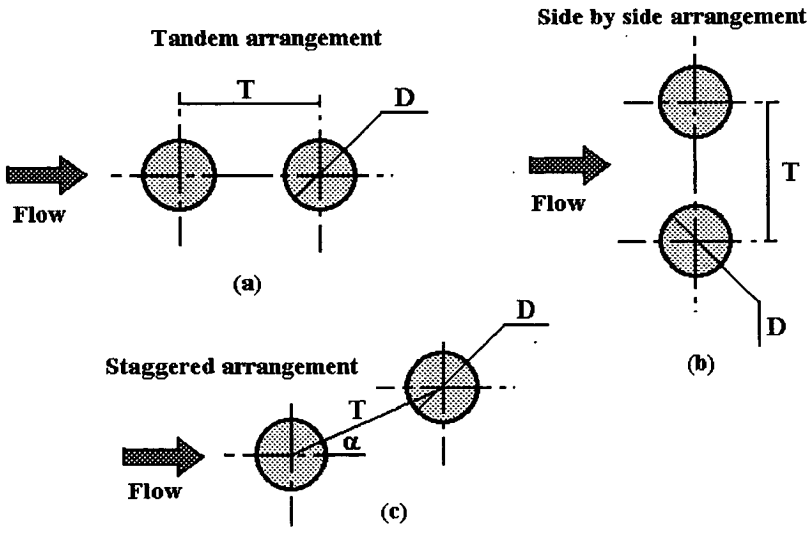

Fig 5.1 The three kinds of basic arrangement

In fact both the tandem and the side by side arrangements are special cases of the staggered arrangement. They are $\alpha=0$ and $\alpha= \frac{1}{2}\pi$.

Hori [2] gave a force coefficient interference skeleton for various arrangement of the two cylinders, it is shown in Fig 5.2. In Fig 5.2 all possible arrangements of two cylinders were classified into regions by taking into account whether the drag force was greater or less than that for a single cylinder and whether the lift force was positive, negative or negligible. These regions are shown in Fig 5.2.

The upstream cylinder can be situated in three regions :

(1) Negligible lift force and reduced drag force.

(2) Small repulsive lift force and reduced drag force.

(3) Repulsive lift force and increased drag force.

The downstream cylinder can be situated, in addition to the above three, in the following regions:

(4) Negligible lift force and increased drag force. This is a small region and beyond it there is no interference.

(5) Negative lift force and decreased drag force. This is a dominant region for the downstream cylinder.

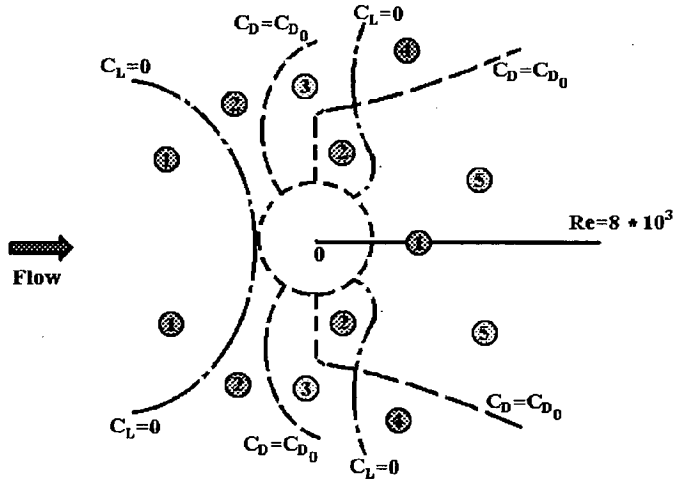

Fig 5.2 Interference force coefficient for all arrangements at Reynolds number of 8×10^3

The upstream and downstream cylinders in any staggered arrangement usually belong to different regions. Zdravkovich thought [1] the complexity of the flow interference between two circular cylinders may be due to differing flow patterns. The flow patterns provide phenomenological explanation, the intrinsic nature of the flow patterns should be a direction of further research.

For the side by side arrangement , Biermann and Herrnstein[1] showed their experimental results and pointed out that the interference drag was zero for all spacings greater than 5 diameters (T>5D). They found that the interference drag increased as the spacing decreased but only down to $2\frac{1}{4}$ diameters . For smaller spacings, very odd changes occurred . They observed a remarkable feature and wrote : "Apparently the type of flow (refers to positive and negative interference drag) changes rapidly with a change in spacing; it may even change while the spacing is held constant." This was the first indication of the bistable nature of two different flow patterns at these spacings. The bistable nature of the flow around the two cylinders means that in the range of spacings from 1.1 to 2.2 diameters there are two bistable forces experienced by the cylinders. The two different forces act on the two cylinders only for some time then change randomly, so these forces should always be taken into account.

For the tandem arrangement, Biermann and Herrnstein's experiments showed that the interference drag of both cylinders went to constant values at spacings greater than about $3\frac{1}{2}$ diameters. The pressure coefficient distribution [2] around the upstream cylinder was affected only at the rear part of it by the presence of the downstream cylinder. The base pressure coefficient increased as the spacing of downstream cylinder increased and, consequently, the drag on the upstream cylinder was reduced. The pressure distribution around the downstream cylinder showed two unusual features. Firstly, the side facing the gap between the cylinders had a very low negative pressure, which was almost the same as the corresponding value of the base pressure of the upstream cylinder. This fact is an indication that the flow in the gap is almost stagnant. The second unusual feature was that the negative gap pressure coefficient in front of the downstream cylinder exceeded that on the base side behind. Hence, the downstream cylinder experienced a negative drag - thrust force. The decrease of the interference drag was caused mainly by the corresponding increase of the gap pressure.

For vortex shedding, smoke observations of the wakes behind the cylinders in the tandem arrangement and at low Reynolds numbers [3] revealed that a vortex street

always formed behind the downstream cylinder, but only for spacings greater than 4 diameters behind the upstream cylinder. There are two flow patterns for the tandem cylinders . The first flow pattern did not produce vortex shedding behind the upstream cylinder and distinctly influenced the vortex shedding behind the downstream one. Therefore, it should be expected that an upstream cylinder should be less prone to vibrations induced by vortex shedding in the range of spacing $1 \leq T/D \leq 3.5$ than the downstream one. In fact the latter should be even more prone to vortex shedding induced vibrations than the single cylinder . The second flow pattern produces periodic vortex shedding behind both cylinders. The commencement of vortex shedding behind the upstream cylinder strongly affects and synchronizes the vortex shedding behind the downstream one. Hence, both cylinders should be equally prone to flow induced vibrations due to vortex shedding. Each of these flow patterns can change rapidly. Ishigai,et al.[1] wrote " There is a critical T/D , the critical T/D is equal to 3.8, below which the regular velocity fluctuation is observed only behind the downstream cylinder. When T/D > 3.8, the vortex streets are formed behind both cylinders and the vortex shedding frequencies are the same."

5.1.2 Oscillatory Flows Past Two Cylinders

The case of cylinder groups in oscillatory flow is a problem which has received far less research attention than the isolated cylinder case[4]. It is possible for the flow and forces to be significantly modified due to hydrodynamic interference effects. Laird & Warren [4] measured the total lift and inline force on a 24-cylinder bundle in sinusoidal flow of large amplitude corresponding to KC=165. They found that the fluctuating total lift could be as large as the total drag. Bushnell [5] investigated the maximum forces on one cylinder in a 3x3 square array of cylinders and on one cylinder in pairs of cylinders in the sinusoidal flow of a pulsating water tunnel. Orientations of these arrays were set at 0°, 20°, 40° between the flow direction and the line joining the cylinder centres. Bushnell conducted his experiments using large amplitudes, corresponding to KC>30, and he kept his cylinder spacing constant at $g^* = 2.0$ (T/D=3.0) where g^* is the gap between the cylinder surfaces divided by the diameter of the cylinders. He found that the shielding effect of an upstream cylinder on a downstream cylinder produced a decrease in the in-line force but a significant increase in the lift, which was greatest at 20°. Sarpkaya [4] arranged a pair of cylinders in a U-tube at orientations

of 0°,30°,60° and 90°, and measured C_M and C_D as well as the lift-force coefficient C_L. The gaps were varied between T/D = 1.5, 2.5 and 3.5 over a range of flow amplitudes corresponding to KC =10 to 100. He found a similar shielding effect and increase of lift for the downstream cylinder as was found by Bushnell for the 30° orientation (when T/D<2.5) , but only for KC>40. Below this amplitude the lift was diminished compared with the isolated-cylinder case. He also found no increase in the lift force at 60° and 90° as the gaps were reduced, even at the smallest spacings. Saparkaya concluded that the cylinder forces gradually approach their isolated-cylinder values as the flow amplitude becomes comparable to or smaller than the cylinder spacings.

In the above studies of cylinder groups in oscillatory flow , only flow force acting on the cylinders were discussed, no flow visualization and velocity fieldmeasurement have been undertaken. Williamson [4] thought flow visualization and simultaneous force measurements could provide the basis for an investigation into the cylinder pair. Williamson also thought that this investigation would reveal the existence of the synchronization of vortex shedding between the cylinders. His study of the vortex motions and fluid forces on cylinders comprised simultaneous flow visualization and force measurements only for β = 255 (our experiments are for β=500) and 0< T/D < 5.0 and 0< KC<55. He found that not only vortex shedding but also induced forces were synchronized in-phase or in antiphase between the cylinders. In-phase synchronization in a complete cylinder array could cause large total lift force oscillations comparable to the total in-line force, but a higher frequency. Williamson divided the flow patterns for a pair cylinders into tow regimes :

1) 7< KC< 15 , named the Transverse-street/single-pair regime.For two cylinders in-line, vortex shedding is found to be predominatly in-phase.
2) KC > 15, named the Flow interference regime. For two cylinders in-line,vortex shedding is synochronized in-phase with great repeatability . When T/D is in the range 3.0-5.0, a double pair wake for each cylinder tends to form in-phase between the cylinders but with less repeatability.

Williamson gave a skeleton map for the first regime, it is shown in Fig 5.3.

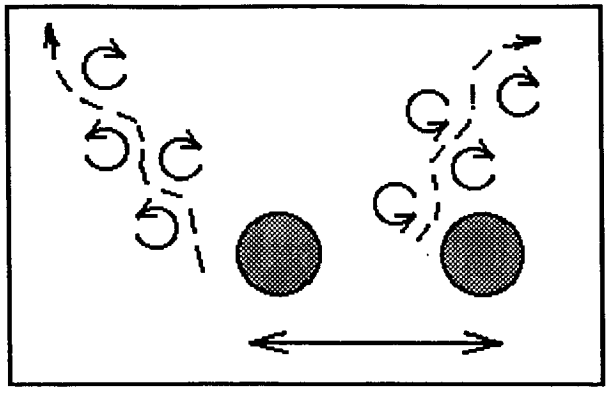

Fig 5.3 A flow pattern of a pair cylinders : Transverse street
$7 < KC < 15$, $T/D < 1.5$

This kind of transverse street seems to be related to the particular value of β or Reynolds number used by Williamson. In section 4.4.1 of chapter 4 we have disccussed the topic of a long transverse street . Because the Reynolds numbers and the relative widths of the tank are different between those used by Williamson and mine, no such long transverse street of vortex has been seen in my experiments.

Flow visualization cannot determine the quantitative strength of the vortices. The discussion about force features on the two cylinder combination needs to find more details. In this thesis the research into the two cylinder case involves the study of oscillatory flows, with a β value of 500, past two cylinders arranged in tandem. Lift and inline forces are measured, at the same time, flow velocity fields are obtained. Consequently, from these velocity fields , the vorticity and the strength of the vortices are calculated. When oscillatory flow reverses its direction ,the two cylinders change their relative position to the flow direction in each half period of the oscillatory flow, so forces tests are only done for one cylinder . The spacing between the two cylinders is set to T/D= 1.5 and T/D=2.0 and the KC numbers used are 5, 8, and 10. These parameters correspond to the first regime of the Williamson's two flow patterns regimes.

5.2 The Results of the Force Measurement

The strengths of the forces experienced by the two tandemly arranged cylinders in oscillatory flow is somewhat difference from that experienced by the single cylinder in oscillatory flow. In addition, the strengths of the forces change with the spacing

between the two tandem cylinders.

5.2.1 Strengths of the forces

The strength of the inline forces are shown in Fig 5.4. All the force strengths in the chart are statistically averaged over all of the experimental results.

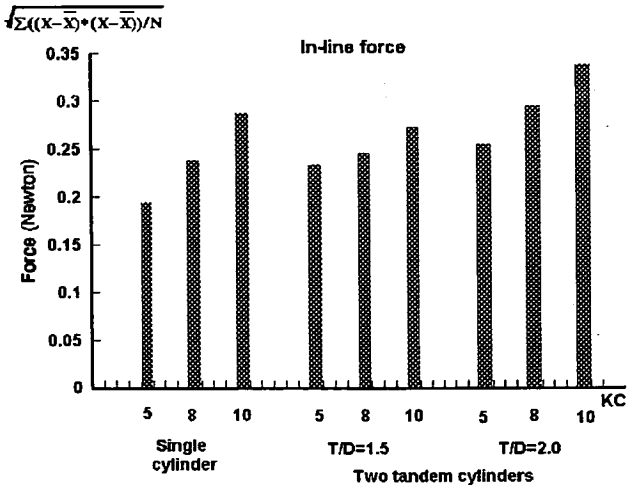

Fig 5.4 The strength of In-line forces

For the two tandem cylinders cases the in-line force strengths are larger than that of single cylinder case, except when T/D =1.5 and KC =10. Also for two cylinders themselves, the inline forces are larger at T/D =2.0 than at T/D = 1.5.

The in-line force includes three parts (See Chapter 3, section 3.6.1.1) : inertia force, pressure drag force and friction drag force. The inertia force is due to the acceleration or the deceleration of the fluid . The pressure drag is associated with the distribution of the velocity of the flow around the cylinder and is proportional to V^2 of the flow. It is largely the difference between the high pressure in the front stagnation region and the low pressure in the rear separated region. The friction drag is the integrated shear stress. Considering other conditions have not been changed and only one cylinder has been added downstream of the first cylinder, the pressure drag force will be the only component of the in-line force which is affected. The other two force components should be the same as they were for the single cylinder case. The pressure in the front stagnation region should not change significantly and the main changes in the pressure are at the rear gap region between the two tandem cylinders. This is caused by the interference between the two cylinders. If the flow doesn't remain in the rear region

but goes through the gap fast, this will cause a lower pressure in the gap area than in the area immediately behind the single cylinder. This phenomenon can be seen in Fig 5.5 (a) and (b)

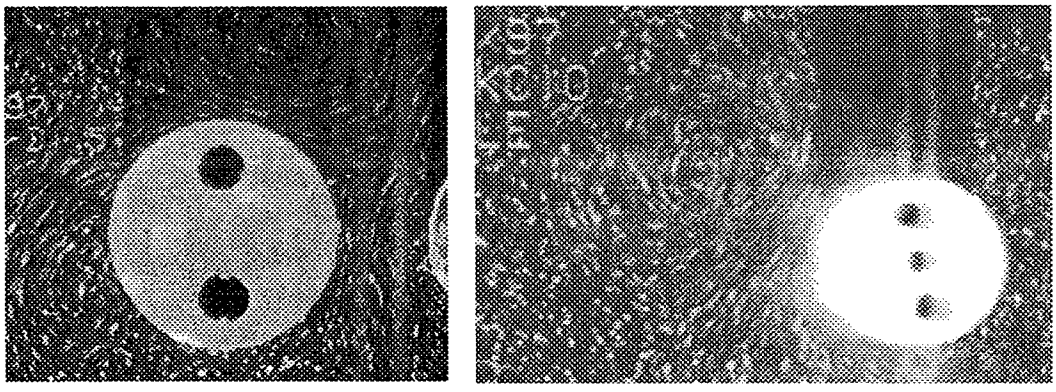

←← Flow direction ←←← Flow direction

(a) Two tandem cylinders (b) Single cylinder

Fig 5.5 Two frames from video recordings

In Fig5.5 the flows are from right to left. From Fig 5.5 (a) it can be seen that the flow in the gap between the two cylinders is almost in the vertical direction. It is different indeed from the wake of the single cylinder (b). At the same KC number or the same velocity, the vertical fast flow in the gap will cause a larger inline force than that experienced by the single cylinder. A wider gap will causes more flux in the gap than in thinner gap, then there will be a lower pressure in the gap and a larger difference in pressure along the horizontal axis through the two cylinder centres. So gap ratio 2.0 will give a larger inline force than that at the gap ratio 1.5.

The strength of the lift force is shown in Fig 5.6.

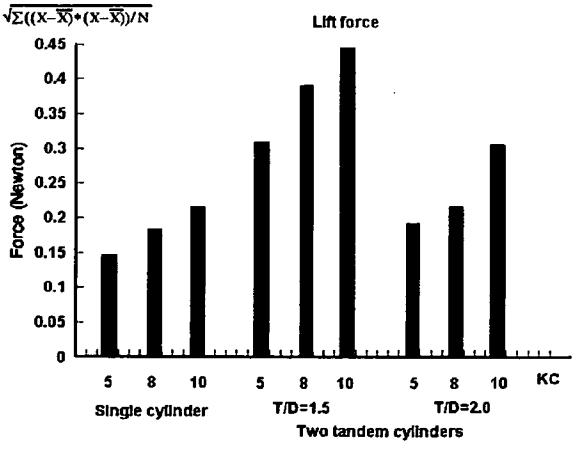

Fig 5.6 The strength of lift force

The strength of the lift force in the two tandem cylinder case is larger than that of the single cylinder case. When the gap between two cylinders decreases, the lift force increases further. The lift force is caused by the difference in the pressure between the top and the bottom of the cylinder because of the vortex shedding. Its direction is normal to the oscillatory flow direction (See Chapter 3, section 3.6.1.2) . This difference in pressure between the top and the bottom of the cylinder can be due to different flow velocities at the top and the bottom of the cylinder; a high flow velocity will result in a low pressure and a low flow velocity will result in a high pressure. When a downstream cylinder exists, it changes the flow patterns on the top and the bottom of the upstream cylinder from the single cylinder. The interference changes the lift force and has been shown in Fig 5.7. Using Fig 5.5, we can make a position comparison between two vortices : the vortex in the wake of the single cylinder(b) and the vortex in the wake of the upstream cylinder(the right one) of the two cylinder case (a) . To compare the two vortices and to find their relative positions to the cylinders then consider Fig 5.7 which gives a skeleton :

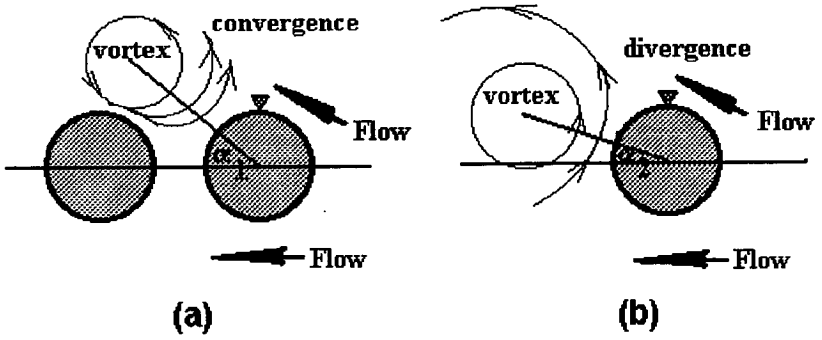

Fig 5.7 Flow skeletons of two tandem cylinders and single cylinder

In the single cylinder case, the vortex in the wake meets with an obstruction. Its position is near the direction of the main flow and position is represented by α_2. For two cylinders, the vortex position is higher than that in single cylinder wake ($\alpha_1 > \alpha_2$).This is caused by block of the downstream cylinder. The block will force a flow convergence at the top of the upstream cylinder (the triangle pointed area). More of the flow stays at the top area and a higher pressure will be generated here. At the bottom of the cylinder, flow past the cylinder at almost same speed with the flow on the bottom of the single cylinder. There is no vortex there because the vortex shedding

is asymmetrical. So the pressures at the bottom have no significant difference for a single cylinder and two cylinders cases. Then the lift force will be larger for the two cylinders case than it in single cylinder case. Following this view point, when the gap between the two tandem cylinders is smaller, the vortex is nearer the top of the upstream cylinder and α will be larger. This process will generate a stronger convergence at the top which leads to a greater pressure difference or a larger lift force such as Fig 5.6. That is why the lift force is bigger for smaller T/D and it is stronger on two tandem cylinders than on a single cylinder when KC numbers are the same.

Fig 5.8 showed some comparisons of the in-line force with the lift force for different gaps between the two cylinders. At the T/D=2.0, the inline forces are stronger than the lift forces (fig 5.8(a)) . To compare with the single cylinder cases in Fig 5.9, the strengths of in-line forces are also larger than the strengths of the lift forces. When the gap between two cylinders is shrunk, the strengths of the lift forces increase and they are stronger than the inline forces at T/D=1.5, see fig 5.8(b). This phenomenon is different from the single cylinder case. The reason for the lift forces being larger than the in-line forces remains unclear.

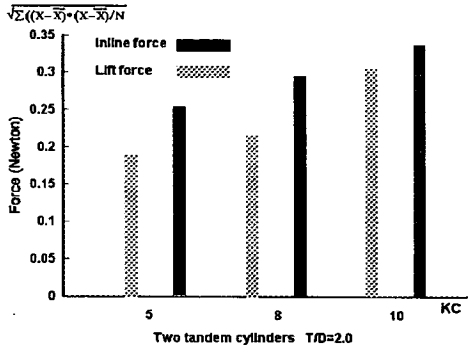

(a) Spacing T/D=2.0

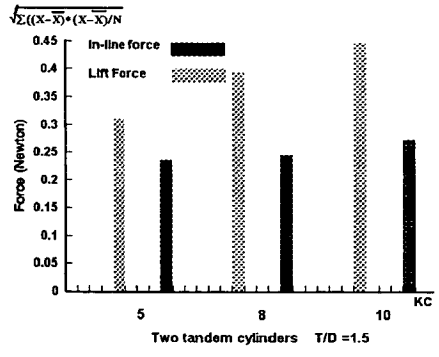

(b) Spacing T/D=1.5

Fig 5.8 The strengths of inline force and lift force

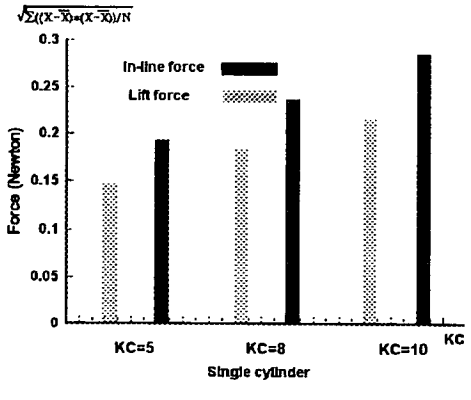

Fig 5.9 The strengths of inline force and lift force of Single cylinder

5.2.2 Frequency of the forces

The main frequencies of the inline forces are the same as that of the oscillatory flow. See Fig 5.10 (a) (b) (c) for the gap of T/D= 2.0 (left side) and Fig 5.11 (a) (b) (c) for a smaller gap of T/D = 1.5 (right side). These features are the same as for the single cylinder, see Fig 4.9 . For the two cylinders, the frequencies of the inline forces have smaller power components of the force power spectrum at a shorter gap T/D = 1.5 than they have at gap T/D=2.0 .

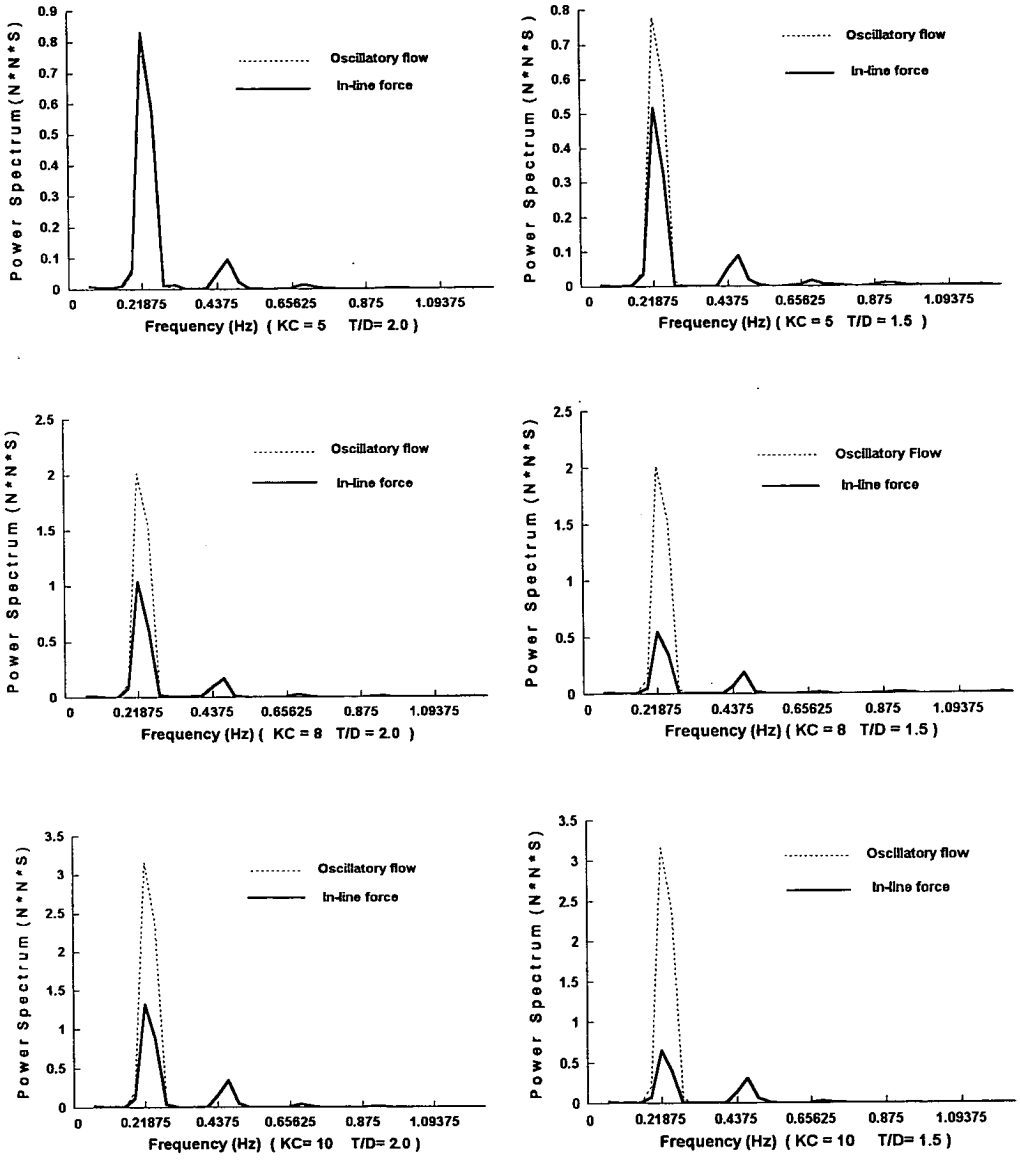

Fig 5.10 (left column) Frequencies of In-line force and oscillatory flow at T/D = 2.0

Fig 5.11(right column) Frequencies of In-line force and oscillatory flow at T/D = 1.5

The frequencies of the lift force are shown in Fig 5.12 (a) (b) (c) for the gap T/D =2.0 on the left side and Fig 5.13 (a) (b) (c) for the gap T/D= 1.5 on the right side. The arrows point at the frequency position of the oscillatory flow.

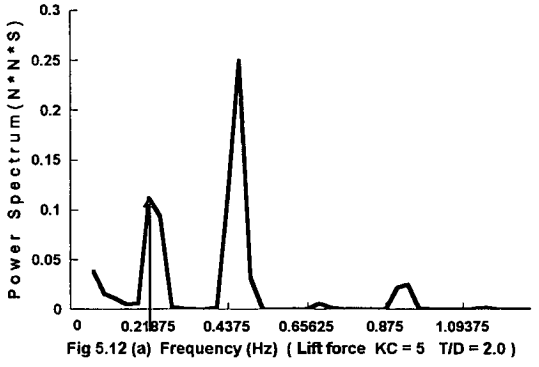

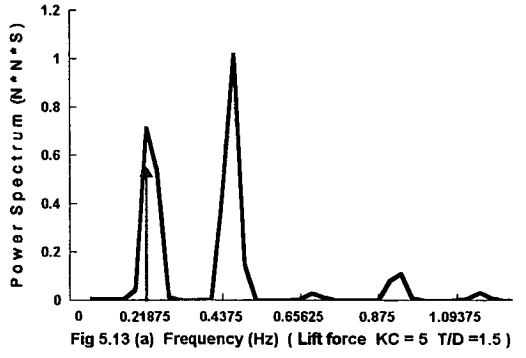

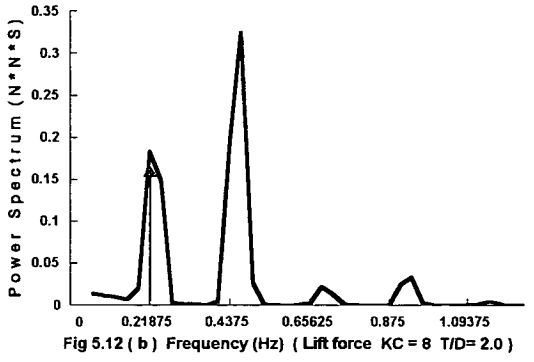

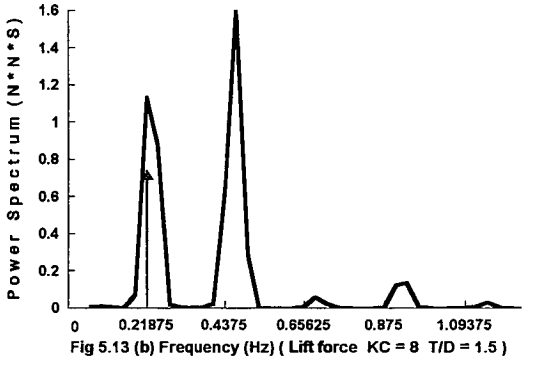

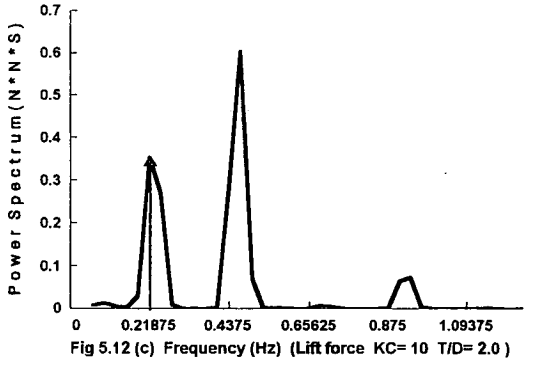

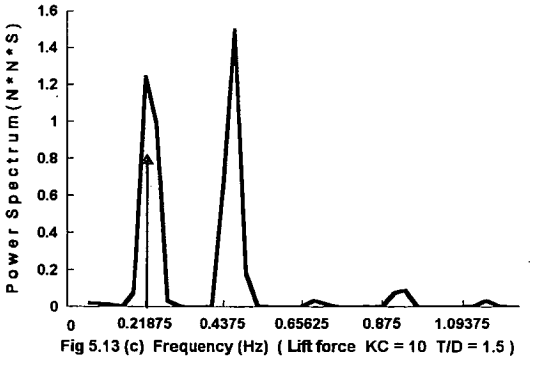

Fig 5.12 Frequencies of lift force at T/D = 2.0

Fig 5.13 Frequencies of lift force at T/D = 1.5

The main frequency of the lift force is the second harmonic of the oscillatory flow frequency(an arrow points at the frequency position of the oscillatory flow) and it can be found for different KC numbers and different gaps. This feature is different from that of single cylinder except for the case at KC =10 and T/D = 1.5 . This situation is

almost the same as the single cylinder at KC =10 , see Fig 4.10 (c). Its main feature is that the first harmonic component of power spectrum has a similar height to the second harmonic component. It is difficult to say which harmonic component is larger, because the first harmonic has a slightly lower peak but wider spectrum area and while the second harmonic has a higher peak but thinner spectrum area.

In the single cylinder case the lift force's main frequencies are the first harmonic at small KC numbers, such as KC=5 and KC = 8 see Fig 4.9 (a) (b), however, the two tandem cylinders' main fequencies are all the second harmonics. This is similar to the description which Williamson has given ' a higher frequency '. The interference of two cylinders has also been reflected by their frequency features.

5.3 The Flow Patterns and Their Velocity Fields

5.3.1 Vortex shedding patterns

The vortex patterns were recorded by video camera. The vortex patterns can be divided into several groups according to the KC number and the distance between the two cylinders:

1.) KC= 10 , T/D= 1.5

During the first half period , the oscillatory flow is from the left to the right (the cylinders move from the right to the left side in the water tank) .

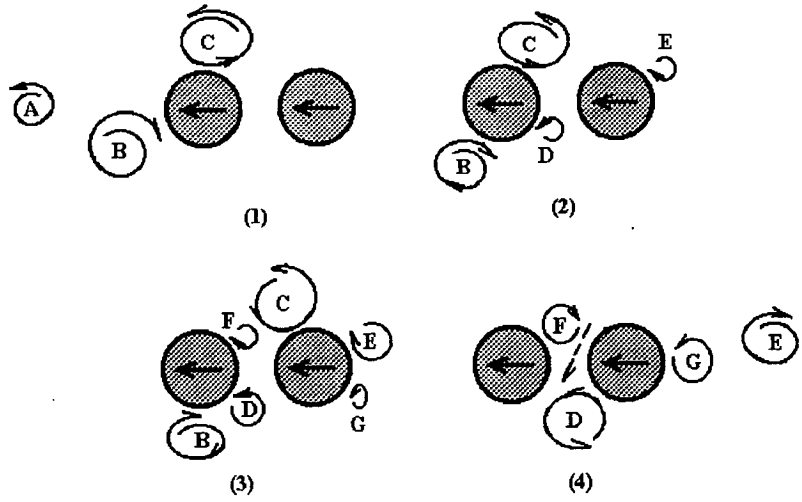

Fig 5.14 Vortex pattern (A) KC=10 T/D=1.5

See (1) in Fig 5.14 , the cylinders start to move to the left. Vortices A B and C survived from the last half period. In (2) as the two cylinders move, two new vortices are generated against the back of the two cylinders , they are D and E. Vortex A has moved away from the two cylinder model. With the cylinders continuing to move forward(3), the vortices B and C passed over the two cylinders and were destroyed. The vortices D and E increased in size and the other two new vortices F and G are generated behind vortices D and E. So, in a half period, there are a pair of new vortices shed for each cylinder. That should be a reason for the lift force to have a second harmonic of the oscillatory flow as its main frequency.

In second half period, the vortex pattern isn't totally the same as the first half period, see Fig 5.15 .

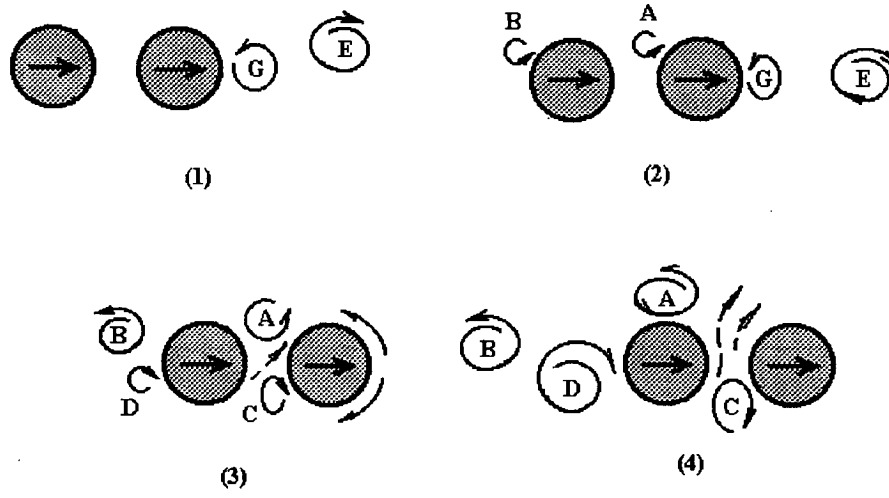

Fig 5.15 Vortex pattern (B) KC=10 T/D=1.5

In the second half period, vortices G and E remain from the first half period (1).Vortices A and B are newly generated after the two cylinders reverse their moving direction and starting to move from left to right (2). Vortex G, at the front of the upstream cylinder, becomes elliptical before vanishing as the cylinders move further to the right. Vortices D and C are formed behind vortices A and B (3). In (3) and (4) a fast flow through the gap is observed. In the second half period there are also two vortices shed from each cylinder.

The main features of the flow patterns are the same in the first half period and the second half period but there are some obvious differences. They are shown in

pattern(A) and pattern (B) , such as the positions of the vortices and flow behaviour in the gap. The vortex shedding normally causes a sudden change of the lift force, so two newly vortices shedding in an oscillatory period can cause the main frequency of the lift force to be the second harmonic of that of the oscillatory flow.

From Fig 5.14 and Fig 5.15, a basic feature of the vortex pattern can be found: it is the width of the wake. At the outside of the combination of the two tandem cylinders, the shedded vortex has no obstruction. Subsequent vortices followed the main flow direction one after another. The width of the wake is similar to that of the single cylinder. But in the gap between the two cylinders, the vortices are effected by the other cylinder and are diverted round it. This causes a wider wake between the two cylinders. For two tandem cylinders their vortex pattern outline can be simply represented by a diamond shape, see Fig 5.16

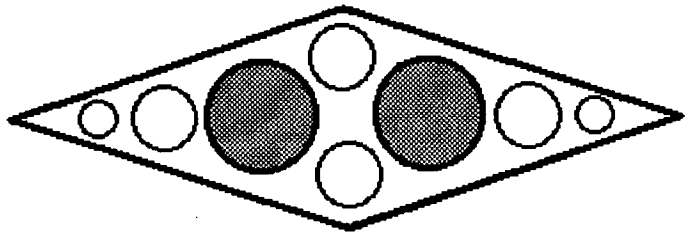

Fig 5.16 A basic wake shape of the two tandem cylinders

So far we have not found the vortex pattern which Williamson mentioned and named " the transverse street ``.

2) KC= 10 , T/D= 2.0

At T/D=2.0, the gap between two cylinders is wider , so shed vortices have a larger space to occupy in the gap between the two cylinders. In this case the vortices activities out of the two cylinder structure are the same as the situations for T/D=1.5. In the gap area, the positions of the generated vortices are nearer the horizontal axis so they give more influence on the in-line force. Before they move over the downstream cylinder, they have been destroyed, see Fig 5.17 . The vortex patterns in Fig 5.17 are only given the area between two cylinders.

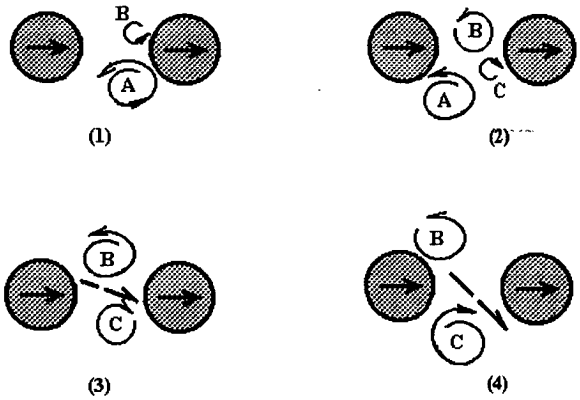

Fig 5.17 Vortex pattern (C) KC=10 T/D=2.0

Fig 5.17 shows a second half period . (1) Vortex A was remained from the last half period. Vortex B is a newly shed vortex from the upstream cylinder . (2)With the cylinders moving forwards to the right side, vortex A moved closer to the downstream cylinder and vortex B increased in its size and moved away from the upstream cylinder. Meantime another new vortex is shed, it is vortex C. Then in (3), vortex A has been destroyed during its interaction with the downstream cylinder. Vortices B and C increased their sizes and moved nearer the downstream cylinder. Unlike outside the two tandem cylinder combination, the vortices in the gap area were almost side by side. (4) Between the two vortices, there was a relatively strong flow from the top to the bottom in the gap.The flow has a smaller angle with the horizontal axis compared with the flow in the thinner gap of T/D=1.5 . In the half period there were two new vortices shedded, so it resulted in the main frequency of the lift force being the second harmonic. The vortex pattern in the other half period was similar to this one.

3) KC=8 , T/D=1.5

When the KC number decreased, the velocity of the oscillatory flow was weaker and the size of the vortices was smaller. So the vortices can go nearer each other in the gap area, see Fig 5.18 .representing a half period.

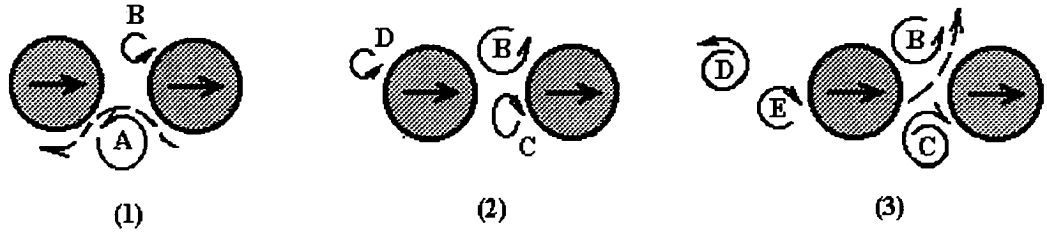

Fig 5.18 Vortex pattern (D) KC=8 T/D=1.5

In Fig 5.18 (1) Vortex A came from the last half period of oscillatory motion. Vortex B was a new one generated after the cylinders changed their moving direction.(2) Another new vortex, C, shed from the upstream cylinder , and vortex A was destroyed before it turned over the downstream cylinder. (3)When vortices B and C increased in size, an observable flow, between the two vortices, was formed in the gap. The behaviour of vortex D and E were similar to those in vortex patterns (A) and (B).

4) KC =8 , T/D = 2.0

In this pattern, the gap was wider and the flow between the two vortices has a curved shape because the two vortices have more space to approach each other and move near the horizontal axis. This can be seen in Fig 5.19 over half a period.

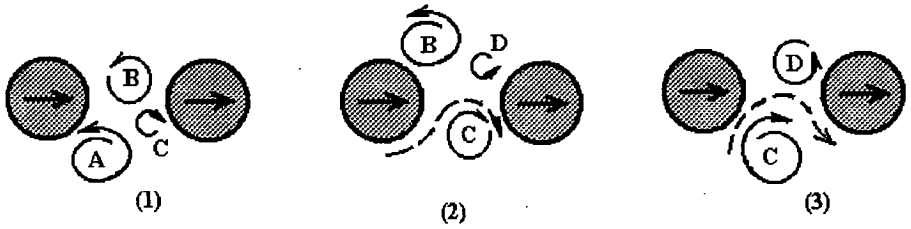

Fig 5.19 Vortex pattern (E) KC=8 T/D=2.0

At KC=8 , the vortices have smaller size than at KC =10, and the energy required to maintain them was also smaller, so they were destroyed before they moved over the downstream cylinder and they have a shorter life cycle than that at KC of 10. Independent of the gap width , there were two vortices shedding from each cylinder and in a half period. So the lift forces have the same main frequency.

5) KC=5 , T/D=1.5

At this KC number, the vortices size decreased further, and they decayed quicker, their life cycles were not longer than a half period of the oscillatory flow. see Fig 5.20

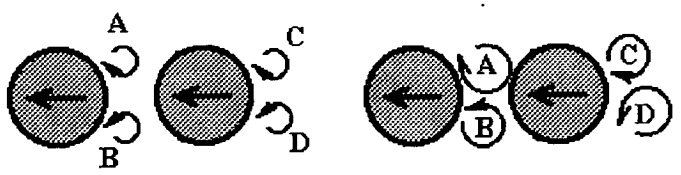

(1) The first half period (2)

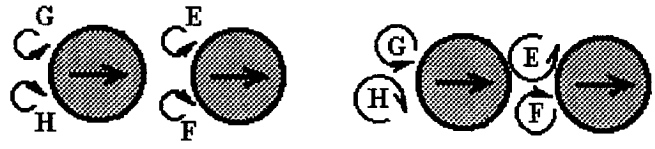

(1) **The second half period** (2)

Fig 5.20 Vortex pattern (F) KC=5 T/D=1.5

When the two cylinders started to change their moving direction, the small vortices were destroyed by the flow running in the opposite direction. No vortex produced in one half period was visible in the next half period. When vortices were forming , their sizes looked the same and their relative positions to the cylinder looked symmetrical. Then their differences in size and position are getting larger and can be observed by video recording, such as in Fig 5.20 (2) . It should be one of the reasons for lift force creation.

For the vortices with different sizes and positions, their vortex strengths should be different and will give contribution to the lift force strengths. Because the limitation of PIV for the flow around the cylinder at small KC number , we have not obtained satisfactory PIV vector map and couldn't calculate vortex strength at KC=5. But these could be the reasons why the main component of lift force power spectrum in the two cylinder case was different from that of the single cylinder case and was the second harmonic .

6) KC=5 , T/D=2.0

When the gap between two cylinders was wider, the flow velocity at KC=5 was too slow to move away from the gap. So a stagnation point is formed in the gap and can be found by obsvering the seeding distribution from the video recordings . In the gap there were more seeding particles than in wake of the dowstream cylinder. This stagnation point will cause a pressure difference between the front and the back of each cylinder. The pressure difference was different from the single cylinder case, see Fig 5.21. This could cause a stronger inline force in the two cylinder case than that in the single cylinder case, as shown in Fig 5.4 .

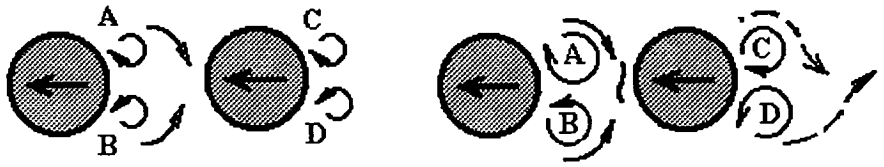

(1) **The first half period** (2)

Fig 5.21(a) Vortex pattern (G) KC=5 T/D=2.0 (the first half period)

(1) **The second half period** (2)

Fig 5.21 (b) Vortex pattern (G) KC=5 T/D=2.0 (the second half period)

From the above vortex patterns at different KC numbers, some features can be summarized.

a) There are more vortices present at larger KC numbers. This is because the vortices last for longer. When the new vortices are generated, the old ones are still present, thus there are more vortices at any time.

b) The position of vortices being destroyed is nearer the horizontal axis when the KC number decreases. At KC = 10, the vortices can slide over the downstream cylinder then be destroyed; at KC = 8 ,the vortices are destroyed before they go up on the top (or down to the bottom) of the downstream cylinder; at KC = 5, the vortices are destroyed as they go along the surface of the downstream cylinder. In fact the obstruction of dowstream cylinder can destroy the vortices because the vortices almost touch the downstream cylinder when the flow changed its direction. The vortices being destroyed is caused by the main flow direction changing and the obstruction of the downstream cylinder.

c) The flow in the gap, its stagnation is getting more obvious as the KC number decreases. At a KC number of 10, the flow passes the gap fast and its path is almost straight perpendicular to the oscillatory flow. At KC = 8, the flow passes the gap as a curve and matches the vortices outline, its path is more flat. At KC = 5 the flow can stays in the gap to form a short stagnation .

d) The size of the vortices increases with KC number increasing. The basic flow shape for two tandem cylinders is a diamond shape. The length of the wake outside of the two tandem cylinders increases with KC.

e) Because there are two vortices shedding from each cylinder in any one period of oscillatory flow , the main frequency of the lift force is the second harmonic for any KC number which is chosen in experiments here (5, 8, 10). At KC =5 the flow velocity is small and it causes the stagnant area in the gap between two cylinders. It results in the inline force strength stronger than that of the single cylinder.

5.3.2 The velocity fields at the special phases

Some velocity fields from PIV exprimental results have been obtained as follows. They are at some prefixed phases of oscillation given by $1/4\pi$, $1/2\pi$, π, $2/3\pi$ and 2π. Fig 5.22 shows a velocity field at KC =10, T/D=1.5 and phase at π. The relative motion of the oscillatory flow is from left to right. (The two cylinders are moving from the right side to the left side of the water tank).

In the vector map , three vortices can be seen. They have been marked by letters D, F and G . These match the vortices in vortex pattern (A (4)) (Fig 5.14) and have the same labels. As well as the vortices, it is also clear that a strong flow goes through the gap between two cylinders from the top to the bottom.

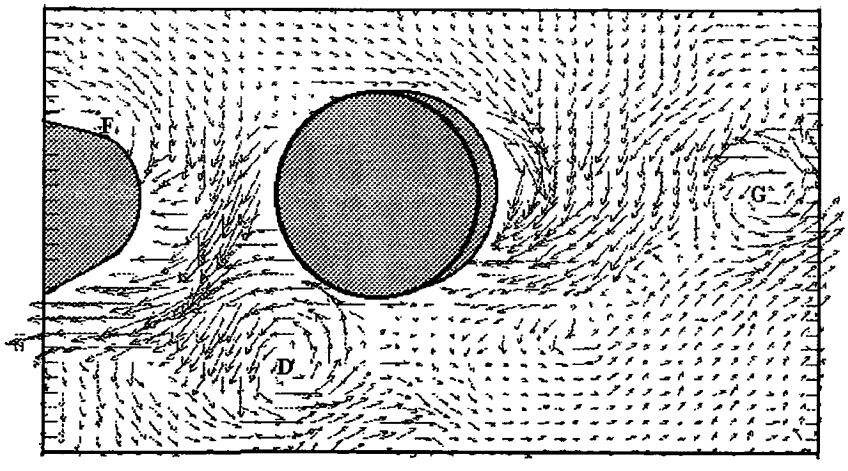

$\rightarrow\rightarrow\rightarrow\rightarrow\rightarrow\rightarrow\rightarrow\rightarrow$ the flow direction

Fig5.22 Velocity field , KC=10 T/D = 1.5 Phase=π

The Fig 5.23 is the velocity field at KC =8 , T/D=1.5 . Phase= 2π . The two cylinders are moving from left to right .

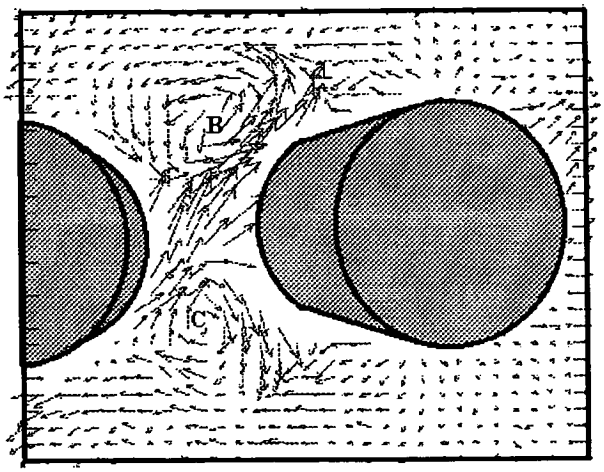

→→→→→→→→→ the flow direction

Fig 5.23 Velocity field, KC=8 , T/D =1.5 , Phase= 2π

There are two vortices in the vector map which compare with the vortex pattern (D(3)) (Fig 5.18) . Between vortices B and C and an obvious flow is clearly shown and it goes up from vortex C to Vortex B.

To compare Fig 5.23 with Fig 5.22, it can be seen that the vortex size is smaller at KC =8 than that at KC=10 in the gap area. Because the gap widths are the same for the two maps , the vortices in Fig 5.23 can stay between the two cylinders, but the vortices in Fig 5.22 have the relative positions further from the horizontal axis through the two cylinder centres, and their relative sizes look also larger than those in Fig 5.23.

Fig 5.24 is a vector map at KC = 10 , T/D= 2.0 , phase at 2π . The cylinders are moving from left to right . The vortices B and C match the vortices in vortex pattern (C (3) (4)) (Fig 5.17) and have the same labels. A strong flow between vortices B and C is very clear.

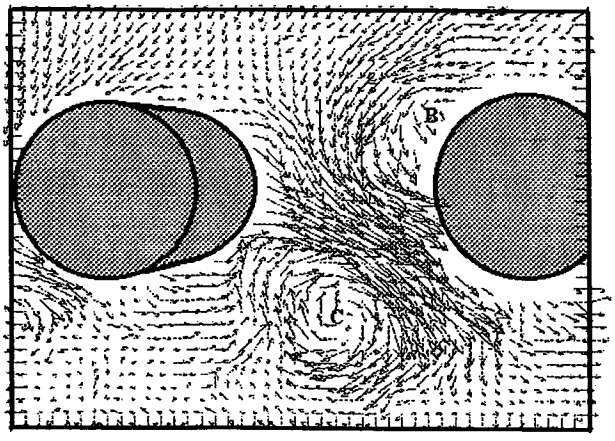

←←←←←←←←← the flow direction

Fig 5.24 Velocity field, KC=10 , T/D =2.0 , Phase= 2π

Fig 5.25 is a vector map at KC = 8 , T/D= 2.0 , phase at 2π . The cylinders are moving from left to right . The vortices C and D match the vortices in vortex pattern (D (4)) (Fig 5.19) and the flow between vortices C and B is weaker than at KC=10 at the same gap width and it is curved and looks like the outline of vortex C.

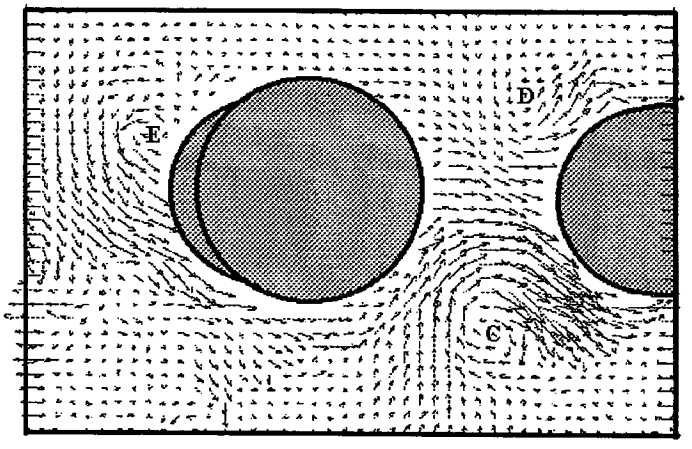

←←←←←←←←← the flow direction

Fig 5.25 Velocity field, KC=8 , T/D =2.0 , Phase= 2π

Comparing Fig 5.24 , Fig 5.25, Fig 5.17 and Fig 5.19 it can be found that at bigger KC number , such as KC=10, the flow through the gap between two cylinders is much stronger than that at a small KC number , KC=8. The vortex size also increases with KC number. So at larger KC number the lift force and inline forces are stronger. For both KC =8 and KC=10, the vortex shedding is one after another. This is different from the vortex shedding at KC=5. In Fig 5.20 and 5.21 , the vortices shedding looks symmetrical to the horizontal axis through the two cylinder centres.

When the KC number is 5 , the oscillatory flow has a small velocity . During the oscillatory flow passes the cylinder , small vortices are produced . The PIV analysis isn't good enough to show the small vortices on the PIV vector map. The reason for this has been metioned in the section 4.4.2 of Chapter 4. So no vector map at KC =5 is shown here.

5.3.3 Some vorticity features

From those vector maps the vorticity of the vortices can be calculated . So the quantitative information of the vortices can be obtained. This is shown below.

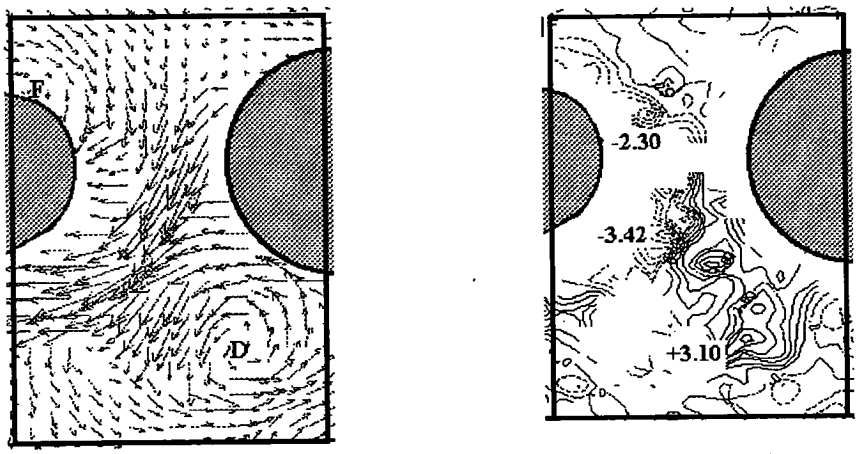

Fig 5.26 Vortices and their Vorticity at KC=10 T/D=1.5

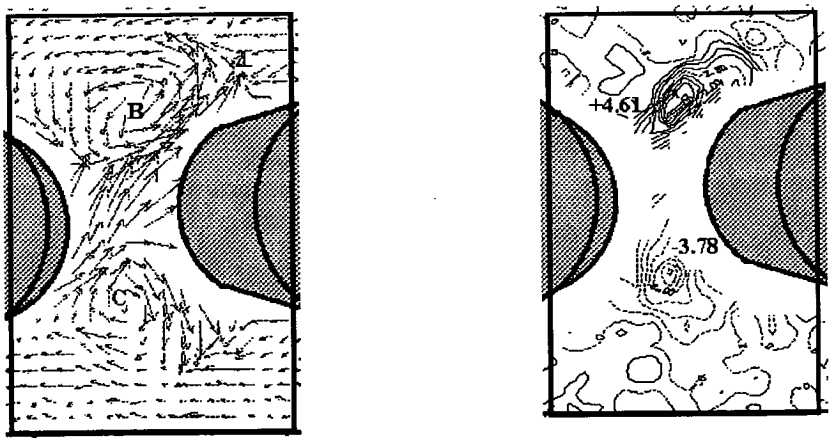

Fig 5.27 Vortices and their Vorticity at KC=8 T/D=1.5

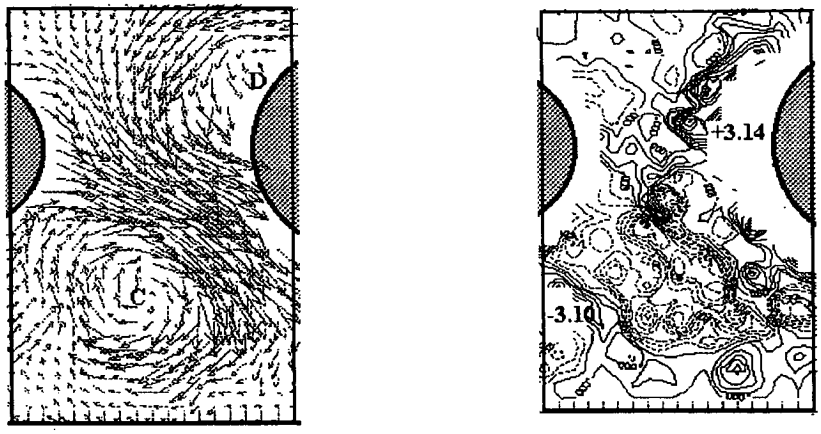

Fig 5.28 Vortices and their Vorticity at KC=8 T/D=2.0

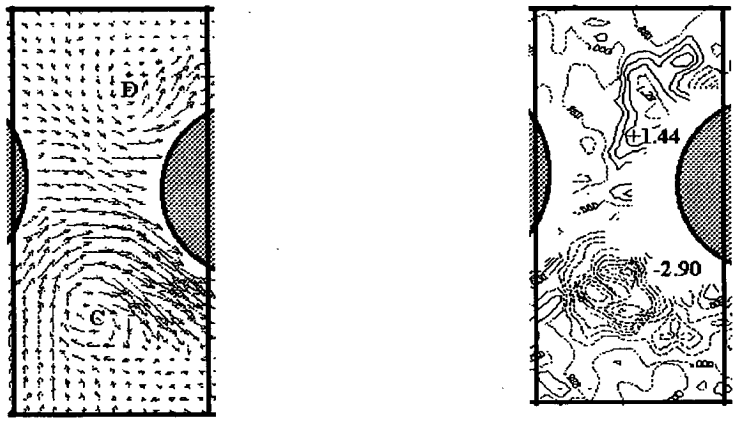

Fig 5.29 Vortices and their Vorticity at KC=8 T/D=2.0

The vorticities in the gap area between the two cylinders have been shown in above Fig 5.26, Fig 5.27, Fig 5.28 and Fig 5.29. The strongest positive and negative vorticity values at the vortex centres have been marked . The difference in the vorticity between the positive centre and the negative centre are respectively :

KC=10 , T/D= 1.5 $\Delta\omega = \omega(+) - \omega(-) = 3.10 - (-3.42) = 6.52$

KC=10 , T/D= 2.0 $\Delta\omega = \omega(+) - \omega(-) = 3.14 - (-3.10) = 6.24$

KC= 8, T/D= 1.5 $\Delta\omega = \omega(+) - \omega(-) = 4.61 - (-3.78) = 8.39$

KC= 8, T/D= 2.0 $\Delta\omega = \omega(+) - \omega(-) = 1.44 - (-2.90) = 4.34$

At the same KC , a thinner gap has a larger $\Delta\omega$. This could be due to the jet caused by the thinner gap. A jet has big velocity gradient, and will give larger values of vorticity . Since vorticity consists of the velocity gradient and curvature of the flow(the detail is given in the section 2.6.1, chapter 2) , so it will be larger in thinner gap case. Fig 5.6 has shown the lift force is stronger at a thinner gap, the larger the difference in the

vorticity centre values will mean that the difference of the two vortices is larger, then it will result in a stronger lift force.

At the same size of the gap, a big KC number should give a bigger $\Delta\omega$. But this only happened at the gap=2.0 . So we have to calculate the vortex strength and find if a large KC number will make a large vortex.

5.3.4 Vortex strength

The vortex strength were calculated for four cases in section 5.3.3 and every vortex was low one in the middle area between two cylinders . The maximum vorticity of every vortex has been shown in Fig 5.30 and the thick lines in Fig 5.30 were the contours with value of 1/10 maximum vorticity, or called the boundaries of the vortices. Because of the background vorticity, the boundary line isn't a closed line.The vortex area is decided by the boundary lines and vortex shape.

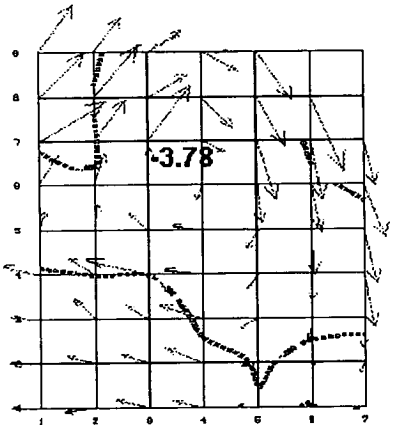

Fig 5.30 (a) KC=8 T/D=1.5 (2π)

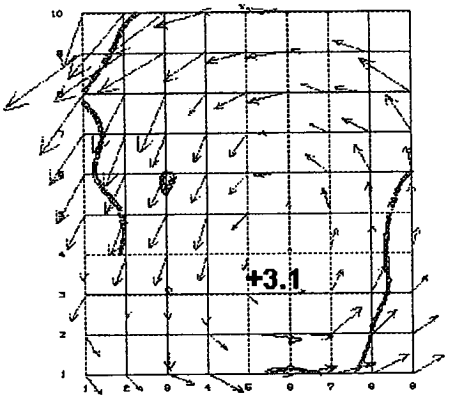

Fig5.30 (b) KC=10 T/D=1.5 (π)

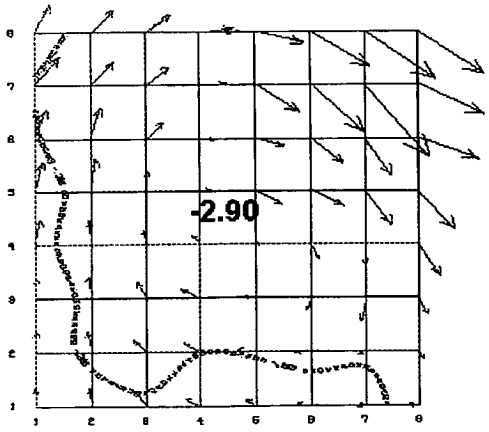

Fig 5.30 (c) KC=8 T/D=2.0 (2π)

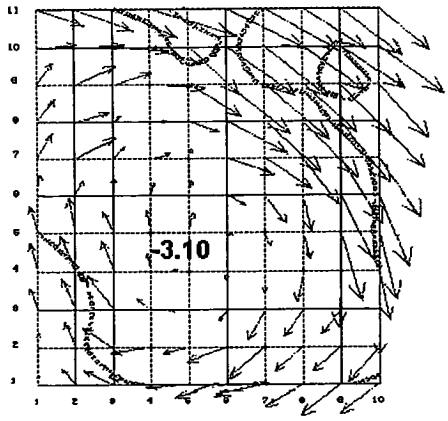

Fig 5.30 (d) KC=10 T/D=2.0 (2π)

The vorticity inside of the boundary was integrated (summed) and the total strength of the vortex and its average strength were obtained. The results were listed in Table 5.1.

T/D ratio	The vortex strength (KC=8)		The vortex strength (KC=10)	
	Total	Average	Total	Average
1.5	49.66 (39points) - vortex	1.27	75.24 (57points) + vortex	1.32
2.0	63.82 (49points) - vortex	1.30	116.96 (81points) - vortex	1.44

Table 5.1 The vortex strength at different KC numbers

In Table 5.1 it can be found that when the gap ratio was fixed, the total vortex strength increased with KC number (75.24 > 49.66 at T/D=1.5 and 116.96 > 63.82 at T/D=2.0). A stronger vortex shedding caused a larger lift force on the cylinder, so the lift force strength also increased with KC number. This was the same as the single cylinder cases , see Table 4.1 in chapter 4. But Table 5.1 also showed the vortex total strength was stronger at a larger gap between two cylinders under the same KC number (63.82 > 49.66 at KC=8 and 116.96 >75.24 at KC=10). It looked that a strong vortex will cause a large in-line force for a wider gap at the same KC number. In a wider gap, the vortex was closer to the horizontal axis of the two cylinders, so it gave more influence on the in-line force than on the lift force as is shown in Fig 5.7. A thinner gap can lift up the relative position of the vortex and caused more convergence on the top of the cylinder , then resulted in a larger influence on the vertical axis of the cylinder or on the lift force.

The average vortex strength showed a feature the same as the total vortex strength, but the value of the difference was small. For a fixed gap the average vortex strength increased with KC number, it was the same as lift force increasing with KC number. For the different gap a stronger vortex could cause a larger inline force at the same KC number.

5.4 The Results of Numerical Modelling

The numerical simulation has been done for the KC numbers 10, 8 and 5 and for the

gap 1.5 and 2.0 . The basic results are comparable with the experimental results.

5.4.1 Frequency of the force coefficients

The numerical simulation can get the forces coefficients for the two cylinders respectively at the same time and additional equipment is not required , so this is an advantage of the numerical simulation. The main frequency of the inline force coefficient has been simulated very well, the frequency is the same as the harmonic with the oscillatory flow. The power spectrum of the lift force coefficient are shown as follows :

Fig 5.31 showed the frequencies of two cylinders at different KC numbers , their gap was T/D =1.5. Fig 5.32 showed the frequencies with a larger gap of T/D=2.0 . In these Figs, the left columns are frequencies of the first cylinder which is at the left side in the model mesh. And the right columns are the frequencies of the second cylinder at the right side in the model mesh, see Fig 3.10 in chapter 3.

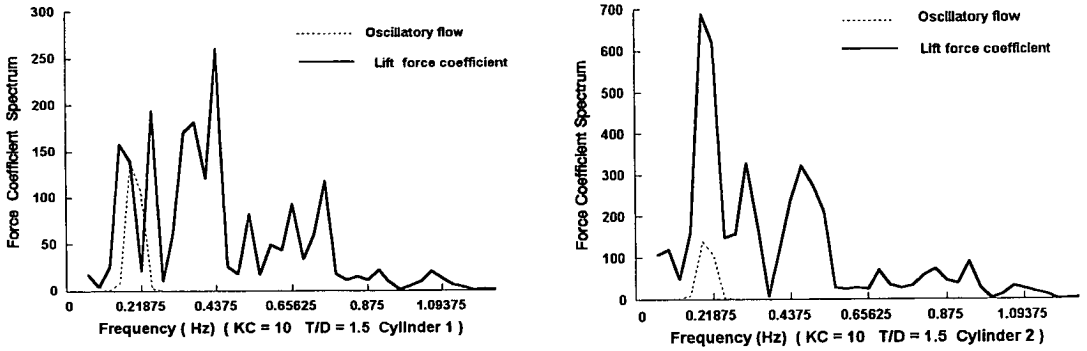

(a) (b)

Fig 5.31(1) Lift force coefficients of two cylinders with the gap T/D=1.5

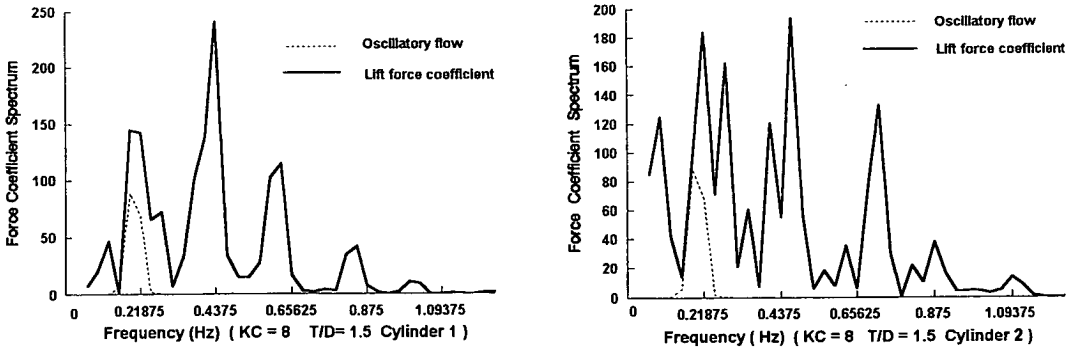

(c) (d)

Fig 5.31(2) Lift force coefficients of two cylinders with the gap T/D=1.5

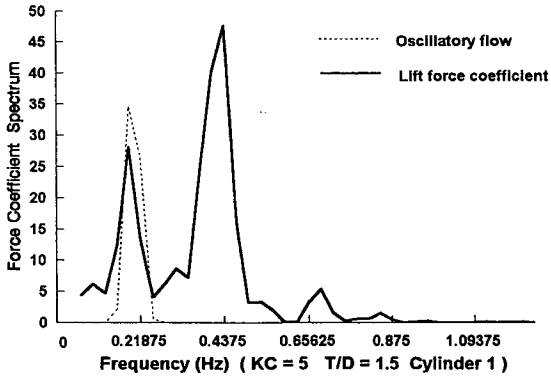

(e)

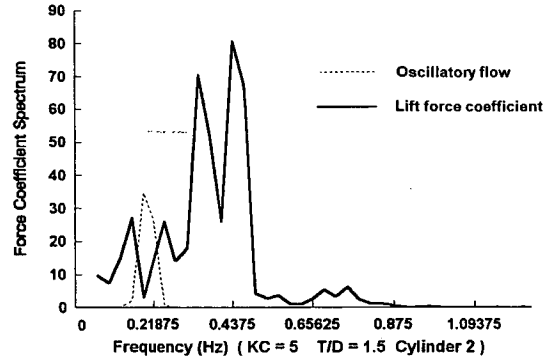

(f)

Fig 5.31(3) Lift force coefficients of two cylinders with the gap T/D=1.5

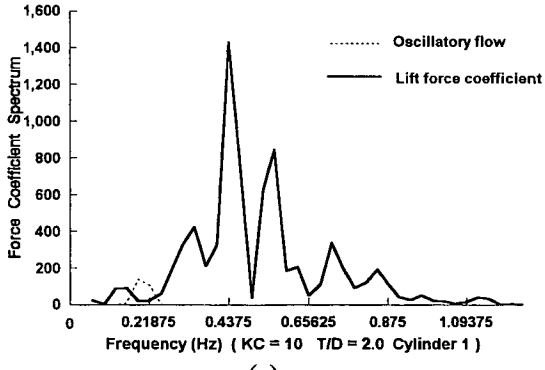

(a)

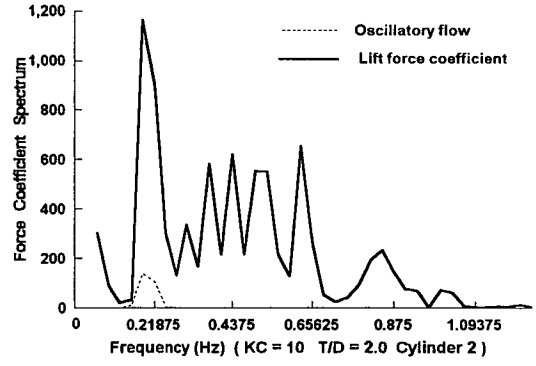

(b)

Fig 5.32(1) Lift force coefficients of two cylinders with the gap T/D=2.0

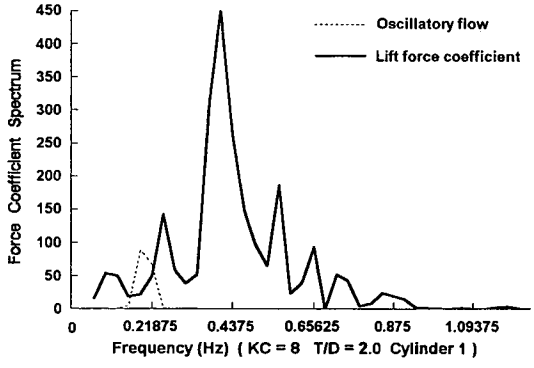

(c)

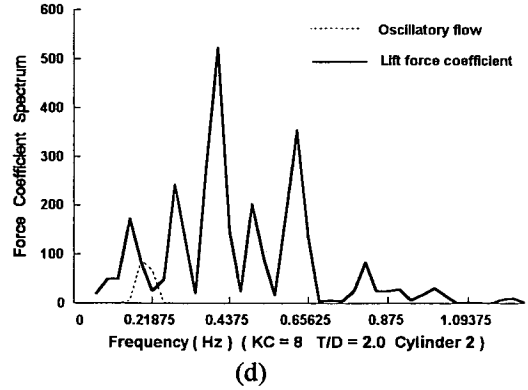

(d)

Fig 5.32(2) Lift force coefficients of two cylinders with the gap T/D=2.0

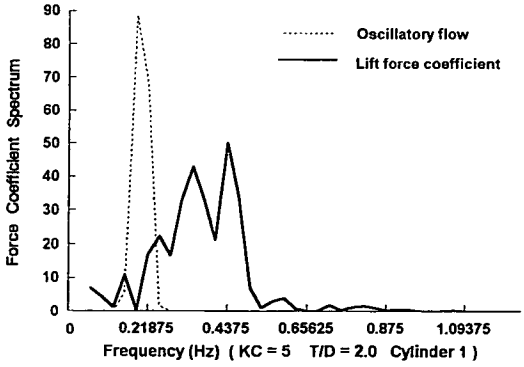

(e)

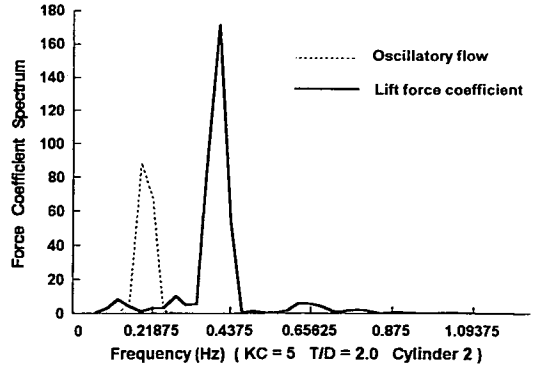

(f)

Fig 5.32(3) Lift force coefficients of two cylinders with the gap T/D=2.0

The results of the numerical simulation compared satisfactorily with the main frequency of laboratory experiments (Fig 5.12 and Fig 5.13) , the main frequencies were the second harmonic of the frequency of the oscillatory flow. There are two inconsistencies in the Figs. One is Fig 5.30 (b) and the other is Fig 5.31 (b). When one cylinder has the second harmonic as the main frequency the other has the first harmonic as the main frequencies. This feature happens at KC number = 10 , but because no force measurement were done on the two cylinders at the same time, this feaure couldn't be confirmed . But the second harmonic has been simulated well.

5.4.2 Vector fields and stream function

PIV mapping has difficulty showing the vortices adjacent the cylinders when there was only small amplitude oscillatory flow past the cylinders. The numerical simulation showed its advantage for this situation. Fig 5.33 showed a half period of oscillatory flow past the two cylinders at the KC=5

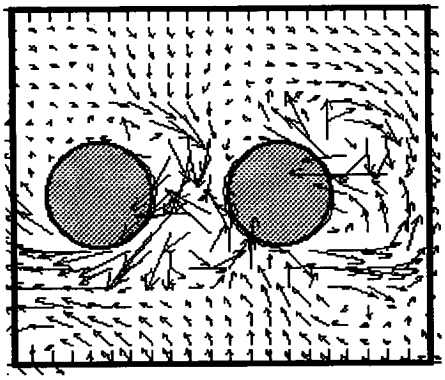

Phase = π Vector map KC=5 T/D=1.5
Fig 5.33 (a) Flow fields of the numerical simulation

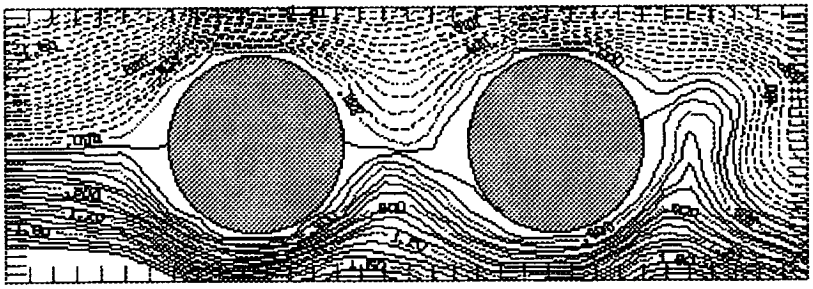

Phase= 5/4 π Streamfunction KC=5 T/D=1.5
Fig 5.33 (b) Flow fields of the numerical simulation

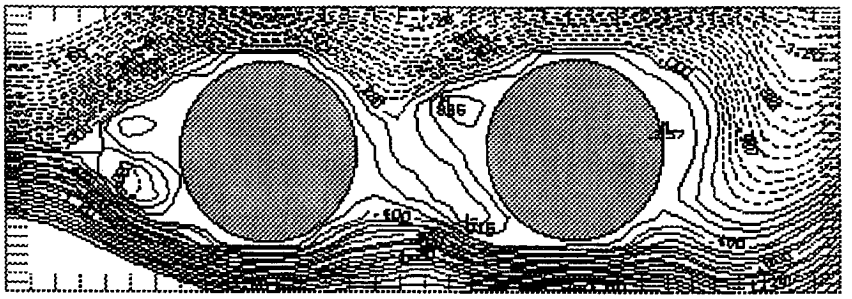

Phase= 6/4 π Streamfunction KC=5 T/D=1.5
Fig 5.33 (c) Flow field of the numerical simulation

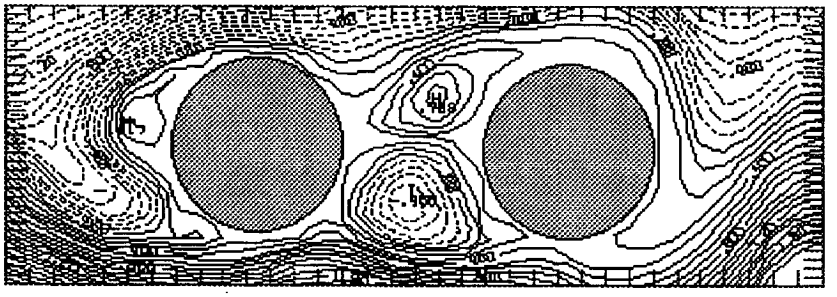

Phase= 7/4 π Streamfunction KC=5 T/D=1.5
Fig 5.33 (d) Flow field of the numerical simulation

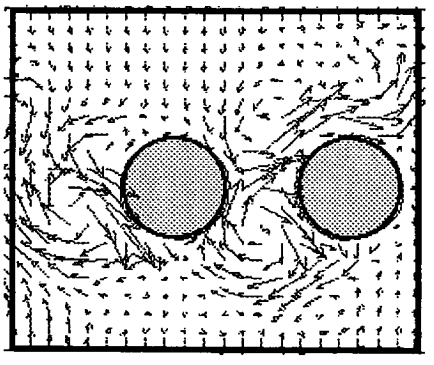

Phase= 2 π Vector map KC=5 T/D=1.5
Fig 5.33 (e) Flow field of the numerical simulation

Fig 5.33 The oscillatory flow past two cylinder in a half period (T/D=1.5)

In Fig 5.33, The oscillatory flow has had a direction change. From phase π to phase 5/4π the flow turned from going towards the left side to going towards the right. At the phase 5/4 π there was no vortex because of the direction variance. After that, the new vortices generated and was getting larger and stronger. For the gap T/D=1.5, the size of the vortices can occupy the gap fully. When the gap increased to T/D=2.0, the relative size of the vortices was smaller than the gap between the two cylinders at the KC number= 5. Then a stagnation of flow happened in the gap. See Fig 5.34.

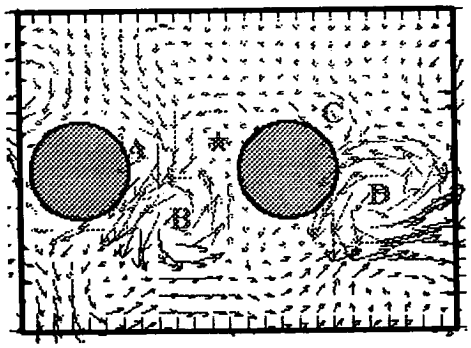

Fig 5.34 The oscillatory flow past two cylinder at KC=5 T/D=2.0 Phase=π

In the Fig 5.34, a mark ✯ pointed at a flow stagnation area. This was identical with the video recordings of experiments (Fig 5.21 vortex pattern 7). For the cylinder at the right side in fig 5.34, there was a flow stagnation at its left side and a relative strong flow went to its bottom at its right side. This flow field will cause a difference in the pressure along the horizontal direction then a strong in-line force on the cylinder. In the single cylinder case, there was no the stagnation area on the left side. The flow in this side only went slower than the right side, so the inline force experienced by the cylinder was weaker than that of the two cylinders .

For the other KC numbers , the numerical simulation also gave satisfactory results. Those vector maps will be shown in the next section 5.4.3.

5.4.3 Vorticity distribution

The vorticity calculation of numerical simulation is much easier than in experimental results. At the first there is no covered data in the output of numerical simulation. Around the cylinder surfaces all of the flow data can be obtained and used. So the vorticity can be calculated to give a detail description of the flow, and the vortices have no missing area which is caused by cylinder body in PIV experiments. In the PIV experiment data are obtained by a camera so the end of the cylinder which is near the camera will leave a bigger image than the far end. This image will cover some data adjacent to the cylinder surface. Additionally no incorrect data appears in the output of the numerical results and all of meshes are regular polygons. For PIV experimental data, sometimes deformed results will happen when the flow or vortices are not normal to the centre of the camera lens. So the numerical data can offer a check to PIV

experimental data. The vorticity distribution from the numerical vector map has been calculated out and shown as follows :

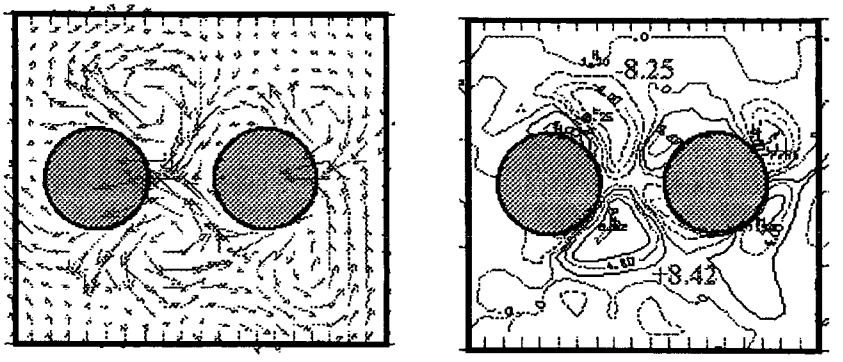

(a) Vector map (b) Vorticity

Fig 5.35 Vortices and their vorticity distribution at KC=10 , T/D=1.5 , π

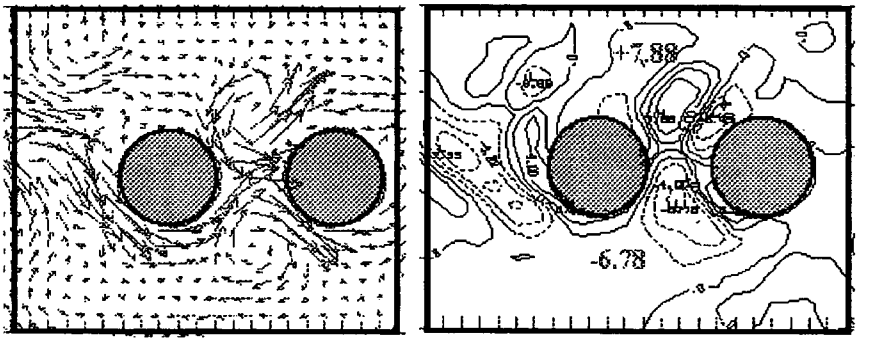

(a) Vector map (b) Vorticity

Fig 5.36 Vortices and their vorticity distribution at KC=8 , T/D=1.5 , 2π

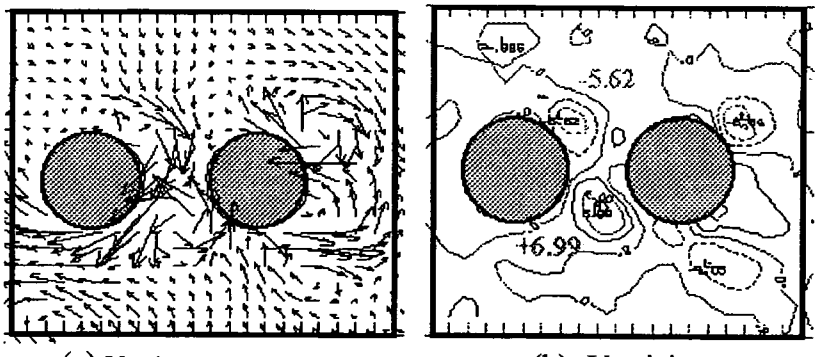

(a) Vector map (b) Vorticity

Fig 5.37 Vortices and their vorticity distribution at KC=5 , T/D=1.5 , π

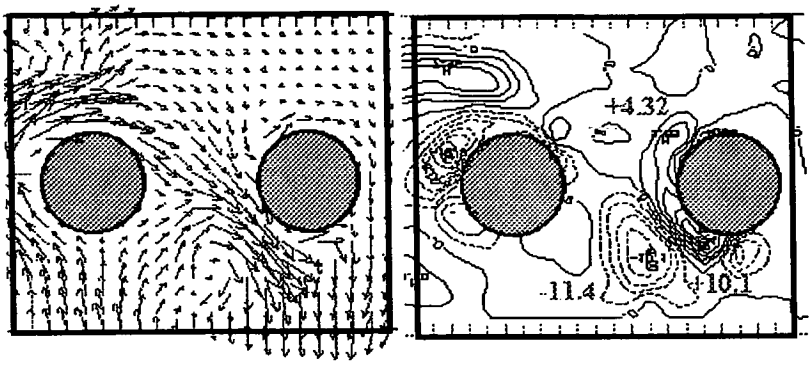

(a) Vector map (b) Vorticity

Fig 5.38 Vortices and their vorticity distribution at KC=10 , T/D=2.0 , 2π

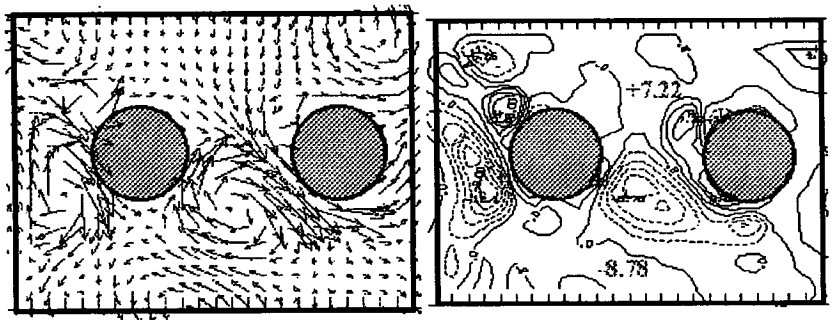

(a) Vector map (b) Vorticity

Fig 5.39 Vortices and their vorticity distribution at KC=8 , T/D=2.0 , 2π

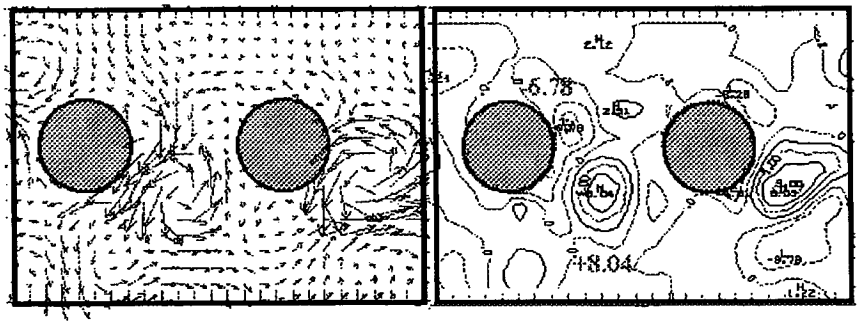

(a) Vector map (b) Vorticity

Fig 5.40 Vortices and their vorticity distribution at KC=5 , T/D=2.0 , π

The vorticity difference between positive and negative vorticity centres in the gap are :

KC=10 , T/D= 1.5	Δω= ω (+)- ω(-) =8.42-(-8.25)= 16.67
KC= 8, T/D= 1.5	Δω= ω (+)- ω(-) =7.88-(-6.78)= 14.66
KC= 5, T/D= 1.5	Δω= ω (+)- ω(-) =6.99-(-5.62)= 12.61
KC=10 , T/D= 2.0	Δω= ω (+)- ω(-) =10.1-(-11.4)= 21.50
KC= 8, T/D= 2.0	Δω= ω (+)- ω(-) =7.22-(-8.78)= 16.00
KC= 5, T/D= 2.0	Δω= ω (+)- ω(-) =8.04-(-6.78)= 14.82

Table 5.2 The difference of the vorticity

From these vorticity data in Table 5.2 it can be found that for the same gap a larger KC number will give a larger difference of vorticity and further result in a larger lift force. Such as in Table 5.1 there are $\Delta\omega$: 21.50 > 16.00 >14.82 at the gap T/D = 2.0 and $\Delta\omega$: 16.67 > 14.66> 12.61 at T/D=1.5 . This feature is the same as found in the single cylinder cases and the same as the results in laboratory experiments. But for the fixed KC number, a wider gap will match a larger difference of vorticity ($\Delta\omega$) between positive and negative centres, such as when KC=10 $\Delta\omega$: 21.50 > 16.67; when KC=8 $\Delta\omega$: 16.00 > 14.66; when KC =5 $\Delta\omega$: 14.82 > 12.61. This may be one of resons of in-line force larger for a wider gap at the same KC number.

5.5 Conclusions

From the above analysis , the interference between two cylinders is obvious when their gap is 1.5 and 2.0. Some conclusions can be summarized as follows.

1) The strength of the inline force and lift force

a) In comparison with the single cylinder, the two tandem cylinders experience a stronger inline force at the same KC number. The reason for this might be that the flow runs faster through the gap area than downstream of the two cylinder model. This causes a larger pressure difference along the horizontal axis, which give a contribution to the strength of the in-line force, then a larger in-line force acts on the cylinders. For the two cylinder models with different gaps, the cylinders with a wider gap will experience a stronger inline force.

b) The two cylinder models experience larger lift forces than the single cylinder's case at the same KC number. For the two cylinder models themselves, a thinner gap will cause a larger lift force on the two cylinders. A possible reason is the position of the vortex moving. Because of the obstructure of downstream cylinder, the shedded vortex with the flow past the cylinder can not go near to the horizontal axis, its position is a bit higher than that in the single cylinder case. The thinner the gap is , the higher the vortex goes. When the main flow runs over the cylinder and meets the vortex, it will cause flow convergence on the top of the cylinder . This sort of convergence does not occur simultaneously at the bottom of the cylinders because the vortex shedding is asymmetry. So a stronger lift force is acted on the cylinder by a

bigger difference of the pressure between the top and the bottom of the cylinders. Of course if the flow convergence appeared at the bottom and a faster flow is on the top of the cylinder, then the results would be the same.

c) When the gap ratio decreases from 2.0 to 1.5 for a fixed KC number, there is a decrease in the strength of the inline force but a significant increase in the lift force and it can be larger than that of the inline force, see Fig 5.8. This phenomenon has been observed by Bushnell[5]. He thought it is caused by the shielding effect of an upstream cylinder on a downstream cylinder. But his experiments were for KC >30, T/D=3.0 .

2) The main frequency of the forces

The main frequencies of the inline forces are the same as that of the oscillatory flow at all KC numbers and different gaps. And the inline force coefficients from numerical simulation have the same feature, too.

The main frequency for the lift force is the second harmonic of the oscillatory flow. That happens for almost all KC numbers chosen here and different gaps. In every half period, there are a pair of the new vortices shedded for each cylinder, that makes the lift force has the second harmonic of the oscillatory flow as the main frequency. The force masurement was done only on one cylinder of two cylinders, so the difference of the force on the two cylinders can not be found. The numerical simulation shows that the frequencies of the two cylinders are almost the same : the second harmonic is matched for both cylinders. But an inconsistency happens at KC number =10 for both gaps. One cylinder has the second harmonic as its main frequency and the other has the first harmonic as its main frequency. This feaure hasn't been confirmed by experiment.

3) Vortex patterns

a) The number and size of the vortices increases with the KC number. At larger KC number, vortices can exist for a longer time. When the new vortices generate, the old ones keep their existance. That causes more vortices in the same time.

b) The position that vortices being destroyed is nearer the horizontal axis when the KC

number decreases. One of the reasons is the size of the vortices increases faster with KC number. At KC number =10, the size of vortex is large and it couldn't squeeze into the gap, so it has to slide over the downstream cylinder then is destroyed by flow changing direction; at KC.= 8 , the size of the vortex is smaller and a half of its body can fall into the gap. It experiences a stronger obstruction from the downstream cylinder, so it is destroyed before it moves along the top (or below at the bottom) of the downstream cylinder; at KC = 5 , the vortices have much smaller size and most part of them fit in the gap. They are destroyed as they touch the front surface of the downstream cylinder. The vortices disappearance is caused by the main flow direction changing and the obstruction of the downstream cylinder. A large vortex has enough energy to delay being destroyed.

c) Because the size of vortices is larger and their moving paths is higher with KC number and with the gap shrinking, it causes a stronger convergence on the top (or the bottom) of the cylinder. Then there will be a larger difference in pressure between the top and the bottom of the cylinder and result in a larger lift force.

d) With KC number decreases, the flow in the gap bewteen two cylinders changes from fast, slow to stagnation . At KC number = 10, the flow passes the gap fast and its path is almost perpendicular to the oscillatory flow. At KC = 8, the flow passes the gap as a curve shape and matches the vortices outline, its path is more flat. At KC = 5 the flow can occupy the gap for a short period . For the downstream cylinder, the velocity difference and pressure difference between the front and the back of it will decrease when KC number getting smaller, so the inline force experienced by the cylinder will be weaker at a smaller KC number.

4) Vortex strength and vorticity features

a) In general, a faster speed flow (large KC number) will cause a stronger vortex behind the cylinder according to vortex strength calculation; a wider gap will be helpful to make a larger and stronger vortex at same KC number. According to the vortex strength calculation , it has been obtained: at gap ratio =1.5 and 2.0 , vortex strength of KC=10 is larger than that of KC=8; if KC number is unchanged, the vortex strength will larger at a wider gap 2.0 than it at gap 1.5. When gap size is fixed, a stronger

vortex will cause a stronger lift force. At the same KC number a wider gap will match a stronger vortex which is closer to the horizontal axis of the cylinder . The stronger vortex will give more influence on the hriozontal direction and cause a stronger inline force.

b) To compare the vorticity differences between positive and negative centres in two and single cylinder cases:

Cylinders / Difference of vorticity / KC number	Two cylinders T/D=2.0		Two cylinders T/D =1.5		Single cylinder	
	Experiment	Simulation	Experiment	Simulation	Experiment	Simulation
KC =10	6.24	21.50	6.52	16.67	3.9	21.0
KC = 8	4.34	16.00	8.39	14.66	2.7	20.0
KC = 5	N/A	14.82	N/A	12.61	N/A	18.0

Table 5.3 The difference of the vorticity between positive and negative centres

For the experimental results, at the same KC , a thinner gap has a bigger $\Delta\omega$. This could be due to the jet caused by the thinner gap. Because a jet has big velocity gradient, and will give larger vorticity. And the larger difference in the vorticity centre values means that the difference of the two shed vortices is large , it will result in a stronger lift force. So at a fixed KC number , there is a larger lift force for the thinner gap. For the same size of the gap, a big KC number gives a bigger $\Delta\omega$ and a larger lift force. It is the same as the single cylinder case and numerical simulation also give the feature. But an inconsistency is at the gap=1.5 for experimental result. The reason remains to research.

5) Results comparing between the computer simulation and laboratory experiments could give us more description about flow past the cylinders, because the computer simulation can show us some information that couldn't be obtained satisfactorily in PIV experiments, because the some limitation of PIV technique.

5.6 References

[1] M.M.Zdravkovich, Review of flow Interference between two circular cylinders in Various Arrangements, Journal of Fluids Engineering , December, 1977 pp 618-633

[2] E.Hori , Experiments on Flow around a Pair of Parallel Circular Cylinders, Proc. 9th Janpan National Congress for Applied Mech., Tokyo,1959, pp.321-234

[3] M.M.Zdravkovich, Somke Observations of Wakes of Tandem Cylinders at Low Reynolds Number, The Aeronautical Journal, (1972) vol 76, pp.108-114.

[4] C.H.K.Williamson, Sinusoidal Flow Relative To Circular Cylinders, (1985), J.Fluid Mech. Vol 155, pp 144-174 .

[5] M.J..Bushnell, Forces on cylinder arrys in oscillating flow. (1977) OTP Paper 2903. Houston. Texas.

[6] A.Slaouti and P.K.Stansby, Flow around Two circular Cylinders by The Random-vortex Method, J.Fluids and Structures. (1992) vol 6, pp. 641-670

[7] H.M.Badr, m.Coutanceau, S.C.R.dennis and C.Menard, Unsteady flow past a rotating circular cylinder at Reynolds numbers 10^3 and 10^4, J.Fluid Mech.(1990) , vol 220, pp 459-484

[8] J. Li, J.Sun and B.Roux, Numerical Study of An Oscillating Cylinder In Uniform Flow And In The Wake of An Upstream Cylinder, J.Fluid Mech. (1992) vol 237 pp.457-478

[9] B. Fornberg , Steady incompressible flow past a row of circular cylinders, J.Fluid Mech. (1991) vol 225 pp.655-671

[10] P.S.Bernard, J. M. Thomas and R.A.Handler, Vortex Dynamics and the production of Reynolds Stress, J.Fluid Mech.(1993) vol 253, pp.385-419

[11] Y.Chen , Y.OU, A.J.Pearlstein, Development of the Wake Behind A Circular Cylinder Impulsively Started Into Rotatory And Rectilinear Motion, J.Fluid Mech, (1993) vol 253,pp.449-484

[12] R.B.Green and J.H.Gerrard, Vorticity Measurements In The Near Wake Of A Circular Cylinder At Low Reynolds Numbers, J.Fluid Mech. (1993) vol 246 pp. 675-691

Chapter 6

Oscillatory Flow Round Four Cylinders

6.1 Fluid Loading on the Legs of the Oil Platform

6.1.1 Environmental Loadings

A four cylinders array is a simple model for the legs of a Tension leg platform. The tension leg platform(TLP) (See Fig 1.2 in Chapter 1) is a concept for petroleum production in deep water. The floating TLP is anchored by vertical tension legs (tethers) which are kept under tension by the excess buoyancy of the platform. The tethers provide a horizontal restoring force in an offset position. The tethers also limit the vertical motion of the platform, thereby easing the problems of riser connections and operation of production facilities.

In this design, vertical members are used to anchor the platform to the seafloor. The upper part of the structure is designed with a large amount of excessive buoyancy so as to keep the vertical members tensioned. Due to this tension, the platform remains virtually horizontal under wave action. Lateral excursions are also limited by the vertical members, since such movements necessarily cause them to develop a restoring force. A major advantage of the tension-leg concept is that its cost does not increase dramatically with increasing water depth. At the present time, it appears that the main limitation on the tension-leg platform arises from dynamic inertia forces associated with the lateral oscillations of the platform in waves. These become significant at water depths of about 3000ft.

Before the response of a proposed offshore structure can be analyzed, it is necessary to have quantitative estimates of all the significant loadings that the structure is likely to experience in the ocean environment. For structureal engineering purposes, this environment may be characterized mainly by overwater wind, by surface waves, and by

currents that exist during severe storm conditions, in addition, a few other environmental loadings such as ice loading and mud loading are also considered, see Fig 6.1

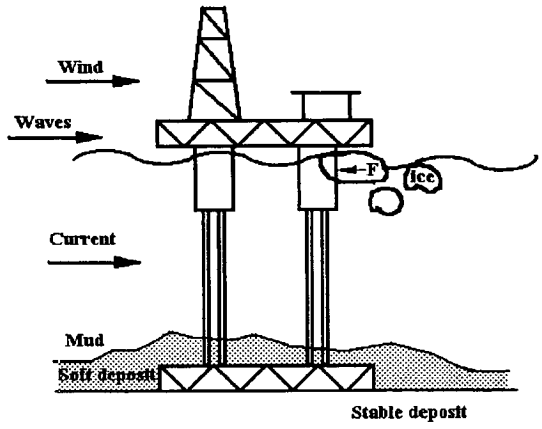

Fig 6.1 Environmental loadings on an offshore structure

Overwater wind during storm conditions is significant in the design of offshore structures because of the large forces, it can induce vibration on the exposed upper parts of the structures.[1] Wind speed during hurricane conditions in the Gulf of Mexico can, for example, exceed 100 mph, causing, in turn, horizontal forces on a typical offshore strucure of 100 kips or more.

Surface Waves during storm conditions are also of major importance in the design of offshore structures because of the large forces produced on submerged parts of the structure by the accompanying water motion. Wave heights (difference between maximum and minimum elevations of the water surface at any instant) in the Gulf of Mexico during storm conditions can exceed 50 ft and these can produce horizontal forces of several hundred kips or more on a typical sturcture. Currents at a particular site can contribute significantly to the total forces exerted on the submerged parts of the structure. Here currents refer to the motion of water that arises from sources other than surface waves. Tidal currents, for example, arise from the astronomical forces exerted on the water by the moon and sun, wind-drift currents from the drag of local wind on the water surface, river currents from the discharge of rivers, and ocean currents from the drag of large-scale wind systems on the ocean. During storm conditions, currents at the surface of 2ft/sec or more

are not uncommon, giving rise to horizontal structural forces which can be in excess of 10% of the wave-induced forces.

Ice Loading can be important in certain offshore site locations, especially in polar regions, where thick sheets of ice can move with the tide and strike the legs of offshore structures with significant force.

Mud Loadings can arise from mud slides in certain offshore sites, particularly in active delta regions, where soft soil is continually being deposited by river discharge. Because the soft deposit may extend appreciably below the seafloor, mudslide forces are usually treated as distributed forces acting on the pile legs. This is in incontrast to ice loadings, which are frequently regarded as concentrated forces because of the relatively small thickness of ice considered.

Thus the relative size of environmental loadings are :
the current-induced forces > the wave-induced forces > the wind-induced forces.

6.1.2 Current Loading

The current loadings are the main component of the total force experienced by the legs of a platform in the sea. Currents refer to the relatively constant motion of water resulting from such sources as tidal action, wind drag, or river discharge. The most common currents considered in offshore structural analysis are tidal currents and wind-drift currents, the latter arising from the drag of local wind on the water surface.

Both of these currents are usually regarded as being horizontal and varying with depth. Fig 6.2 shows the wind-drift process as the wind blows along the water surface. In a surface wave, water particles advance slightly further in the crest than they retreat in the trough, so a small net forward motion results, which is the wave drift. In deep water, this motion may be of the order of several millimeters to several centimeters per second.

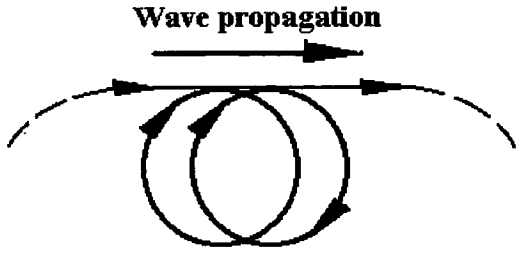

Fig 6.2 Wind-drift

The magnitude and direction of the tidal current at the water surface is generally estimated from local field measurements, the direction of the current reversing with the rise and fall of the tide. For engineering purposes, it is frequently assumed that the depth variation of tidal currents is governed by a one-seventh power law while wind-drift current is assumed to be governed by a linear law. These variations are illustrated in Fig.6.3.

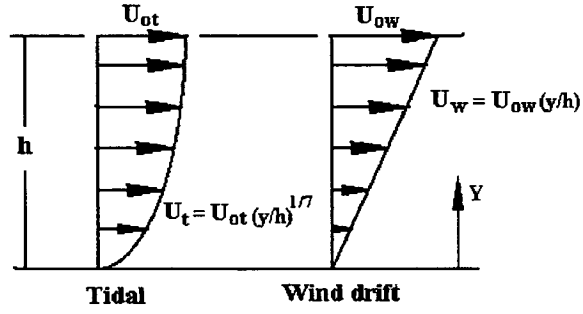

Fig 6.3 Assumed vertical distribution of tidal and wind-drift currents

During storm conditions, currents exist simultaneously with the water motion arising from surface waves. The direction of the tidal current may be at angle to that of the direction of wave propagation. However, the wind-drift current is always assumed to be in the same diection as that of the wave movement.

Surface waves which exist simultaneously with currents are modified from those that would exist in the absence of any currents. The strength of the modification can generally be expected to vary with the ratio of maximum current to wave-speed. For design waves in extreme storm conditions, this ratio is usually sufficiently that any modification of the wave caused by the current can be neglected. Thus, for regular design waves and a

horizontal current of arbitrary depth variation, the force exerted on an offshore structure is normally calculated by simply adding the horizontal water velocity caused by the waves to the component of the current velocity in the direction of wave propagation and using this resultant horizontal velocity, together with the vertical water velocity and the two acceleration components to determining the maximum force and joint loadings.

6.1.3 Fluid Loading Approach

The loading imposed on members of an offshore structure subject to wave and current action represents one of the major design considerations in offshore engineering. Wave loading is due to the relative motion between the fluid and the structure, and consideration of the problem must logically begin with a specification of the wave or wave-current field. Because the wave environment within the generation zone is strictly a random process, the mathmatical description of waves become a difficult problem since the convective term in the Navier-Stokes equations is nonlinear and the surface boundary condition of is unknown. So simplification and approximation of waves and currents have to be done in order to investegate the fluid loadings on an offshore structure.

For the research here, the oscillatory flow of sinusoidal motion has been used . It is determined according to the laboratory facilities and the approximations of the wave and current theory. Simple harmonic motion is a basic result of linearizing the wave theory. A two dimension oscillatory flow can give us the main characteristics of the interaction between the wave and structure. Being an unconstant and periodic motion, on the other hand, periodic flow round an immersed body is a major research problem. The parameters of the oscillatory flows has been introduced in chapter 4 and charpter 5. For the four cylinder model case, the KC numbers are 5, 8 ,10 , 13 and 20. The ratio of the distances between two neighbor cylinder centres and the diameter of the cylinder is 129mm:50mm, or 2.58 :1. According to the application in chapter 5, it can be written : T/D = 2.58. Once the appropriate wave model is established a load mechanism is employed which relates the fluid motions to the resulting forces experienced by a structural element. The in-line component of loading is normally evaluated using the well-known Morison's equation.

The lift force is produced as a result of changes in the boundary layer and the formation of vortices within the flows. The numerous experimental studies in oscillating flow have shown that the lift force is irregular and weakly correlated with the in-line flow but may be of the same order of magnitude as the in-line force. Sarpkaya's work(for a single cylinder) indicates that the frequency content of the transverse force may not always be composed of exact harmonics of the fundamental wave frequency. The data available in this area for prototype conditions is still not enough, and more work is required to develop a complete in-line and transverse loading mechanism for analyses of wave loads on offshore structures.

6.2 The Results of Force Measurement

Force measurement is carried out for one of the four cylinder combination. The basic hypothesis is that the four cylinder array is a symmetric structure and the relative motion of the oscillatory flow is also symmetrical .

6.2.1 The strength of the forces

The strength of the inline force increases with KC number for the four cylinder array as the same as a single cylinder case, it can be seen in Fig 6.4 . When KC numbers are relative low, such as 5, 8 and 10, the strength of the inline force on the four cylinders is similar to that on the single cylinder , but for the KC number of 13 and 20, the strength of the in-line force on the four cylinder array has an obvious increase and is larger than it on the single cylinder.

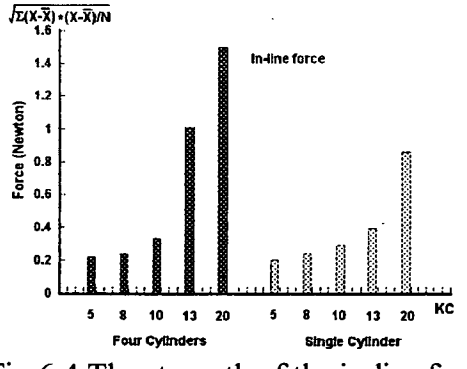

Fig 6.4 The strength of the in-line force

The chart shows that for the four cylinder array with gap 2.58 between two neighbour cylinders, the effect of neighbour cylinders on-inline force can be ignored at KC = 5, 8 and 10, because the in-line force experienced by the cylinder in the four cylinders array is almost the same as the single cylinder. But with KC numbers increasing further, the interferential effect of the combination structure has to be considered.

The strengths of the lift force are shown in Fig 6.5. The strength of the lift force also increases with the KC number, and for the four cylinder array, the cylinder can experience a larger lift force than that on the single cylinder at the same KC numbers.

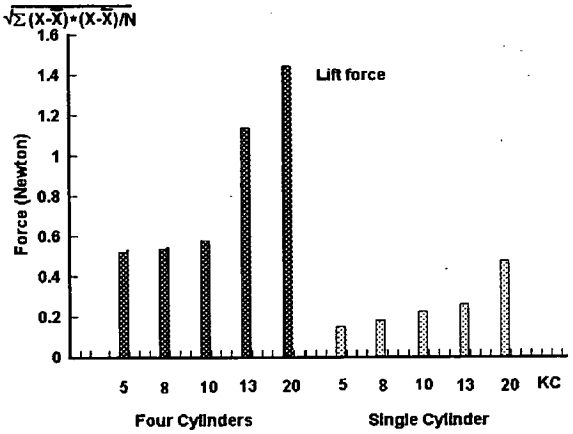

Fig 6.5 The strength of the lift force

A possible reseason could be the enviromental vortex field of the four cylinders structure which is different from that of the single cylinder. Fig 6.6 is a flow visualization map of four cylinder array from the video recordings. In the picture, the white spots are the seedings in the water. They move with the flow and leave their paths on the picture under Laser sheet illumination. It can be seen that there are vortices on both sides of the two downstream cylinders. It is a main difference from the case of the single cylinder which is shown in Fig 6.7, the single cylinder has only vortices in its wake. Because of the existence of these vortices around the four cylinders, the flow and its velocity between the two rows of cylinders are changed and uneven, see Fig 6.6(b). These will cause a larger flow convergence on the bottom of the upper cylinder and the top of the lower cylinder, which is larger than those on the top of the upper cylinder and the bottom of the lower

cylinder. Further the flow field causes larger pressure difference between the top and bottom of the cylinders than that of the single cylinder case. This results in the lift force on the four cylinder arry is larger than that on the single cylinder .

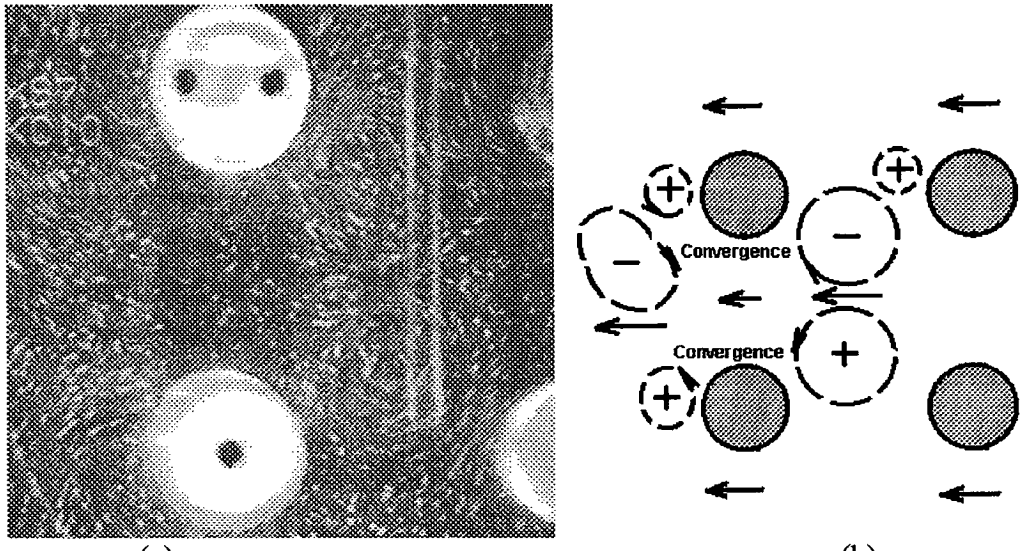

(a) (b)

Fig 6.6 The flow visualization of four cylinders (a), a skeleton (b)

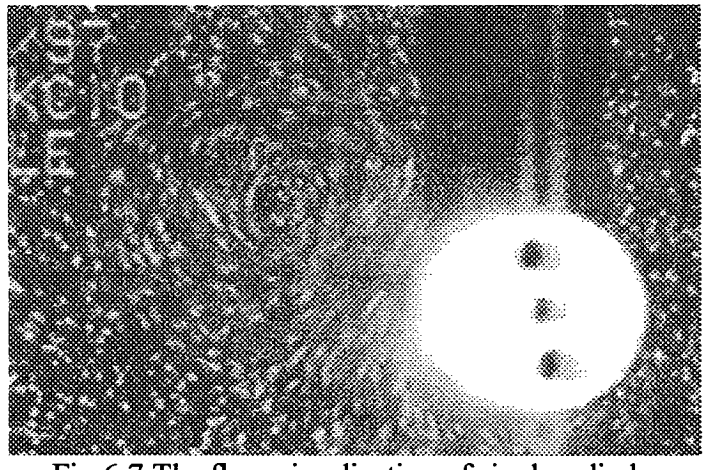

Fig 6.7 The flow visualization of single cylinder

To compare Fig 6.6 with Fig 6.7, it can be found that the occupancy area of a vortex is bigger at single cylinder case than those in four cylinder structure when the KC number is the same. It is because the growth of the vortex is restricted by the surrounding tructure. Because the gap is wider than those of two cylinders arrangement (T/D=1.5 and 2.0), it can hold the vortices in the gaps between two cylinder columns. In the two cylinder cases the vortices had to stay the top of the cylinders and can not squeeze into the gap at the

same KC number. See Fig 5.5 (a) in Chapter 5. When the size of the vortices can occupy the whole gap , the four cylinders structure will limit the further increse in the size of the vortices. It will cause the strength and size of the vortices in the four cylinders system to be different from that of the single cylinder.

6.2.2 The frequencies of the forces

The main frequencies of the inline forces are, as expected, the same as that of the oscillatory flow. The frequencies of the lift force are shown in Fig 6.8 . As a comparison, the frequencies of the single cylinder are also shown in Fig 6.9. Fig 6.8 is the left column for four cylinder array and Fig 6.9 is the right column for a single cylinder. The arrows in the Figs pointed at the frequency position of the oscillatory flow

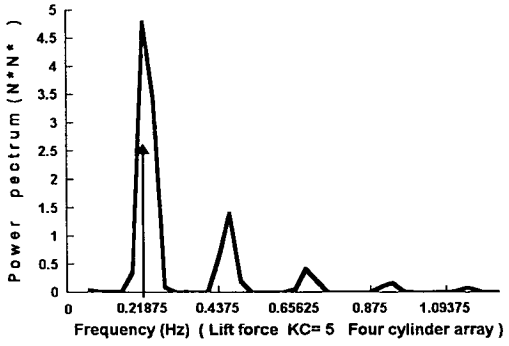

Fig 6.8 (a)

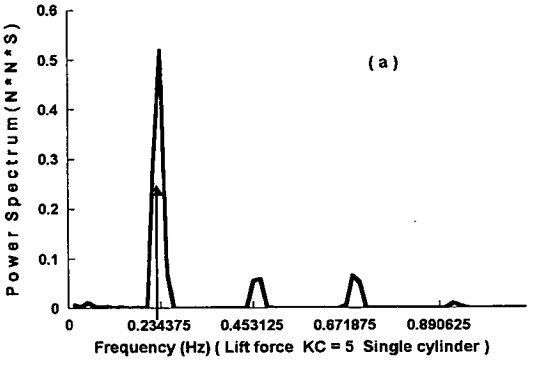

Fig 6.9 (a)

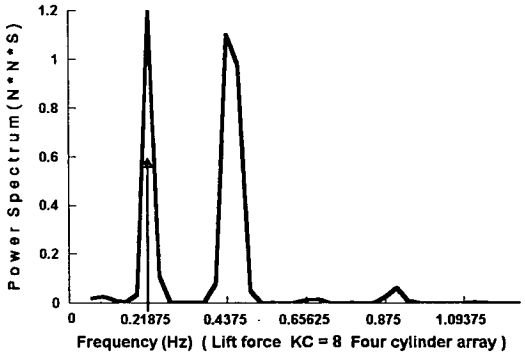

Fig 6.8 (b)

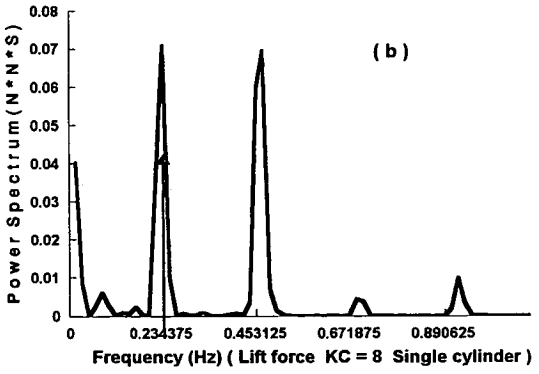

Fig 6.9 (b)

Fig 6.8 Frequencies of lift force of four cylinder array (left)

Fig 6.9 Frequencies of lift force of single cylinder (right)

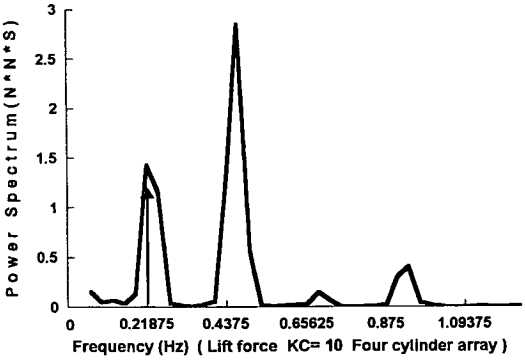

Fig 6.8 (c)

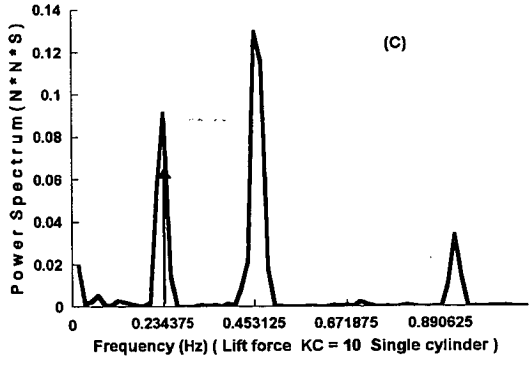

Fig 6.9 (c)

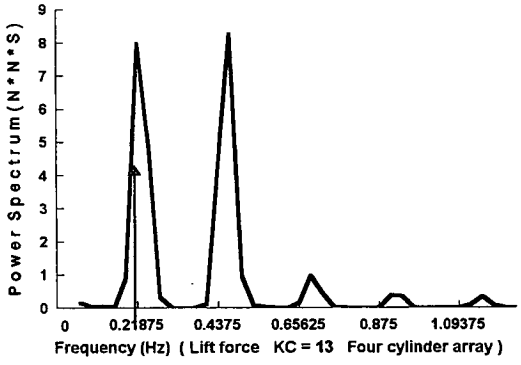

Fig 6.8 (d)

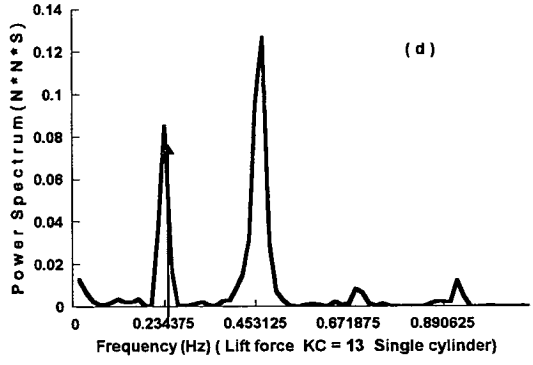

Fig 6.9 (d)

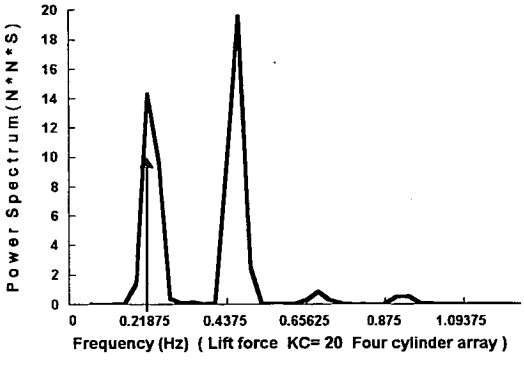

Fig 6.8 (e)

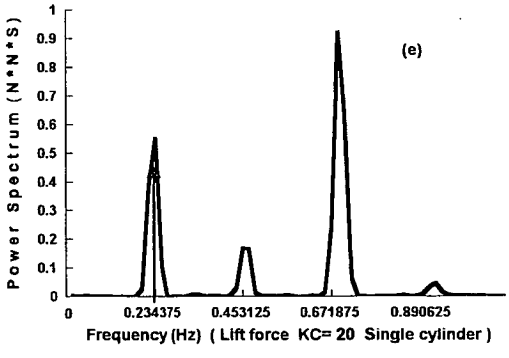

Fig 6.9 (e)

Fig 6.8 Frequencies of lift force of four cylinder array

Fig 6.9 Frequencies of lift force of single cylinder

With KC number increasing, the main frequency of the lift force gradually moves from first harmonic to second harmonic of the oscillatory flow. Unlike the single cylinder, the four cylinder array has no the third harmonic as its main frequency at KC=20. To compare

the results from the two models, it can be found that the main frequencies of the four cylinder array are similar to the main frequencies of a single cylinder when the arrangement of the four cylinder array is T/D $\geq$ 2.5 . Or it can be said that the four cylinder structure does not significantly affect the frequency feature of the lift force for the gap larger than 2.5 times the diameter of the cylinder when the KC number is lower than 13. In the design of oil rigs it is reasonable to arrange the distance between any two neighbor cylinder legs to be greater than 2.5 times their diameter.

6.3 The Flow Patterns and Their Velocity Fields

6.3.1 Vortex shedding patterns

To investigate the interaction between the four cylinder structure and the oscillatory flow , some skeletons of the vortex patterns have been drawn from the video recordings. The analysis emphasis is in the middle area of the four cylinder array.

When the KC number > 5 the size of the vortices are limited by the space between the cylinders. So the vortices evolutions in the middle area are similar to each other at KC = 8, 10, 13 and 20. They are shown in Fig.6.10. In the outside of the four cylinder array, the length of the wakes increases with the KC numbers. Fig 6.10 shows the vortex shedding patterns at special phases 1/2 π , π , 3/2 π and 2π as follows.

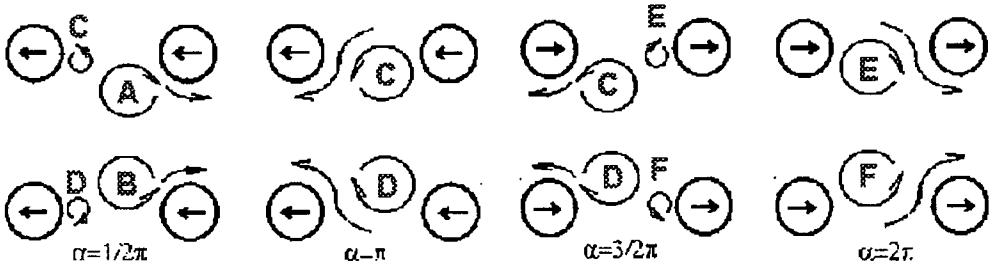

Fig. 6.10 Vortex shedding pattern (1) : at some special phases .

The skeletons show that at phases $1/2\pi$ and $3/2\pi$ there are four vortices between the two cylinder columns. The two big vortices are generated in the last half period and have

remained there . The two small vortices are newly generated in the current half period. At the phases π and 2π, the two large vortices have developed from the new small vortices observed at phases $1/2\pi$, $3/2\pi$ while the large vortices observed have disappeared after running over the downstream cylinders. So in the middle area of the four cylinder array, there are always two large vortices. In every half period of the oscillatory flow, there are one new vortex generated and one transverse flow running over the cylinder, such as Fig 6.10 $\alpha=1/2\ \pi$ and $\alpha=\pi$. These cause the difference in pressue between top and the bottom of the cylinder two times in a half cycle. So the lift foece has the second harmonic as the main frequency.

After comparing the skeletons of the four cylinders with that of a single cylinder, it has been found that the structure of four cylinders caused special flow motions which are perpendicular to the directions of oscillatory flow. During the flow developing from $1/2\pi$ to π and from $3/2\pi$ to 2π, the large vortices slid over the cylinders to the outside of four cylinder structure and the small vortices become larger and move closer to the downstream cylinders. There were more transverse motion in this procedure as shown by the dash line and arrows in Fig.6.11 .

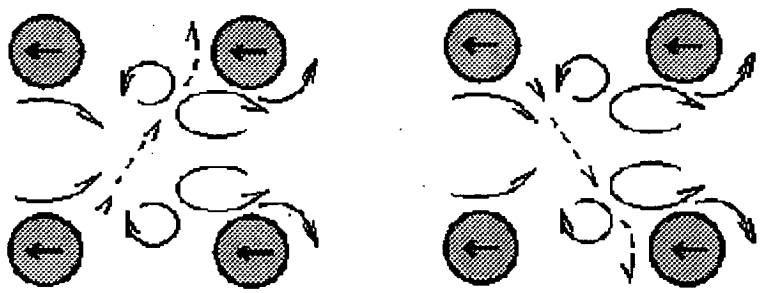

(a) (b)

Fig. 6.11 Vortex shedding pattern(2) : the two kinds of the flow transverse motions

With the KC number increasing, the strenght of the transverse flow is stronger

At KC=5, flow transverse motion was slow, taking two periods of oscillation to move across the four cylinder structure, see Fig 6.12.

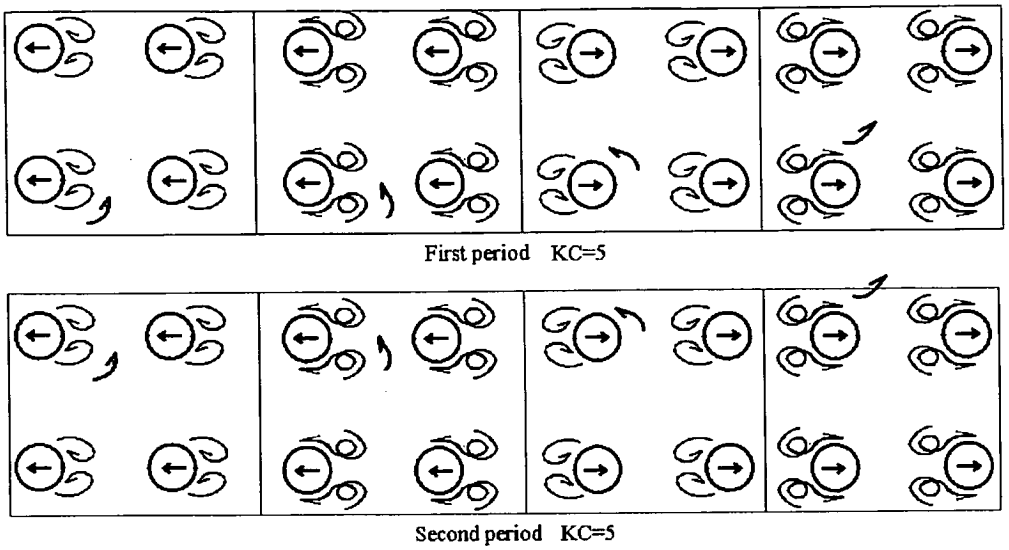

Fig. 6.12 Vortex shedding pattern(3) : KC number = 5

So the four cylinder array arrangement will help transverse flow development and be maintainced. At KC =5, the behaviour of the vortices is similar to the single cylinder case. The only difference is the existence of the downstream cylinders which help some of the flow in the middle area goes across the four cylinder structure in a zig zag path.

6.3.2 The velocity field at the special phases

The oscillatory flow velocities around the four cylinder array have been obtained from PIV mapping. They are shown as follows. The flow in Fig 6.13 is from the right to the left.

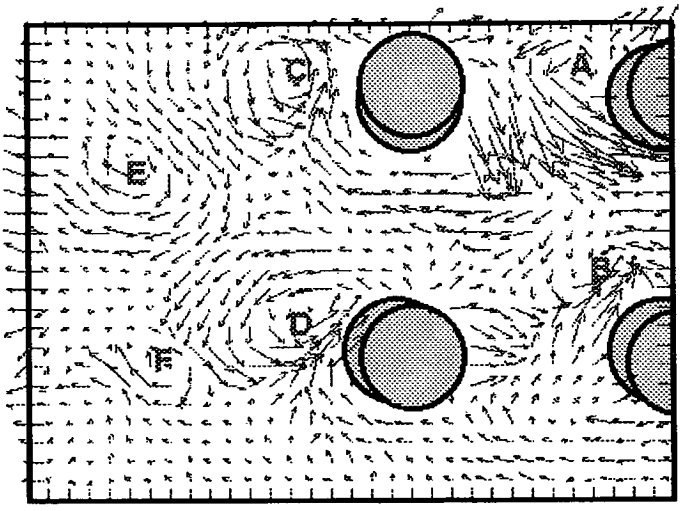

Fig 6.13 Velocity field at KC= 20 , Phase =2π

In Fig 6.13, a few features can be found. 1) There were more vortices in the wake. A wide and long wake in the down stream area of the model is occupied by disturbance, at leaset four vortices can be found in the wake. 2) There were flow convergence and divergence in the area between the two cylinder rows. It was caused by the vortices existence on both sides of the cylinder. 3) There are the transverse motion. The vortices in the middle area of the four cylinder array introduce the flow going cross the horizontal axis from the bottom (top) to the top (bottom).

Fig 6.14 is a velocity field at KC= 13. The flow in the map is from the left to the right.

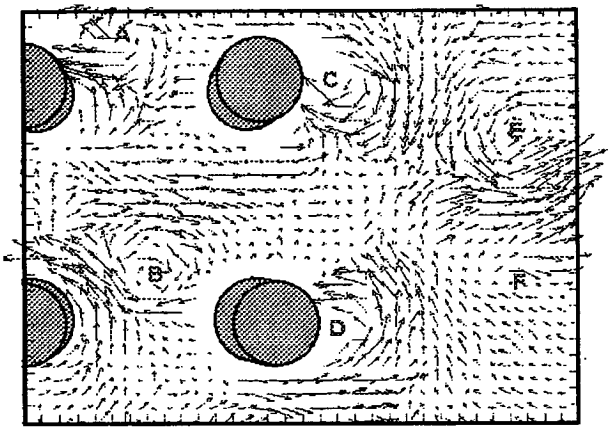

Fig 6.14 Velocity field at KC= 13 , Phase = π

Fig 6.13 and Fig 6.14 have shown a wide and long wake caused by the four cylinders structure. They affected a larger area than the wakes of the single cylinder and the two cylinders.

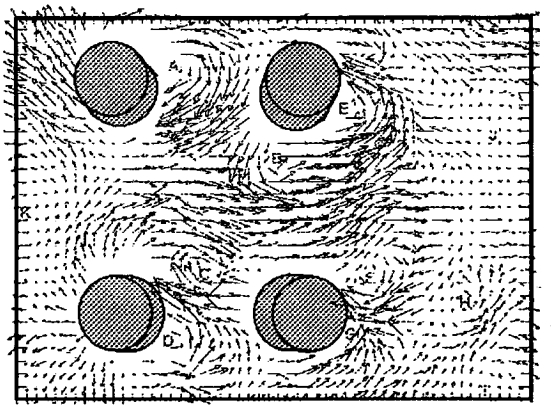

Fig 6.15 Velocity field at KC= 20 , Phase = ¼ π

In Fig 6.15, the flow is from the left to the right. From the map it can be found that there are vortices on both sides of the four cylinder array (see the letters K and E, F, G, H, I, J). The vortex K corresponds to the vortex D in Fig 6.13. It is was produced in the last half period. In this case the area of fluid containing vortices is much larger than when there is only a single cylinder present. For the four cylinder combination its influence on the basic oscillatory flow can be expended up to an area several times the size of the structure.

In order to learn the detail in the middle area of the four cylinder array, Fig 6.16 gives a vector fields with higher resolution than that in Fig 6.13--6.15. Fig 6.16 is for four different phases at KC=10. Because of the higher resolution being used, the camera can only catch a smaller area of image, and record a small part of the wakes area outside the four cylinder structure.

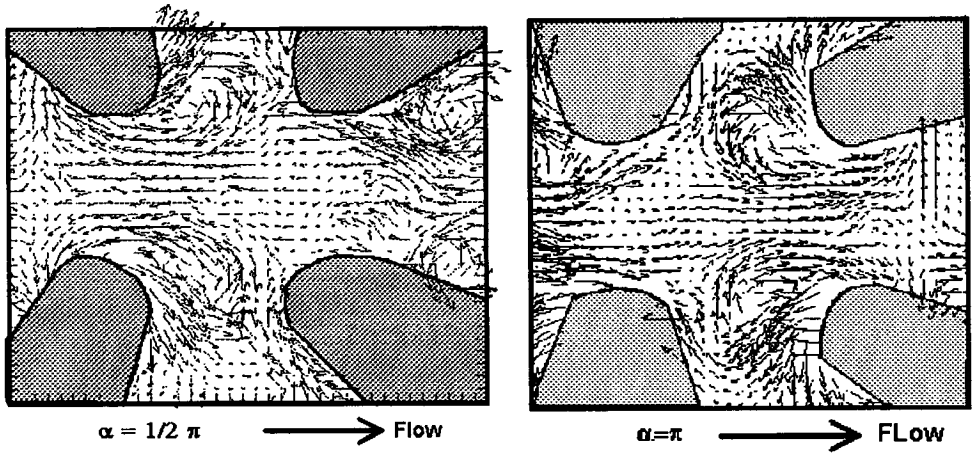

Fig 6.16 (a) (b) Velocity field at KC=10

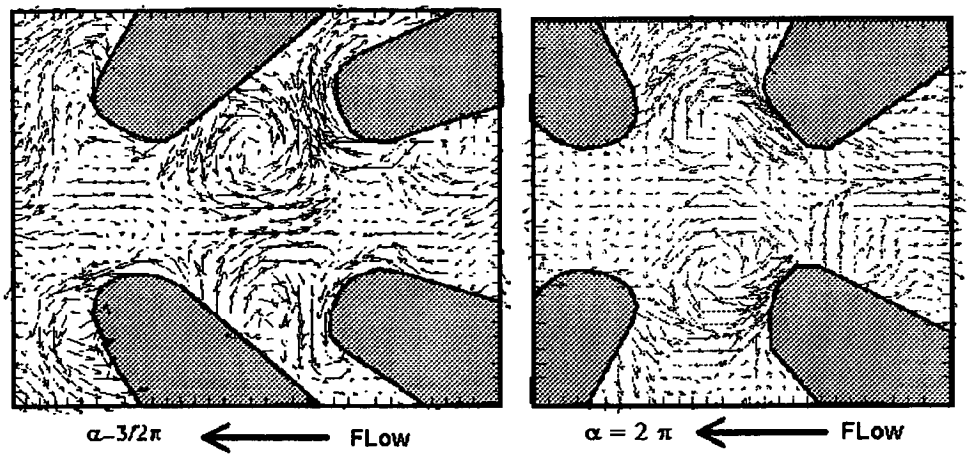

Fig 6.16 (c), (d) Velocity field at KC=10

Fig 6.16 has a basic vortex pattern which is the same as the Fig 6.10. At the phases ½ π and 3/2 π , the vortices in the middle area were produced in the perivous half period. And the vortices in wake of the whole array were generated in the present half period . So the rotating dirctions of the vortices in the middle area were different from the vortices in the outside wakes. At the phases π and 2π , the vortices in the middle area shed from upstream cylinders. Between the two rows of the cylinders, the vector sizes were different along the rows. In the gap area the vectors were larger than those in the columns of the cylinders, so velocity convergence happened on the column areas and made the larger difference in pressure on the cylinders than in the single cylinder case. Then the lift forces were larger than that on the single cylinder at the same KC number.

6.3.3 Some vorticity features

To compare the vorticity fields at KC = 20 and KC= 13 , Fig 6.17 and Fig 6.18 showed the contour of the vorticity and the centre values of the vorticity were written on the outside of the map frames.

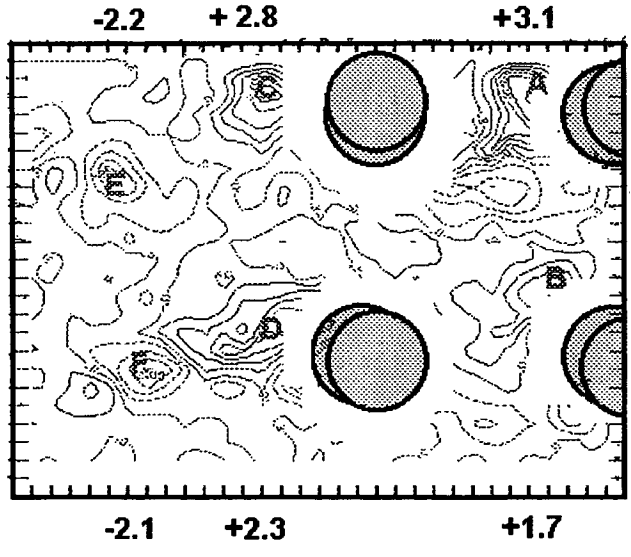

Fig 6.17 Vorticity field at KC=20

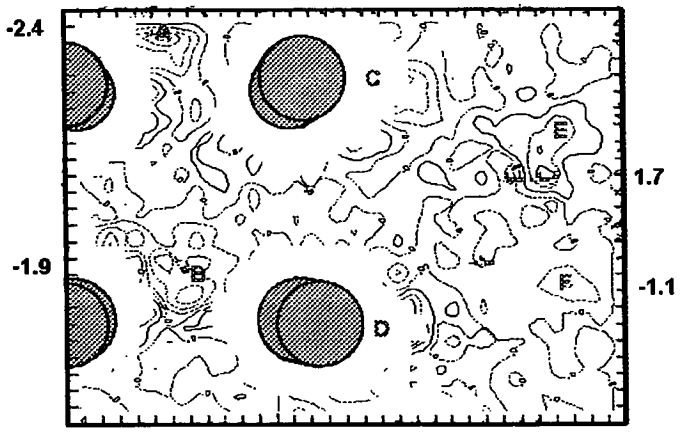

Fig 6.18 Vorticity field at KC=13

The vorticity values of the vortices centres at KC = 20 were slight larger than those at KC= 13. So the vorticity difference between positive and negative centres was larger at KC=20 than at KC=13 . For KC = 20, $\Delta\omega$ = + 3.1-(-2.2) = 5.3 ; For KC = 13 , $\Delta\omega$ = +1.7 -(-2.4) = 4.1 This feature is the same as in the cases of a single cylinder and two cylinder structures.

About the vorticity strengths at different phases at the same KC number, Fig 6.19 showed the vorticity fields at four phases. Their KC number was 10.

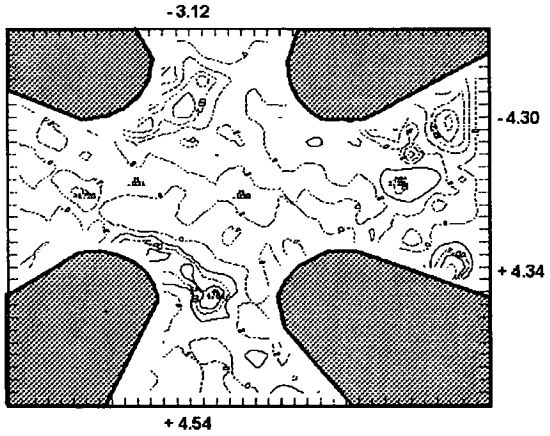

Fig 6.19 (a) Vorticity field at phase ½ π , KC =10

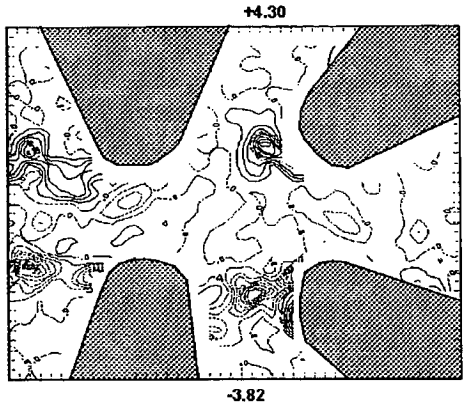

Fig 6.19 (b) Vorticity field at phase π , KC =10

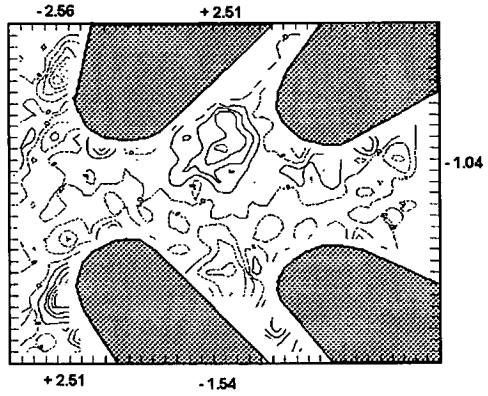

Fig 6.19 (c) Vorticity field at phase 3/2 π , KC =10

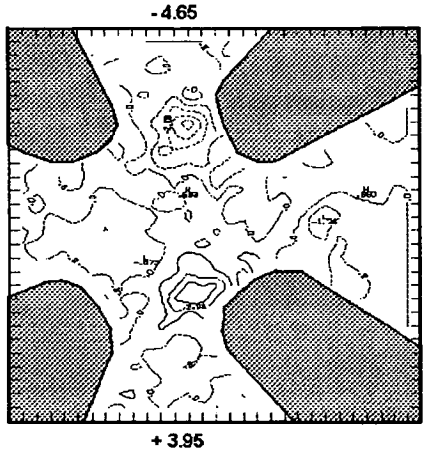

Fig 6.19 (d) Vorticity field at phase 2 π , KC =10

The vorticity values in the vorticity centres were similar at phases ½ π and 2 π. At phases π, it was a slight larger and at 3/2 π the values were weaker.

6.4 The Results of Numerical Modelling

The numerical simulation has been done for KC numbers of 10, 8 and 5 . The basic results are comparable with the experimental results.

6.4.1 Frequency of the lift force coefficients

The frequency peak of the oscillatory flows was at 0.21876 .as shown in Fig 6.20.

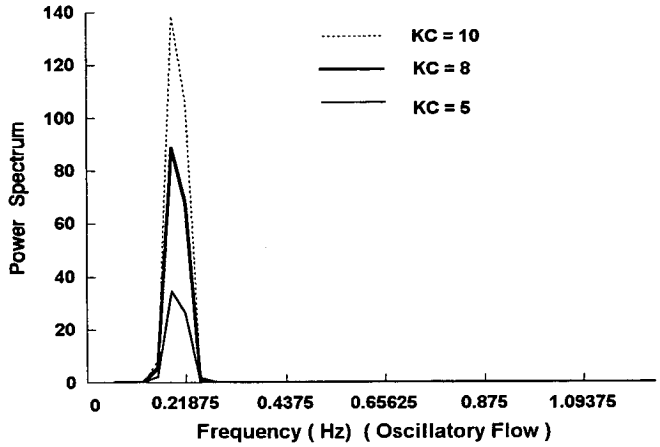

Fig 6.20 Frequency of the oscillatory flows

Fig 6.21 and Fig 6.22 showed the main frequencies of the lift force coefficient for the four cylinder array(right) and the single cylinder (left). At KC =5, the main fequencies of both cases were the first harmonic of the oscillatory flow . When KC number increased up to 8 and 10, the main frequencies moved to the second harmonic . The results were the same as the results of laboratory experiments. The arrows in the Figs pointed at the frequency position of the oscillatory flow.

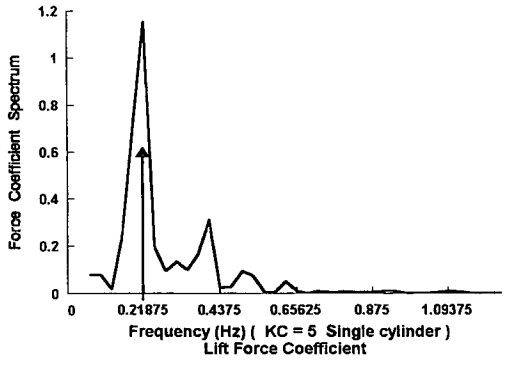

(a)

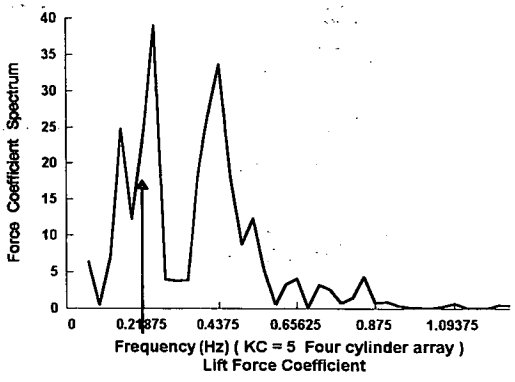

(a)

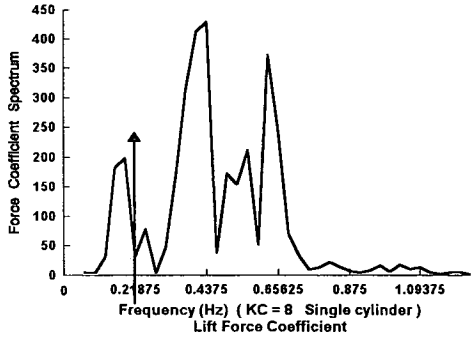

(b)

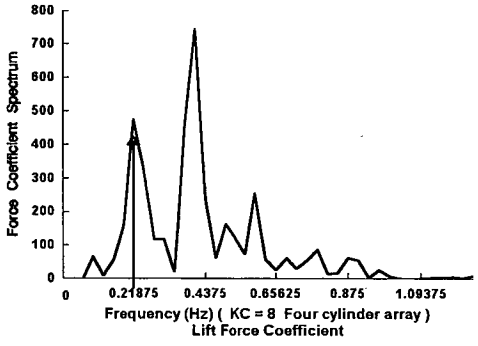

(b)

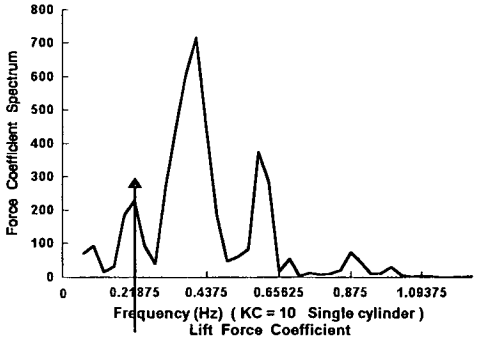

(c)

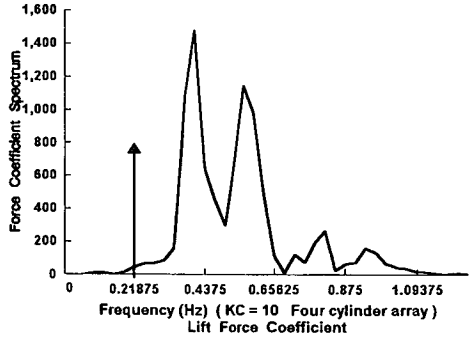

(c)

Fig 6.21 (left column) Frequency of the lift force coefficients for the single cylinder
Fig 6.22 (right column) Frequency of the lift force coefficients for the four cylinder arry

An advantage of the numerical simulation is that it can calculate the force coefficient of any cylinder in the four cylinder array at the same time. It is not so easy to investigate the results in a labolatory wave tank. Because it will involve in adding many equipments in experiments.

Fig 6.23 is a result of numerical simulation which showed the main frequency of the lift force coefficients of the four cylinders at KC = 8.

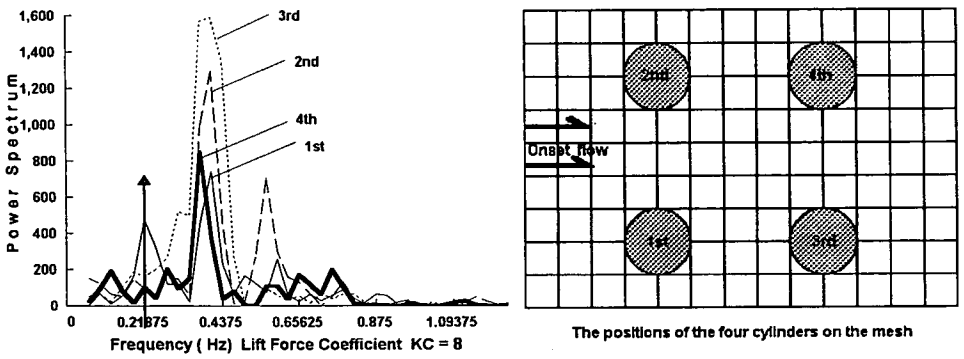

(a) (b)

Fig 6.23 Frequency of lift force coefficients and their positions of the four cylinders

The main frequencies of the four cylinders were the second harmonic of the oscillatory flow, that of the 4^{th} is near to the second harmonic. When the design of the oscillatory flow was symmetry to the four cylinder structure, the main frequencies of the lift force coefficient of the four cylinders were basically identical. In general, the second harmonic should be the main freqency of the lift force coefficient at the KC number . If ,however, suitable equipment was available, it should be better to simultaneously make measurements at each of the four cylinders.

6.4.2 The streamline fields

The numerical simulation has given some good results at the phases for which the velocities of the oscillatory flow are smallest, that is at π and 2π . Fig 6.24—6.26 show the streamline fields at KC 10, 8 and 5 at phases π (a) and 2π (b).

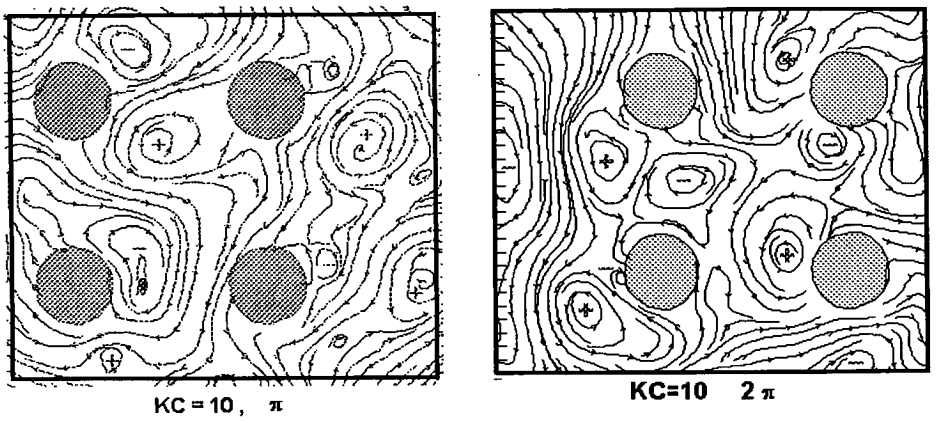

(a) (b)

Fig 6.24 The streamline field around the four cylinders at KC = 10

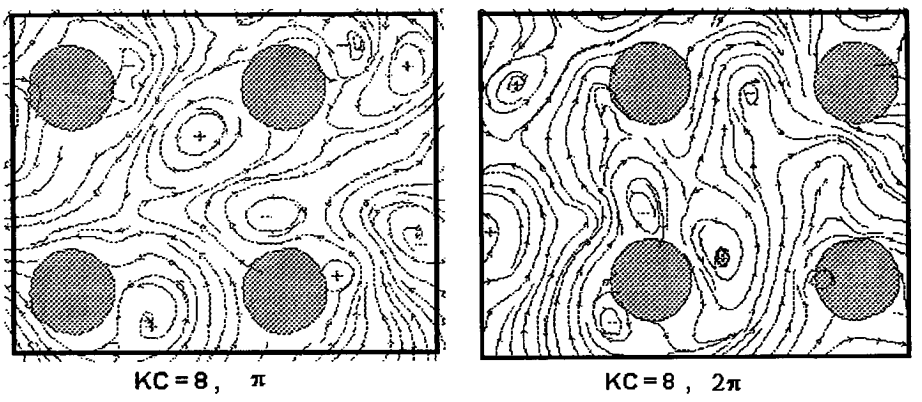

(a) (b)

Fig 6.25 The streamline field around the four cylinders at KC = 8

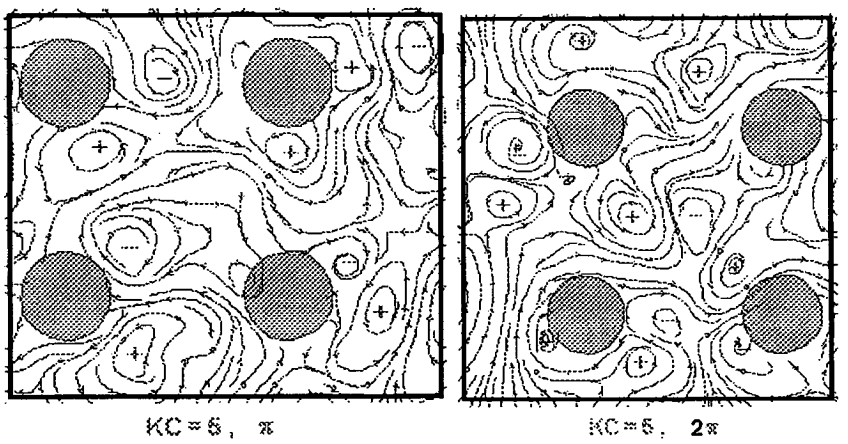

(a) (b)

Fig 6.26 The streamline field around the four cylinders at KC = 5

The vortices in the middle area of the four cylinder array and in the wake of the four cylinder structure have been simulated, they were comparable with the results of the water

tank experiments in Fig. 6.16. As the KC number decreased, the size of the vortices was reduced. This can be found through seeing how many vortice in the gap area and the number increased when the KC number decreased.

Basicly every cylinder has two vortices with opposite rotating directions in its wake. The existence of the four cylinders structure made an impact on the path the vortices moving and the length of time they exist. The activities of the vortices have also changed the velocities of the original oscillatory flow in the four cylinders area. At relative small KC numbers the interaction between the oscillatory flow and the four cylinders may be not remarkable for a cylinder array with gap ration 2.58 : 1. When the KC number incresed further, the interaction could be shown not only in vortices flow maps, but also from the force frequency and strength charts. For example, at KC = 20, the single cylinder had its main frequency of the lift force at the third harmonic of the oscillatory flow frequency (Fig 6.9(e)); but no the third harmonic has been observed in the four cylinders cases at the same KC number. The vortices shedding has been affected by the interaction between the flow and the structure.

The influence was also shown in the variance of the pressure distribution around the cylinder surfaces. In Fig 6.27 the pressures calculated by numerical simulation were shown for a single cylinder and a four cylinder array at KC =10. They were the average values of the integral time steps and the thickest line was the pressure of the single cylinder .

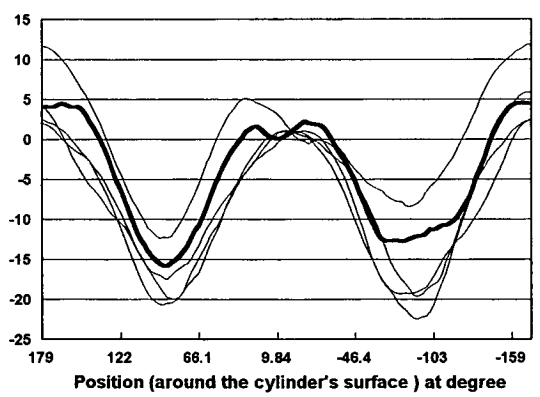

Fig 6.27 The pressure on the surfaces of the cylinders

It can be seen that the amplitude of the thickest line was smaller than the amplitudes of the thinner lines which represented the pressures on the four cylinders. The interaction between the flow and the structure caused different pressure differences between a single cylinder and the combined cylinders. They also produced the different pressure distribution on the surface of the cylinder in the two cases. A main reason for this kind of the stronger pressure difference was the convergence and divergence of the flow field in the area between the upper cylinder row and the lower cylinder row in the four cylinder array.

6.4.3 The vorticity features

The differences in the vorticity between centres of positive and negtive vortices increased with KC numbers and the feature was similar to those of single and two cylinders cases. The details were shown in Fig 6.28 – Fig 6.30.

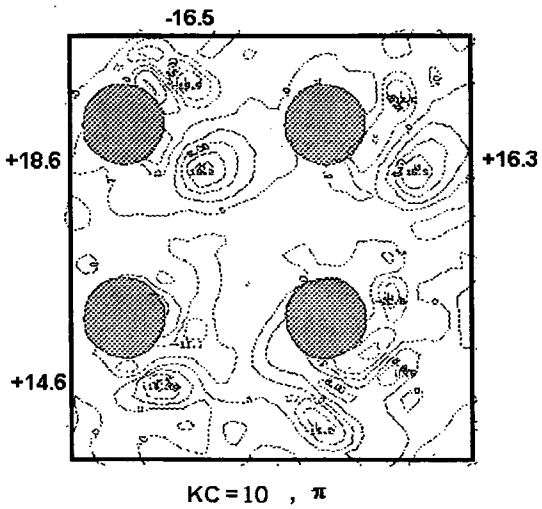

Fig 6.28 Vorticity distribution at KC = 10

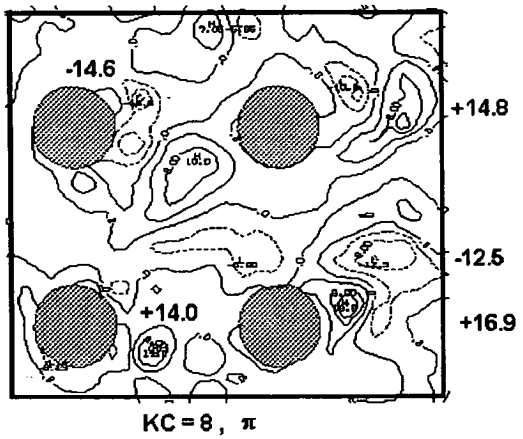

Fig 6.29 Vorticity distribution at KC = 8

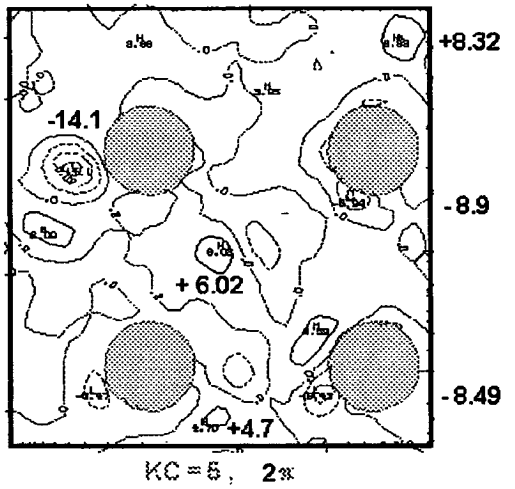

Fig 6.30 Vorticity distribution at KC = 5

The difference in vorticity centres were :

$\Delta\omega = 18.6-(-16.5) = 35.1$ at KC = 10

$\Delta\omega = 16.9-(-14.6) = 31.5$ at KC = 8

$\Delta\omega = 8.32-(-14.1) = 22.42$ at KC = 5

The above results showed that the values of the vorticity difference gradually decreases as the KC number became smaller. For a single cylinder the values obtained for $\Delta\omega$ are:

$\Delta\omega = 21$ at KC=10 ;

$\Delta\omega = 20$ at KC = 8

$\Delta\omega = 18$ at KC = 5

Comparing these values we can find that $\Delta\omega$ for the four cylinder array was slightly larger than $\Delta\omega$ for a single cylinder. So at a larger KC number and the four cylinder structure, the possibility of strong vortex appearing will be large. In the section 6.2.1, we have metioned that the four cylinder structure experienced a larger lift force than a single cylinder. Following these results the material of the four cylinder array should be chosen stronger or thicker (if a tube was used) than that used for a single cylinder which has the same diameter.

6.5 Summary for Different Cylinder Combinations

After investigating the oscillatory flows past the different cylinder combinations, some features and laws can be summarized.

6.5.1 The strength of the force

6.5.1.1 The strength of the in-line force

The in-line forces acting on the different cylinder combinations increased with KC number. See Fig 6.31.

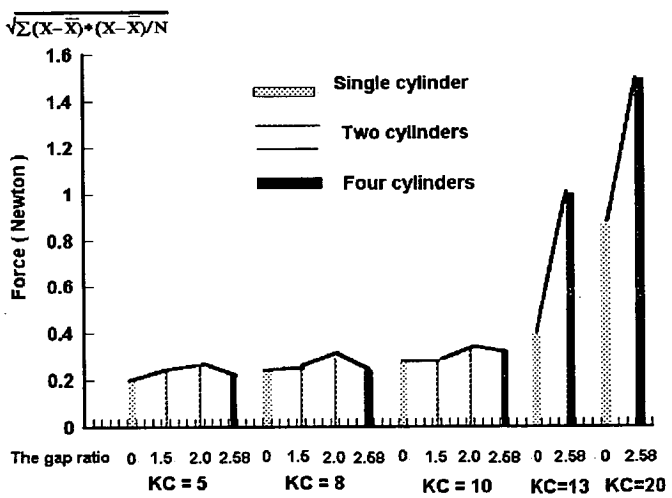

Fig 6.31 The strengths of the inline forces

Here the gap ratio is the distance between two neighbor cylinder centres to the diameter of the cylinder. A single cylinder has a zero gap ratio; the two tandem cylinders have two ratios : 1.5 and 2.0; for the four cylinder array its gap ratio is 2.58.

It can be found that there is a critical value of gap ratio at 2.0 , which affect the in-line forces. When the gap ratio is less and equal to it, the in-line force experienced by the cylinder is proportional to the gap. For a gap ratio > 2.0 the force decreases slightly. The phenomenon happens for KC = 5, 8 and 10. It is uncertain whether or not the phenomenon occurs for KC > 10, due to no data being collected at higher values of KC for the two cylinder cases

6.5.1.2 The strength of the lift force

The lift force increases with KC number for any cylinder combination, see Fig 6.32. For the single cylinder, the average lift force is less than that of the in-line force, but at some moments the amplitude of the lift force can be larger than that of the inline force. All of multi-cylinder combinations suffer a larger lift force than that on the single cylinder.

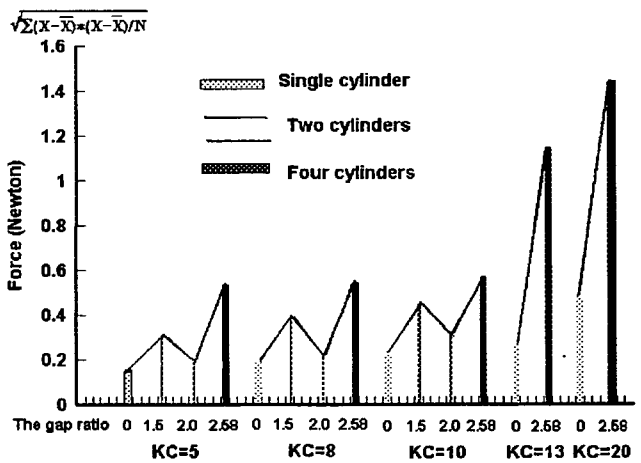

Fig 6.32 The strengths of the lift force

Like the strength of the in-line force, the gap ratio =2.0 is also a special value. Although the lift forces at the gap ratio are larger than those of the single cylinder, they are indeed

smaller than at gap ratios 1.5 and 2.58. A possible reason is that the strength of flow convergence on the top (bottom) of the cylinder is larger at gap ratio 1.5 and 2.58. Because of the obstructure of the downstream cylinder, the shed vortex has to move to the direction higher from the cylinder centre. When the main flows pass over the cylinder and meet the vortex, the flow convergence will happen on the top(bottom) of the cylinder. There is no such convergence on the bottom(top) of the cylinders at the same moment because the vortices are asymmetry shedding . At gap ratio =1.5, the vortex moves higher than ratio 2.0, this will cause a stronger flow convergence and pressure, so a larger lift force. For ratio 2.58 (the four cylinder array), there are vortice in both side of the cylinder, this disturbance cause a stronger flow convergence than ratio 2.0 then a stronger lift force.

6.5.2 The main frequency of the forces

When the KC number increases in the range 5 to 20, the main frequency components of the in-line force are the same as the oscillatory flow. This is true for any multi-cylinder combination including the single cylinder.

For the frequency of the lift force, at the single cylinder cases, the main frequency of the lift force shift from the first up to the third harmonic of the oscillatory flow. The third harmonic happened at KC=20. At KC =8 10,13 the vortex shedding is asymmetry, in one cycle there are the two vortices shedding from and two vortices moving over the cylinder. These cause the pressure differences between the top and the bottom of the cylinder four times in one cycle, then they form the main frequency of the lift force to be the second harmonic. When KC number increases to 20, there are more small vortex shedding is observed (Fig 4.16(b)), they result in the third harmonic as the main frequency of the lift force.

For the two tandem cylinders, their main frequency of the lift force are the second harmonic of the oscillatory flow. That happened almost for any KC numbers and different gaps. Beacuse the force masurement is carried out only on one cylinder of the two

cylinders, so the difference of the force on the two cylinders can not be found. The numerical simulation shows that they are almost the same , the second harmonic matched both two cylinders. But an inconsistency happens at KC number =10 for both gaps of 2.0 and 1.5. One cylinder of the two tandem cylinders has the second harmonic as the main frequency and the other has the first harmonic as the main frequency. This feaure hasn't been confirmed by experiment. Using video recording, two vortex sheddings in a one oscillatory period have been found for any two tandem cylinders so their main frequencies of the lift force are the second harmonic of the oscillatory flow.

For the four cylinder array, with KC number increasing, the main frequency of the lift force gradually shift from the first harmonic to the second harmonic of the oscillatory flow. Unlike the single cylinder , the four cylinder array has no the third harmonic as the main frequency at KC = 20 . According to the video recording one vortex shedding and one vortex running over the cylinder have been seen in a half oscillatory flow period, so their main frequencies of the lift force are the second harmonic. The interaction between the four cylinder structure and the oscillatory flow is not remarkable on the frequency feature of the lift force for the gap larger than 2.5 times of the diameter of the cylinder and KC number lower than 13. So it is a reasonable design that the four cylinders array in real case are arranged into distance between two neighbor cylinder centres being larger than 2.5 times of the cylinder diameter

6.5.3 The flow patterns

The vortex patterns show that size of the vortices and the wake width expand with KC number. The vortices area and wakes of the cylinder combinations can be roughly classified into three kinds, they are shown in Fig 6.33.

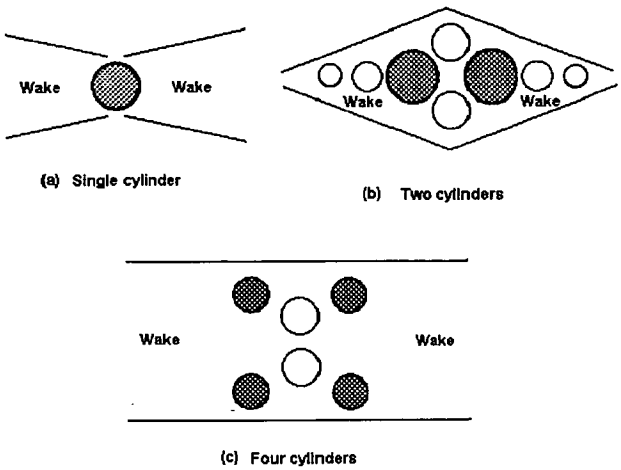

Fig 6.33 Three types of vortices and wake area for different cylinder combinations
(The white circles represent the vortices)

The wake of the single cylinder looks like two wing shape ; for two tandem cylinders the vortices action area round the cylinders seems a diamond shape; and in the four cylinder case , the vortices move about in a rectangle zone.

A basic process of the vortex shedding from a single cylinder is that at KC =5 the vortices shedded symmetrically from the top and bottom of the cylinder. Then they were carried by the oscillatory flow to pass over the cylinder. Before leaving the cylinder's surface they broke by the flow changing direction. When KC number increased further, the vortices shedding became into asymmetrical, one after another.

For two cylinders, a large KC number will cause the flow pass the gap fast and the flow path is alomst straight perpendicular to the cylinder row. With KC number decreasing, the flow passes the gap as a curve shape and matches the vortices outline. Its path is getting more flat. At KC = 5 the flow can stay the gap and form a short stagnancy .At the same KC number, a thinner gap will be easier to make a flow jet in the gap.

In the middle area of the four cylinder array, there are always two vortices with opposite rotating directions . The four cylinder array arrangement can lead to a transverse flow development in the middle area of the four cylinders and also causes the larger and wider

wakes at both outsides of the whole structues. Their size increases with KC numbers and can be maintained over a half period .

6.5.4 The vorticity features

Since using the PIV technique , it has become possible that the vorticity is calculated from PIV velocity maps. So we can investigate the flow feature quantitatively. Table 6.1 shows a vorticity values list for different KC number and different cylinder combinations. These vorticity values are the difference between positive and nagetive vorticity centres round the cylinders. They show the difference between two shed vortices.

Cylinders / Difference of vorticity / KC number	Four cylinders T/D=2.58		Two cylinders T/D=2.0		Two cylinders T/D =1.5		Single cylinder	
	Experiment	Simulation	Experiment	Simulation	Experiment	Simulation	Experiment	Simulation
KC =20	5.3	N/A	N/A	N/A	N/A	N/A	11.7	N/A
KC =13	4.1	N/A	N/A	N/A	N/A	N/A	5.4	N/A
KC =10	8.2	35.1	6.24	21.50	6.52	16.67	3.9	21.0
KC = 8	N/A	31.5	4.34	16.00	8.39	14.66	2.7	20.0
KC = 5	N/A	22.42	N/A	14.82	N/A	12.61	N/A	18.0

Table 6.1 The difference of the vorticity between positive and negative centre

From the vorticity analysis a tendency can be found that the vorticity difference between the positive and the negative centres of vorticity will decreases when KC number is smaller. This tendency was presentated very well in single cylinder case, no matter the results came from experiment or numerical modelling. For the other cylinder combinations, the numerical simulation can always have the tendency. But the the experimental results, sometimes, have some unexpected values, which are possible to be caused by deform of the vortices on a negative when the camera didn't collimate the centre of the cylinder diameter or by different resolutions, for example, the resolutions of the four cylinder model at KC=13 and KC=20 are lower than those at KC =10 ,8 and 5.

The vortex strength show that the vortex will be stronger at a larger KC number. For the two tandem cylinders, the vortex strength increases with the gap ratio , this may be a reason of that the inline force is stronger at a wider gap.

6.6 Conclusions

Some main conclusions can be obtained from above results and analysis for the oscillatory flow round a four cylinder array.

1) The strenght of the inline force and lift force

For the four cylinders array with a gap ratio of 2.58 :1, every cylinder can experience an inline force which is almost the same as the inline force on a single cylinder when the KC numbers are small. With the KC number is increased to 13 or over , the inline force on a cylinder in the four cylinder structure noticeably larger than that on a single cylinder at the same KC number.

The lift force acting on the cylinder in the four cylinder array is larger than that on the single cylinder case for all KC numbers which are chosen here, those are 20, 13, 10, 8 and 5. Because there are vortices at both sides of each cylinder in the four cylinder structure while for the single cylinder the vortices only appear in its wake side, a more stronger flow convergence happens on the cylinder in the four cylinder array than on the single cylinder, so four cylinder array experiences a larger lift force.

More detail about the vortex shedding still remain unclear due to the limitation of the observation tools and simulation methods. So near future work is to obtain the velocity maps of vortex life cycle which could show vortex generation on the surface of the cylinder until vortex shedding from the cylinder. These will help us to find the positions of the flow separation and vortex shedding and to understand the force evolution.

2) The main frequency of the forces

The main frequencies of the inline forces are, as usual, the same as that of the oscillatory flow for any KC number chosen here.

When the KC number increased, the main frequency of the lift force gradually moves from the first harmonic to the second harmonic of the oscillatory flow. Unlike the single cylinder , the four cylinder array has no the third harmonic as the main frequency at KC = 20. The main reason for that the lift force main frequency being the second harmonic of the oscillatory flow is that there are one vortex shedding and one transverse flow running over the cylinder in each half period. These cause two large differences in pressure on the cylinder in every half period of the oscillatry flow.

With the exception of the KC = 20, result the main frequency of the lift force on a cylinder in the four cylinder combination is similar to that on the single cylinder. The influence of the four cylinder structure is not remarkable on the frequency feature of the lift force for a gap between two neighbour cylinders longer than 2.5 times the cylinder diameter and a KC number lower than 13. So it is a reasonable design that the four cylinder array in a real situation has the neighbour cylinders been seperated by distances longer than 2.5 times their diameter.

3) Vortex pattern features

The size of the vortices increases with the KC numbers.

In the middle area of the four cylinders array , there are always two vortices with opposite rotating directions. Although ,in fact, they experience a period from disappearance to regeneration with the oscillatory flow, the replacing process maintains two big vortices staying in the middle area no matter what the phase is. The numerical simulation is not good at simulating this, at some phases of the oscillatory flow there is no vortex or only a few small vortices .

The four cylinder array arrangement can lead to a transverse flow developing in the middle area of the four cylinders and can cause bigger and wider wakes at both outsides of the whole structues. Their size increases with KC numbers and they can be maintained over half a period . So the four cylinder structure can influence the basic oscillatory flow over an area several times its own size.

4) Vorticity features

The rotation of the vortices caused the flow divergence and convergence between upper cylinder row and lower cylinder row in the four cylinder model. This process gave stronger lift force on the four cylinder structure compared to that on the single cylinder. According to vorticity analysis, the strength of the vorticity difference between positive and nagetive centres round the cylinder surfaces gradually increases with the KC number. Comparing these $\Delta\omega$ with those in the single cylinder cases, we found that the four cylinder structure has a sligtly larger $\Delta\omega$. The results of numerical simulation for the phenomena are satisfactory.

5) The pressure distribution

The time average pressure around every cylinder has a larger amplitude for the four cylinder structure than that of the single cylinder. The interaction between the flow and the structure causes the different vortex sheddings in the single and combined cylinder cases. This results in the different pressure distributions on the surface of the cylinder in both cases. As the cylinder will experience a stronger lift force and variance of pressure in four cylinder array, the material of the four cylinder array should be chosen a stronger or thicker (if a tube was used) than that of the single cylinder which has the same diameter. Then a using period with the same long time could be maintained for both situations.

6) Computer simulation

Computer simulation has given more descriptions about the oscillatory flow past the cylinders, such as pressure distribution, forces acting on each cylinder in the four cylinder

array, and details of the vortices at small KC number. These are a complementary to the laboratory investigation. In general, the results of the numerical simulation are satisfactory.

6.7 References

[1] T.H.Dawson , Offshore structureal Engineering, 1983, Prentice-Hall, Inc., Englewood Cliffs, New Jersey, U.S.A.

[2] O.C.Zienkiewicz, R.W.Lewis,K.G.Stagg, (Edited) Numerical Methods in Offshore Engineering, 1978, John Wiley &Sons Ltd., Bristol, U.K.

[3] C.C.Mei, The Applied Dynamics Of Ocean Surface Waves, 1989, World Scientific Publishing Co. Pte.Ltd. Singapore

[4]Howard Georgi , The Physics Of Waves, 1993, A Simon & Schuster Company, Englewood Cliffs, New Jersey , U.S.A.

[5] K.Lam and W.C.Cheung , Phenomena Of Vortex Shedding And Flow Interference Of Three Cylinders In Different Equilateral Arrangements, (1988) J.Fluid Mech. Vol 196 pp 1-26.

[6] R.P.Nordgren , Analysis Of High-Frequency Vibration Of Tension Leg Platforms, Journal of Offshore Mechanics ands arctic Engineering, (1987) vol 109, pp119-125

[7] S.A.Higgins , J.B.Hinwood and K.P.Thiagarajan , Response Prediction of a TLP in Cyclonic Storm Conditions, (1997) , The Proceedings of the Seventh International Offshore and Polar Engineering Conference, U.S.A

[8] M.Kobayashi, K.Shimada and T. Fujihira , Study on Dynamic Responses of a TLP in Waves, (1987) Journal of Offshore Mechanics and Arctic Engineering, vol 109 pp61-66.

[9] G.Godin , The Analysis of Tides , (1972) , William Clowes & Sons Limited, London, U.K.

[10] Sarpkaya & Isaacson, Mechanics of Wave Forces On Offshore Structures, (1981) Van Nostrand Reihold Company Inc. New York, U.S.A

Chapter 7

General Conclusions And Discussions

7.1 Main Conclusions

After investigating oscillatory flows past the different cylinder combinations: a single cylinder, two tandem cylinders and a four cylinder array, some features and laws can be summarized, which give details of the interaction between the flow and the cylinders. These results have been obtained from velocity fields and force measurements , with simultaneous data recording and quantitative analysis . Little research similar to this was been done before, and so this work should be helpful for research further in the area.

7.1.1 The strength of the forces

(1) The strength of the in-line force experienced by the cylinder is proportional to KC number. This is true for single cylinder and multi-cylinder structures. In the two tandem cylinder case , the cylinder will experience a larger in-line force for the gap ratio 2.0 than for the gap ratio 1.5. For the four cylinder array, with the gap ratio 2.58, the in-line force acting on the cylinder is almost the same as that on the single cylinder when the KC number is lower than 13. Then with the KC number increasing further the in-line force increases rapidly, to a value much larger than that on the single cylinder.

The inline force is composed of three components : the inertia force, the pressure drag force and the friction drag force. The inertia force is due to the acceleration, or the deceleration, of the oscillatory flow. The pressure drag is associated with the distribution of the velocity of the flow around the cylinder and is proportional to V^2. It is largerly the difference between the high pressure in the front stagnation region and the low pressure in the rear separated region. The friction drag is the integrated shear stress. A large KC number produces large velocities and accelerations. The inertia force will, therefore, be

large, as well the pressure drag and friction components of the net force . So the inline force increases with KC number.

Comparing the two cylinder flow with the single cylinder flow, both at the same KC number , the pressure drag force will be the only component of the in-line force which is affected. The other two force components should keep the same as they were for the single cylinder case. The pressure in the front stagnation region should be the same as on the single cylinder. The main changes in the pressure are at the rear gap region between the two tandem cylinders. If the flow goes through the gap sufficiently fast, this will cause a lower pressure in the gap area than in the area immediately behind the single cylinder. At the same KC number, or the same velocity, the vertical flow in the gap will cause a larger inline force than that experienced by the single cylinder. A wider gap will cause more flux in the gap than a smaller gap, with a resulting lower pressure and a larger pressure drag force . So a gap ratio of 2.0 gives a larger in-line force than a gap ratio of 1.5.

For the four cylinder array, its in-line force is almost the same as that for the single cylinder when the KC number is lower than 13, because the gap ratio is 2.58 the effect of the downstream cylinder can be ignored. But when the KC number increases further, the in-line force will be greater than that on the single cylinder and the effect of the downstream cylinder becomes important.

(2) The lift force acting on the cylinder also increases with KC number for all cylinder combinations. The average strength of lift force is weaker than that of the in-line force, but at some instances the amplitude of lift force evolution can be larger than that of the inline force. All the multi-cylinder combinations experienced a larger lift force than that acting on the single cylinder. In the tandem cylinder case the cylinder experienced a larger lift force for the gap ratio 1.5 than for the gap ratio 2.0; this is different from the situation of the in-line force. For the four cylinder array, the lift force is much stronger than that acting on the single cylinder.

The lift force arises from the asymmetry of the flow around the cylinder about the axis in the flow direction; The asymmetry is associated with the vortex shedding and shed vortex strength. When vortex shedding happened, it will cause the difference in pressure between the top and the bottom of the cylinder so the cylinder will experience a transverse force --- lift force. When the KC number increases, the strength of the shed vortex will be stronger and the difference in pressure between the top and bottom of the cylinder will be larger. So lift force increases with KC number.

Because the downstream cylinder obstructs the flow behind the upstream cylinder, the vortex shed from the upstream cylinder is deflected away from the horizontal line between the centres of the cylinders. When the main flow passes over the cylinder and meets the vortex, flow convergence will happen on the top (bottom) of the cylinder. There will be no such convergence on the bottom(top) of the cylinder at the same moment because the vortex shedding is asymmetrical. It will cause a stronger difference in pressure between the top and the bottom of the cylinder. At a gap ratio of 1.5 the vortex moves higher than when the ratio is 2.0; and this causes a stronger flow convergence and pressure. Consequently, a larger lift force acts on the two cylinder structure than on the single cylinder, and a stronger lift force is experienced by the cylinder in the gap ratio 1.5 than in the gap ratio 2.0.

For the four cylinder array, there are vortices on both sides of the cylinder; and because of the existence of these vortices around the four cylinders, the flow and its velocity between the two rows of cylinders are changed and uneven. These will cause a larger flow convergence on the bottom of the upper cylinder and the top of the lower cylinder, which is larger than that on the top of the upper cylinder and the bottom of the lower cylinder. Further the flow field causes a larger pressure difference between the top and bottom of the cylinders than that for the single and tandem cylinder cases. It results in the lift force on the four cylinder array being larger than that of on the single cylinder and the tandem cylinders.

7.1.2 The Main Frequency of The Forces

(1) The main frequency component of the in-line force is the same as the frequency of the oscillatory flow.

This is true for both multi-cylinders combinations and the single cylinder, for all KC numbers used in our experiments (KC= 5---20).

(2) There are differences in the main frequency of the lift force for the different cylinder arrangements. In the single cylinder case, the main frequency of the lift force shift from the first to the second, and then the third harmonic of the oscillatory flow as the KC value increases to 20. For the two tandem cylinders, the main frequency is the second harmonic of the oscillatory flow for all KC numbers and the different gaps. For the four cylinder array, with KC number increasing, the main frequency gradually moves from the first harmonic to the second harmonic of the oscillatory flow, but there is no third harmonic at KC=20.

Because the force is measured on only one of the two cylinders, the difference between the lift forces acting on the two cylinders can not be found. The numerical simulation has shown that the lift forces on the two cylinders are almost equal , both two cylinders have the second harmonic as their main frequencies. But the simulation predicts an inconsistency at a KC number of 10 for both gaps of 2.0 and 1.5. One of the cylinders has the second harmonic as its main frequency whilst the other has the first harmonic. This feature has not been confirmed by experiment. The numerical simulation for the four cylinders has shown that the force acting on each cylinder of the four cylinder array has similar main frequency. Sometimes one cylinder has a slight deviation on the main frequency. These have not been confirmed by the experiment .

For the single cylinder, at KC=5, the vortices stay attached to the cylinder and have different strengths. The difference is quite small, and below the threshold of our PIV technique, but because of its exsitence, it results in a weak lift force. One pair of vortices is created in each half period of the oscillatory flow, so the main frequency of the lift force

is the same as the oscillatory flow. At KC = 8, 10, 13 the vortex shedding is asymmetrical, with two vortices shedding from cylinder and two vortices moving over the cylinder. These cause the pressure difference between the top and the bottom of the cylinder to change four times in each cycle with the result that the main lift force frequency is the second harmonic. When the KC number increases to 20, there are more small vortices shed and they result in the third harmonic being the main frequency of the lift force.

Using video recording, it was observed that two vortices were shed in each half oscillatory period for the tandem cylinders with gap ratios 1.5 and 2.0. So the main frequencies of the lift force are the second harmonic of the oscillatory flow. In the four cylinders case, one vortex is shed and one vortex runs over the cylinder in a half oscillatory flow period, so the main frequency of the lift force is the second harmonic.

7.1.3 Flow Patterns

The vortex patterns show that the size of the vortices and the wake width expand with increasing KC number . The wakes of the cylinder combinations can be roughly classified into three kinds : 1) the two wing shape for a single cylinder in oscillatory flow, 2) the diamond shape for the tandem cylinders, and 3) the larger rectangle area for the four cylinder array.

In the single cylinder case, at KC =5, the vortex shedding looks symmetrical about the flow direction. The vortices are then carried back to the cylinder by the oscillatory flow before they leave off the cylinder's surface then they are broken. When the KC number is increased further, the vortex shedding becomes asymmetrical, and the vortex size also increases.

For two cylinders and a large KC number, the flow through the gap is fast and is almost straight vertical to the axis through the two cylinders. For lower KC numbers, the flow direction in the gap becomes closer to the main flow direction. At KC = 5 some parts of

the flow can stay in the gap and form a short stagnancy . At the same KC number, a thinner gap will be easier to make a flow jet in the gap.

In the middle region of the four cylinder array, there are always two vortices with opposite rotations, no matter what the oscillatory flow phase is. The four cylinder array arrangement can also lead to a transverse flow developing in the central region of the four cylinders .The relationship between all of the flow patterns with the force features have been disccussed in 7.1.1 and 7.1.2.

7.1.4 The Vortex Strength and Vorticity Features

The vortex strength, in general, increases with KC numbers for both a single cylinder and the tandem cylinders. For two cylinders, at a given KC number, a larger and stronger vortex forms in the gap when the gap itself is larger. When gap size is fixed, a stronger vortex will cause a stronger lift force. At the same KC number a wider gap will match a stronger vortex which is closer to the horizontal axis of the cylinder . The stronger vortex will give more influence on the horizontal direction and cause a stronger inline force.

The difference in vorticity value between the positive and the negative centres of vortices will decrease as the KC number decreases. For the single cylinder, both the experimental and numerical results show this tendency very obviously. However, for other cylinder combinations, Though the numerical simulation always shows this tendency, the experimental results, sometimes, do not. It is possibly caused by the deformation of the vortices under the non-vertical angle between cylinder centre and the camera, when errors can arise in velocity analysis and vorticity calculation. The difference in vorticity central value shows the difference between two shed vortices. If the difference is larger , the pressure difference on the cylinder will be larger, then there will be a larger inline force and lift force acting on the cylinder.

7.1.5 Some Improvements

(1) Interpolation in the PIV mapping

In almost all applications of PIV there will be a number of interrogation points with incorrect values for the velocities. These values arise from the detection of a distorted displacement correlation peak, or from a complete loss of the signal. After removing these invalid values, a reliable interpolation, or extrapolation, techniques have to be used to put suitable velocity values in their place.

A comparison of different interpolation methods has been carried out for the special nature of the validated PIV data. The weight function interpolation was found to be the most suitable algorithm. So the new version of VIDPIV has adopted the weight function interpolation. which is better and faster than previous interpolation algorithms which have been used.

(2) Flow Pattern Visualization

The flow has been visualised by using a laser to illuminate the seeded flow and recording the flow using a video. It was found that the behaviour of the vortices would be followed clearly.

According to the KC number , the flow patterns found for the single and two cylinders cases match well the classifications of Williamson [1][2] and Bearman[3]. However, the transverse vortex street with four vortices observed by Williamson was not seen in the present experiments; and it is interesting that Bearman did not observe it either. This difference might possiblely be a result of the different Reynolds numbers. For a KC value of 12 (Williamson's experiment), the Reynolds numbers for Williamson , Bearman and the present case are, respectively 3060, 5000 and 6000. The long transverse street might be established at low Reynolds numbers, but not at high ones. There is another difference, the ratio of the cylinder diameter to the tank width was 0.005 for Williamson , whereas it is 0.1 for the present case.

(3) Numerical modelling

(A) The vortex method has the feature : that during the integration , new vortices appear at the cylinder's surface and old vortices move away from the cylinder, so that the number of vortices in the integration area increases quickly with time.This rapid increase in the number of vortices will be especially obvious at big Keulegan-Carpenter numbers and for the multi-cylinders cases. The vortices occupy a huge space of memory in the computer, so it is therefore necessary to regularly reduce the number of vortices present in the simulation. There are several ways this reduction may be achieved in the model. These are Control of Number of New Vortices, Absorption at Surface, Diffusion Reduction, Limitation Of Minimum Vorticity and Combination Of Vortices. For the investigation of an oscillatory flow over a combination of cylinders, some of the reduction ways have to be modified then the model can run successfully.

For the Combination Of Vortices method, the appropriate combination area and position , the start time and frequency of combination have to be dermined by test. The combination area is at the down stream side of the model, and for an oscillatory flow, the position of the combination area has to be changed with each half period. The size of the combination depends on how many cylinders have been in the model . The combination starts after the integration has run for several periods. In a oscillatory period the combination is done twice and usually they are done every several periods interval which depends on the KC number and cylinder number.

(B) In the code a minimum vorticity strength is specified before integration begins. The vorticity of every vortex is compared to the minimum value regularly during integration. If the strength of the vorticity is smaller than the specified minimum , the vortex will be removed from the flow field. But the Vmin not only influences the computing space but also the output of the force coefficients, because the force coefficients are calculated from the surface circulation which is determined by surface vortices.

After testing different Vmin values , from 0.001 to 0.01, for different cylinder structures and different KC numbers, it has been found : if a larger Vmin is choosen , more vortices

will be deleted from the vortex collectional queue and more space can be saved . This will allow the integration to carry on smoothly but the force coefficient simulation may be unsatisfactory.A good simulation is found by comparing the force coefficient frequency of the output of the model with results of the laboratory experiments. A small Vmin may result in the integration stopping after only a few oscillatory periods. After a lot of tests, it was found that a Vmin with value around 0.005 is suitable.

7.2 Some Problems And Discussions

7.2.1 PIV Application

The PIV technique is an effective method to measure flow velocities. It will obtain a wider application in the future.The main problem of the PIV technique is that flow past the cylinders is on the boundary area of the cylinder surface. When used to measure the flow past oscillating cylinders , some areas of the flow close to the cylinder will be obscured by the cylinder itself. This is especially unfortunate as it is in these areas that vortices are created and shedding is being initiated.

Possible ways of resolving this may be

1) to move the camera nearer to the laser sheet; this will reduce the viewing area and give a higher resolution picture which could give greater detail of the flow;
2) to use different angles and positions of the camera to obtain pictures of the different areas around the cylinder , and then to gather together a more complete picture of the flow around the cylinder.
3) to use several cameras to achieve the same result as in 2).
4) to choose a two CCD camera system and use crosscorrelation. This will give more spaces on the negative for more particle images which will fall in the gap or close to the surface of the cylinders. Because the velocity calculation by crosscorrelation requires only one image on one negative for one particle. With PIV equipment development, the two CCD technique will be a good chioce.

7.2.2 Velocity Calculation

The velocity given by PIV is the average velocity over a square interrogation area on the negative. Improvements could be made , for example to combine the tracking method with the area average method together, then find a more precise direction and size of the velocity on the interrogation areas. Or using a spectrum coefficient polynomial to simulate the path of the particles, then obtaining a better velocity.

7.2.3 The Numerical Simulation

The numerical simulation can give many good simulational vector fields especially at the phases π and 2π which are at minimum velocities phases. But at some phases the numerical simulation can only give results without vortex, these usually happen at the phases which the oscillatory flow has maximum velocity or has changed its direction and increases its velocity from minimum values . In the lab experiments, PIV mapping and video recordings have shown that the vortices exist around of the cylinder for all phases in one whole period. So the further improvement needs to be tried for the computer simulation.

7.2.4 Vortex Shedding Analysis

The computer simulation is a helpful tool which can investigate the evolution of vortices in succesive phases and show the strength and moving path of vortices. The numerical simulation can choose a short integral step(after meeting the condition of the integral) and output the result at every step. But when the time step we used is $\Delta t=0.0625$, we did not still find an exact position of the vortex shedding (see Fig 4.32 in Chapter 4); a further test should be done to simulate the vortex shedding.

7.3 References

[1] Sheldon I. Green (Editor) , Fluid Vortices, Charpt V Vortex Dynamics In The Wake Of A Cylinder, 1995, Kluwer Academic Publishers , Netherlands .

[2] C.H.K.Williamson, Sinusoidal Flow Relative To Circular Cylinders, (1985), J.Fluid Mech. Vol 155, pp 144-174 .

[3] E.D.Obasaju, P.W.Bearman and J.M.R. Graham , A study of forces, circulation and vortex patterns around acircular cylinder in oscillating flow, (1988) J.Fluid Mech. Vol 196, pp467-494

Appendix
List of Publications

The following papers have been finished during the course of my Ph.D. studies

[1] J.Wang, C.A.Greated, F.H.Barnes, A Comparison Between PIV Experimental Results and Numerical Simulation on Oscillatory Flow Round Cylinders, International Workshop on Flow Diagnosis Techniques Proceedings, pp77-84, June 1998 St.Petersburg, Russia

[2] J.Wang, H. Kang, C.A. Greated , A Study of Lift Force and Instantaneous Velocity Field Around an Oscillating Circular Cylinder, Journal of China Ocean Engineering (English version) 1997, No 4, pp.419-430.

[3] J.Wang, C.A.Greated, P.K.Stansby , Laboratory and Computer Simulation Study of Oscillatory Flow Round a Combination of Cylinders,
BOSS'97 Proceedings (8th International Conference on the Behaviour of Off-Shore Structures), Volume 2 (Hydrodynamics), pp25-35. July, 1997, The Hague, Netherlands

[4] J.Wang, Y.Zhang, K.N.C.Bray, Measuring Turbulent Premixed Impinging Flow: Dynamic PIV Visualisation and Analysis,
16th International Colloquium on the Dynamics of Explosions and Reactive Systems , August, 1997 , Poland
Submitted to Journal of Combustion Science and Technology

[5] J. Wang, F.H.Barnes, C.A.Greated, Forces Acting on A Leg of A Model TLP In Oscillatory Motion ,
Ninth Scottish Fluid Mechanics Meeting, June, 1996, Paisley , U.K.

[6] J.Wang, C.Gray, F.H.Barnes, A Comparison Between Interpolation Algorithms For Post Processing Of Particle Image Velocimetry Data,
Proceedings Of The Third International Seminar On Optical Methods And Data Processing
In Heat And Fluid Flow, pp291-300, April, 1996, London, U.K.

[7] J. Wang, Y.Zhao, C.Miao, C.A. Greated, A Streamline Animation System, Proceedings of The Seventh International Symposium On Flow Visualization, pp244-248,
September, 1995, Seattle , Washington, USA

[8] J.Wang, F.H.Barnes, C.A.Greated, An Experimental and Numerical Study on Oscillatory Flow Round Two Cylinders
will be submitted to a Journal (1998)

[9] J.Wang, C.A.Greated, P.K.Stansby, A Study on Forces and Instantaneous Velocity Fields of Oscillatory Flow around a Four Circular Cylinder Array
will be submitted to a Journal (1998)